WOODHEAD PUBLISHING
IN MECHANICAL ENGINEERING

Aerodynamic measurements

From physical principles to turnkey instrumentation

Giuseppe P. Russo

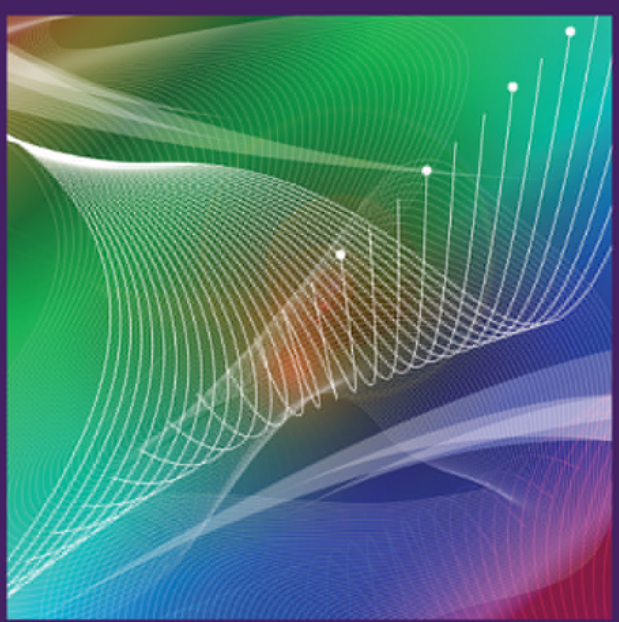

WP
WOODHEAD PUBLISHING

Aerodynamic measurements

1

Pressure sensors

Abstract: This chapter highlights pressure sensors ranging from the classical manometers, based on the displacement of the surface of a liquid or on the deflection of the walls of a metallic chamber, to pressure transducers where the deflection of a disk or of a cantilever beam is converted into an electric signal eventually digitalized and sent to a computer. Only the basic principle of pressure-sensitive paints is reported as this technique is still a subject of research.

Key words: hydrostatic manometers, mechanical manometers, pressure transducers.

1.1 Fundamental features

Pressure measurements are essential in aerodynamics for the calculation of velocity, direction and mass flow rate of a fluid stream, and are complementary to balances in measuring the aerodynamic forces acting on a body.

Pressure sensors range from the classical hydrostatic and mechanical manometers to pressure transducers and to pressure-sensitive paints (PSP). The choice depends on the magnitude of the pressure to be measured, on its steadiness, on the required accuracy and resolution, and on the ease with which data can be handled and stored.

It is important to realize that all pressure sensors measure a differential pressure, either between two pressures associated with the flow or between a flow pressure and the atmospheric pressure. Thus, if pressure data are referenced to the contemporary atmosphere pressure (gage pressure sensors), it is imperative to measure this value enabling later reduction of the data to an absolute or other standard condition. Only if the reference is vacuum absolute values of pressure are obtained.

The main desirable characteristics in a pressure gage, whether they are feasible or not, are given below. In practice, the best possible compromise is needed to adapt the instrument to the specific case:

1. *Range*. The lowest pressure obtained with techniques for the vacuum are of the order of 10^{-14} atmospheres. At the other extreme, in the laboratory pressures greater than 10^5 atmospheres were obtained. The field is so vast that a particular type of manometer may cover only a small fraction of it.
2. *Frequency response*. In many applications the pressure changes so slowly that it can be considered constant. On the other hand, the jump in pressure that occurs through a shock wave propagating in a gas at rest can occur in a time less than 10^{-7} s. Fluctuating pressures that are generated in gas guns, engine cylinders, and in gas turbines have characteristic times that cover the whole field between the two above-mentioned extremes. Frequencies range therefore from 0 to 10 MHz (but no pressure sensor developed so far is able to approach this limit).
3. *Accuracy*. Usually the accuracy of pressure transducers is referred to the full scale, i.e. the maximum measurable pressure. It is clear that if the instrument is accurate within 1% of the full scale, the measurement of a pressure that is equal to one-tenth of the full scale will be affected by an error of 10%. Therefore, for good accuracy, an instrument should be chosen whose full scale is only slightly higher than the maximum pressure to be measured.
4. *Sensitivity*. All things being equal, a high sensitivity is always to be preferred: the output signal requires less amplification (pressure transducers) or allows a more precise reading (manometers).
5. *Linearity*. Usually it is considered convenient to have the output signal proportional to pressure, but this is not only not essential but in some cases not even desirable if the measurement range is very large.
6. *Size*. The boundaries of the system to be explored can limit the size of the sensor (for example, the need to measure pressure between turbine blades or the need to insert many sensors in a wing model); the size of the sensor may affect its interaction with the stream, disturbing the measurement; because the reading is only an average on the surface of the sensor, size limits the level of detail that can be detected.
7. *Calibration*. In some cases, the response of the sensor can be calculated by an analytical equation (e.g. hydrostatic manometers). For simple systems, the dynamic response can be inferred from the

static calibration; but in most cases only a dynamic calibration provides a sufficiently reliable basis from which the results can be interpreted.

8. *Data acquisition and handling*. The hydrostatic or metal manometers require manual reading and transcription of the data. Some types of transducers produce a frequency modulated signal that has to be read by a system of demodulation to obtain pressure. Obviously, the ease and certainty with which data can be interpreted and recorded are important factors in choosing a pressure sensor.

1.2 Hydrostatic manometers

In this kind of manometer, the difference between two pressures is balanced by the difference of level in a liquid. To measure pressure in a liquid, a manometer can use the working fluid itself, this is obviously not the case when pressure is measured in a gas: the choice of the manometer fluid (or separating liquid) will be affected by the pressure field, the required sensitivity and the physical and chemical properties of the liquid. The properties of the most common manometer liquids are shown in Table 1.1.

The liquids that work best are those that are chemically stable, are not affected by moisture and have the following qualities: low viscosity, as this reduces the response time; low surface tension, low volumetric expansion coefficient, low volatility, consistency, and resistance to contamination.

1.2.1 The U-tube manometer

The fluid is contained in a glass tube with *U*-shaped vertical arms (Figure 1.1) with internal diameters more or less constant. The pressures p_1 and p_2 will be applied through suitable piping connection to the two arms of the manometer. If the difference between the heights of the columns of fluid in the two arms is Δh, it will be:

$$p_1 - p_2 = (\rho_\ell - \rho_a) g \Delta h \cong \rho_\ell g \Delta h \tag{1.1}$$

where g is the acceleration of gravity and ρ_ℓ and ρ_a are the densities of the manometer liquid and of air, respectively. The approximation made when

Table 1.1 Properties of the most common manometer liquids

Liquid	Density at 15°C (g/ml)	Surface tension (dynes/cm)	Angle of contact	Coefficient of cubical expansion per C × 10^5	Remarks
Water	0.999	74	8°(*)	5°C ÷ 10°C 5.3 10°C ÷ 20°C 15.0	(*) 0° if the glass is quite clean. Surface tension may be lowered by adding wetting agent. Corrodes iron and steel
Ethyl alcohol C_2H_5OH	0.8 (**)	22		110	(**) Rises if water is present Corrodes iron and steel
Ethylene bromide, $C_2H_4Br_3$	2.18	38		High	Attacks natural and synthetic rubber, corrodes iron and steel. Surface tension can be reduced by adding toluol.
Acetylene tetrabromide $C_2H_2Br_4$	2.98–3.00				Attacks natural and synthetic rubber, corrodes iron and steel. Surface tension may be reduced by adding toluol
Mercury Hg	13.56	465	127°	18	Combines with gold, copper and brass. Attacks iron and steel very slowly
Carbon tetrachloride CCl_4	1.58	26	0°	124	Attacks rubber, but not metals

Figure 1.1 *U*-tube manometer

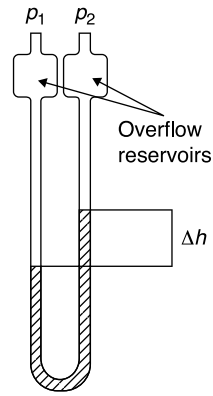

ρ_a is considered negligible with respect to ρ_ℓ is of the order 10^{-3} when water is the manometer liquid and 10^{-4} when mercury is used.

Usually one of the two arms of the manometer remains connected to the environment; in wind tunnels, sometimes it is connected to the static pressure of the stream, p_∞, so the manometer indicates the value of $p - p_\infty$ which actually determines the forces acting on the body: in fact, p_∞ is the hydrostatic pressure acting all around the body, thus giving a net zero contribution.

The manometer is susceptible to blowing its liquid into the attached pressure lines if the range of the instrument is exceeded; however, all good manometers employ overflow reservoirs at the end of the tubes to retain the fluid in case of accidental overloading.

This type of manometer is very simple and requires no calibration because pressure is obtained from the analytical Equation (1.1). Furthermore, if the internal diameters of the two arms are equal, the effects of capillarity are balanced, though small errors can arise due to the fact that the tube wall next to the liquid surface is wet in the arm in which the level decreases and is dry in the other one. Errors like these can be eliminated by raising beyond the equilibrium position the column of liquid that must rise and letting it fall back into position before taking the reading.

The only adjustments necessary are those for changes from their standard values of the density of the liquid and of the length of the scale due to changes in temperature. If the level difference measured at temperature T is Δh_T and the scale is properly calibrated to the temperature T_0, the corrected height difference, Δh, is given by:

$$\Delta h = \frac{1+\alpha\left(T-T_0\right)}{1+\delta\left(T-T_0\right)}\Delta h_T \tag{1.2}$$

where $\alpha[K^{-1}]$ is the coefficient of linear expansion of the material of the scale and $\delta[K^{-1}]$ is the coefficient of volumetric expansion of the manometer liquid. Under normal conditions the temperature changes are not large enough to introduce appreciable errors if the density and the calibration of the scale are referred to the standard temperature of 15°C.

1.2.1.1 Measurable pressure range

With a *U*-shaped vertical manometer, in order to limit the reading error to less than 2%, differences in heights less than 50 mm cannot be measured since the accuracy of the naked eye in reading the height of liquid in each tube is limited to 0.5 mm; the presence of the meniscus does not recommend the use of systems of magnification. On the other hand it is impractical to build manometers with arms longer than 5 or 6 meters.

The minimum and maximum differential pressures measurable by *U*-tube manometers using water or mercury can therefore be calculated approximately, using Equation (1.1):

Water	$\Delta p_{\min} \cong 0.5\ [kPa]$	$\Delta p_{\max} \cong 60\ [kPa]$
Mercury	$\Delta p_{\min} \cong 6.6\ [kPa]$	$\Delta p_{\max} \cong 810\ [kPa]$

For low pressure, alcohol is preferred to water because it has a surface tension which is 30% that of water and the meniscus is negligible, but its density must be controlled because it changes rapidly since it absorbs moisture from the environment. The other liquids listed in Table 1.1 and having an intermediate density are corrosive and used more rarely.

1.2.1.2 Response time of the *U*-tube manometer

The manometer will not immediately sense pressure changes because a flow has to be generated in the pipe connecting the measuring point and the manometer to compensate for the change in density of the gas inside the tube and the manometer as well for the displacement of the manometer liquid (the first cause of delay is negligible in measurements performed in liquids).

If there is a sudden change in pressure, $\pm\delta p$, a very slow viscous flow (the Poiseuille flow) is generated in the tube connecting the pressure tap to the manometer; the average speed in the section is proportional to the pressure difference between the tap and the manometer:

$$\overline{V} = \frac{1}{2} V_{\max} = \frac{p_{\text{in}} - p_{\text{out}}}{32\mu\ell} d^2 \tag{1.3}$$

where μ is the dynamic viscosity of air, and ℓ and d are the length and the diameter of the tube.

The air flow rate passing through the tube produces a change in the mass in the manometer due to both a change in density and a variation in the volume available (Vol) caused by the displacement of the liquid:

$$\dot{m} = \rho \overline{V} \frac{\pi d^2}{4} = \frac{dM}{dt} = \frac{d}{dt}(\rho \text{Vol}) = \rho \frac{d\text{Vol}}{dt} + \text{Vol} \frac{d\rho}{dt} \tag{1.4}$$

Since the displacement of the liquid surface in the tube connected to the tap is half of Δh, by using Equation (1.1), is it obtained:

$$\frac{d\text{Vol}}{dt} = A \frac{dh}{dt} = A \frac{d(\Delta h)}{2dt} = \frac{A}{2g\rho_\ell} \frac{dp}{dt} \tag{1.5}$$

where A is the area of the section of the manometer tube. In isothermal conditions, the change in density is related to the change in pressure [5]:

$$\frac{d\rho}{dt} = \frac{\rho}{p} \frac{dp}{dt} \tag{1.6}$$

Substituting Equations (1.3), (1.5) and (1.6) into Equation (1.4) yields [5]:

$$\frac{p_{\text{in}} - p_{\text{out}}}{128\mu\ell} \pi d^4 = \left(\frac{A}{2g\rho_\ell} + \frac{\text{Vol}}{p} \right) \frac{dp}{dt} \tag{1.7}$$

The pressure in the manometer varies with speed decreasing gradually as the pressure difference between inlet and manometer decreases, therefore the manometer adapts only asymptotically to the new pressure, $p + \delta p$.

We define the *time constant*, τ^*, as the time the manometer would take to adapt to the change in pressure δp if the rate of change of pressure

were maintained equal to the initial value obtained by putting $p_{in} - p_{out} = \delta p$ in Equation (1.7):

$$\tau^* = \frac{\delta p}{dp/dt} = \frac{128\mu\ell}{\pi d^4}\left(\frac{A}{2g\rho_\ell} + \frac{\text{Vol}}{p}\right) \tag{1.8}$$

For normal-sized gages the time constant varies from 1 to 10 ms (frequency range 0.1 ÷ 1 kHz). For this reason, and the difficulty of registering pressure fluctuations by hand, no hydrostatic manometers are suitable for unsteady pressure measurements.

1.2.2 The single tube manometer

The *U*-gage requires the reading of two levels since it is not advisable to measure the displacement of one meniscus from zero, assuming that this is half the difference in height, unless the inside diameter of the tube is perfectly constant.

This difficulty can be avoided by building the manometer with one arm (reservoir) with an area many times the area of the other one (Figure 1.2):

Figure 1.2 Single tube manometer

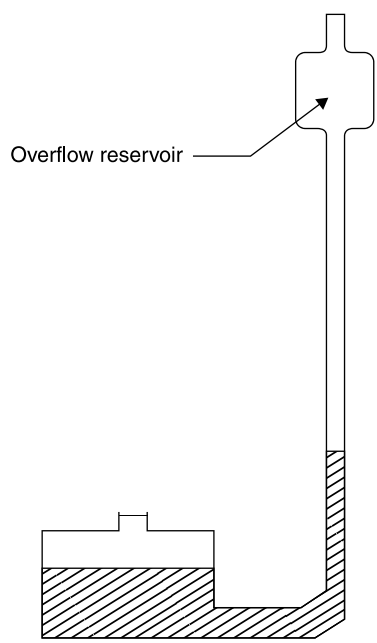

in this way, it is sufficient to read the level in the narrow tube, the change in level in the reservoir being negligible. On the other hand, the height of the reservoir can be adjusted in order to adjust the zero of the scale before making the reading. However, the single-tube manometer requires the taps to be switched to change from positive to negative differentials while either can be read without tap changes on the *U*-tube instrument.

Since the internal diameters of the two arms in this case are very different, strictly speaking, the reading should be corrected for the different effects of surface tension in the two arms. Since the magnitude of the correction depends very much on the cleanliness of the tube manometer (the presence of grease in particular has a significant effect), it would be better to reduce the effects of surface tension by adopting a pipe diameter that is not too small.

1.2.3 Inclined manometer

The sensitivity of a hydrostatic manometer can be extended by a factor of 10 using an inclined tube manometer (Figure 1.3) while preserving the simplicity and robustness of the single tube manometer.

Assuming that the change of level in the reservoir is negligible and that the effects of surface tension can be ignored, for an inclined tube manometer:

$$p_1 - p_2 = \rho_\ell g L \operatorname{sen} \alpha \tag{1.9}$$

where L is the length of liquid column above zero, and α is the inclination of the tube with respect to the horizontal. The sensitivity of the manometer increases with decreasing inclination, α; the use of angles below 5° with the horizontal brings problems due to surface tension even if alcohol

Figure 1.3 Inclined manometer

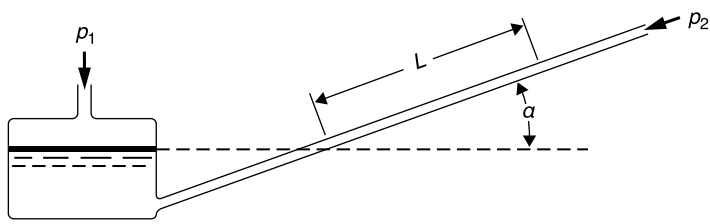

is used, because the meniscus becomes too stretched, and also the perfection of the glass tubes to the degree of precision required cannot be guaranteed.

Unfortunately, a manometer of this type must be calibrated because errors can arise due to a slight curvature of the tube or to the effects of surface tension caused by the small non-uniformity of the internal diameter.

1.2.4 Betz (or projection) manometer

A hydrostatic manometer that is easier to be read, if not more accurate, is the projection or Betz manometer. The operating principle is illustrated in Figure 1.4. The difference in level between the liquid in the cylinder *C* and the reservoir *R* is indicated by a scale suspended to a float. The scale directly shows the difference in level (the decrease in the level of *R* is accounted for in the calibration of the scale).

An enlarged image of the scale located on the plane XX is projected onto a frosted glass on which a reference line is marked. The scale can be engraved in order to show centimeters of difference in level; the fractions of a centimeter can be appreciated by comparison with a scale etched on the frosted glass.

The Betz manometer was used primarily to control the operating speed of a wind tunnel: the large internal volume makes it too slow for the measurement of unsteady pressures, as in turbulent boundary layers, and the quite high cost does not permit the use of many Betz manometers each connected to a pressure tap.

1.2.5 Multi-tube manometer

Many pressures can be measured simultaneously with a multi-tube manometer (Figure 1.5), having one or more dozens of tubes connected to a common tray connected to a reservoir open to the reference pressure. For convenience, the reference pressure is also applied to one tube (or rather to the two extreme tubes of the manometer) to allow zero adjust-ment. Tubes are laid side by side on a solid table provided with a scale and covered by a sheet of protective glass or plastic that is usually also provided with a scale: the double scale serves to eliminate the error of parallax. The position of the reservoir is adjustable and sometimes the table can be rotated; the inclination of the table can be read on a circular scale.

Figure 1.4 Betz (projection) manometer

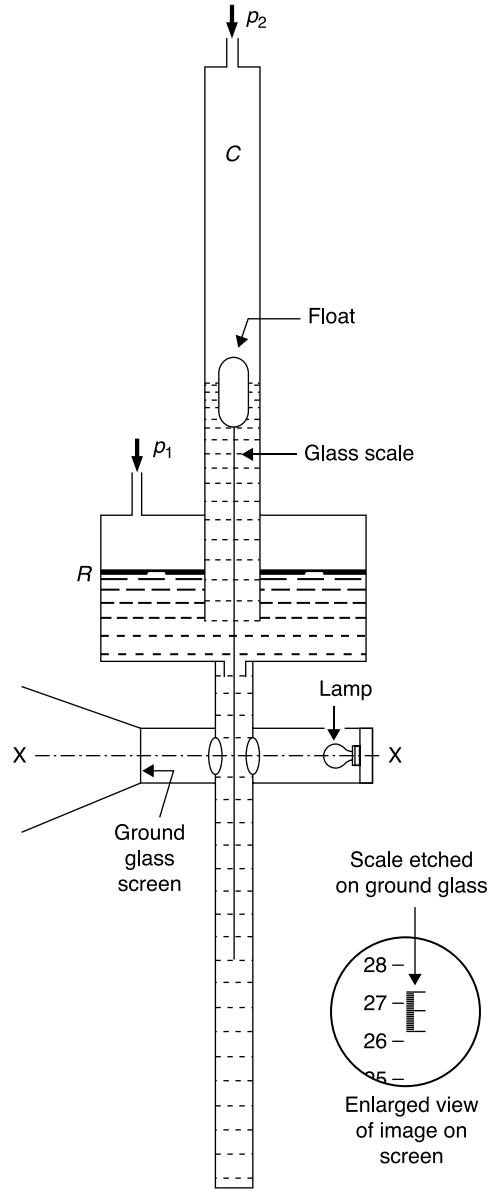

Figure 1.5 **Multi-tube manometer**

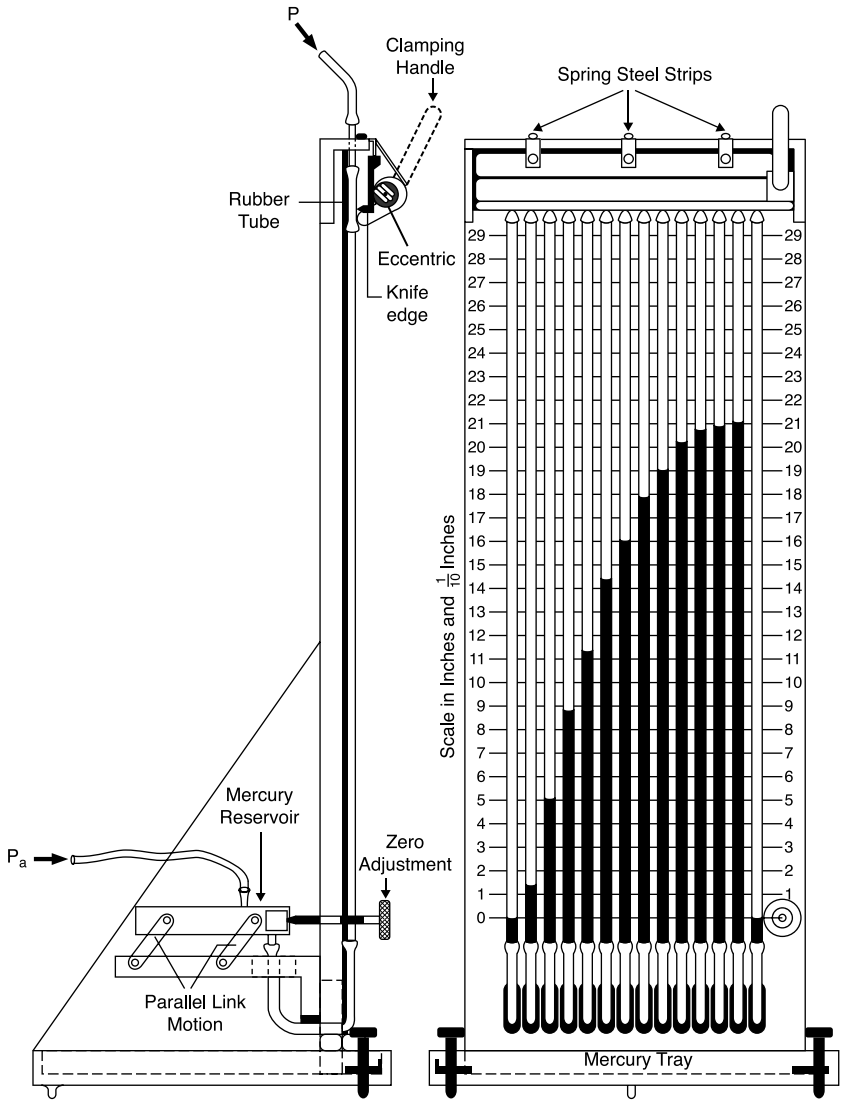

To reduce the test time, especially in intermittent wind tunnels, a means of freezing the readings of the many tubes is needed; an example can be seen in the side view of the multi-tube manometer of Figure 1.5: it consists of an eccentric placed at the top of the pipe manifolds which, when rotated, squeezes the rubber tubes, thereby blocking the pressure in them. Alternatively, results can be frozen with a camera.

1.3 Mechanical manometers

Hydrostatic manometers become impractical if pressures higher than 3 atmospheres have to be measured because, even if mercury is used, the column length exceeds 2 meters. On the other hand, hydrostatic manometers are fragile, are not portable and are therefore only suitable for laboratory applications. In an industrial environment, manometers are therefore used in which the difference in pressure causes the deformation of an elastic element.

In the Bourdon gage (Figure 1.6), the sensor is a tube with a flattened section closed at one end and bent as an arc of a circle. The pressure to be measured, applied inside the tube, tends to straighten it, the closed end is free to move and its deflection is communicated through a rack-and-pinion or helical-cam mechanism to a pointer that moves on a graduated scale which is obtained through factory calibration. The range of this type of gage extends from about 1/30 to hundreds of atmospheres.

In the aneroid (or diaphragm) manometer (Figure 1.7) the sensor is a capsule covered with a thin metal diaphragm with concentric corrugations that make it easily deformable. These gages are reliable for accurate indication of differentials as low as 2 mm of water. Such a mechanism is commonly employed in recording pressure indicators and in barometers.

Both the tubular elements and the diaphragm are temperature sensitive and therefore require further calibration in the laboratory when used at temperatures different from the standard.

Figure 1.6 Bourdon gage

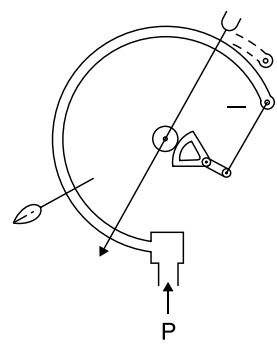

Figure 1.7 Diaphragm gage

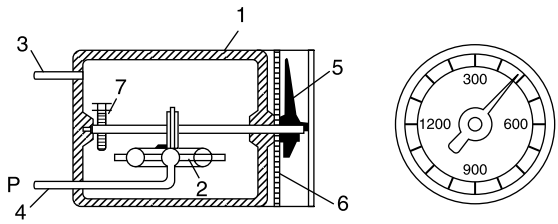

1.4 Pressure transducers

The low natural frequency of the pressure gages described so far has limited their use to essentially steady pressures. Although the pressures to be measured in many experiments are substantially steady, there are cases, as in the study of turbulent or separated flows, of flutter or in tests carried in a shock tube, where it is essential to measure unsteady pressures.

To meet these requirements *pressure transducers* that convert a pressure signal into an electrical signal are required. In fact, transducers can do the following:

- can be built having high resonant frequencies;
- can be miniaturized and thus can be installed adjacent to or even within the model to be tested, thus reducing the delays due to the transmission of pressure signals in pipes.

Transducers greatly simplify the procedure for getting and recording data since the electrical signal from the transducer can be digitized and sent to a computer. This characteristic has led in time to the adoption of transducers even when pressure is steady, especially when many pressure measurements are needed.

1.4.1 Capsule transducers

Pressure transducers derived directly from the diaphragm gage can be used for moderate frequencies. The displacement of the diaphragm due to the pressure difference can be converted into an electrical output in different ways:

- *Potentiometric*: the motion of a wiper along a resistive mechanism modifies the electrical resistance of a circuit powered by direct current; the presence of a sliding contact, which is subject to wear, limits the life of the instrument.
- *Electromagnetic*: a block of magnetic material is moved in a coil so as to affect the inductance (Figure 1.8) of the circuit. It is necessary to feed the coil with a high frequency alternate current which must then be filtered out in the output signal in order to show only the changes induced by pressure oscillations; power supply and signal processing are expensive.
- *Capacitive*: the diaphragm and the pressure cavity powered by direct current create a variable capacitor; the advantage in terms of natural frequency is the lack of moving masses, apart from the vibrating plate.

The output signal is the voltage if the measure is made on site; if the signal has to be sent at a distance, without taking into account the voltage drop in the transmitting wires, it is appropriate that the signal is the current flowing in the circuit: in this case, one talks about a *pressure transmitter* instead of a *pressure transducer.*

Capsule transducers of moderate size are commercially available, typically with a diameter of 4–6 cm, an accuracy approaching 0.1% FS (full scale) and a response time of the order of 5 ms. They are made entirely of steel and are particularly suitable for industrial applications in the presence of shock, vibration, or temperature changes. The measuring range extends up to 700 bars.

Figure 1.8 Electromagnetic transducer

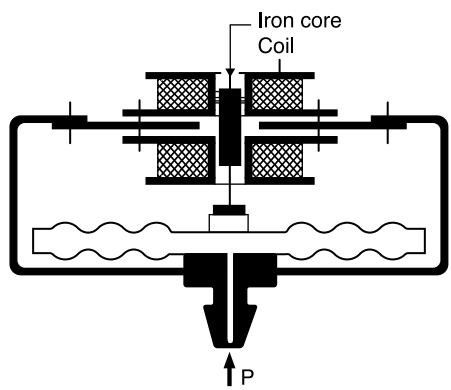

1.4.2 Strain gage transducers

One class of pressure transducers is based on the detection, with a *strain gage*, of the deformation of a plate (*diaphragm*) or the deflection of a cantilever beam, subjected to the pressure to be measured.

The strain gage consists of a wire or a ribbon glued, or sometimes deposited under vacuum, to an insulating support. The electrical resistance, R, of a conductive wire is given by

$$R = \rho \frac{\ell}{S} \tag{1.10}$$

where ρ is the resistivity of the conductor, l its length and S its cross-sectional area.

Differentiating Equation (1.10), is obtained:

$$\frac{dR}{R} = \frac{d\rho}{\rho} + \frac{d\ell}{\ell} - \frac{dS}{S} = \frac{d\rho}{\rho} + \varepsilon - 2\varepsilon_t \tag{1.11}$$

where ε and ε_t are the longitudinal and transverse strains, respectively.

The *gage factor* is the ratio of unit change of resistance and longitudinal strain

$$\text{gage factor} \qquad \frac{1}{\varepsilon}\frac{dR}{R} = 1 + 2\nu + \frac{d\rho}{\varepsilon\rho} \tag{1.12}$$

where ν is the Poisson's ratio ($\nu = \left|\varepsilon_t/\varepsilon\right|$).

The gage factor for metallic wires ranges between 2 and 5. Since usually the strain gage is one of the resistances of a Wheatstone bridge, the bridge output signal, for a given strain, is proportional to the gage factor.

The sensitivity of a transducer is proportional to the inverse stiffness (compliance) of its flexural element. The compliance, defined as the deflection (Δx) per applied load, of a cantilever beam subjected to an end load, F, is:

$$\frac{\Delta x}{F} = \frac{L^3}{3EI}\,\text{mN}^{-1} \tag{1.13}$$

where E is the Young's modulus and I is the moment of inertia of the beam's cross-sectional area.

The compliance of the center of an edge-fixed circular plate to a uniform load p is:

$$\frac{\Delta x}{p\pi r^2} = \frac{3(1-\nu^2)r^2}{16\pi Et^3} \text{ mN}^{-1} \tag{1.14}$$

where t is the thickness and r is the radius of the plate.

The natural frequency for the fundamental mode of vibration of a cantilever beam is:

$$f_n = 0.5596\sqrt{\frac{EI}{\mu L^4}} \text{ Hz} \tag{1.15}$$

where μ is the mass per unit length.

The natural frequency for the first circular mode of vibration of a fixed edge circular plate is:

$$f_n = \frac{1.6183}{r^2}\sqrt{\frac{Et^3}{12\rho(1-\nu^2)}} \text{ Hz} \tag{1.16}$$

where ρ is the mass per unit area.

The relationships between flexibility and natural frequencies of vibration are therefore:

for the edge-fixed circular plate $$\frac{\Delta x}{p} = \frac{0.041}{f_n^2\rho} \text{ m}^3\text{N}^{-1} \tag{1.17}$$

for the cantilever beam $$\frac{\Delta x}{F} = \frac{0.104}{\mu L f_n^2} \text{ mN}^{-1} \tag{1.18}$$

If high flexibility is needed to get a strong enough signal, the natural frequency of the element is limited and hence the maximum frequency detectable by the transducer.

Pressure transducers with strain gages of the smallest size (6 mm in diameter) are commercially available with a frequency response of 10 kHz, which are particularly useful in applications where the sensing element can be flush-mounted on a wall so to avoid interference with the stream. They are fairly cheap and easy to manufacture and are robust.

The diaphragm deflection is transmitted to a displacement transducer element which consists of four sets of unbounded wire strain gages

Figure 1.9 Circuit diagram of a strain gage transducer

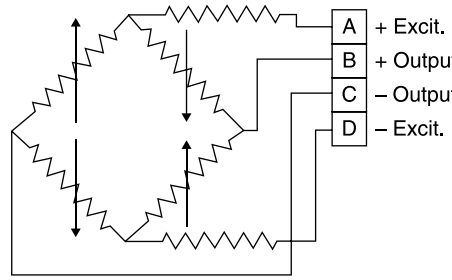

forming the four arms of a resistance bridge (see Figure 1.9). A galvanometer, oscilloscope or recording instrument indicates the bridge imbalance arising from changes in the bridge resistances after a strain is imposed on the wire. The galvanometer output is calibrated to yield the pressure indication. The use of four strain elements, two of which are shortened and two of which are lengthened by the diaphragm displacement, increases the instrument sensitivity. These instruments are also supplied with a temperature compensator to eliminate thermal resistance changes and consequent error in the pressure indication.

1.4.3 Piezoresistive transducers

Semiconductors, such as silicon crystals, show a strong change of resistivity following a deflection (*piezoresistivity*), so for them the term $d\rho/\varepsilon\rho$ of Equation (1.12) is much greater than for metals: a strain gage made of a semiconductor has a gage factor that can vary from 50 to 200. This high gage factor makes semiconductor strain gages very attractive, as with them the problem of obtaining a useful signal from a very rigid transducer with a high natural frequency can be solved.

The dizzying development of semiconductor technology and the realization of integrated circuits in the 1970s strongly influenced the market for transducers. The rationale for this influence is significant even in the mechanical properties of silicon crystals: the elastic modulus is of the same order of magnitude as that of steel, the tensile strength is greater, and the relationship between the modulus of elasticity and the density is three times that of steel.

It must be emphasized that crystal silicon is both the flexural element which deforms and the transducer. Transducers are commercially

available in which the four arms of the Wheatstone bridge are diffused into a silicon diaphragm. The diameter of the transducers ranges from 1 to 30 mm, the resonance frequency varies from 55 kHz to 1 MHz, and the accuracy is 0.1 ÷ 0.25% of the full scale.

1.4.4 Piezoelectric transducers

Piezoelectricity is the other transduction technology used in transducers intended to measure time-varying forces, pressures and accelerations. As the technology of piezoresistive materials has developed since the 1960s, a similar effort in the years 1920 to 1950 was accomplished in piezoelectric technology. The crystals belonging to those classes that do not have a center of symmetry of the structure of the lattice are piezoactive, i.e. the material develops a varying electric potential difference when subjected to a change in stress (pressure) and, conversely, undergoes a variable deformation if subjected to the action of a variable voltage (oscillator). Twenty of the 32 crystal classes lack this symmetry, and all crystals belonging to these classes, except one, exhibit piezoelectric characteristics.

The resulting charge is distributed on certain crystal faces in a manner determined by the symmetry of the crystal and the nature of the efforts applied. Some materials, such as tourmaline, lithium sulfate and barium titanate, are sensitive to hydrostatic pressure; other materials, such as quartz and Rochelle salt, develop a charge only under the unilateral application of force, the charge is spread through the influence of a normal component of the stress, such as quartz, or tangential stress, such as Rochelle salt. Some ferroelectric ceramic materials can be made artificially piezoelectric.

The *piezoelectric constant* of a material expresses the charge generated per unit of applied force or the deflection per unit of electrical voltage applied. The constant is typically given in tensor notation, such as d_{33}, with the first subscript identifying electrical direction and the second subscript identifying mechanical direction. Typical units are Coulombs/Newton or meters/volt.

A piezoelectric transducer is effectively a capacitor that produces a charge proportional to the force applied to it, the load can be applied in a unilateral direction by a piston or a diaphragm or the material may be subject to a hydrostatic load. Unlike piezoresistive transducers, piezoelectric probes do not have response to zero frequency: they are therefore not suitable for measuring stationary or slowly varying

pressures and can only be used for the measurement of fast transient ones. This shortcoming can be avoided by making transducers in which the pressure, even when constant, can be measured indirectly by measuring the frequency of the oscillation of the crystal, which is a function of the pressure.

As the crystals grow polarization due to the movement of the "center of gravity" of positive and negative charges under the influence of elastic deformations, we expect that the expansion and contraction under the influence of temperature changes will produce similar effects. This type of *pyroelectric effect* is frequently a source of interference, especially when the measured pressure transients are accompanied by violent fluctuations in temperature. Hydrostatically sensitive materials such as tourmaline are especially susceptible to this interference and are much more sensitive than non-hydrostatic crystals, such as quartz. In the latter case, the pyroelectric charge will not grow at all if the temperature changes uniformly through the crystal.

Of course, it is impossible to precisely define the limits of application of piezoelectric pressure transducers but to give a rough idea of the magnitude of the practical limits of pressure and frequency, it can be said that these sensors have been used to measure transient changes in pressure from 10^{-2} to 10^{3} atm. It is relatively easy to measure transients lasting up to one-fifth of a second, but it becomes difficult to measure slower phenomena because of pyroelectric interference. The high frequency response is limited, in most applications, by the time taken by the pressure impulse to propagate in the transducer rather than by the natural frequency of the crystal. So the upper limit is determined by the size of the transducers (the smallest transducers are 1 mm in diameter). Their usable frequency response can extend to 300 kHz with an accuracy of 0.01% FS.

1.4.5 Pneumatic and electronic scanning of multiple pressures

Before the production of cheap piezoresistive transducers, the use of a transducer for each of many pressure taps was considered too expensive; thus, pneumatic scanning valves, *Scanivalve*, were produced, from 1960 to 2000, connecting a single transducer of excellent quality with each of the pressure taps sequentially (Figure 1.10): the transducer is sequentially connected to the various Px ports by a single hole in the rotor which

Figure 1.10 **Inside view of a Scanivalve and how it works**

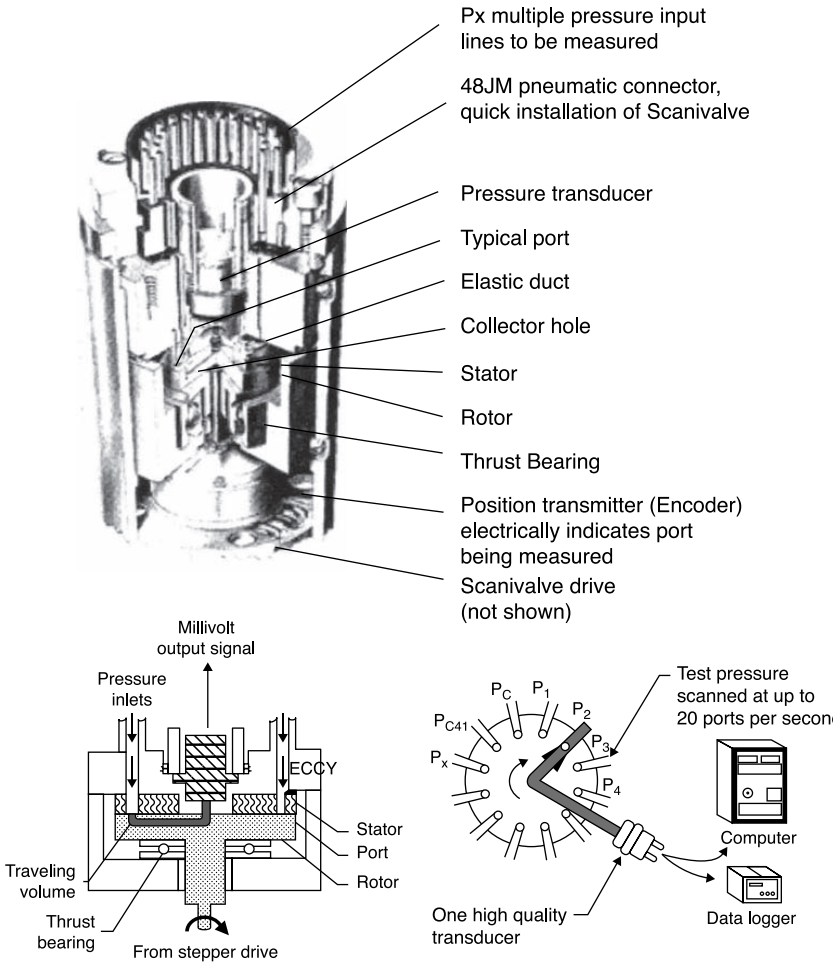

Source: [2]

terminates at the collector hole. As the rotor rotates, this collector passes under the Px input pressure ports in the stator. Because of the extremely small traveling volume, scanning rates of 20 ports per second are possible. The stator is elastically connected to the block in a manner which allows the stator to follow the surface of the rotor. Thus the pneumatic forces at each port, which tend to blow the rotor away from the stator, are withstood by the thrust ball bearing. Each Px pressure is elastically ducted from the block to its port in the stator.

Each valve can scan up to 48 pressure tubes and a single stepper motor can operate up to 5 valves. When one of the 48 ports is used for span and one for zero calibrating pressures, the pressure transducer can be automatically calibrated on every scan.

The Scanivalve is not suitable for a field survey of many rapidly varying pressures, in fact, the reading of each tap can only be done at each complete revolution, but even if the engine is stopped, reading of a variable pressure is affected by delays introduced by the pipe connecting the pressure tap and the Scanivalve, which has small diameter and considerable length. The size of the Scanivalve in fact prevents its accommodation within the model being tested.

The advent of cheap piezoresistive transducers, with their qualities of high natural frequency and very small dimensions (in the order of mm) led to the creation of packages of transducers that can be accommodated within the models, e.g. a package of 64 transducers 105 mm × 36 mm × 14 mm in size (Figure 1.11). The scanning is done electronically and allows a sampling rate of up to 10 kHz per channel.

The reference pressure is sent simultaneously to all transducers. At each scan cycle it can be sent to a pressure transducer to control the calibration (Figure 1.12). At the same time cleaning of the pipe can be made to prevent clogging of the various tubes.

Figure 1.11 **Electronic pressure scanner with 64 transducers**

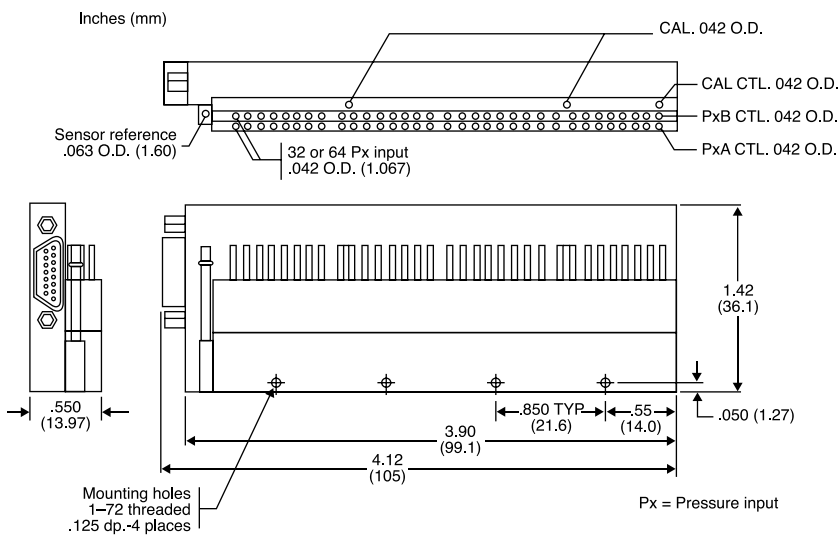

Source: [3]

Figure 1.12 Calibration valving of the electronic pressure scanners ZOC22B, 23B and 33

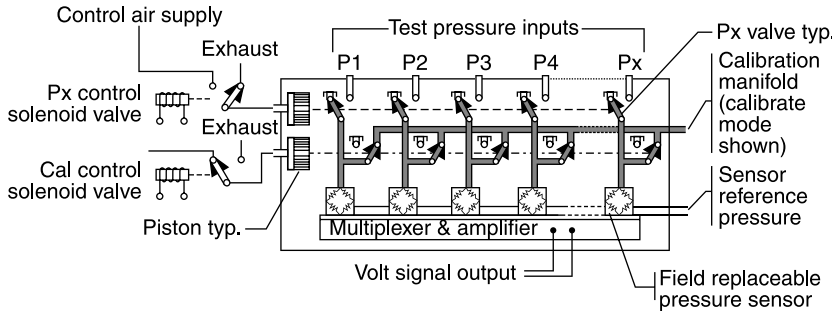

Source: [4]

1.5 Pressure-sensitive paints

Pressure-sensitive paints (PSP) have been used since 1980 to display and measure the distribution of pressures throughout the model. The advantages of the method are:

- continuous pressure measurements on the whole surface;
- non-intrusiveness, since there are no probes to be introduced in the fluid flow;
- reduced time and cost of preparing the model (there are no orifices to be made, transducers or pressure tubes or scanning valves to be inserted in the model);
- high resolution, limited only by the size of the pixels of the camera system.

Disadvantages are:

- sensitivity to temperature;
- the need for prior calibration;
- filming techniques and sophisticated data processing.

The paints are made of luminescent substances, embedded in a binder, that, when excited by light radiation (*UV* or visible light), re-emit (Figure 1.13) part of it as light with a different wavelength (*fluorescence*), transforms a part of it in internal energy (*internal conversion*), and a part of the energy goes to excite oxygen molecules (*oxygen quenching*).

Figure 1.13 Re-emission of a luminescent molecule

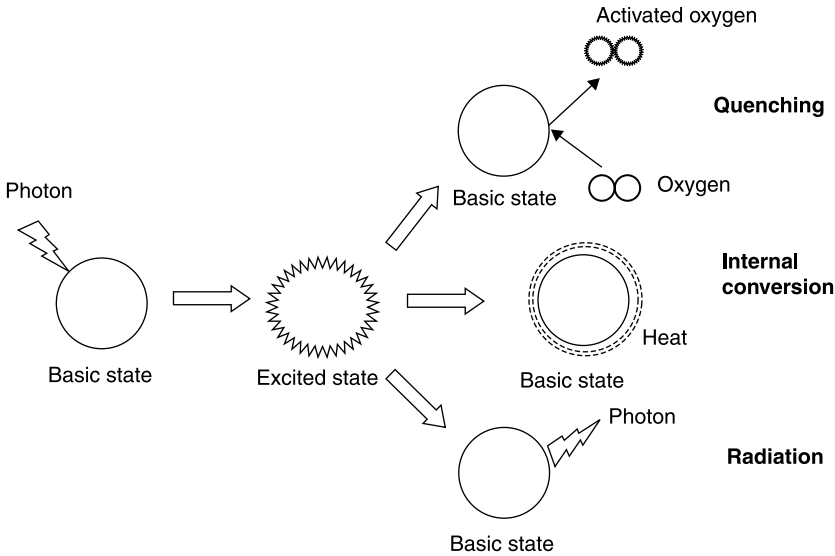

Since the luminescence is reduced by the presence of oxygen molecules, increasing pressure, and thus the partial pressure of oxygen, tends to mitigate the intensity of the light emitted: a measure of the distribution of the latter on the surface of the model therefore allows the distribution of pressure to be traced.

References

1. Patrick L. Walter (1999) "Dynamic force, pressure and acceleration measurement," *Measurement & Control*, June: 76–81.
2. Scanivalve Corp Systems (2003) *MODEL J1: The J Scanivalve*. Available at: http://www.scanivalve.com.
3. Scanivalve Corp Systems (1998) *Single Scanivalve System Details*. Available at: http://www.scanivalve.com.
4. Scanivalve Corp Systems (2000) *Model ZOC22B*. Available at: http://www.scanivalve.com.
5. T.W. Chubb (1968) "The response of a narrow bore pressure measuring system to step and oscillatory pressures" *R.A.E. Report 68010*.

2

Velocity and mass flow by pressure measurements

Abstract: This chapter will address the measurement of velocity in a steady flow, in magnitude and direction, and of mass flow in pipes, obtained from pressure measurements.

Key words: direction probes, Pitot tube, Prandtl tube, Venturi tube.

2.1 Introduction

Speed at a point in a fluid flow can be measured in the following ways:

- By measuring the distance, ds, travelled by fluid particles in a known time interval, dt (particle image velocimetry, PIV), or by measuring the time taken by particles to travel a fixed distance (laser two focus anemometer, L2F). Because air is transparent to light, it must be seeded with visible solid or liquid particles assumed to have the same speed as the air stream. These methods require fairly sophisticated equipment and data processing.
- More frequently by a measure of other parameters (pressures, Doppler effect produced by particles carried by the stream, heat exchange between the stream and a metal wire heated by the Joule effect, speed of rotation of a windmill, etc.) from which the speed can be calculated from theoretical considerations and/or a preliminary calibration. The most commonly used method, when speed is constant in time, is based on pressure measurements; other methods such as hot-wire or laser-Doppler anemometers, are particularly effective when the flow is turbulent. In supersonic flows another method is used based on the measurement of the inclination of Mach waves or of shock waves on wedges and cones.

2.2 Measurement of flow speed by pressures

The speed, U, in a gas can be calculated from the ratio between stagnation pressure, p_0, and static pressure, p, using the relationship valid for a thermally and calorically perfect gas:

$$\frac{p_0}{p} = \left(1 + \frac{\gamma - 1}{2} M^2\right)^{\frac{\gamma}{\gamma-1}} = \left(1 + \frac{\gamma - 1}{2\gamma} \frac{U^2}{RT}\right)^{\frac{\gamma}{\gamma-1}} \tag{2.1}$$

where M is the Mach number, γ is the ratio of specific heats at constant pressure and constant volume, T the static temperature and R the gas constant, ratio between the universal gas constant and the molecular weight of the gas.

From Equation (2.1), the speed U is obtained:

$$U = \sqrt{\frac{2\gamma RT}{\gamma - 1}\left[\left(\frac{p_0}{p}\right)^{\frac{\gamma-1}{\gamma}} - 1\right]} = U(p_0, p, T) \tag{2.2}$$

The calculation of speed hence requires the measure of two pressures, p_0 and p, and the measure of the static temperature of the stream, which is impossible to obtain, as we shall see, when the Mach number is high; it is easier in this case to calculate the Mach number, which is a function of pressures only:

$$M = \sqrt{\frac{2}{\gamma - 1}\left(\frac{p_0}{p}\right)^{\frac{\gamma-1}{\gamma}} - 1}$$

In the case of flow at low Mach numbers ($M << 1$), Equation (2.1) can be expressed in a power series of M^2 (U^2) as follows:

$$\frac{p_0}{p} = 1 + \frac{\gamma}{2} M^2 + \ldots\ldots\ldots\ldots = 1 + \frac{U^2}{2RT} + \ldots\ldots\ldots\ldots = 1 + \frac{\rho U^2}{2p} + \ldots\ldots\ldots$$

This yields, by truncating the series at the second term:

$$p_0 = p + \frac{\rho U^2}{2}$$

which is the Bernoulli equation for an incompressible flow. This equation underestimates the stagnation pressure compared to Equation (2.1) (the next terms in the series, all positive, are ignored) and hence for the same p_0 and p, provides a higher speed.

In this scheme, the speed can be calculated, once the density (constant) is known, from the difference between the stagnation pressure and the static pressure (dynamic pressure, q) according to the equation:

$$U = \sqrt{\frac{2(p_0 - p)}{\rho}} = \sqrt{\frac{2q}{\rho}} \tag{2.3}$$

From Figure 2.1, which shows the ratio, Equation (2.4), between the speed calculated with Equation (2.3) and the speed calculated with Equation (2.2), we see that Equation (2.3), strictly valid only for $M = 0$, can be used, accepting an error of less than 1% up to $M = 0.3$, or up to $M = 0.4$, if an error of 2% can be accepted.

Figure 2.1 **Ratio of speed calculated by the Bernoulli theorem and true speed for $\gamma = 1.4$**

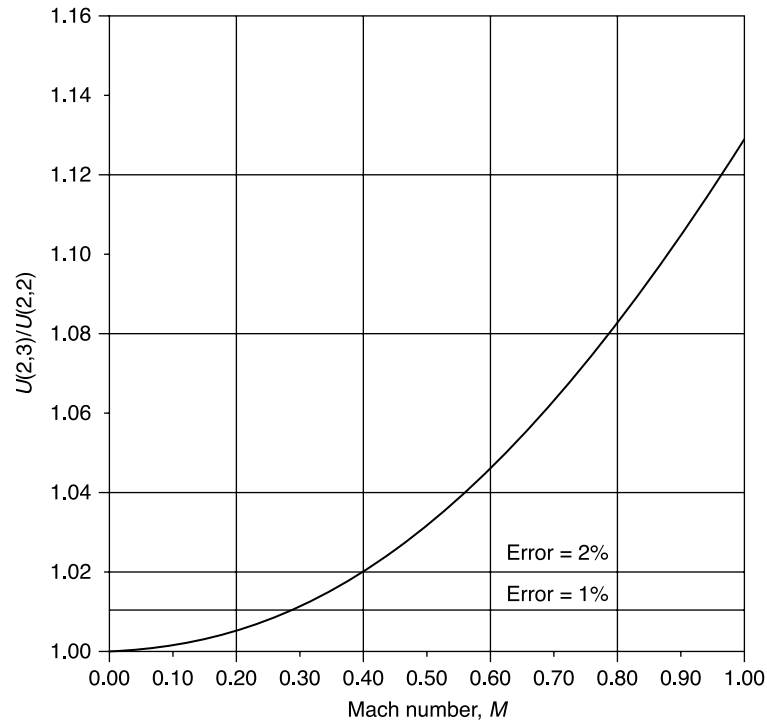

$$\frac{U_{(2.3)}}{U_{(2.2)}} = \sqrt{\frac{2}{\gamma M^2}\left[\left(1+\frac{\gamma-1}{2}M^2\right)^{\frac{\gamma}{\gamma-1}}-1\right]} \qquad (2.4)$$

In compressible flows, as can easily be seen from Equation (2.1), the dynamic pressure is no longer equal to $q = \rho V^2/2$ but the latter term is still used to define pressure coefficient and aerodynamic forces coefficients.

Speed of a stream can then be measured on whatever body is immersed in the stream because on it both the stagnation pressure, in the stagnation point, and the pressure of the undisturbed stream can be found. For example, on an infinite cylinder of circular cross-section immersed in a non-viscous and incompressible flow with velocity V_∞ perpendicular to axis of the cylinder (Figure 2.2): defining as pressure coefficient the ratio

$$C_p = \frac{p - p_\infty}{\rho U^2 \pm 2}$$

- $C_p = 1$ ($p = p_0$ at the stagnation points) at $\alpha = 0°$ and $180°$
- $C_p = 0$ ($p = p_\infty$) at $\alpha = \pm 30°$ and $\pm 150°$

On a sphere:

- $C_p = 1$ ($p = p_0$ at the stagnation points) at $\alpha = 0°$ and $180°$
- $C_p = 0$ ($p = p_\infty$) at $\alpha \cong \pm 40°$ and $\alpha \cong \pm 140°$

Figure 2.2 **Diagrams of pressure coefficient, C_p, on a cylinder and a sphere in a theoretical potential flow, and in real laminar and turbulent regimes**

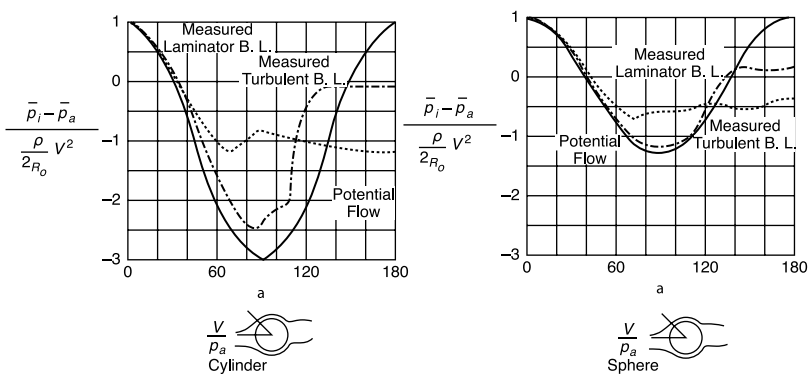

Source: Goldstein, S., *Modern Developments in Fluid Dynamics*

In practice, a flow is never potential: if the Reynolds number is large but not infinite, a boundary layer will exist all around the body; nevertheless, the pressure on the body will be the same as that outside the boundary layer because of the relationship $\frac{\partial p}{\partial y} \simeq 0$. Therefore the distribution of pressure in the field outside the boundary layer can be detected through orifices made on the surface of the body. It must be noted, however, that the distribution of pressure on the body is different from that of potential flow; in fact, in the wake, the recovered pressure is lower than the stagnation pressure. Furthermore, the position of the points where the pressure is equal to p_∞ is moved downstream about 5°; pressure on the afterbody is strongly influenced by the nature of the boundary layer and hence by the location of the boundary layer separation.

However, there are special cases, such as measuring the speed profile within the boundary layer itself with very small probes and in the presence of very low speed: in these cases the Reynolds number referred to the size of the probe is very small and the flow in the proximity of the probe must be considered viscous and corrections to measured pressures will be made (cf. Section 2.3.5).

It can be noted that measuring p_0 and p_∞ on blunt bodies, such as circular cylinders and spheres, is impractical both because of the large dimensions, leading to a poor resolution, and because of the great variability of the pressure on the body with flow direction. Tubular probes of smaller size and lower sensitivity to direction are therefore preferred.

In some cases, the measurement of speed can be simplified:

- In a wind tunnel, the stagnation pressure of the undisturbed stream can be known by measuring the static pressure in the settling chamber of the wind tunnel, where the speed is low enough. Similarly, the static pressure of the undisturbed stream can be measured in an orifice drilled in the wall in the entrance station of the test chamber. From the two measures the Mach number of the tunnel can be determined by Equations (2.2) or (2.3), without introducing probes into the stream. The measure will, however, be slightly wrong because the stagnation pressure is not exactly the same in the settling chamber and in the test chamber.
- In a subsonic free jet, static pressure must be equal to ambient pressure and can be measured with a barometer; to measure the speed profile in the jet, it is then sufficient to measure the profile of the stagnation pressure.

- Similarly, as the static pressure in each section of a straight tube is constant and can be measured in an orifice drilled in the wall, the speed profile in a section can be obtained by taking only the measurements of the stagnation pressure.

2.3 Pitot tube

Recalling the definition of stagnation pressure as the maximum pressure that can be obtained by stopping the fluid isoentropically and adiabatically, it can be measured in an orifice drilled in the stagnation point of a body. The simplest body is a tube aligned with the direction of the stream with the open end facing the stream (Figure 2.3) called a *Pitot tube* after its inventor, Henri Pitot (1732). The other end of the tube is connected to a pressure-indicating instrument so that in equilibrium there is no motion in the tube ($U = 0$, stagnation).

If the opening is also normal to the tube axis and with circular cross-section, free of obstacles, the reading of the instrument is, in the subsonic regime, virtually independent from the shape of the front and the length of the tube.

Figure 2.3 The Pitot tube

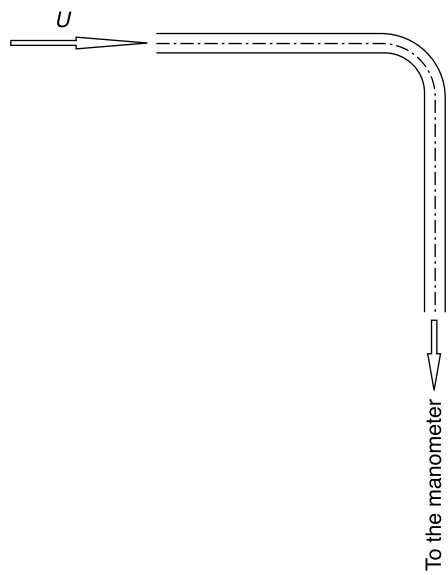

2.3.1 The Pitot tube in yaw

If the Pitot tube is not aligned with the stream, the measured pressure is lower than the stagnation pressure since only the velocity component normal to the entrance section is stopped. The effect of the angle of incidence is negligible for angles less than, approximately, ±10° in the subsonic regime (Figure 2.4). This insensitivity is particularly beneficial in the Pitot tubes mounted on the nose of airplanes flying at non-zero angles of attack.

Figure 2.4 shows that the influence of the angle of attack also depends on the ratio of the hole diameter, d, and the outer diameter of the probe, D: in particular, the error for a given angle of incidence, decreases with the increase of the ratio d/D.

To increase the insensitivity to the alignment of the probe, a Kiel tube can be used (Figure 2.5), which is a Pitot tube immersed in a Venturi tube, which shows an insensitivity to angles of attack up to ±40° (Figure 2.6), or even ±60° with a modified version (on the right in Figure 2.5), obtained by changing the mouth of the Venturi: these features are achieved in the Kiel tube because the stream separation takes place only at very high angles of attack.

Figure 2.4 **Effects of the angle of incidence on the reading of a Pitot tube with different ratios between internal and external diameters**

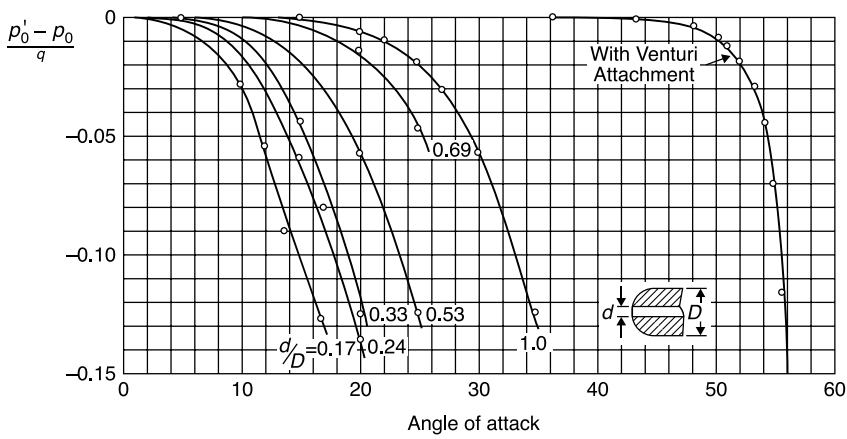

Figure 2.5 The Kiel tube

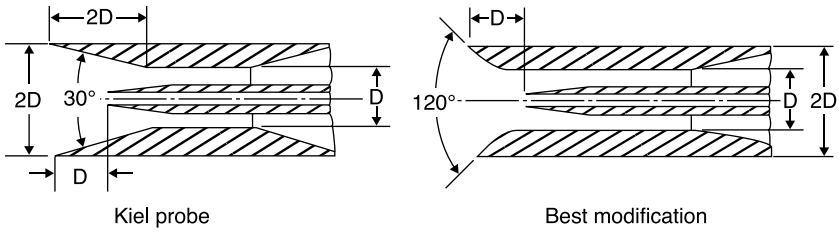

2.3.2 Effect of gradients of stagnation pressure

In a viscous layer, the variation of speed, and hence of stagnation pressure, along the opening of the tube causes two effects:

- first, the tube senses the average of the squared speed that is greater than the square of the speed on the axis of the tube;
- second, the deviation of the stream towards the region of lower stagnation pressure brings down the streamlines with a stagnation pressure higher than that corresponding to the axis of the tube.

The experimental results show that the pressure detected by a Pitot tube is equal to the pressure existing at a stagnation point moved about

Figure 2.6 Sensitivity of the Kiel tube to the angle of attack

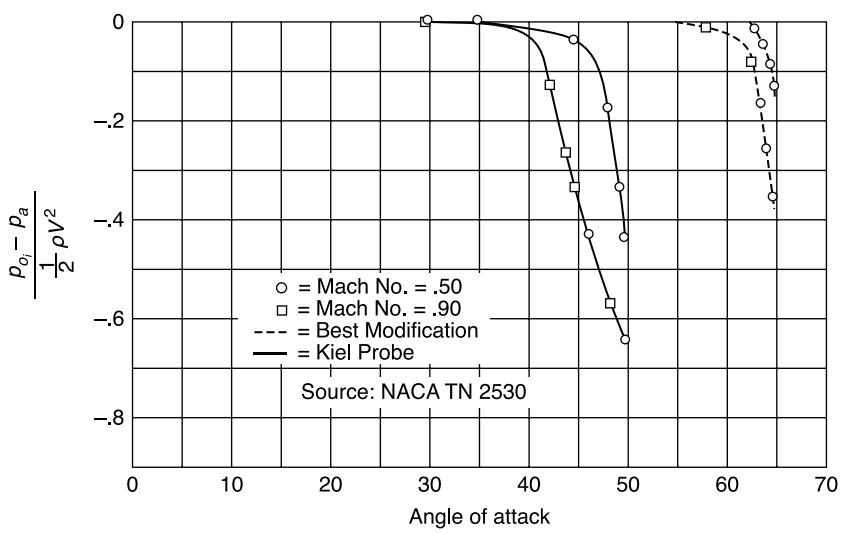

Figure 2.7 **Displacement of the effective center of the Pitot tube in the presence of a shear layer**

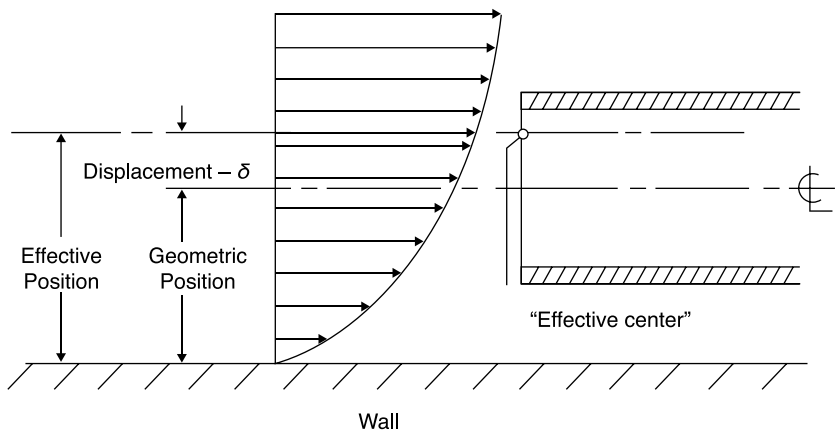

0.18 d from the axis of the tube in the direction of increasing speed (Figure 2.7).

For this reason, to perform measurements in the boundary layer or other viscous layers (the stagnation pressure in many flows is constant outside these layers), appropriate Pitot tubes available on the market (Figure 2.8) are used, ending with very small tubes (with a diameter of 0.6 mm with the end flattened) to minimize both the effect of shifting the "effective center" and the effect of proximity of a solid wall. Probes for the boundary layer can easily be made in the laboratory from suitably truncated hypodermic tubes, bent at 90° and made flat.

Flattened tubes are very sensitive to the angle of incidence and are not suitable for use in highly turbulent flows because of the considerable delay (of the order of seconds) that they introduce in the transmission of pressure signals.

2.3.3 Effects of the proximity of a wall

The correction to the reading of a Pitot tube placed near a wall are less immediate than the corrections for the gradient of stagnation pressure since the error depends on the whole speed profile between the tube and the wall. A process of successive approximations could be developed to deduce the true profile from the profile measured but this procedure would require a large amount of experimental work. As said above, for

Figure 2.8 Pitot probes for boundary layer

measurements in thin boundary layers very small tubes are used for which the correction for the effect of proximity to a wall can be ignored; for cylindrical tubes the effect tends to zero at distances greater than 2 diameters from the wall (Figure 2.9); the correction for a flattened tube is more uncertain since the effect of the wall is to prevent the deviation of the streamlines induced by the presence of the Pitot tube and a flattened tube deforms the streamlines more than a circular pipe.

2.3.4 Effects of the Mach number

For a probe perfectly aligned with the stream, the reading is independent of the Mach number up to Mach numbers close to 1 (Figure 2.10). At supersonic speeds in front of the tube, a detached shock wave is generated, which is locally normal to the axis of the tube, so that the pressure detected by the Pitot tube is the stagnation pressure downstream of a

Figure 2.9 Error induced by the proximity of a wall on a Pitot tube

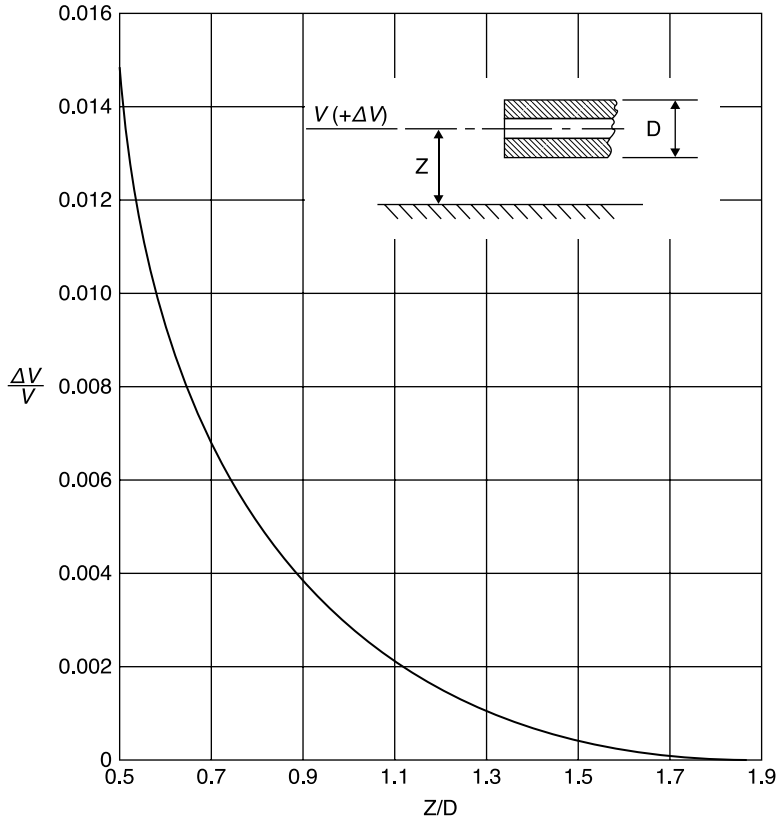

normal shock wave. The measured pressure (subscript 2) can be used to calculate the Mach number of the stream ($M_1 > 1$), if the stagnation pressure upstream of the shock wave (subscript 1) is known, through the equation, known as the Rayleigh formula:

$$\frac{p_{01}}{p_{02}} = \left[\frac{(\gamma-1)M_1^2+2}{(\gamma+1)M_1^2}\right]^{\frac{\gamma}{\gamma-1}} \left(\frac{2\gamma}{\gamma+1}M_1^2 - \frac{\gamma-1}{\gamma+1}\right)^{\frac{1}{\gamma-1}} \tag{2.5}$$

The stagnation pressure upstream of the shock wave must be measured independently, as the pressure in the stagnation chamber that feeds the de Laval nozzle that generated the supersonic stream.

The Mach number can also be calculated, if the static pressure upstream

Figure 2.10 Effects of the Mach number on the readings of a Pitot tube with a hemispherical head (d/D = 0.3)

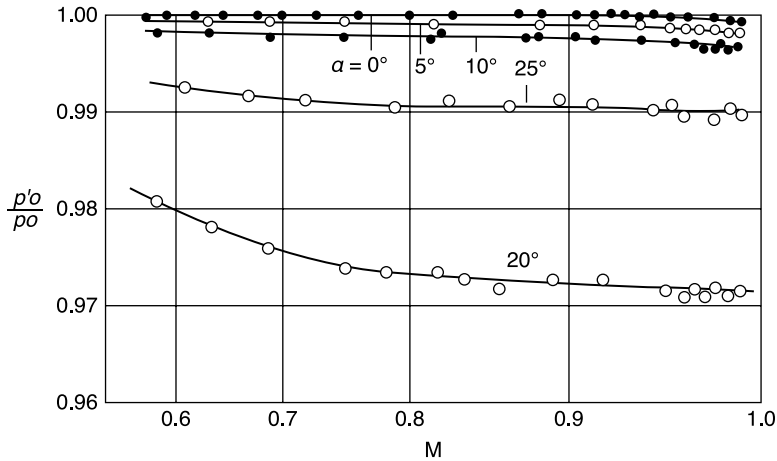

of the shock wave is known, by Equation (2.6) obtained by dividing Equation (2.5) by Equation (2.1):

$$\frac{p_1}{p_{02}} = \left[\frac{2}{(\gamma+1)M_1^2}\right]^{\frac{\gamma}{\gamma-1}} \left(\frac{2\gamma}{\gamma+1}M_1^2 - \frac{\gamma-1}{\gamma+1}\right)^{\frac{1}{\gamma-1}} \tag{2.6}$$

The static pressure upstream of the shock wave can be measured on a wall at the entrance of the test chamber.

2.3.5 Effects of the Reynolds number

For Reynolds numbers lower than 1000 (based on the diameter of the orifice), corrections are required due to the presence of a completely viscous flow; Figure 2.11 shows the calibration curve for very low Reynolds numbers. For Reynolds numbers less than 50, the error increases rapidly and the curve tends to become

$$\frac{p_{oi} - p}{q} = 1 + \frac{11.2}{\mathrm{Re}_d}$$

Such small values of the Reynolds number are typical of measurements made in the boundary layer, where speeds are low (down to zero) and

Figure 2.11 **Effects of low Reynolds numbers on the readings of a Pitot tube (d/D = 0.64)**

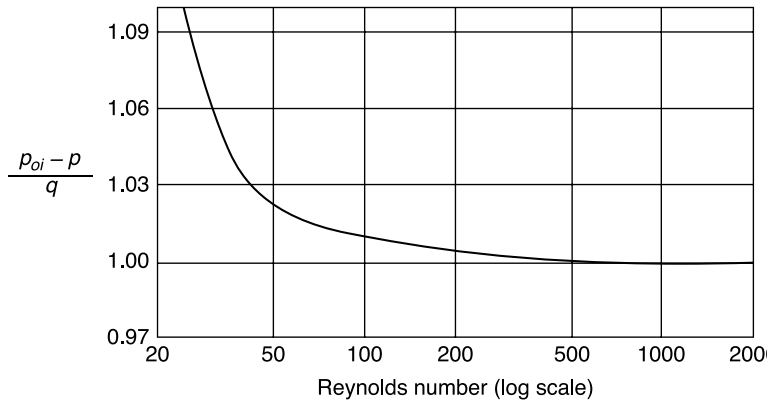

Pitot tubes are very small to avoid both the displacement of the virtual centre in the presence of velocity gradients and the effects of proximity to the wall.

2.3.6 Effect of stream turbulence

Assuming that the motion is nearly steady and that the lateral components of turbulence are so low that they have a negligible effect on the angle of incidence, the resulting velocity U equals the sum of the average speed, $\overline{U}$, and the fluctuating component u: the Pitot tube then reads

$$p + \frac{\rho U^2}{2} \cong p + \frac{\rho \overline{U}^2}{2} + \frac{\rho}{2} u^2 \tag{2.7}$$

If velocity is constant in value but varies widely in direction, it is expected that the tube will detect a pressure lower than real because, for angles other than zero, the measured pressure is less than the stagnation pressure.

The current state of knowledge is very unsatisfactory, particularly as regards the use of Pitot tube in jets with strong turbulence, but it is hard to believe that a simple formula can give the corrections to be made to measurements in turbulent flows without knowledge of extensive data on the turbulence itself; if measures of turbulence are needed as primary data, they must be obtained with a hot wire or a laser-Doppler or a 2-focus laser anemometer.

2.4 Prandtl tube

The local static pressure, equal to that prevailing outside the boundary layer, can be measured in an orifice on the surface of a body immersed in a stream. If, in particular, the static pressure of undisturbed stream, p_∞, is to be measured, an orifice can be drilled where, from a theoretical point of view, the pressure reaches this value, e.g. in the presence of the boundary layer (Figure 2.2) on a cylinder of circular cross-section in the locations at ±35°. Small deviations from these points, however, lead to large changes in pressure, so, as in the case of stagnation pressure, the use of slender bodies, like tubes, which introduce small disturbances in the stream, is preferred.

The basic concept is that in the absence of curvature of streamlines there is not a centrifugal force to be balanced with a gradient of pressure: keeping streamlines straight equals cancelling the variation in pressure normal to the streamlines themselves. Strictly speaking, only on a flat plate p_∞ could be measured through orifices on the surface because any body disturbs the stream: in practice, a slim body can be used if the pressure is read in a position where the initial disturbances are sufficiently damped and streamlines are straight and parallel to the main flow.

The instrument used, designed by Prandtl, consists of a thin tube aligned with the stream with a closed-end upstream, and backed by a stem perpendicular to it (Figure 2.12). The pressure is detected in a number of orifices in the pipe wall.

Figure 2.12 **Static pressure probes: top, the Prandtl tube; bottom, the NPL tube**

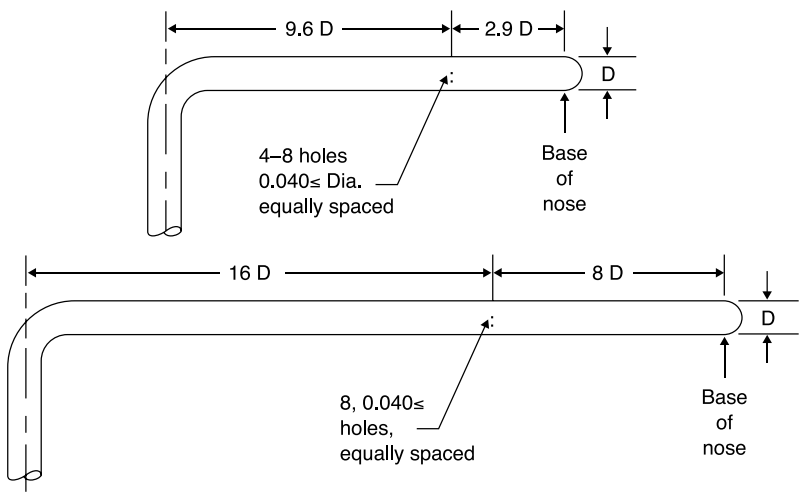

2.4.1 Effects of the position of pressure taps

The measured pressure is appreciably influenced by the position of the taps with respect to the head and to the stem (Figure 2.13): downstream of the head an increase in speed will be generated with a consequent decrease in pressure, the presence of the stem introduces an error of the opposite sign. The position of the orifices should be chosen such that the error due to the presence of the head is approximately equal and opposite of that due to the stem. Using this technique, Prandtl made a very compact probe (Figure 2.12) where the taps were located at 2.9 D from the head (error ≅ –1%), and 9.6 D from the stem (error ≅ 1%). In a more reliable probe, built at NPL, the taps are positioned at 8 D from the head (error ≅ – 0.5%) and 16 D from the stem (error ≅ 0.5%).

2.4.2 Effects of non-alignment

If the static probe is not aligned with the direction of the velocity, there is a distortion of streamlines, or even separation with consequent

Figure 2.13 **Errors in static pressure due to the position of taps**

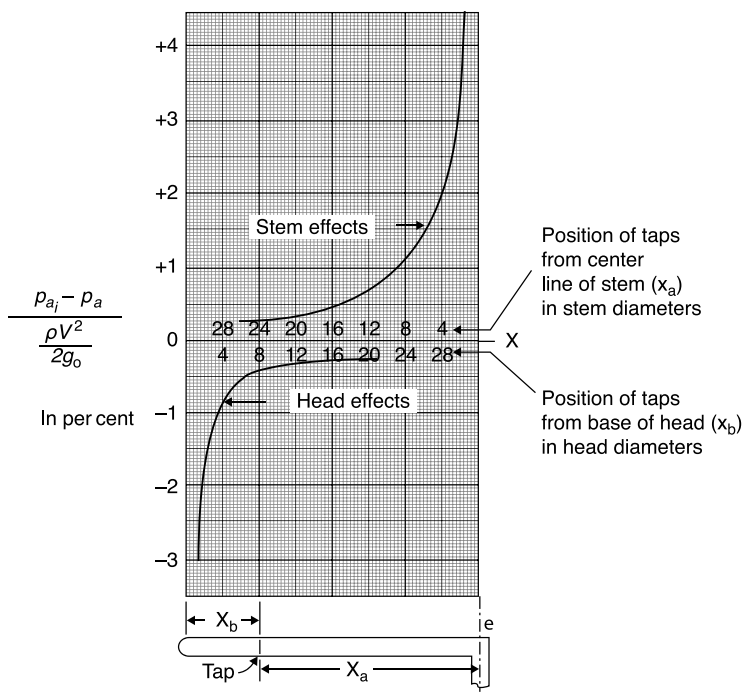

Figure 2.14 Influence of the angle of attack on the readings of a static probe

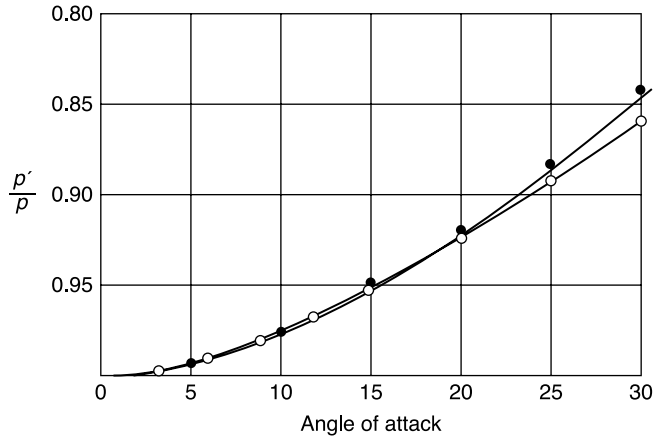

pressure changes. The influence of angle of attack on the reading of the static tube, as shown in Figure 2.14, is larger than that for the Pitot tube (Figure 2.4). To reduce the effects of the angle of attack, from 4 to 8 orifices are drilled, depending on the pipe diameter, distributed on a circle: the presence of several orifices causing flows inside the tube tends to average in some way the values read by the various orifices.

2.4.3 Effect of shear rate and proximity of a wall

The presence of a velocity gradient in a boundary layer does not involve a gradient of static pressure but the gradient of stagnation pressure produces a deviation of streamlines towards the lowest speed and then induces variations in the pressure read by the probe. A similar phenomenon occurs for the downwash on the support of the probe. The proximity of a wall increases the speed and decreases the pressure on one side of the probe; errors less than 1% in detecting the static pressure are made only if the probe is kept at a distance of at least 5 diameters from the wall.

Both phenomena actually discourage the use of static probes for measurements in the boundary layer: since static pressure is constant in the layer, it can be measured in a hole in the wall.

2.4.4 Effects of the Mach number

By increasing the Mach number of the undisturbed stream, a critical value is reached ($M_{cr} \cong 0.7$) for which $M > 1$ is generated on the tube, and upstream of the holes the first shock waves change the static pressure; with the growing Mach number the supersonic zone extends and the shock waves moving downstream step over the holes which are therefore in a supersonic flow. When this happens, reading the pressure becomes independent of the position of the support and the distribution of velocity on the front of the tube differs appreciably from that which occurs at low speeds.

Under these conditions, therefore, a static tube designed to operate at low speed can result in appreciable errors. This is illustrated in Figure 2.15 which shows the results obtained with a tube in which the phenomena are accentuated by the blunt shape of the head. By using tubes with a very slender head, a critical Mach number can be increased up to values close to 1.

At supersonic speeds, the head of the tube should be conical: the opening angle must be less than that for which a detached shock wave is

Figure 2.15 **Influence of compressibility on the readings of a blunt static probe at different angles of attack**

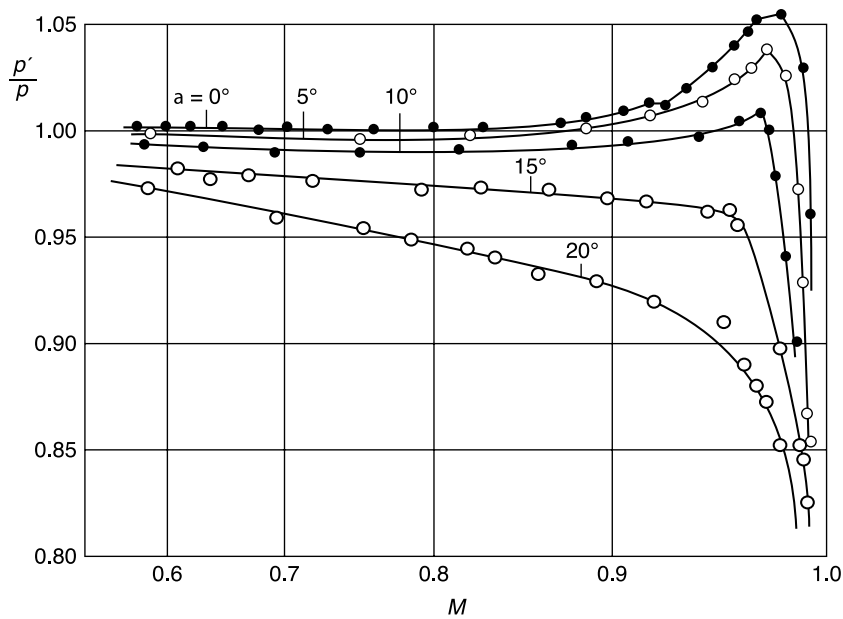

Figure 2.16 **Effect of position of holes in a static pressure supersonic probe**

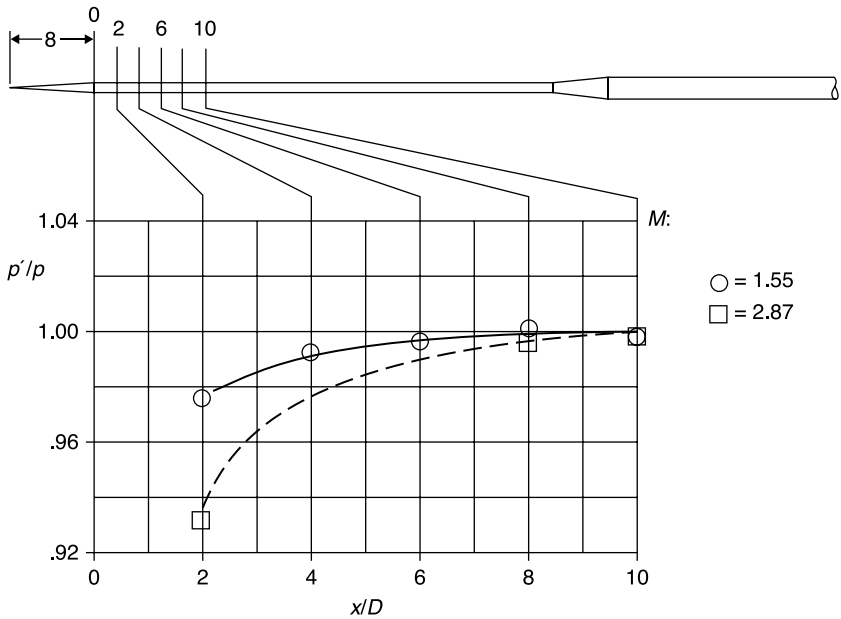

Source: [2]

formed and static holes should be placed at least ten diameters after the beginning of the cylindrical tube (Figure 2.16) where the effects of shock waves are offset by the expansion that occurs at the beginning of the cylinder.

2.4.5 Effect of stream turbulence

The effects of turbulence on the reading of a static tube are complex. In the case of isotropic turbulence, it is estimated that the reading error is 1% when the intensity of turbulence is 10%. There are difficulties only in the zones of separation and wakes.

2.4.6 Effect of size and shape of holes

Each hole in a wall alters the boundary conditions producing a curvature of the streamlines and hence a pressure change, these effects decrease with the decreasing size of the holes. Usually the streamlines entering the

Figure 2.17 **Influence of size and shape of holes on pressure readings**

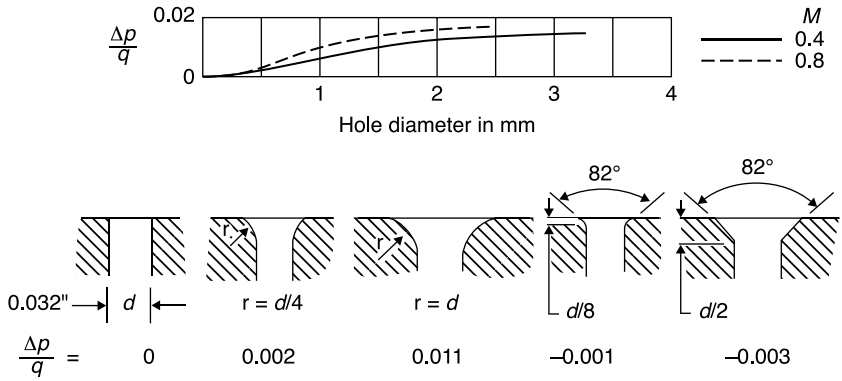

Source: [3]

hole raise the pressure. In some cases the separation of the stream on the leading edge of the hole causes a decrease in pressure.

The size of the holes of static pressure must therefore be the smallest possible (see Figure 2.17, which also indicates the effect of the shape of the hole) but this is not consistent with the need not to increase excessively the inertia of the system static hole–connection pipe–pressure gage.

Typical diameters of holes in experiments at low speeds are 0.5–1 mm; in the experiments at higher speed, the size of the hole is usually chosen as the smallest that can be achieved with a power drill, e.g. 0.02 mm.

2.5 Pitot-static tube

A Pitot tube and a static tube can be combined into a single probe, called a *Pitot-static tube*; if the flow is incompressible the dynamic pressure and hence the speed can be directly measured from Equation (2.3).

The outline of a NASA standard probe is given in Figure 2.18: this probe consists of a Pitot tube inserted into a pipe with a hemispherical head in which static holes are positioned so that, for all sufficiently high Reynolds numbers, pressure disturbances induced by the head and those induced by the stem perpendicular to the axis of the pipe are below 0.5% and balanced. The performance of the probe at varying angles of incidence is shown in Figure 2.19.

Pitot-static tubes can be used without appreciable scale effects in the same range of Reynolds numbers of static tubes. In general, however, the head of the tube is quite blunt, and the effects of compressibility discussed

Figure 2.18 Standard Pitot-static tube

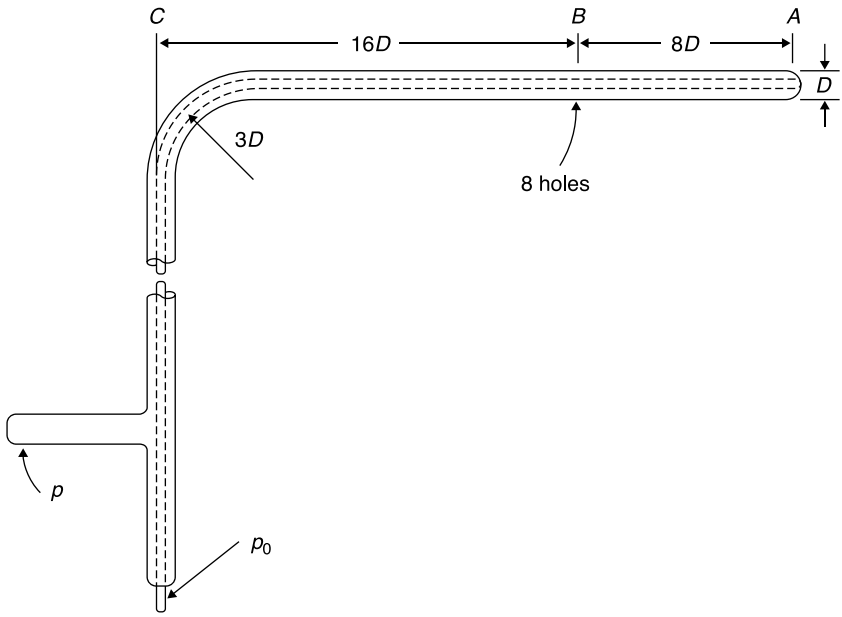

above usually produce an error in static pressure at Mach numbers of the stream appreciably lower than 1. For this reason Pitot-static tubes are often not appropriate at high speeds where separate Pitot tubes and static tubes are preferred.

2.6 Flow direction measurements

The probes used to measure flow speed, as we have seen, must be aligned with the direction of velocity and must have low sensitivity to the angle of attack. If the direction of the flow has to be known, it is mandatory to use probes with high sensitivity to the angle of attack (direction probes). Typically the shapes of these probes are simple bodies (sphere, cone, wedge, tube etc.). In all configurations, one or two pairs of taps, arranged symmetrically to the axis of the probe, are inclined on the direction of stream. With a pair of taps, measures of direction in 2D fields are obtained, in 3D fields, at least two pairs of taps are used.

For each body the aerodynamic sensitivity to the angle of attack is represented by the tangent to the curve $C_p(\alpha)$: the sensitivity of a Pitot tube (Figure 2.4) is negligible up to 10° and its maximum between 40°

Figure 2.19 Performance of standard Pitot-static tube in yaw

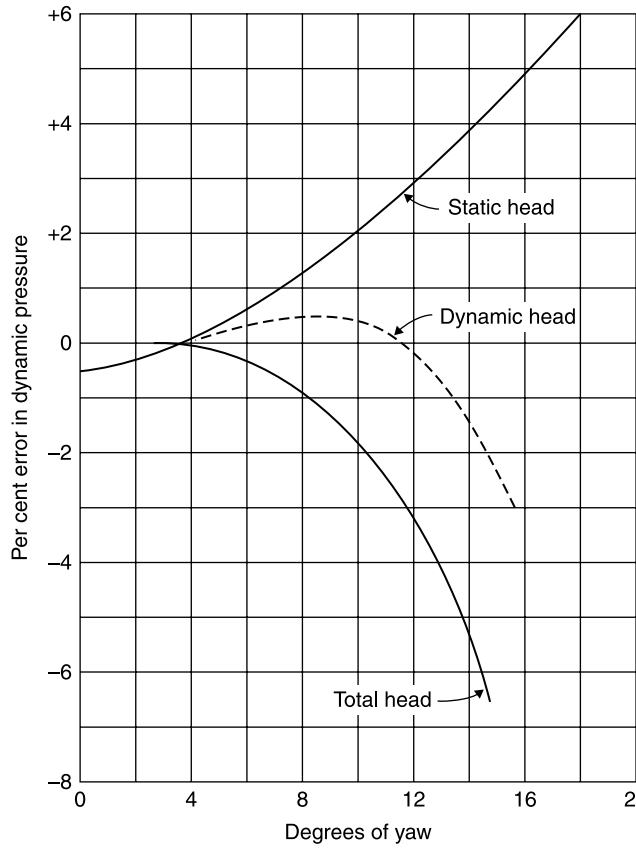

Source: [1]

and 60°. The sensitivities of cylinders and spheres show a similar behavior (Figure 2.2). Usually the pressure taps are positioned where the sensitivity is greatest, the only exception is the position where $C_p = 0$ used when, with the probe axis aligned with the speed, also the pressure p_∞ must be measured. However, if precise measurements of p_∞ are required, it is preferable to use a separate static tube.

Two different strategies able to measure the direction of velocity can be used:

1. The direction probe is rotated into the stream until the pressure difference between two opposite taps is zero (*null reading method*). The axis of the probe is then in the same direction of the stream in the limits of the accuracy of the instrument; construction errors can be

eliminated by repeating the test with the probe rotated at 180° and making an average between the two readings.

2. The probe is fixed in a reference direction (*fixed method*): the pressure difference between opposite taps is read and the corresponding angle between the axis of the probe and the direction of stream velocity is obtained from a calibration curve.

The first method is more immediate because it does not require calibration but has the disadvantage that the probe must be oriented with precision, which is particularly difficult if the probe is to be moved in a closed test chamber, or two angles in two orthogonal planes are to be measured (3D probes).

Calibration is often performed in a free jet flowing from a nozzle placed at the exit of a large stagnation chamber; the pressure difference between each pair of orifices divided by dynamic pressure is reported for each angle of the probe with the known velocity direction:

$$\frac{p_2 - p_1}{q} = f(\alpha)$$

Many types of probes are used, the choice is influenced by the Mach number of the stream, the type of flow (2D or 3D) and by considerations of robustness and ease of calibration. At low Mach numbers, the sensitivities of all the usual types of direction probes are of the same order, with values of $d[(p_2 - p_1)/q]/d\alpha = 0.04 \div 0.08$ per degree. Using a suitable gage the direction of stream can therefore be determined with an approximation of 0.1°. The sensitivity decreases with increasing Mach number.

Measures of direction of velocity are rarely made in a uniform stream: there are almost always gradients of speed and therefore the errors due to gradients of stagnation pressure are present. If, on the other hand, the shear rate is strong, the measure of a direction probe is meaningless: even when the probe is aligned with the stream, there is a difference in pressure between the two taps because they see different speeds. These effects can be mitigated by minimizing the distance between the taps and using taps with small diameters.

2.6.1 Claw probe

This probe consists of two Pitot tubes, inclined at ±45° with the axis of the probe (Figure 2.20). This probe is commonly used because it is easy

Figure 2.20 Claw probe; variation of sensitivity with Mach number

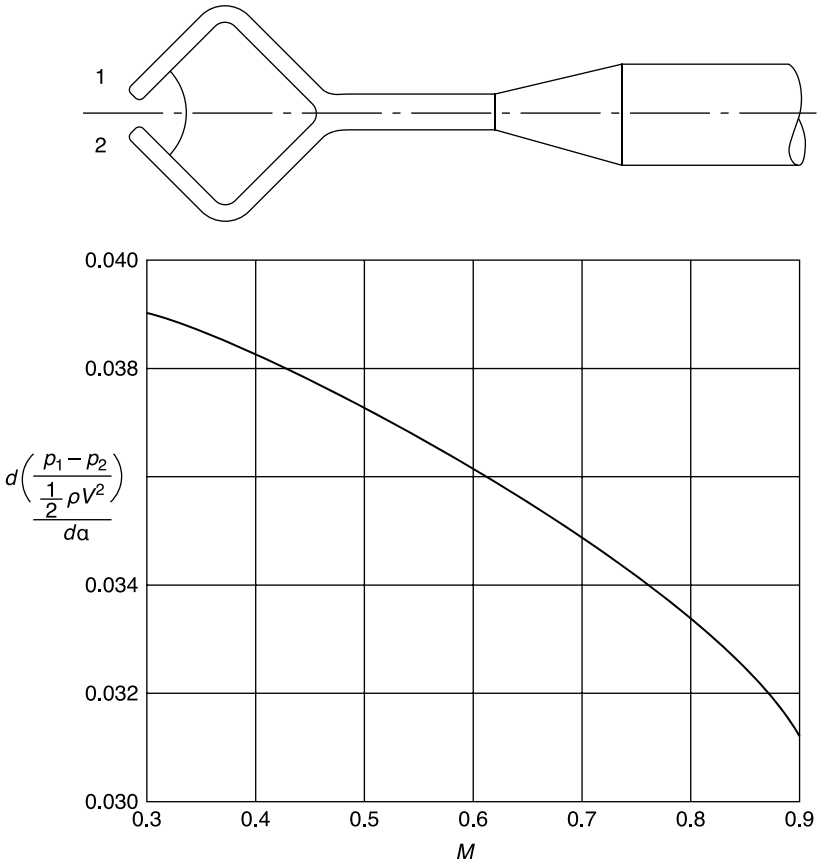

to build but has some serious drawbacks: the structure is delicate and can easily be deformed with use; tube diameters, to reduce the distance, are small and show a slow response.

One version of the claw probe, to be used in the three-dimensional field, is sketched in Figure 2.21. It consists of four tubes which lie in pairs in two planes perpendicular to each other. There is also a version with five tubes with a central tube for the measurement of p_0. Also the static pressure can be calculated through the use of appropriate empirical constants by combining the reading of the Pitot tube with that of one of the directional tubes. This probe suffers from the same limitations as the two-dimensional probe, and does not allow measurements in the vicinity of a wall.

The *Y* probe (Figure 2.22) has a higher sensitivity but, due to the

Figure 2.21 A 3D claw probe

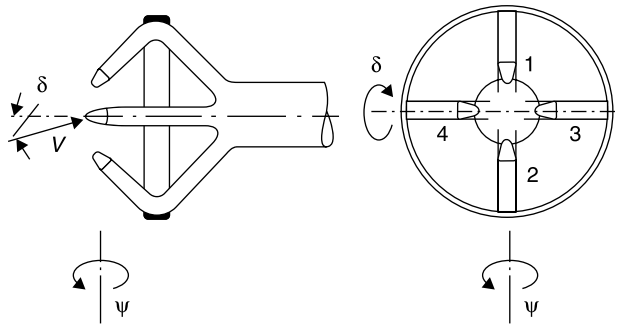

Figure 2.22 *Y* probe; variation of sensitivity with Mach number

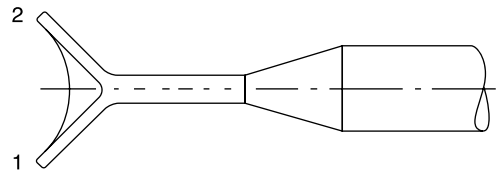

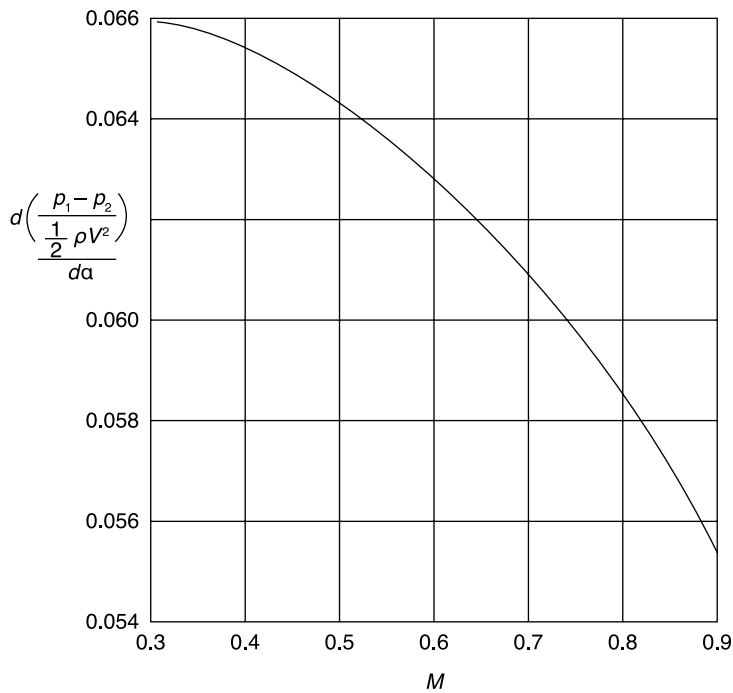

greater distance between the taps, is not suitable for measurements in the presence of gradients of velocity.

2.6.2 Cylindrical probe

The probe consists of a cylinder perpendicular to the stream on which three holes are drilled, the central one for the measurement of stagnation pressure (Figure 2.23). The probe has a sensitivity of about 0.05 per degree.

As can be seen from Figure 2.2, the separation of the wake also changes the distribution of pressure in the upstream part of the cylinder and also in different ways according to the flow regime, laminar or turbulent. If the null reading method is used, that does not lead to errors because the situation is symmetrical about the axis, problems arise in the transitional regime in which there are oscillations of the wake and thus in the pressure.

The sensitivity of the instrument depends on the position of the holes (Figure 2.24): at low Mach numbers, it is highest when the holes are placed at ±45°; for higher Mach numbers, the optimal angle increases, e.g. at $M = 0.7$ would be about ±70°. The critical Mach number, not to be exceeded, is 0.55.

Figure 2.23 A 3-hole cylindrical probe

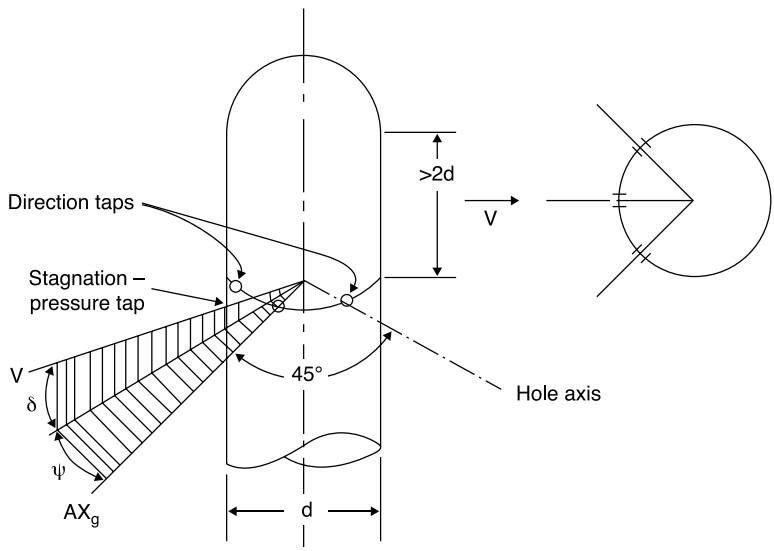

Figure 2.24 **Effects of positioning of holes on a cylindrical probe at different Mach numbers**

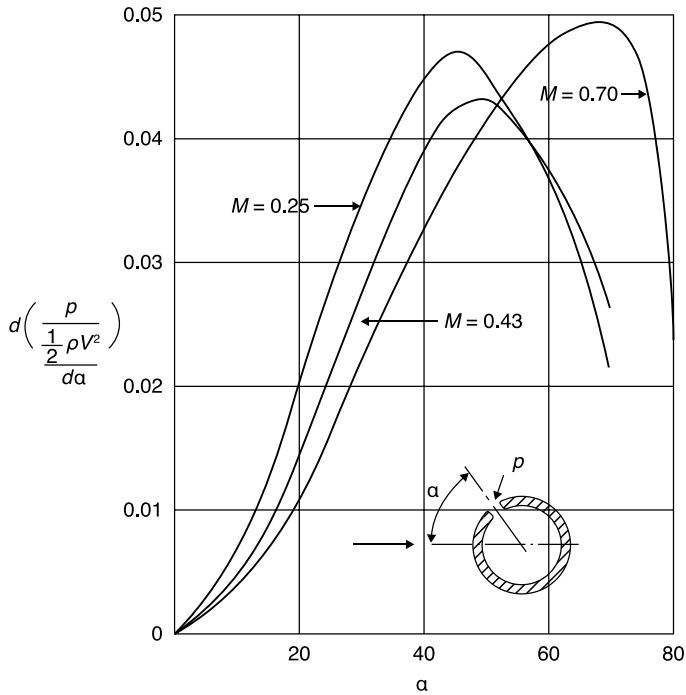

In a 3D version, a fourth hole on the cap that closes the cylinder is used to measure the pitch angle from the difference between measured pressure and stagnation pressure. This probe is small and is therefore used for measurements in tight spaces such as those typical of turbo machinery blades. Because of the distance between the holes, it is not very accurate in the presence of velocity gradients.

2.6.3 Supersonic probes

The wedge probes (Figure 2.25) have the advantage over the cylindrical ones of having higher critical Mach numbers (depending on the angle of opening) and of being much less sensitive to the position of the holes.

They are also suitable for supersonic flows. The influence of the Mach number on the sensitivity of some cones and a wedge can be seen from Figure 2.26; the sensitivity of a wedge of 8° turns out to be equivalent to that of a cone of 30° in the field $2 \leq M \leq 5$. In the hypersonic regime,

Figure 2.25 A wedge probe

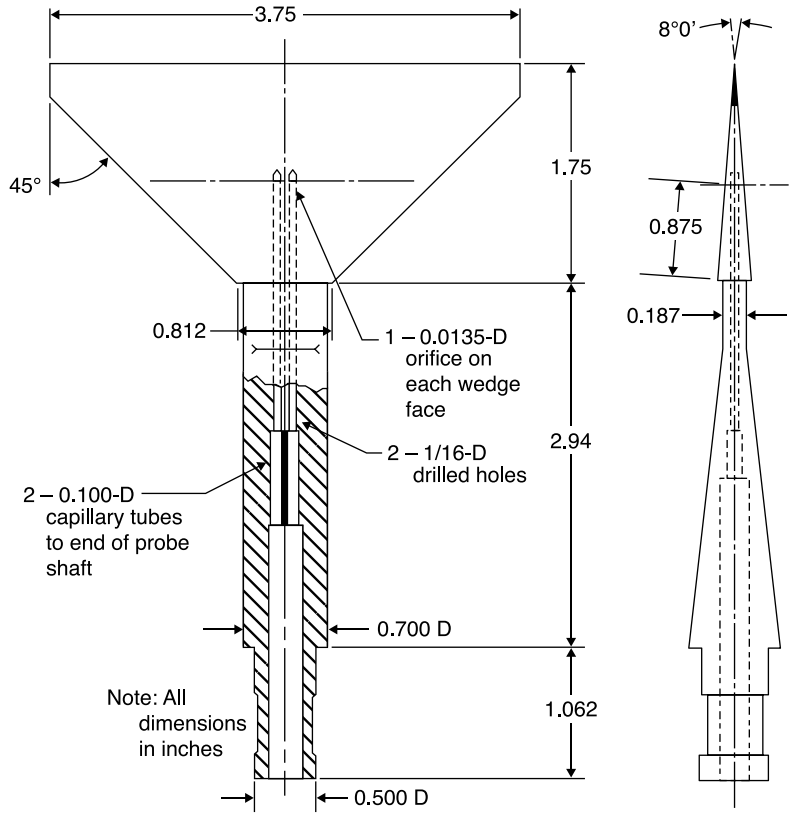

Source: [5]

a conical configuration is almost universally used (with angles from 20° to 90°).

2.6.4 The cobra probe

The previous probes have significant distances between the holes and therefore are not suitable for measurements in boundary layers. The cobra probe eliminates this problem because it consists of two tubes mounted side by side with entrances inclined to ±45° or ±60° (Figure 2.27). To reduce the response time, tapered tubes can be used so that the connecting tubes to the manometer have a larger diameter than the probe. These characteristics make it the best probe for the null reading method.

Figure 2.26 Sensitivities of the cone and wedge probes as functions of the Mach number

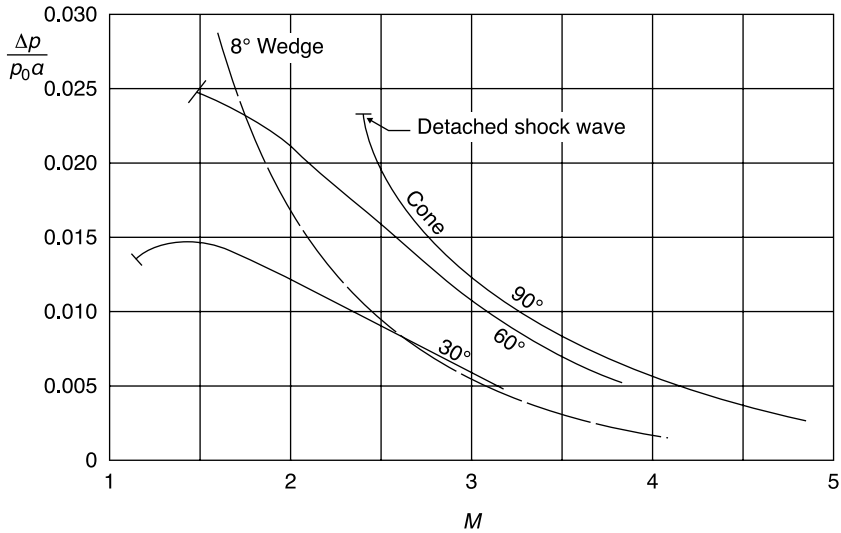

Source: [5]

Figure 2.27 The cobra probe

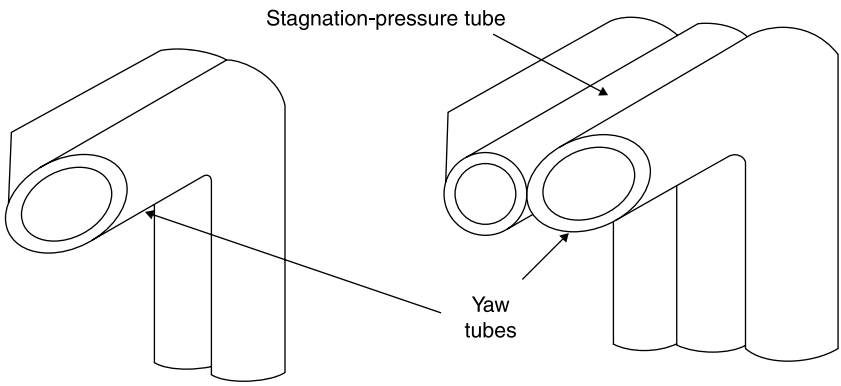

Often a squared third central tube is provided for the measurement of p_0, but in this case the distance between the holes increases. It should not be used to calculate the dynamic pressure and static pressure because the pressure difference between each of the side holes and the central one is only a relatively small fraction of the dynamic pressure. The probe is also used in supersonic flows and has a better sensitivity than the wedge for $M \geq 2$.

2.6.5 Spherical five-holes probe

Another type of tool for subsonic 3D fields, shown in Figure 2.28, consists of a sphere supported on a stem parallel or orthogonal to the stream with 4 holes on the front located at 90° from each other and a central hole for the measurement of p_0. The sensitivity of the instrument is about 0.08 per degree.

Figure 2.2 shows the theoretical and measured pressure around a sphere in laminar and turbulent flows. Assuming a potential flow maximum sensitivity is obtained at 42°, experimentally the maximum sensitivity is obtained around 50° and depends on the position of separation and thus on the Reynolds number. The transition point may move randomly producing asymmetry and indeterminate results. The maximum pitch angle detected is about 60°.

The presence of velocity gradients and the proximity of a wall restrict the use of this probe as they do for all probes with well-separated holes.

2.6.6 Cylindrical five-holes probe

Variants of the previous instrument are a cylinder with hemispherical head (Figure 2.29), a truncated pyramid (Figure 2.30) or a truncated cone. The advantage of these probes compared to the spherical probe is the elimination of separation.

Figure 2.28 The five-holes spherical probe

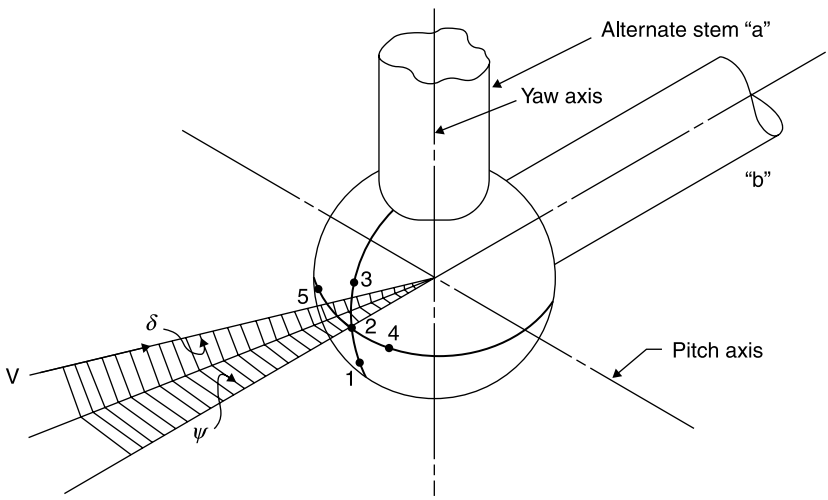

Figure 2.29 A five-holes probe with hemispherical head

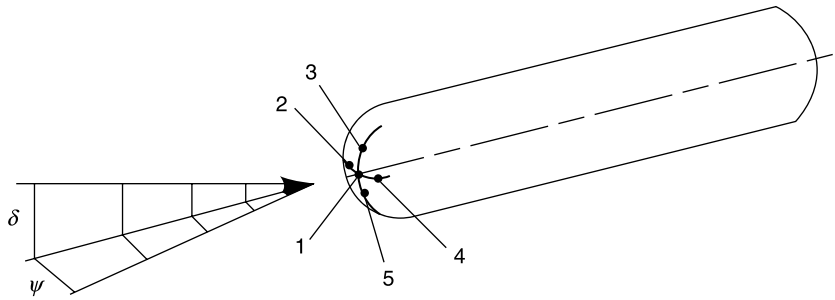

These probes measure the angles of pitch and yaw of the stream, the stagnation and the dynamic pressure; therefore provide sufficient data to fully calculate the fields of velocity and pressure. The maximum measurable angle is about 60°.

Figure 2.30 A five-holes probe with a truncated pyramidal head

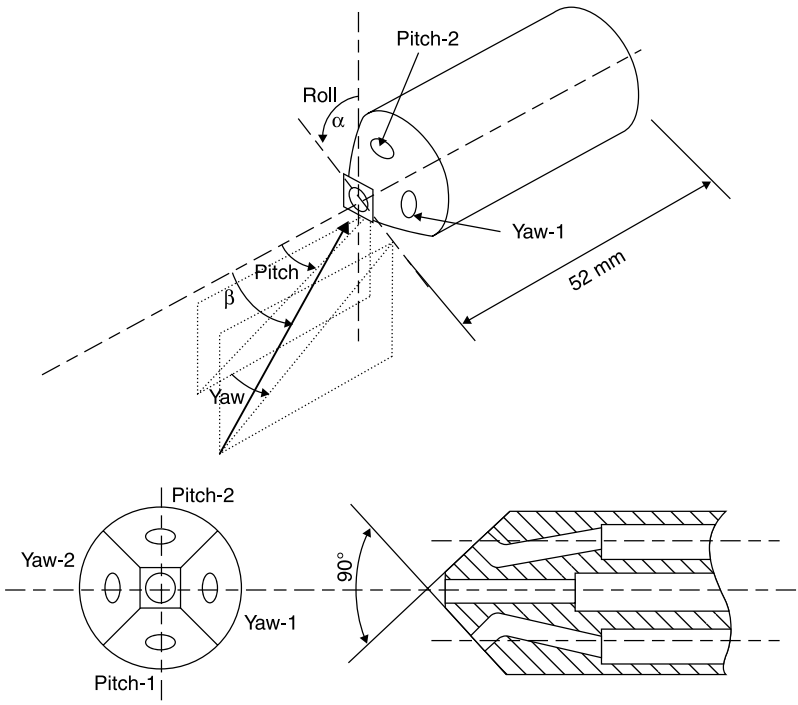

2.6.7 Seven-holes probe

To overcome the limitations on the maximum measured angle, seven-holes probes with a spherical or conical head are used (Figure 2.31). The angular resolution reaches 70° ÷ 80°. The typical diameter of the measuring head is about 3 mm.

The process of calibration of such complex probes, as well as five-holes probes, consists in putting the probe in a known and uniform stream (known in terms of speed, direction of velocity, density, temperature, pressure) and in rotating the probe in a few thousand (e.g. 2000) different angles with respect to the stream and storing the readings of the various pressure taps. A map of calibration is obtained to find magnitude and direction of velocity on the basis of the pressures detected by the seven taps.

2.6.8 Omniprobe

Omniprobe is a marked improvement on the angular resolution of the multi-hole probes. With the use of 18 holes distributed on a spherical surface, streams can be evaluated from virtually any direction. The probe is able to detect velocity vector tilted up to 165° with respect to the probe.

Figure 2.31 A seven-holes truncated cone probe

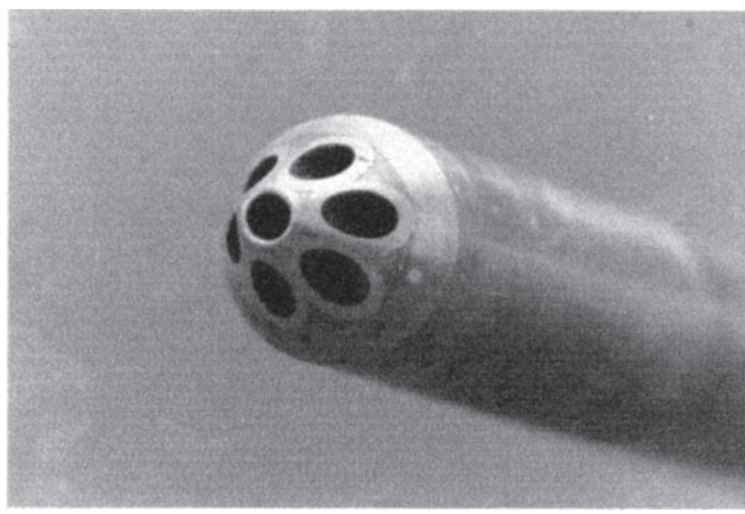

Source: [6]

These features allow measurement in highly inclined streams or even in reverse flow. The probe is useful in the exploration of wakes of bluff body, cars, wings, atmospheric wind.

Calibration is a fairly costly process that requires at least 7000 different tests. The diameter of the spherical head is about 10 mm. The Mach number can vary from 0.02 to 0.95.

2.6.9 Fast-response multi-hole probes

In unsteady flow fields it is necessary to use diagnostic instrumentation with a high frequency response. A probe capable of giving instant information on the three components of velocity and static and stagnation pressures in a stream is achieved by including unsteady pressure transducers directly into the body of the probe.

The highest response rate of 5 kHz is obtained with the transducers positioned in the head of the probe (Figure 2.32) with a diameter of

Figure 2.32 Sectional view of a quick-response probe with transducers embedded in the tip

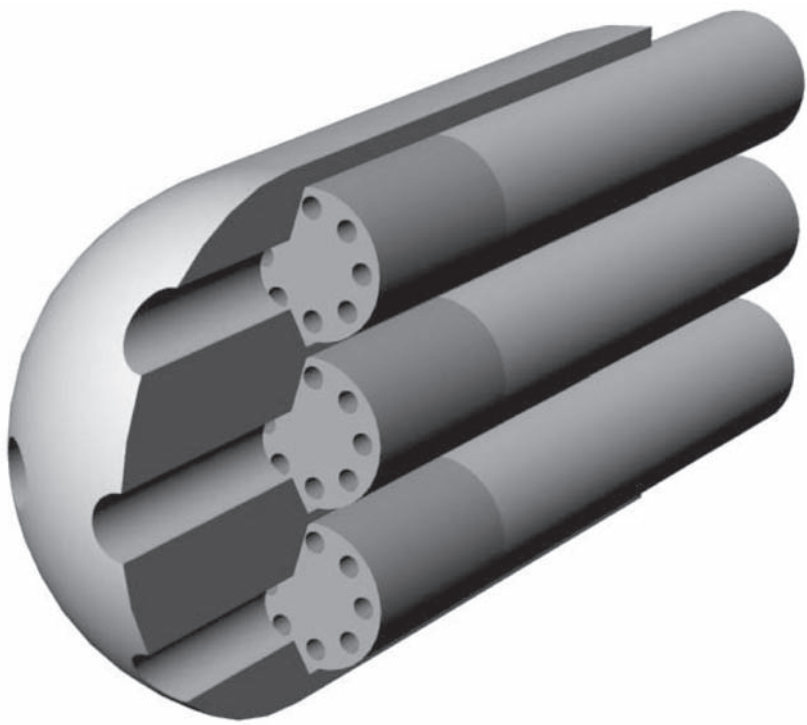

Figure 2.33 Sectional view of a five-hole probe with transducers embedded in the shaft

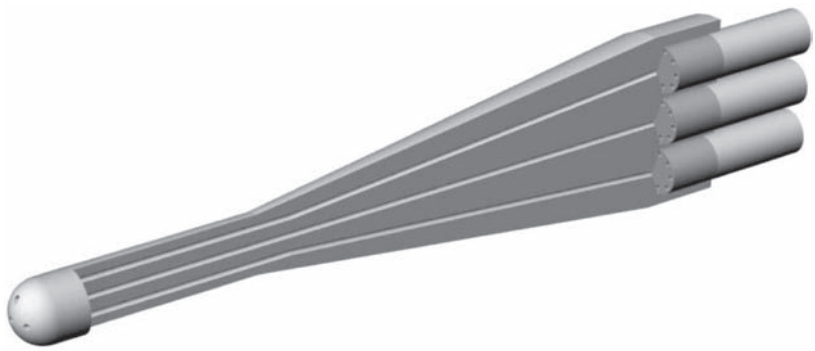

about 13 mm. If smaller heads are needed (about 2 mm in diameter), the transducers must be placed in the shaft (Figure 2.33).

2.7 Mass flow measurements

To measure the mass flow of a fluid in a duct through measures of pressure, it is necessary that the station in which the measure has to be made be free of vortices and that the axis of the duct be straight (no centrifugal forces and thus no pressure gradient in the direction normal to the axis). The international regulations provide, for any kind of flowmeter, the length of pipe (in diameters) with constant section and straight axis that must separate the measuring station, both upstream and downstream, from valves, elbows, intersections with other tubes and changes in section. For difficult cases, a flow conditioner, consisting of a circular or hexagonal (honeycomb) block of tubes or by one or more perforated plates, should be included in the duct upstream of the measuring station.

Only under these conditions is the static pressure constant in the section and measurable on the wall; for greater safety, usually four holes, placed at 90° in the same section, are placed in communication with each other in a groove around the tube, measuring the resulting pressure gives, somehow, an average of the possibly different pressures prevailing in the four holes.

As with all probes, any reason to disturb the magnitude of the variable to be measured must be avoided; in this case, one must avoid generating a drag in the duct that modifies the flow rate.

2.7.1 Mass flow measurement by the velocity profile

The mass flow can be determined, by definition, by integrating the distribution of speed in a section of the duct. If the static pressure is constant in each section, it can be measured in a tap on the wall; to know the distribution of velocity it is sufficient to measure the distribution of stagnation pressure.

It is sufficient to introduce a Pitot tube in the duct through the wall and to explore a whole diameter. The exploration should also be repeated along a diameter orthogonal to the first. The method is laborious and unsuitable for routine work but has a high degree of accuracy and should be applied when calibrating a flowmeter. The procedure can be simplified if, as in all practical cases, the flow in the duct is fully developed: under these conditions the average velocity can be determined by measuring the speed on the axis and knowing the relationship existing between the average speed and the speed on the axis (Figure 2.34) which is a function of Reynolds number referred to the diameter of the duct: this ratio is 0.5 in laminar flow and increases to about 0.8 in the turbulent regime.

Figure 2.34 Ratio between average and maximum speed in a tube as a function of the Reynolds number

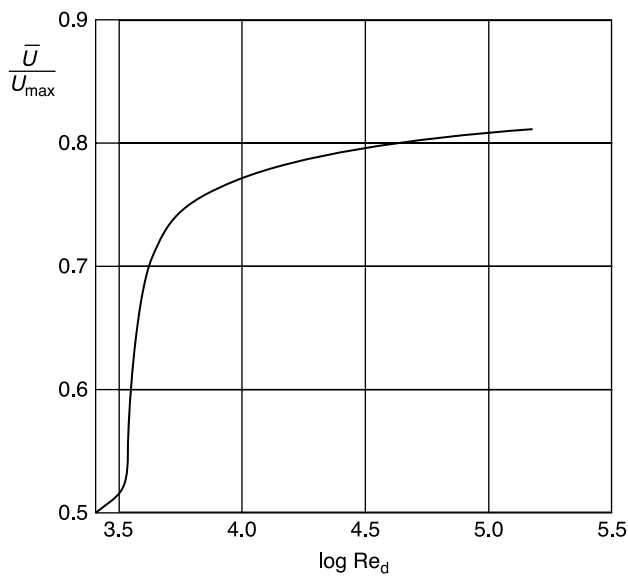

Because the Reynolds number is not known a priori, it is necessary to follow an iterative process:

1. Assume a Reynolds number.
2. Read in Figure 2.34 the corresponding ratio between the average speed and the speed on the axis.
3. Measure the speed on the axis.
4. Calculate the average speed.
5. Calculate the Reynolds number.
6. Start again from step 2 until the speed difference between two consecutive iterations is less than the desired approximation.

Since in usual industrial applications the motion is always turbulent, Preston devised an instrument consisting of a tube with a constant section in which four Pitot tubes are placed at intervals of 90° on a circle whose radius is 3/4 of the radius of the pipe; four static taps are made on the wall corresponding to the heads of the Pitot tubes (Figure 2.35). The idea is that at 3/4 of the radius the speed is a constant fraction of the average speed in a wide range of Reynolds numbers and surface roughness.

Figure 2.35 The Preston tube

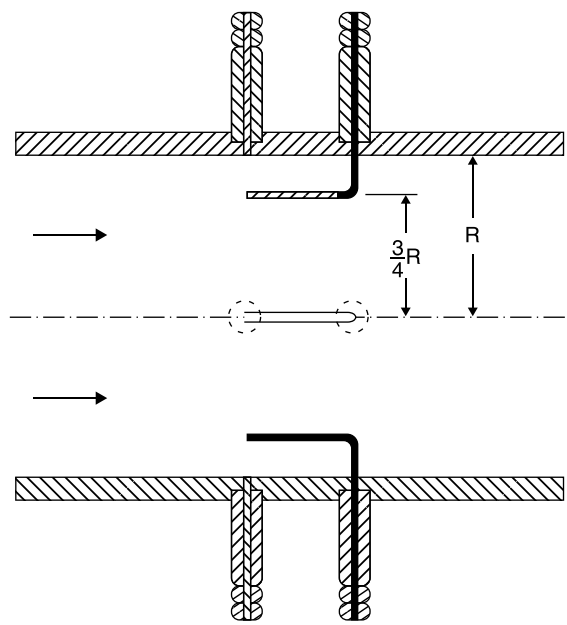

The Preston tube is an ideal instrument to measure the flow in a duct connected to a pumping system of limited power because inherent losses are negligible.

2.7.2 Mass flow measurement by throttling devices

Measurement of mass flow can be made easier assuming that the motion in the duct is almost one-dimensional (gradual and small variations of area, constant speed in each section, no production of entropy) and incompressible. Between two stations of the tube both the incompressible Bernoulli equation and the conservation of volumetric flow are valid:

$$p_1 + \frac{\rho U_1^2}{2} = p_2 + \frac{\rho U_2^2}{2}$$

$$U_1 A_1 = U_2 A_2$$

from which the mass flow in the pipe can be found:

$$\dot{m} = \rho U_2 A_2 = A_2 \sqrt{\frac{2\rho(p_1 - p_2)}{\left[1 - (A_2/A_1)^2\right]}} \tag{2.8}$$

This method of measuring the mass flow rate is used in throttling devices. The advantages of these devices include robustness, reproducibility of the calibration and their insensitivity to the Reynolds number, above certain minimum values, and to the asymmetry and the disturbance caused by duct obstructions and deviations upstream.

Calibration formulas of these devices are always in the form of Equation (2.8) even if the assumptions of validity of that formula are far from being met. Correction factors are introduced:

- the *flow coefficient*, C, takes into account that the flow is not truly one-dimensional and isentropic;
- the *expansion factor (coefficient of compressibility)*, ε_2, takes into account the variation in density that occurs when the ratio of pressure generated by the throttling device reaches high values.

The formula for throttling devices then becomes:

$$\dot{m} = \rho_2 U_2 A_2 = C\varepsilon_2 A_2 \sqrt{\frac{2\rho_2(p_1 - p_2)}{\left[1 - (A_2/A_1)^2\right]}} \tag{2.9}$$

2.7.2.1 Plate orifice

The plate orifice (Figure 2.36) is used in cases where the high pressure drop introduced by the device can be tolerated. The duct is obstructed by a plate with a circular hole, the static pressure is measured at the tube wall immediately upstream and immediately downstream of the orifice.

Figure 2.36 **Plate orifice**

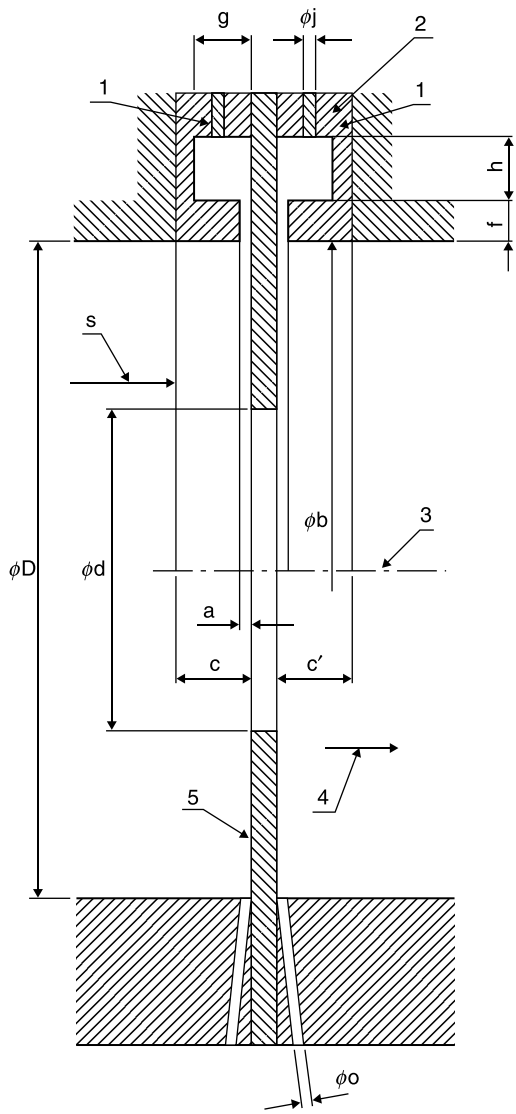

Source: [9]

Since the stream separates from the walls of the duct both upstream and downstream of the orifice, the outflow is strongly swirling and cannot be considered isentropic. Furthermore the stream continues to accelerate downstream of the orifice because of the formation of a *vena contracta* and thus the static pressure is lower than that corresponding to the assumed uniform flow through the orifice. Of course, due to the strong deviation from the assumption of isentropic motion assumed in the formulation of Equation (2.8), the discharge coefficient, C, is not very close to 1: it varies from 0.6 to 0.8 for area ratios, A_2/A_1, ranging between 0.2 and 0.75 and for Reynolds numbers, based on the diameter of the orifice and the speed in the orifice, in excess of 5×10^4.

The device is inexpensive, it can easily be adapted to different ranges by simply changing the perforated plate, and it is therefore suitable for laboratory activities.

2.7.2.2 Mouthpiece orifice

Discharge coefficient much closer to 1 can be obtained using a mouthpiece orifice (Figure 2.37) so as to obtain a more regular outflow; the construction is obviously more complex. The instrument is more expensive than the plate orifice and is therefore more suitable for a permanent installation. The corresponding discharge coefficients are between 0.96 and 0.99 for $0.3 \leq A_2/A_1 \leq 0.8$ and for Reynolds numbers above 10^4.

2.7.2.3 Venturi tube

The outflow through the plate orifice (to a lesser extent through the mouthpiece) is accompanied by significant losses generated in the vortex produced by the sudden contraction regions, so it is more efficient to use a Venturi tube (Figure 2.38), which is made of a convergent, a constant section tube and a diffuser with a small angle of divergence; the losses of stagnation pressure slightly exceed those that are generated in a tube with a constant section of equal length. The device is rather long and expensive, it is used in permanent installations in power stations and chemical plants.

The static pressure is measured at the entrance of the convergent and in the throat, the discharge coefficient is approximately 0.995.

It must be emphasized here that the quoted values of C are valid only for a well-defined geometry and thus are only a guide for different geometries. In ISO regulations, from where the previous figures are taken,

Figure 2.37 Mouthpiece orifice

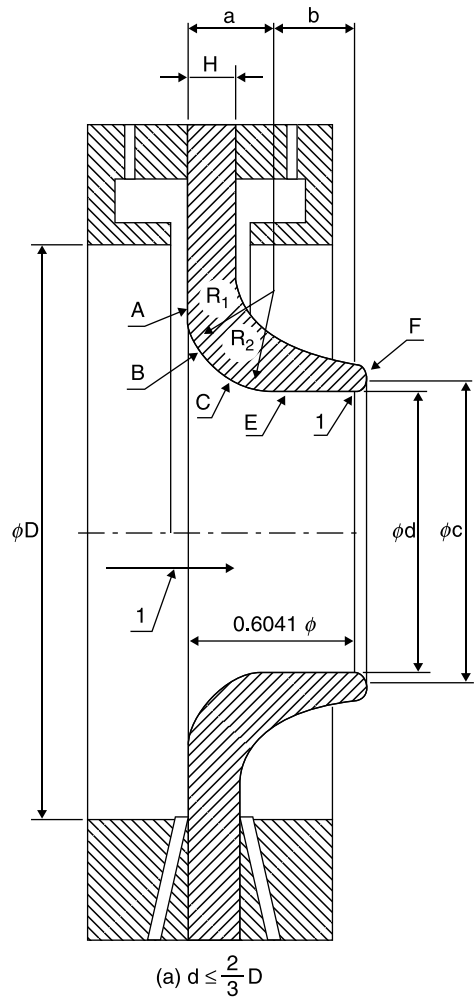

Source: [9]

detailed plans of the various types of flowmeters, the rules to be followed when installing and measuring, quality of workmanship and materials to be used are given.

2.7.2.4 Sonic nozzle

If a large pressure drop can be accepted, a sonic nozzle can be used as a mass flowmeter. In the throat, where the unit Mach number is attained:

Figure 2.38 The Venturi tube

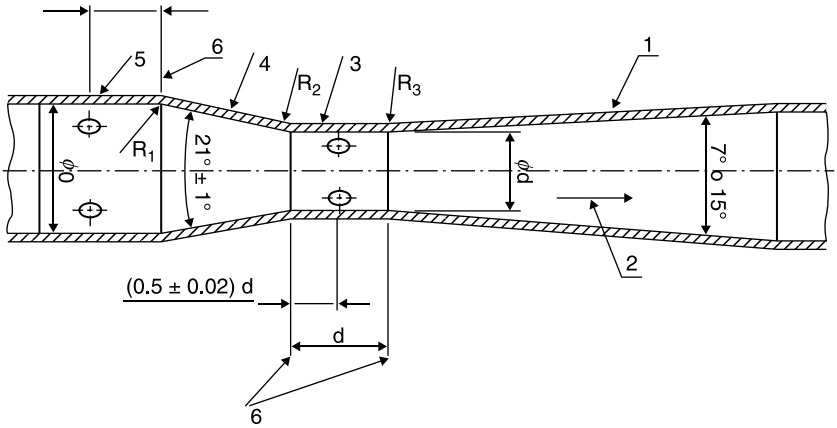

Source: [9]

$$\dot{m} = \rho^* U^* A^* = \frac{p_0}{\sqrt{RT_0}} A^* \sqrt{\gamma \left(\frac{2}{\gamma + 1} \right)^{\frac{\gamma+1}{\gamma-1}}} \tag{2.10}$$

so the mass flow rate can be calculated from a measurement of stagnation pressure and stagnation temperature. Even in this case a flow coefficient is used.

2.7.3 Variable area orifices

There are other systems for measuring flow, based on the measurement of the speed of rotation of a small turbine or gear cam. These systems are typically used to know the total mass passed in a given time (gas or fuel meter).

A particular type of mass flowmeter, called a "rotameter," is widely adopted both in the laboratory and in industrial plants, providing a visual indication of the mass flow rate. The instrument consists of a vertical, transparent and slightly conical tube (Figure 2.39), in which the fluid is introduced from below. A floating body is inserted in the tube and the mass flow rate is read on a scale printed on the wall of the tube: the floating body is in equilibrium at the height where the drag added to the buoyancy force equals its weight. As mass flow rate increases, drag tends to increase and the body moves up to a new larger section where speed, and hence drag, goes back to the previous value.

Figure 2.39 The rotameter

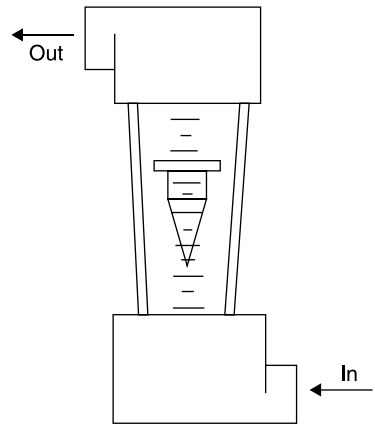

Often a set of floating bodies of different masses is provided with each rotameter in order to use the same tube for different ranges of mass flow rates. Rotameters are available for a large number of gases at different pressures and for many liquids of industrial interest.

References

1. J.S. Thompson and D.W. Holder (1958) "Notes on Wind Tunnel Pressure Measurements from the Operator's Point of View," Royal Aircraft Establishment Tech. Note No. Aero. 2547.
2. A. Pope (1961) *Wind Tunnel Calibration Techniques*, AGARDograph 54.
3. L.W. Walter and E.J. Redman (1954) "Needle Static Pressure Probes Insensitive to Flow Inclination in a Supersonic Stream," NAVORD Report 3694.
4. W. Gracey (1959) "Measurement of Static Pressure on Aircraft," NACA TN 4184.
5. G.G. Goranson et alii (1957) "*A Method for the Calibration of Flexible Plate Supersonic Wind Tunnels and Calibration Results for the 12-inch Wind Tunnel at the Jet Propulsion Laboratory*," JPL Report No. 20-110.
6. R.W. Gallington (1980) "Measurement of very large flow angles with non-nulling seven-hole probe," *Aeronautics Digest*, USAFA-TR-80-17: 60–88.
7. Aeroprobe by Dantec Dynamics Inc., *Omniprobes*. Available at: www .dantecdynamics.com.
8. Aeroprobe by Dantec Dynamics Inc., *Fast-Response Multi-Hole Probes*. Available at: www.dantecdynamics.com.
9. UNI EN ISO 5167-1:1997.

3

Hot wire anemometer

Abstract: This chapter will address the measurement of velocity in unsteady flows in 1D, 2D and 3D fields obtained with hot wire anemometers, from the first analog constant current anemometer in the 1930s to the current solid state digital constant temperature anemometer.

Key words: hot wire, King's law, turbulence intensity.

3.1 Introduction

As seen in Chapter 2, speed can be obtained from pressure measurements only in almost stationary streams. In turbulent flows it is necessary to use the hot wire anemometer, which has a very high frequency response, or, alternatively, the laser-Doppler anemometer (LDA), the laser-2 focus anemometer (L2F), which are able to infer the intensity of turbulence from a statistical survey of the speeds of many particles carried by the stream.

The sensor of the hot wire anemometer (Figure 3.1) is a metallic wire heated by the Joule effect and cooled by the fluid flow. Because the

Figure 3.1 Sensing element of a hot wire anemometer

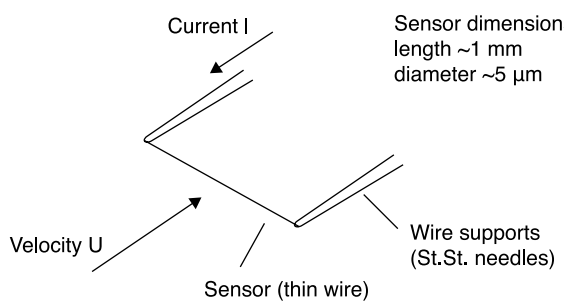

Figure 3.2 Comparison of output signals from CTA, LDA and PIV

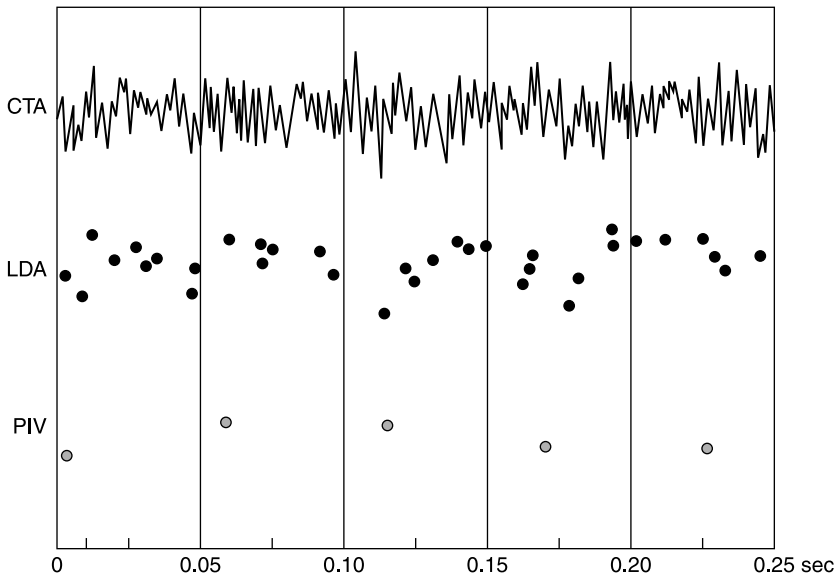

electrical resistance of the wire changes with temperature, by the changes in the difference of potential at the ends of the wire the corresponding changes in flow velocity can be deduced. Fluctuations in speed can be measured, using appropriate electronics, at a very fine scale at high frequency.

The output signal of the hot wire anemometer is compared in Figure 3.2 with those from the laser-Doppler anemometer and particle image velocimetry (PIV): the advantages of hot-wire anemometer on other systems, in addition to being less costly, are the ease of use, the analog output and a high temporal resolution that allows spectral analysis of the signal.

Note that LDA signals (like those of the L2F) are random: a signal is provided each time a particle passes in the measuring zone, and those of the PIV are cadenced by the frequency with which pairs of consecutive images are taken by a charged-couple device camera.

3.2 Materials for probes

The operation of the hot wire anemometer is based on the fact that the resistance of the wire, R_w, varies with temperature, T_w, according to the linear equation:

$$R_w = R_a\left[1+\alpha\left(T_w - T_a\right)\right] \tag{3.1}$$

where R_a is the resistance at the reference temperature, T_a, and $\alpha[K^{-1}]$ is the temperature coefficient of the resistance.

The overheating ratio of the resistor is defined as:

$$\frac{R_w - R_a}{R_a} = \alpha\left(T_w - T_a\right)$$

The ideal material for the sensor must have a high value of α coupled with a high mechanical strength, be weldable or able to be soft soldered and reduced to wires with a very small diameter, order of μm. Table 3.1 shows the characteristics of the most used materials.

- The tungsten wires are robust (they are used successfully in supersonic flows) and have a high temperature coefficient of resistance but cannot be used at high temperatures in air because they oxidize easily; they cannot be soldered.
- Platinum has a good resistance to oxidation, has a good temperature coefficient, but has a low mechanical strength, especially at higher temperatures.
- The platinum-iridium alloy is to be avoided because it is unstable at high temperatures.
- The platinum-rhodium alloy is a compromise between tungsten and platinum, with good resistance to oxidation and strength greater than platinum, but has a low temperature coefficient.

To fix ideas about the orders of magnitudes involved, we will refer to a typical sensor consisting of a tungsten wire with length ℓ = 1.2 mm, diameter d = 5 μm, operating temperature T_w = 300°C. Cold resistance is R_a = 3.5 Ω, the resistance at 300°C is R_w = 7 Ω, the overheating ratio = 1.

3.3 Probes

A wire is stretched between two metal prongs, similar to sewing needles (Figure 3.3). The diameter of the wire is limited by the need to have an adequate electrical resistance, a very rapid response and a high resolution. The diameter normally employed is 5 μm. To increase the size of the

Table 3.1 Sensor materials for hot wire probes

	Breaking stress $\times 10^{-4}$ (Ncm^{-2})	Maximum temperature (°C)	Soft-solderable	Weldable	Available as Wollaston wire	Minimum diameter (μm)	$\alpha(K^{-1})$	Resistivity at 0°C $\times 10^{6}$ Ω (cm)	Thermal conductivity at 0°C ($Wcm^{-1}K^{-1}$)
Tungsten	20 ÷ 25	300 (oxidizes) melting point 3382	No	Yes if plated	No	2.5 ÷ 3.8	0.0035 ÷ 0.0047	4.9 ÷ 5.5	1.9
Platinum	2 ÷ 3.6	800 ÷ 1200 melting point 1800	Yes	Yes	Yes	1.0 ÷ 1.25	0.0030 ÷ 0.0038	9.8 ÷ 10	0.7
Platinum-iridium (80/20)	7	750	Yes	Yes		38	0.00085	32	0.2
Platinum-rhodium (90/10)	6	1400 melting point 1600	Yes	Yes	Yes	0.6	0.0016	9	0.4

Figure 3.3 Miniature probe

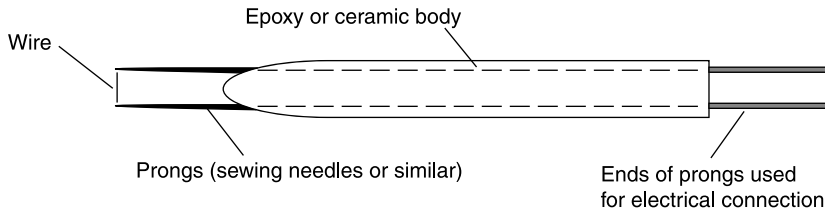

wires in order to make them more manageable during processing and assembly and/or improve the weldability, platinum wire covered with a thick coating of silver (Wollaston wire) or gold-plated tungsten wires are used. After the wire is welded to the supports, the plating is removed with an acid in the zone to be used as a sensor.

The length of the wire is limited by the need to have a good spatial resolution: the sensor simply senses an average speed on its length and the objective is to measure the speed at one point. The length must also be much smaller than the size of the vortices. Plated tungsten wires are used with the minimum length of 1.2 mm (miniature probes). These probes are best used in air flow with turbulence intensity less than 10% and have the highest frequency response; they can be repaired.

If the wire is too short, aerodynamic interference of the prongs has a not negligible effect and, due to the conduction towards the supports, the temperature of the wire is not uniform. These drawbacks can be alleviated using a longer wire ($\cong$ 3 mm) of the Wollaston type or plated tungsten and using as a sensor only the central part of it (1 mm) after removing the plating with a chemical attack (Figure 3.4). These probes are used in air streams with intensities of turbulence up to 25% and have a frequency response less than that of miniature probes; they can be repaired.

Figure 3.4 Gold-plated sensor

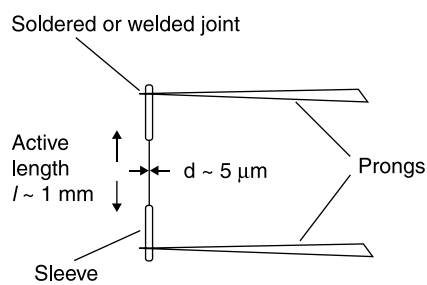

Figure 3.5 Hot-film probes (bottom right, the fiber probe)

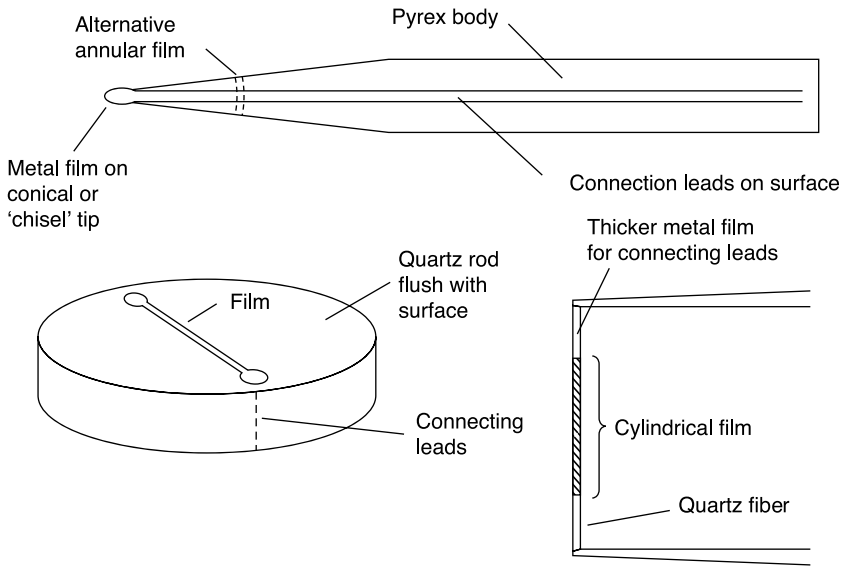

Another type of sensor, called fiber hot film, has replaced the wire in many heavy duty applications (air containing powder, liquid). This type of sensor is made with a quartz fiber on which a film of conductive material covered with quartz is deposited (Figure 3.5). The diameter in this case is the order of 70 μm, the frequency response is lower than that of the wires; they can be repaired.

In addition to the form of wire, hot film sensors can be realized in the most varied shapes: cone or wedge, cylinder, etc. (Figure 3.5). They can be used from low to moderate frequencies of fluctuation of speed; they cannot easily be repaired.

The films are usually made of platinum or nickel, the support is made of Pyrex glass or quartz fiber. If the fluid is a conductive liquid, the sensor must be electrically insulated from the liquid using a thick quartz coating.

3.4 Operating principle

From the energy balance of the wire of the anemometer, heated by the Joule effect and cooled by a fluid stream, we have:

$$\frac{C_w dT_w}{dt} = W - \dot{Q} \tag{3.2}$$

where C_w is the heat capacity of the wire, W is the electrical power supplied to the wire and $\dot{Q}$ is the thermal power exchanged among the wire and the environment by convection, conduction and radiation.

3.4.1 Conduction to the supports

The supports have a diameter much greater than that of the wire, partly for reasons of robustness and partly to avoid heating up at the passage of electric current; for this reason, the temperature at the end of the wire is very close to the temperature of the fluid, T_a, and thus the heat transfer by conduction along the wire is appreciable (Figure 3.6). Since this effect is quite complicated, especially when there are fluctuations of speed that over time will change the temperature distribution on the wire, it is difficult to make a theoretical evaluation valid in general and it is necessary to calibrate each individual probe.

3.4.2 Radiation

Radiation is negligible because the temperature of the wire (up to 300°C) is not too high compared to the ambient temperature.

Figure 3.6 **Effects of conduction to the supports on the distribution of wire temperature**

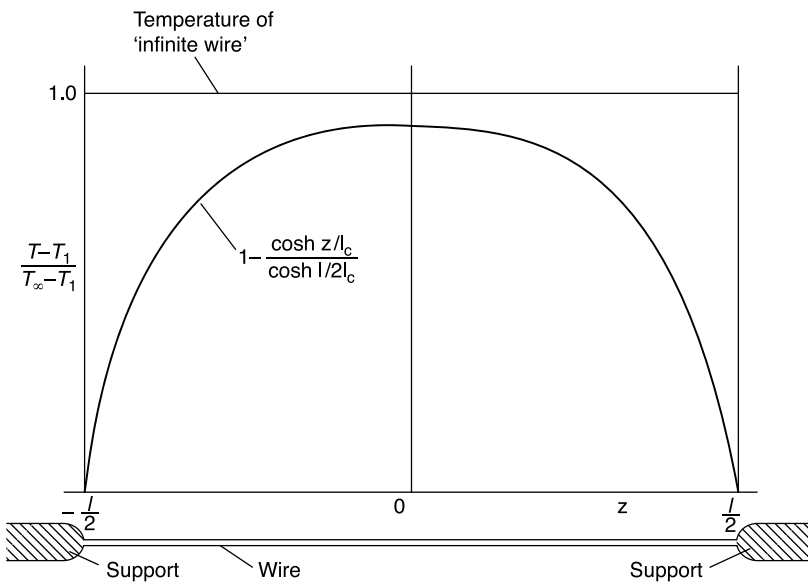

3.4.3 Free convection

Free convection losses are usually negligible, so only forced convection can be taken into account, if:

$$\mathrm{Re}_d > 2\sqrt[3]{Gr} \qquad \text{where} \qquad Gr = \frac{d^3\beta g(T_w - T_a)}{\nu^2}$$

where Re_d is the Reynolds number referred to the diameter, d, of the wire, Gr is the Grashof number, which measures the relative importance of the buoyancy force with respect to the viscous force, β is the coefficient of thermal expansion (= $1/T$ for perfect gases), g is the acceleration of gravity, ν is the kinematic viscosity.

For the reference probe $Gr = 5.3 \times 10^{-6}$, so the minimum speed for which the free convection can be ignored is 5 cm/s.

3.4.4 Forced convection

The wire can be considered as a cylinder of diameter d and length ℓ, with the ratio $d/\ell << 1$ (1/240 for the reference probe), placed perpendicular to the direction of the velocity U, which is considered uniform over the entire length of the wire. The thermal power exchanged by convection between the wire at temperature T_w, and the fluid at temperature T_a can be calculated from the equation

$$\dot{Q} = hA(T_w - T_a) = \pi\ell Nu_d\lambda(T_w - T_a) \tag{3.3}$$

where h is the *film coefficient* of heat transfer, A is the lateral surface of the wire, Nu_d is the Nusselt number referred to the diameter of the wire ($Nu_d = hd/\lambda$) and λ is the coefficient of thermal conductivity of the fluid.

In Equation (3.3) the following assumptions are made:

- the wire is so thin that the wall temperature is equal to the body temperature
- flow is incompressible ($M << 1$), it is indeed assumed that the adiabatic wall temperature and the static temperature, T_a, coincide.

For an indefinite cylinder ($\ell/d \to \infty$) the Nusselt number can be expressed as a power function of the Reynolds number (referred to the diameter of the cylinder) and the Prandtl number whose exponents depend on whether the motion is laminar or turbulent. If the motion is laminar ($\mathrm{Re}_d < \mathrm{Re}_{dcr}$), which is always true for the hot wire anemometer, as the

diameter of the wire is very small (of the order of μm), it can be considered valid for the empirical equation:

$$Nu_d = 0.42\,\mathrm{Pr}^{0.2} + 0.57\,\mathrm{Pr}^{0.33}\,\mathrm{Re}_d^{\,0.5} \tag{3.4}$$

after Kramers and van der Hegge Zijnen. For the reference probe immersed in a stream of air at standard temperature and pressure and velocity U = 30 [m/s], Re_d = 10 and Nu_d = 2.

In practice, even an indefinite cylinder does not follow Equation (3.4) with sufficient accuracy: the exponent of the Reynolds number is 0.48 at lower speeds and 0.51 at higher speeds. The variation of the exponent is still larger for sensors of finite length such as those used in anemometers. The sensors shaped as cones, wedges or domes show exponents significantly different from 0.5.

Because it is only relevant to have a functional relationship between the Nusselt number and velocity of the stream, as a calibration must be carried out for each probe, one can write:

$$Nu_d = a_1 + b_1\sqrt{\mathrm{Re}_d}$$

Equation (3.3) becomes:

$$\dot{Q} = \pi\ell\lambda\left(a_1 + b_1\sqrt{\mathrm{Re}_d}\right)\left(T_w - T_a\right) = \left(a + b\sqrt{U}\right)\left(T_w - T_a\right) \tag{3.5}$$

where a and b are two constants to be determined by calibration, which include the geometric properties of the wire and the fluid parameters. Since the response of the hot wire anemometer depends on many fluid dynamics parameters, the probe could be used to measure temperature, thermal conductivity, pressure, heat flux in addition to speed. For the same reason, when a single variable is measured, care must be taken to keep constant all the other variables: in particular, when measuring speed, it is important to compensate for any temperature difference between test and calibration or any change in fluid temperature during the test.

3.4.5 King's law

From Equation (3.2) it follows that in steady state the thermal power exchanged between the hot wire and the fluid stream is equal to the electrical power, W, dissipated in the wire by the Joule effect:

$$W = I^2 R_w = E^2/R_w$$

where I is the electric current and E is the potential difference across the hot wire. From Equation (3.5), King's law [1] (Equation 3.6) is obtained, linking the speed, U, to the fourth power of E:

$$I^2 R_w = \frac{E^2}{R_w} = \left(a + b\sqrt{U}\right)\left(T_w - T_a\right) \quad \text{King's law} \tag{3.6}$$

that taking into account Equation (3.1) becomes:

$$I^2 R_w = \frac{E^2}{R_w} = \left(a + b\sqrt{U}\right)\frac{R_w - R_a}{\alpha R_a} \tag{3.7}$$

Equation (3.7) is a relationship between three variables: stream speed, U, electric current, I, and wire resistance, R_w. If the stream speed has to be related to a single variable (current or electrical resistance or potential difference) there are two possible alternatives:

- holding the electrical resistance (or temperature) of the wire constant and allowing fluctuations of the electrical current with speed (constant temperature anemometer, CTA);
- holding the electrical current constant: in this way the change in velocity causes a temperature change of the wire and hence of its electrical resistance (constant current anemometer, CCA).

Operating at constant resistance, differentiating Equation (3.7) yields:

$$\frac{1}{E}\left(\frac{\partial E}{\partial U}\right)_{R_w} = \frac{1}{4\left(U + \frac{a}{b}\sqrt{U}\right)} > 0 \tag{3.8}$$

From Equation (3.8) it follows that (Figure 3.7):

- the potential difference across the wire increases with increasing speed;
- the instrument sensitivity decreases with increasing speed.

Operating at constant current the temperature of the wire is free to vary with speed; differentiating Equation (3.7) yields:

$$\frac{1}{E}\left(\frac{\partial E}{\partial U}\right)_{I} = -\frac{\left(R_w - R_a\right)/R_a}{2\left(U + \frac{a}{b}\sqrt{U}\right)} = -\frac{\alpha\left(T_w - T_a\right)}{2\left(U + \frac{a}{b}\sqrt{U}\right)} < 0 \tag{3.9}$$

Figure 3.7 Calibration curve of a CTA

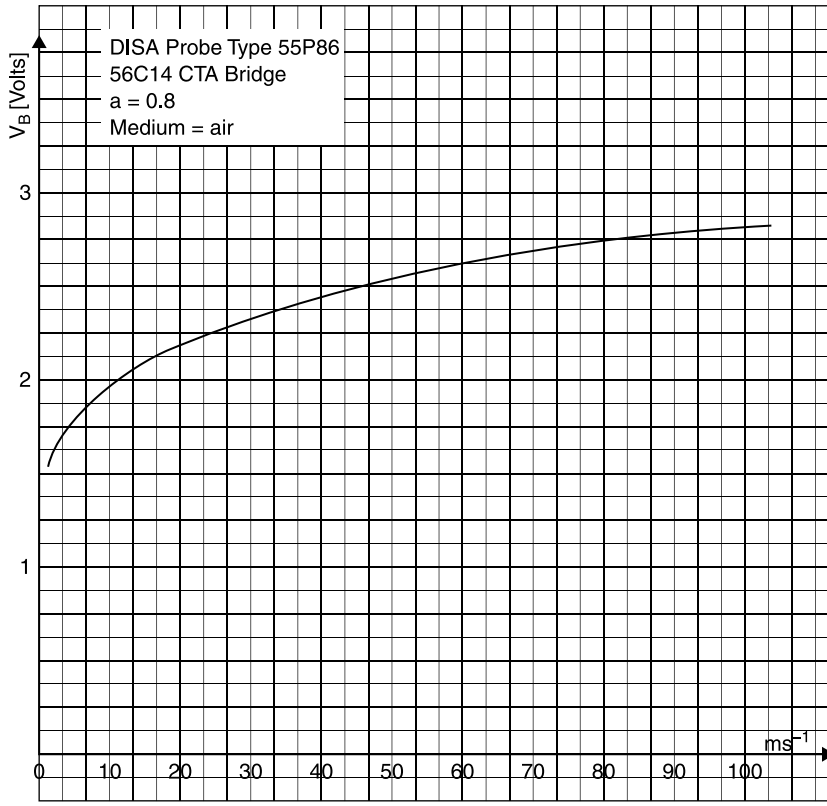

From Equation (3.9) it follows that (Figure 3.8):

- the potential difference across the wire decreases with increasing speed;
- as for the CTA, the sensitivity decreases with increasing speed.

A final consideration must be made on the effects of free convection that is taken into account by the term "a" in Equations (3.5), (3.6) and (3.7).

The fact that there is a small but finite convective velocity near the wire makes measurement of very low flow speed random. Furthermore, the value of free convection depends on the orientation of the wire (horizontal or vertical), so calibration and measurement have to be made in the same position. In practice, the King's law, as mentioned earlier, has a lower limit of validity at stream speeds of the order of 5 cm/s.

Figure 3.8 Calibration curve of a CCA

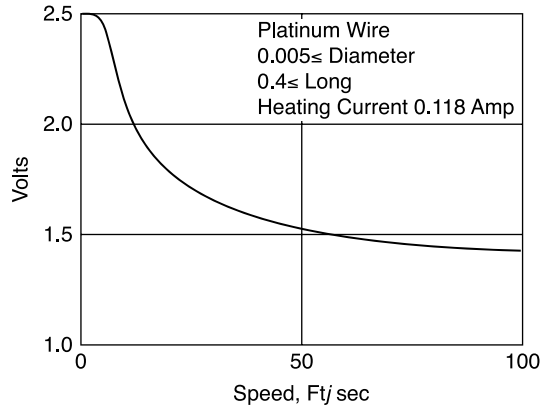

3.5 Constant current anemometer (CCA)

The preceding paragraphs have been devoted mainly to the sensor and its heat exchange with the fluid stream. The sensor must be controlled by an electronic circuit, which is a very important element of the anemometer. It provides a controlled electric current to the sensor and ensures the compensation of frequency. A sensor itself cannot follow speed variations at frequencies above 300 Hz; with electronic compensation this response may be increased to values of the order of kHz.

3.5.1 Schematic of a CCA

The current in the sensor is maintained essentially constant by using a large resistor in series with the sensor: since the current flowing in the circuit is $I = E/(R + R_w)$, if $R >> R_w$, the current will be practically independent of R_w. In practice, a Wheatstone bridge (Figure 3.9 b) is used and the voltage drop across the sensor is measured by the unbalance of the bridge.

A physical point of view confirms the trend of $E = E(U)$ of Figure 3.8: if the speed increases → heat transfer between the sensor and the fluid increases → the sensor cools down → its electrical resistance decreases → the potential difference across the resistor decreases (as the current through the sensor is constant). An amplifier picks up this change in voltage and then amplifies the signal to levels useful for recording.

Figure 3.9 Circuits of constant current anemometers

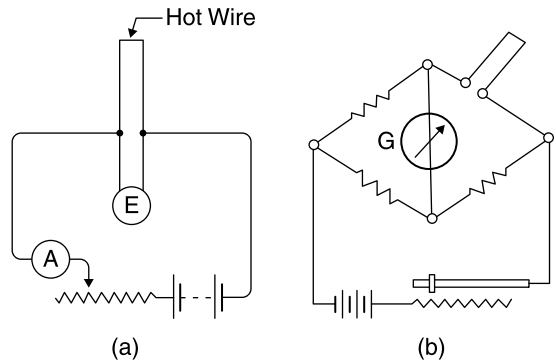

One of the limitations of the CCA is the fact that if too low an electric current is chosen, at the higher stream speeds the wire is too cold, its temperature tends to air temperature and the sensitivity of the anemometer decreases. Conversely, if too high an electric current is chosen, when the stream speed is too low, the danger of burning the wire exists: this is the case for measures in the boundary layer, where the velocity tends to zero, or in the case of removing the probe from the stream before shutting down the power supply to the wire.

3.5.2 Time constant

One of the main reasons for the use of the hot wire anemometer in fluid mechanics is its ability to follow turbulent fluctuations in speed. In the CCA, the key parameter is the heat capacity of the wire which opposes temperature changes; at increasing frequency of speed fluctuations the sensor follows the change of velocity with an increasing delay and the amplitude of the oscillations in output will become smaller compared with that in input. This behavior can be expressed quantitatively by evaluating the frequency response of the CCA.

From Equation (3.2), taking into account Equation (3.7):

$$\frac{C_w}{\alpha R_a}\frac{dR_w}{dt} - I^2 R_w + \left(a + b\sqrt{U}\right)\frac{R_w - R_a}{\alpha R_a} = 0$$

The differential equation that links the resistance of the wire with time is linear of the first order and it follows that in response to a sudden increase in speed (Figure 3.10) the resistance decreases with the law

$$R_w = R_{w1} - \Delta R_w \left(1 - e^{-t/\tau_w}\right) \tag{3.10}$$

Figure 3.10 Response of the resistance of the probe of a CCA to a step increase in the speed of the stream

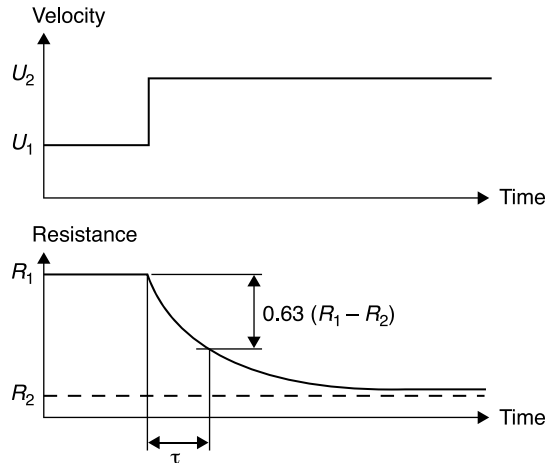

where R_{w1} is the initial resistance and $R_{w2} = R_{w1} - \Delta R_w$ is the resistance that the wire would reach asymptotically for $t = \infty$.

τ_w is the *time constant* of the wire

$$\tau_w = \frac{C_w R_w}{R_a\left(a + b\sqrt{U}\right)} \tag{3.11}$$

that represents the time that resistance takes to reach the value

$$R_w = R_{w1} - \Delta R_w\left(1 - \frac{1}{e}\right) \cong R_{w1} - 0.63\Delta R_w$$

or, similarly to what has been said for the time constant of a *U*-tube manometer (cf. Section 1.2.1.2), the time it would take to reach the new equilibrium value if the rate of change were the initial one. As shown in Equation (3.11), the time constant, which is a measure of the change of wire resistance (temperature), increases with the overheating ratio and with the decrease in speed. For the reference probe $\tau_w \cong 0.6$ ms.

The time constant can be associated with a *cut-off frequency* or *frequency limit:*

$$f_c = \frac{1}{2\pi\tau_w} \tag{3.12}$$

which is also the *bandwidth of the frequency* of the sensor (for the reference probe $f_c \cong 300$ Hz).

Figure 3.11 Frequency response of sensor, amplifier and CCA

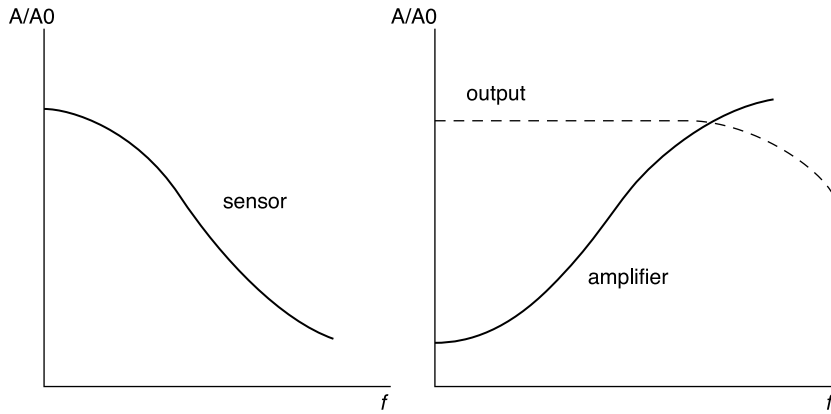

Dryden in 1929 showed that if applying to the sensor a speed variable with a certain frequency, *f*, the amplitude of the output signal from the sensor is not equal to that which would occur in the steady case but decreases in the ratio (Figure 3.11)

$$\frac{A}{A_0} = \frac{1}{1+\left(f/f_c\right)^2} \tag{3.13}$$

and that the output signal has a delay of phase with respect to the input signal equal to

$$\Delta\alpha = tg^{-1}\left(f/f_c\right) \tag{3.14}$$

From Equations (3.13) and (3.14) it can be seen that the frequency limit can also be defined as the frequency at which the reduction in amplitude of the power is equal to 1/2 (–3*dB*) and the phase delay is 45°.

In order to offset the effect of reducing the amplitude of the signal, the amplifier connected with the sensor should have a gain variable with frequency (Figure 3.11) with a reverse law with respect to Equation (3.13); of course also the amplifier has its own inertia for which the best that can be obtained is an extension of the bandwidth of the wire sensor-amplifier system from 300 Hz to a few kHz.

3.5.3 Dynamic balancing

The overall time constant of the anemometer may be calculated by theoretical considerations; in practical applications, however, the

Figure 3.12 Response of a CCA to a square wave test at two different speeds of the stream

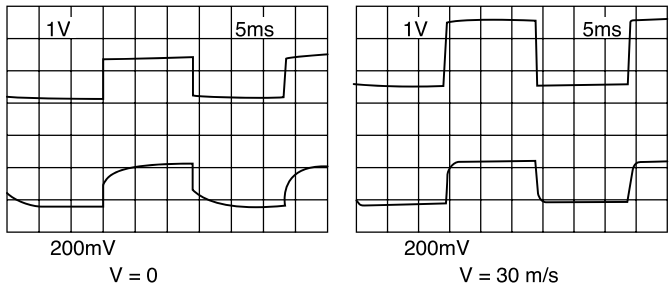

configuration of the probe introduces so many and uncontrollable parameters as to make unreliable the value of τ_w calculated. On the other hand, to perform even in this case a calibration, one should have either a sample turbulence or make the probe oscillate with the desired frequency in a flow with a constant speed. It is therefore necessary to use indirect methods.

The most accepted method is to send a square wave voltage signal in the wire (in all the commercial anemometers, a square wave generator is provided), which simulates a similar variation of speed, and displays the response of the wire on an oscilloscope at various flow speeds (Figure 3.12). Acting on the circuit components (resistors, overheating ratio, gain of the amplifier), the frequency response of the anemometer can be optimized.

The biggest flaw in the constant current system is the fact that the frequency response of the sensor depends not only on the characteristics of the sensor but also on the characteristics of the fluid stream: the answer depends, as we have seen, both on the heat capacity of the wire and on the coefficient of heat exchange between sensor and environment. In particular, since the sensor response changes with fluid speed, the frequency compensation of the amplifier should be readjusted at every change in the average speed. This is not practical and therefore the anemometer at constant current is used only in cases where the average speed remains constant (steady turbulence).

3.6 Constant temperature anemometer (CTA)

In the constant temperature anemometer the influence of the thermal inertia of the sensor is eliminated as the temperature of the wire is

constant whatever the velocity of the stream; the frequency limit of the instrument is therefore essentially determined by the electronic circuit.

3.6.1 Schematic of a CTA

Figure 3.13 illustrates the basic pattern of a CTA: the wire is again in an arm of a Wheatstone bridge opposed to a variable resistor that adjusts the operating resistance, and hence the temperature of the hot wire; the output of the bridge is in this case connected to an amplifier whose output is in turn the supply voltage of the bridge. If the bridge is balanced, there is no potential difference across the diagonal. When the fluid speed increases, the sensor tends to cool and its resistance decreases; an imbalance of the bridge is generated that changes the input signal of the amplifier. The phase of the amplifier is such that the voltage reduction causes an increase of the output signal of the amplifier which increases the current in the sensor and then the temperature until it restores the balance of the bridge.

Figure 3.13 Schematic of a CTA

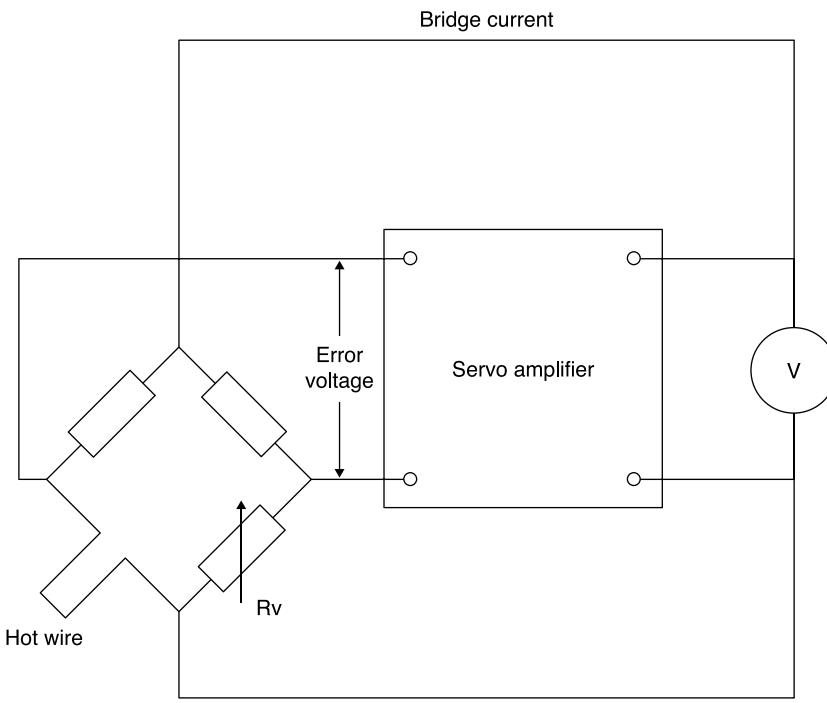

If the amplifier has a sufficient gain, it is able to hold the input signal much closer to a balanced bridge, so any change in the resistance of the sensor is immediately corrected by an appropriate variation of the current. The output signal of the system at constant temperature is the output voltage of the amplifier, which, in turn, is the voltage required to ensure the required current through the sensor.

The physical reasoning confirms the trend of $E = E(U)$ of Figure 3.7: if the speed increases → heat transfer between the sensor and the fluid increases → the sensor tends to cool and its electrical resistance to decrease → the amplifier sends more current in the wire to maintain the same resistance → the potential difference across the resistor increases.

3.6.2 Time constant

The time constant of the *CTA* depends on the speed with which the electronic circuit, in response to the attempt to change the temperature of the wire, sends more or less current in the wire; it depends on certain factors such as the thermal properties of the sensor and the fluid, the overheating ratio, the temperature coefficient of resistance, the speed of the fluid, the gain of the amplifier, the resistance of the bridge and the bandwidth of the amplifier. However, it can be said that the time constant of the *CTA* is linked to that of the *CCA* by the ratio:

$$\tau_{CTA} = \frac{\tau_{CCA}}{2S\dfrac{R_w - R_a}{R_a}}$$

where S = gain of the amplifier. The time constant of the wire is thus reduced a few hundred times, from fractions of ms to some μs. The frequency limit is typically in the order of hundreds of kHz.

3.6.3 Dynamic balancing

To obtain the dynamic balance of the bridge also, in this case a square wave is sent in the probe and the output signal of the bridge is observed on an oscilloscope. The purpose of the test is twofold: it can be used to optimize the bandwidth of the combined circuit sensor/amplifier, or simply to ensure that the behavior of the servo is stable. The time that the system takes to bring the bridge to balance is linked to the time constant, and therefore to the bandwidth of the system. On the arrival of the square

Figure 3.14 Balancing a CTA with a square wave

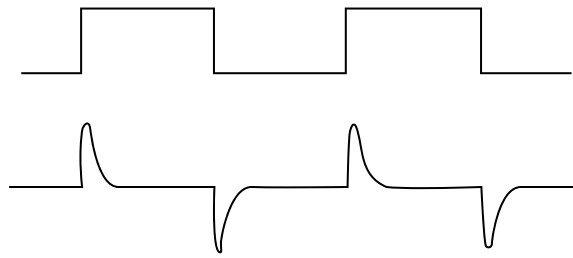

wave, the system reacts in order to restore the resistance (and therefore the voltage) to the initial value (Figure 3.14).

The response time (Figure 3.15) is measured as the time, $\tau_{w,}$ between the beginning of the pulse and a point on the descending curve whose ordinate is 3% of the total pulse. The bandwidth, or cut-off frequency, defined as the frequency at which the amplitude of the output signal is $-3dB$, can be expressed by

$$f_{(-3dB)} = 1/1.3\tau_w$$

The frequency response can be optimized by adjusting the filter and the gain of the amplifier.

Instability of the system causes the appearance of oscillations in the response of the anemometer bridge that can take two aspects (Figure 3.16):

1. This type of oscillation, due to the difference in inductance between the active and passive arm of the bridge (e.g. the cable connecting the

Figure 3.15 Determination of the time constant of a CTA

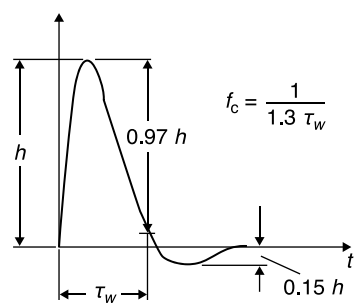

Figure 3.16 Types of instability

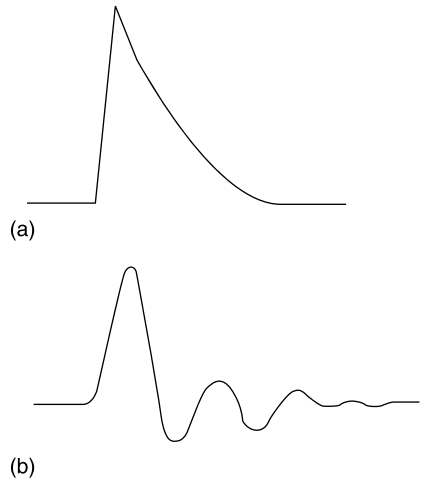

probe to the anemometer is too long), can be removed by adjusting a winding in series with the passive resistance.

2. This oscillation is due both to low bandwidth, in which case it can be removed by increasing the gain, and to an excessive damping of the system, which may be reduced by acting on another winding.

3.7 Comparison of CCA and CTA

Whatever the type of anemometer, the amplifier must increase the compensation for the delay in sensor response with increasing frequency, but so does the noise of the system. In the past, constant current systems, especially systems that were not compensated, were considered superior because they had levels of noise lower than the constant temperature systems. However, this is only true at low frequencies and in any case the use of compensating amplifiers significantly reduces this advantage. It is now believed that, through the adoption of solid-state circuits, the two systems are equivalent in terms of noise level.

In addition to noise level and frequency response, other practical considerations are important such as ease of use and flexibility of the system. In this, the system at constant temperature has many advantages:

- It keeps constant the overheating ratio of the sensor at all speeds and prevents the sensor burning when the flow speed falls abruptly.
- It is compatible with the film sensor while the constant current system is not due to the complex frequency response of the films.
- It allows measurements in liquids, where large changes in heat transfer occur when speed fluctuates.
- It allows linearization of the voltage with speed.
- It can compensate for the temperature of the fluid.

For these reasons, the constant temperature system is nowadays preferred to the constant current system, which is used only for temperature measurements.

3.8 Operating temperature of the wire

As shown, the operation of the anemometer is based on the heat exchange between the hot wire and the fluid stream which is more effective the higher the operating temperature of the sensor. There must, however, be a limit to temperature due to the acceleration of the oxidation of the wire and the decrease in its tensile strength at high temperatures.

The usual operating temperature for sensors operating in the air at room temperature is in the range $150 \div 250°C$. This implies that the electrical resistance of the sensor is $1.5 \div 2$ times the resistance at room temperature.

In practice, the operating temperature is established by inserting an appropriate resistance in the arm of the bridge opposite to the sensor: this is a fixed resistor suitable to the sensor, or a winding compensated for ambient temperature, or a variable resistance in order to allow changes at will of the sensor temperature.

3.9 Compensation of the stream temperature

Since the output voltage of the anemometer depends on the fluid stream temperature, T_a, this must be taken into account every time it varies during the test or between calibration and measurement, for

example, an increase in ambient temperature looks like a decrease in stream speed.

There are various methods for correcting temperature:

- the temperature is measured separately and the data are corrected referring to a family of calibration curves plotted for different temperatures (Figure 3.17) or by using the theoretical equations of heat transfer;
- using two active sensors operating at two different temperatures and making the difference between the output signals to obtain a signal independent of the stream temperature; in particular, the compensation sensor operates at low temperature and is therefore insensitive to velocity. The following equations can be written for the power outputs of the two sensors:

$$W_1 = \left(a + b\sqrt{U}\right)\left(T_1 - T_a\right) \qquad W_2 = \left(a + b\sqrt{U}\right)\left(T_2 - T_a\right)$$

$$W_1 - W_2 = \left(a + b\sqrt{U}\right)\left(T_1 - T_2\right)$$

- a temperature-sensitive resistor of appropriate value and having the same temperature coefficient of the sensor is placed in the arm of the

Figure 3.17 Calibration curves of a CTA at different temperatures of the stream

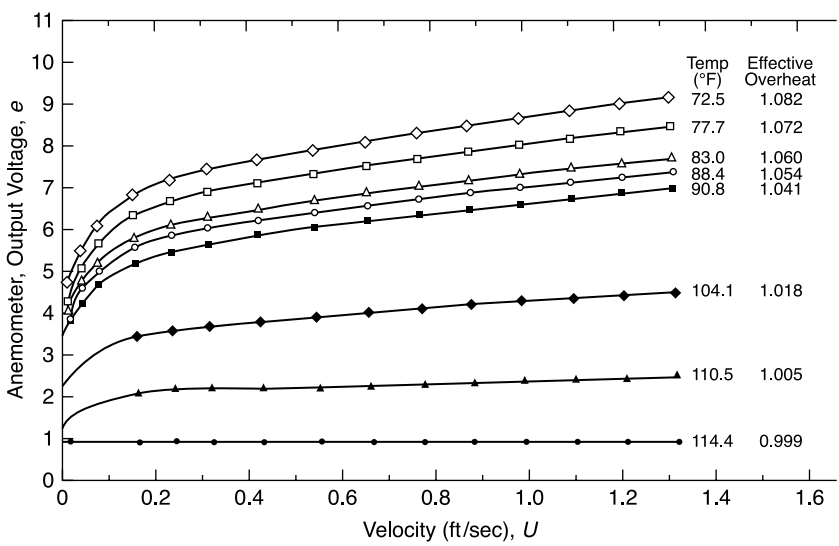

bridge opposite to the sensor and mounted in the stream near the speed sensor. Its resistance varies with temperature by forcing the speed sensor to vary of the same entity.

3.10 The linearizer

The non-linearity of the hot wire anemometer in the measurement of speed has been emphasized. The relationship between the electric power supplied to the sensor and velocity of the fluid stream that invests it, given in Equation (3.7), for a CTA (in which T_w = const, R_w = const), can be written as

$$E^2 = \left(a + b\sqrt{U}\right)\left(T_w - T_a\right)R_w = A + B\sqrt{U} = E_0^2 + B\sqrt{U} \qquad (3.15)$$

where E_0 is the difference of potential that occurs at $U = 0$.

To determine the average speed of the stream, it is only necessary to measure the average voltage output of the anemometer and use the calibration curve. But this is fully satisfactory only if the level of turbulence is low; if this level is high, due to the nonlinearity of the calibration curve, the average voltage does not match the average speed but a lower speed.

In order to linearize Equation (3.15), it is necessary to pass the output of the anemometer through an apparatus with a transfer function which is the inverse of King's law. Consider:

$$E_{\text{out}} = k\left(E_{\text{in}}^2 - C^2\right)^m$$

where M, C and k are constants.

If the output voltage of the anemometer is replaced by E_{in} (Equation 3.15):

$$E_{\text{out}} = k\left(E_0^2 + B\sqrt{U} - C^2\right)^m$$

Making $C = 0$: $\quad E_{\text{out}} = k\left(B\sqrt{U}\right)^m$

making $m = 2$ $\quad E_{\text{out}} = kB^2U$

But $kB^2 = K$, then $E_{\text{out}} = KU$. In this way, the output of the linearizer is a voltage proportional to velocity.

3.11 Measurements of absolute value and direction of average velocity

3.11.1 Calibration

To carry out any measure of average speed a calibration curve is needed. For measurements in gases at speeds between 10 and 100 m/s calibration can be made with reference to the difference in pressure read in a Venturi tube (a mini-subsonic wind tunnel) where the sensor is placed. For very low speeds, the use of a laminar flow tube is recommended. For higher speeds, a cylinder powered by compressed air and equipped with a set of interchangeable nozzles is used.

Obviously the accuracy of the calibration curve increases with the number of measured points. This involves a tedious procedure to be repeated frequently, even if the same probe is used, to check that the wear of the sensor or the presence of impurities in the stream have not altered the characteristics of the probe itself. The linearizer could alleviate the problem because it allows calibration by measuring only the voltage corresponding to the maximum speed.

In the classical analog anemometer, output voltage was measured with a DC voltmeter, that is a voltmeter with a considerable inertia, that even in the presence of fluctuations due to the turbulence of the fluid current, did not follow the fluctuations but showed an average value.

In modern anemometers, the signal passes through an analog/digital converter and is given as a large number, n, of numerical data representing the succession in time of voltage fluctuations. The average voltage is thus obtained by the equation:

$$\overline{E} = \frac{\sum_n E_i}{n}$$

3.11.2 Directional sensitivity in the plane wire/supports

If the stream direction is not normal to the sensor, the collected data are biased compared to those provided by the calibration. If the velocity vector lies in the wire/support plane, i.e. $\theta = 0$ in Figure 3.18, and if the angle from the normal to the wire is small, the component normal to the wire can be considered as the *effective speed* on the sensor

$$U_{eff} = U\cos\alpha \tag{3.16}$$

Figure 3.18 Decomposition of the velocity vector on the axes of the probe

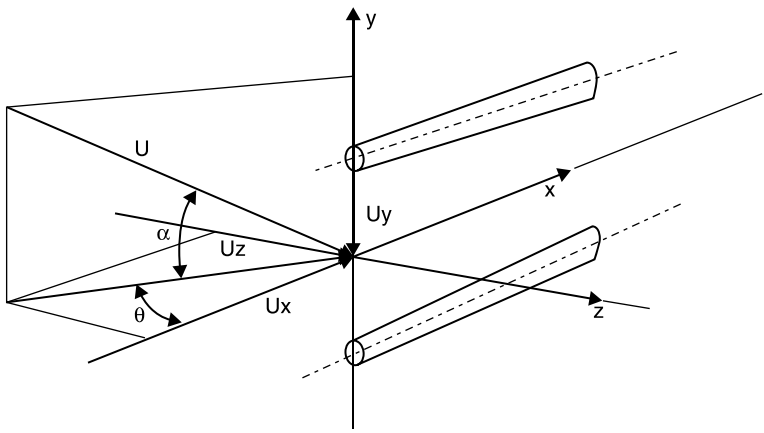

For greater angles, the velocity component parallel to the sensor contributes, albeit with minor effectiveness, to cooling and that is why the more accurate Equation (3.17) must be used

$$U_{eff}^2 = U^2\left(\cos^2\alpha + k^2\text{sen}^2\alpha\right) \tag{3.17}$$

The value of k^2 (*yaw factor*) depends on the sensor type and on the length/diameter ratio of the wire and should be evaluated for each probe by varying the angle α in a known stream; alternatively, the average values provided by the manufacturers and listed below can be used:

	k^2
Miniature probe	0.04
Gold-plated probe	0.0225
Fiber probe	0.04

If the probe is inclined with a known angle with respect to the direction of speed, the true value of the speed can be found from that measured by the probe by using, depending on the required accuracy, Equation (3.16) or Equation (3.17).

If the direction of velocity is unknown, it is not possible by Equation (3.16) or Equation (3.17) to obtain simultaneously the value and the

direction of speed (two unknowns from a single equation). It is necessary to use two sensors in two directions to obtain two independent measurements from which both unknowns can be calculated.

3.11.3 The X probe

The typical tool for determining both the unknown direction and absolute value of the velocity vector in a plane is the X-probe (Figure 3.19), consisting of two mutually perpendicular sensors, both at 45° with respect to the direction of the probe. The choice of these particular angles significantly simplifies the solution because the sine and cosine of 45° are equal and the sum of the angles formed by the velocity vector with the two wires is always 90°.

In the calibration phase, the probe is aligned with the stream and both wires are at 45° with respect to the direction of the velocity vector; the effective speed on each wire is

$$u_{eff}^2 = \frac{1}{2}\left(1 + k^2\right)u_{cal}^2$$

In the calibration phase, from the voltages measured on the two wires the corresponding values u_{cal1} and u_{cal2} are obtained. If in a test the speed is not aligned with the axis of the probe, the velocity components in the direction of the wires, u_1 and u_2 are derived from the following equations obtained by applying Equation (3.16) to the special case of the X-probe,

Figure 3.19 The X-probe

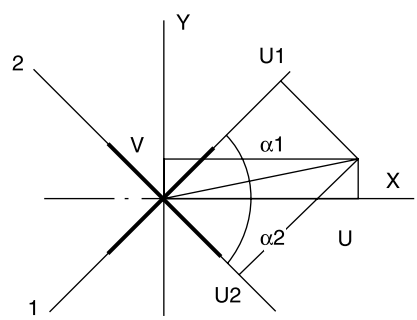

in which case, since the two wires are mutually orthogonal, the component parallel to a wire is orthogonal to the other:

$$k_1^2 u_1^2 + u_2^2 = \frac{1}{2}\left(1 + k_1^2\right) u_{cal1}^2$$
$$u_1^2 + k_2^2 u_2^2 = \frac{1}{2}\left(1 + k_2^2\right) u_{cal2}^2$$

$$u_1 = \frac{\sqrt{2}}{2}\sqrt{\left(1 + k_2^2\right) u_{cal2}^2 - k_2^2 u_{cal1}^2}$$
$$u_2 = \frac{\sqrt{2}}{2}\sqrt{\left(1 + k_1^2\right) u_{cal1}^2 - k_1^2 u_{cal2}^2}$$

Finally, the components of the velocity vector in the direction of the probe and in the direction normal to it, u and v, respectively, are given by:

$$u = \frac{\sqrt{2}}{2}\left(u_1 + u_2\right) \qquad v = \frac{\sqrt{2}}{2}\left(u_1 - u_2\right)$$

3.11.4 Directional sensitivity in 3D fields

If the velocity vector is at an angle $\theta \neq 0$ with the wire/support plane (Figure 3.18), the effective speed detected by the wire is

$$U_{eff}^2 = U_x^2 + k^2 U_y^2 + h^2 U_z^2$$
$$= U^2\left(\cos^2\alpha\cos^2\theta + k^2\mathrm{sen}^2\alpha + h^2\cos^2\alpha\mathrm{sen}^2\theta\right)$$

where k = *yaw factor*, h = *pitch factor*.

Average values of h^2 provided by the manufacturers are shown in the following table:

	h^2
Gold-plated probe	1.04
Fiber probe	1.20

In the particular case of planar flow ($\theta = 0$), one finds the sensitivity of the probe to the angle of yaw Equation (3.17)

$$U_{eff}^2(\alpha) = U^2\left(\cos^2\alpha + k^2\mathrm{sen}^2\alpha\right) \qquad \theta = 0$$

Similarly the sensitivity of the probe at the pitch angle can be found by putting $\alpha = 0$:

$$U_{eff}^2(\theta) = U^2\left(\cos^2\theta + h^2\text{sen}^2\theta\right) \qquad \alpha = 0$$

3.11.5 Triaxial probe

To determine the three-dimensional velocity vector, a set of three mutually perpendicular sensors, the triaxial probe of Figure 3.20, is needed to allow measurement in a cone of 70° around the axis of the probe.

Velocity components are calculated from the voltages measured at the three wires by using velocity curves obtained by calibration. The speeds on the three wires are obtained by equations:

$$k_1\ddot{u}_1 + u_2 + h_1 u_3 = \left(1 + k_1 + h_1\right)\cos\ 35.3°\, u_{cal1}$$
$$h_2\ddot{u}_1 + k_2 u_2 + u_3 = \left(1 + k_2 + h_2\right)\cos\ 35.3°\, u_{cal2}$$
$$u_1\ddot{} + h_3 u_2 + k_3 u_3 = \left(1 + k_3 + h_3\right)\cos\ 35.3°\, u_{cal3}$$

Putting, for simplicity, the values of h and k for all wires equal to those provided by the manufacturers, the velocity components in the direction of three sensors can be found from the equations:

$$u_1 = \sqrt{-0.3676u_{cal1}^2 + 0.3747u_{cal2}^2 + 0.3453u_{cal3}^2}$$

$$u_2 = \sqrt{0.3453u_{cal1}^2 - 0.3676u_{cal2}^2 + 0.3747u_{cal3}^2}$$

$$u_3 = \sqrt{0.3747u_{cal1}^2 + 0.3453u_{cal2}^2 - 0.3676u_{cal3}^2}$$

Figure 3.20 Triaxial probe

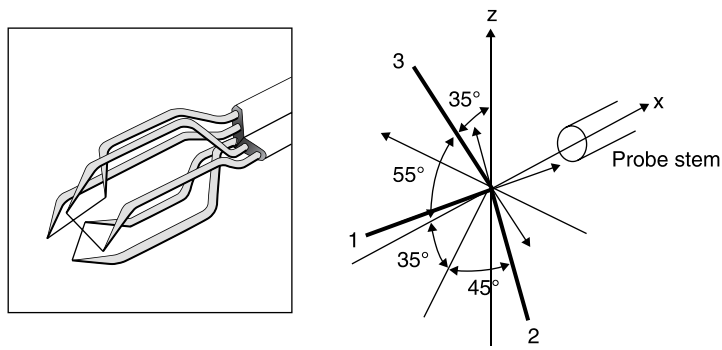

Finally, the three components of the velocity vector in the coordinate system of the probe can be calculated from the equations:

$$u = u_1 \cos 54.74° + u_2 \cos 54.74° + u_3 \cos 54.74°$$

$$v = -u_1 \cos 45° - u_2 \cos 135° + u_3 \cos 90°$$

$$w = -u_1 \cos 114.09° - u_2 \cos 114.09° - u_3 \cos 35.26°$$

3.12 Measurements in turbulent flows

If the stream velocity varies in time, both in absolute value and in direction, turbulent regime, the situation can be summarized as in Figure 3.21:

$$U(t) = \overline{U} + u(t) \quad V(t) = v(t) \quad W(t) = w(t)$$

Figure 3.21 Velocity components in a turbulent flow

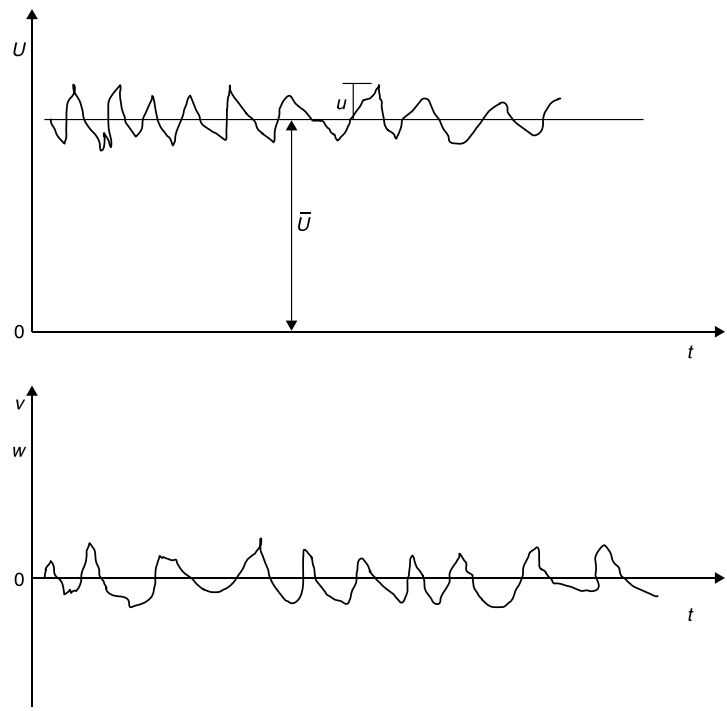

where the instantaneous value of the fluctuations of velocity components have been indicated with lower case letters and by $\overline{U}$ the average speed in a time interval much larger than the period of oscillations.

Since, obviously, the average values of fluctuations are identically zero,

$$\overline{u} = \overline{v} = \overline{w} = 0$$

to have a measure of turbulence along the three axes it is necessary to make the square of the signal, thus eliminating the negative areas, make the average (Figure 3.22) and then extract the square root (the so-called *root mean square value,* rms)

$$\sqrt{\overline{u^2}} \qquad \sqrt{\overline{v^2}} \qquad \sqrt{\overline{w^2}}$$

Turbulence intensity is defined as the ratio between the root of the arithmetic average of the rms values of the three components of the unsteady velocity and average speed:

$$T_u = \frac{\sqrt{\dfrac{\overline{u^2} + \overline{v^2} + \overline{w^2}}{3}}}{\overline{U}}$$

3.12.1 Turbulence in the direction of the average speed

The component of turbulence in the direction of speed $\sqrt{\overline{u^2}}$ can be measured with a sensor perpendicular to the average speed. In the analog

Figure 3.22 The rms values of the turbulent velocity components

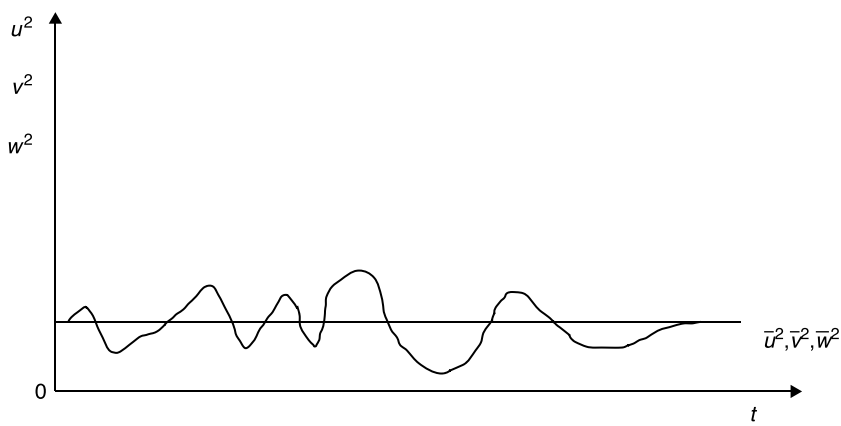

anemometers, the corresponding voltage was measured with an rms voltmeter, based on the Joule effect, from the signal filtered to remove the *DC* component. In the modern computerized anemometers, the rms voltage value is obtained from

$$e_{rms} = \sqrt{\frac{\sum_n \left(E_i - \overline{E}\right)^2}{n}}$$

To obtain the rms value of velocity in linearized systems a factor of proportionality is simply applied. In non-linearized systems, conversion is accomplished by determining the slope of the calibration curve at the point of measurement. If the turbulence is large, an error of distortion is introduced in this way due to the uncertainty in choosing the proper curve slope.

3.12.2 Intensity of turbulence in the direction of the average speed

The intensity of turbulence in the direction of the average speed is defined as

$$T_u = \frac{\sqrt{\overline{u^2}}}{\overline{U}}$$

As we have seen, Equation (3.15), in a CTA, King's law can be written as:

$$E^2 = A + B\sqrt{U} = E_0^2 + B\sqrt{U}$$

By differentiating this equation:

$$2EdE = \frac{B}{2\sqrt{U}}dU \qquad \Rightarrow \qquad \frac{4E}{E^2 - E_0^2}dE = \frac{1}{U}dU$$

Interpreting E and U as the average values of voltage and speed and the differentials dE and dU as their rms values, a peculiar expression for the intensity of turbulence, may be found:

$$T_u = \frac{dU}{U} = \frac{\sqrt{\overline{u^2}}}{\overline{U}} = \frac{4\overline{E}\sqrt{\overline{e^2}}}{\overline{E}^2 - \overline{E_0}^2}$$

In order to measure the intensity of turbulence, it is only necessary to know the output voltage and the rms value of voltage, it is not necessary to know the calibration curve.

If the relationship $E(U)$ is linearized, $E = KU$, to determine the intensity of turbulence, it is sufficient to make the ratio of the rms and the average value of voltage:

$$T_u = \frac{dU}{U} = \frac{dE}{E} = \frac{\sqrt{\overline{e^2}}}{\overline{E}}$$

Reference

1. L.V. King (1914) "On the convection of heat from small cylinders in a stream of fluid: determination of the convection constants of small platinum wires with application to hot-wire anemometry," *Phil. Trans. Roy. Soc., Ser. A.*, Vol. 214, pp. 373–432.

4

Laser anemometry

Abstract: This chapter will address the measurement of velocity with non-intrusive optical methods based on a laser in a fluid stream seeded with submicron light-scattering particles.

Key words: laser Doppler anemometer (LDA), particle image velocimetry (PIV), two focus velocimeter (L2F).

4.1 Introduction

In the previous chapters, methods for measuring the velocity of a fluid involving the use of probes immersed in the stream have been described; the perturbations due to the probe itself can be reduced but not eliminated by using small probes. On the other hand, there are cases where it is quite impossible to introduce a probe into the stream: this may be due to high temperatures (flames, plasmas), to a too high dynamic pressure or to an abrasive or chemically aggressive fluid. In all these cases the use of an optical (and hence non-intrusive) method is mandatory.

The air and plenty of fluids, however, are transparent to light radiation, therefore the optical anemometers may be used only if the fluid is seeded with light-scattering particles. Because these particles act as indicators of stream velocity, even when it changes rapidly in time (turbulent flow), they must have a low inertia which implies a low density and/or a very small volume (diameter of the order of μm). Table 4.1 lists some types of particles used in various fluids and their maximum allowed diameter at two frequencies of speed fluctuation.

Since the particles have a diameter of the same order of magnitude as the wavelength of light, when they are hit by a light beam, they spread it in all directions (Mie's theory): the back-scattered light (Figure 4.1) is hundreds of times smaller than the forward-scattered light.

Table 4.1 Maximum diameter (μm) of tracer particles

Particle	Fluid	f = 1 kHz	f = 10 kHz
Polystyrene, polyamide, hollow glass spheres	Water	5–100	
Water + glycerin (50% +50%)	Air	2–5	
Silicone oil	Air	2.6	0.8
TiO_2	Air	1.3	0.4
MgO	Methane-air flame 1800 [K]	2.6	0.8
TiO_2	Oxygen plasma 2800 [K]	3.2	0.8

Given the small size of the particles, only a small fraction of the total light is diffused, so only a laser can be used as a light source, as in it all the light output is concentrated in a beam approximately 1 mm in diameter.

The anemometers using a laser are:

- the laser-Doppler anemometer (LDA): the speed of the particle is calculated from the difference between the frequency of the scattered light as perceived by an observer and that of the incident light;
- the laser 2 focus (L2F) or laser transit anemometer (LTA): the speed is measured from the time the particle takes to travel the distance between two focused laser beams;
- the PIV (particle image velocimetry): the velocity of many particles is measured from the distance that they trail in the time interval between two consecutive images of the test chamber.

Figure 4.1 Polar plot, in logarithmic scale, of the intensity of light scattered by particles

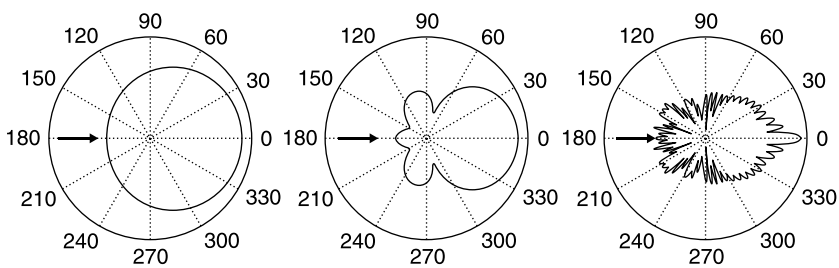

Note: d_p is the diameter of the particles, λ the wavelength of the incident light.

4.2 The gas laser

The gas laser (light amplification by stimulated emission of radiation) emits a thin, intense beam of light, coherent over time and space, whose wavelengths depend on the gas used.

Lasers have numerous applications: sophisticated tools are commercially available that use lasers, which have often revolutionized measurement techniques such as engineering non-destructive testing, vibration analysis, measures of speed, quality control and surface roughness, micron positioning, control of flatness and inclination, precision measurements at a distance of thicknesses, diameters and distances; lasers have also found applications in medicine, spectroscopy, information technology and graphics, printing techniques and display; with CD and DVD readers and writers, lasers have also entered the market for consumer products.

All these different applications are based on the specific characteristics of coherent beams of laser light; some use only the great brightness and collimation resulting from these properties, others use the more complex features of temporal and spatial coherence, e.g. in flow visualization. Laser sources have not only been successfully used in conventional optical methods but also have developed completely new methods such as holography and holographic interferometry.

4.2.1 Principle of operation

A laser source is made with materials and construction techniques similar to those used for vacuum tubes (Figure 4.2). In it a current of plasma is generated since electrons are attracted by the anode and ions are attracted by the cathode. A capillary tube with a diameter of 1 mm is inserted into

Figure 4.2 Schematic of a low-power laser source

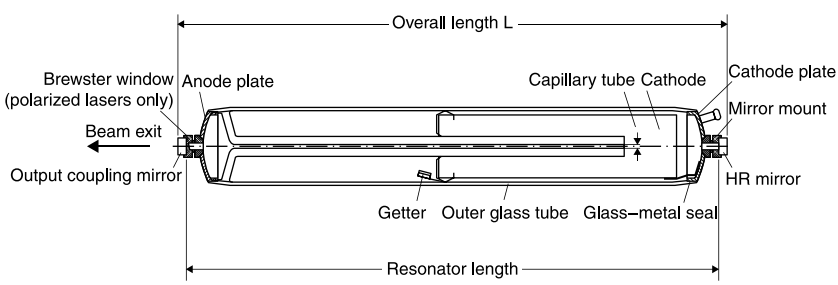

the central part of the tube. To turn on the lasers, a starter is needed that allows the initiation of the arc that is then supported only by the power supply.

If the kinetic energy of electrons, depending on the difference of potential between the electrodes, is sufficient, one or more electrons of the atom move to a higher energy level in the collision with the ions, this phenomenon is called *pumping*. The electrons remain in this state for some time and then randomly and spontaneously return to a lower energy level, emitting energy as photons (*spontaneous emission*); the color, or wavelength, λ, of this radiation depends on the difference of potential energy between the two levels.

Radiation, emitted in all directions, is neither coherent nor monochromatic, as a result of the superposition of electromagnetic waves with different wavelengths. To obtain laser light from this radiation, two small mirrors are needed, normal to the axis of the laser, at either end of the capillary tube; the photons directed along the axis of the capillary, and only those, are subject to repeated (infinite) reflections provoking another phenomenon called *stimulated emission*: when a photon hits an electron, this is moved to a higher energy level, it returns to its state of equilibrium with the emission of a photon exactly in the same direction as what it has invested. There is thus a multiplication of photons of the same type in the direction of the line joining the two mirrors in the capillary tube, and this leads to the formation of a thin, intense beam.

To obtain useful laser light outside, one of the two mirrors, the said transmitter, is not totally reflective and allows the escape of a small percentage of the light present in the cavity of the laser.

From the standpoint of the wave theory, the laser operation is linked to the fact that standing waves are generated in its optical cavity only if twice the length of the cavity is an integer multiple, m, of the wavelength: $2L = m\lambda$. Since m is large (order 10^6), there will always be many wavelengths λ_m satisfying this criterion for which the light emitted from a laser will consist of a range of frequencies ($f = c/\lambda$ where c = speed of light) separated by $\Delta f = c/2L$. These extremely narrow lines of which laser light is made are the *longitudinal modes*.

Since the mirrors and the capillary diameters are not zero, standing waves at small angles to the axis of the cavity can also exist. This gives rise to electric and magnetic transverse modes (TEM_{nm}). Most of the laser operates in TEM_{00} mode, which has a Gaussian intensity profile (Figure 4.3) that provides the minimum divergence and can be focused on the smallest possible spot. Because the laser beam is not bounded by a sharp edge, its diameter is defined as that where the light intensity drops to $1/e^2$ ($\approx 13.5\%$) of its peak value.

Figure 4.3 Gaussian distribution of light intensity in a section of the laser beam

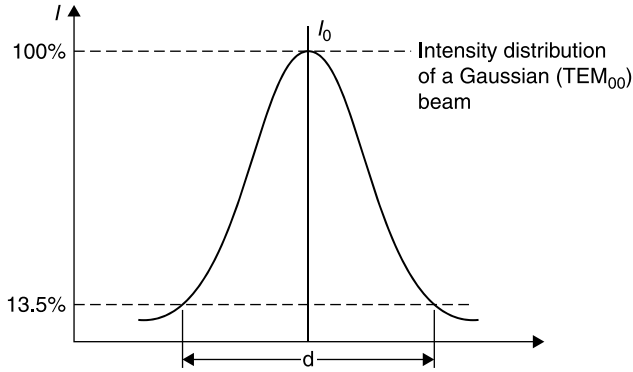

The emission of radiation can be within a broad spectral range, or a single wavelength can be optimized. Argon emits in a wide range of wavelengths ranging from ultraviolet to low infrared (Figure 4.4): this is

Figure 4.4 Emission spectrum of argon

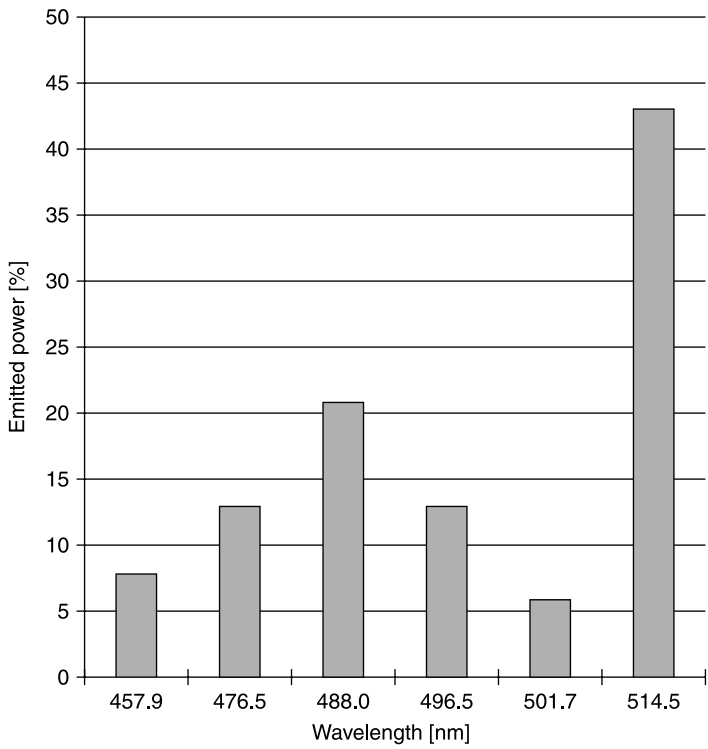

because the atoms of an element have a limited number of excited states in which certain transitions from state to state, called allowed transitions, are more favored than others, called forbidden transitions. For a noble gas, a few dozen transitions are allowed: for argon, over 40% of the total power is emitted at a wavelength of 514.5 nm, which corresponds to the green color, more than 20% is emitted at 488 nm (blue), about 13% is emitted at 476.5 nm (purple).

In order to have emission of monochromatic light, it is necessary that the laser beam be purified from all radiation of wavelengths other than that required; this is achievable with the use of a prism that divides the rays allowing the choice of a particular color. With this system, much of the energy of total radiation will be lost; a more modern system, called a *single-line operation,* is equipped with a prism that selects the beam before it hits the total reflector, limiting the emission of photons at the desired wavelength.

4.2.2 Characteristics of laser light

The wavelengths of light emitted by the two main types of lasers are: 632.8 nm (red) for the HeNe laser and 514.5 nm (green) for the Argon laser. The power output of a standard HeNe laser ranges from 0.5 to 50 m*W* (the power supply is 10,000 times larger). Compared to conventional light sources, such as high pressure xenon or mercury lamps, the light output is surprisingly low, in fact, due to the collimation of the beam, even the smallest 0.5 mW laser has a brightness which is several orders of magnitude higher than that of conventional sources. A HeNe laser beam is visible and can be easily identified at a distance, even in daylight. Argon ion lasers have a light output in the order of W (and power supply in the order of kW) and require a circulation of cooling air or water.

The light from a conventional source cannot really be focused: a lens creates an image of the source in its focus according to the laws of geometrical optics and hence the power density of the image will be limited (Figure 4.5). A laser beam consists of parallel rays that are focused by a lens in a very small spot with high brightness: the relationship between the light power density in the spot and in the laser beam increases with the square of the inverse ratio of diameters; in a lens with a small focal length, this increase in light density can be of several orders of magnitude.

Figure 4.5 Focusing of an incoherent light source and of a laser beam

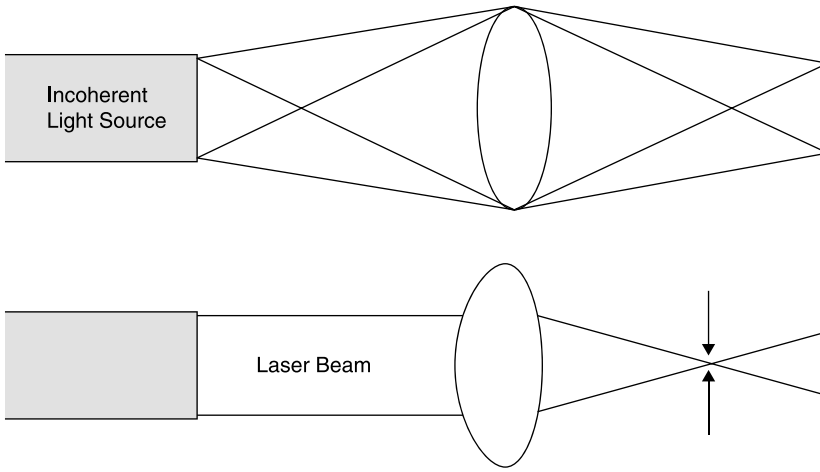

4.2.3 Temporal and spatial coherence

The interference between two beams can exist only if the frequency of the two beams remains constant in a certain period of time, this is indicated by the term *temporal coherence*. This condition is usually satisfied only if the two waves are generated by the same electronic transition in a particular atom. The time interval in which the characteristics remain constant, the *time of coherence* t_{co}, is related to the frequency range of the emitted light by the equation

$$t_{co} \propto \frac{1}{\Delta f} = \frac{\lambda}{f \Delta \lambda}$$

The *coherence length* $\ell_{co} = ct_{co} = \lambda^2/\Delta\lambda$ limits the difference in path lengths of the two beams for which interference can still be generated. The light originated from a light source with thermal spontaneous emission, passed through a filter with an interferometric bandwidth, has a coherence length of the order of mm; for a laser, the coherence length is of the order of 1m ($\ell_{co} = c/\Delta f = 2L$).

It must also be ensured that the light emitted from two different points of a source of finite dimensions (width d) and a certain divergence angle Θ can still interfere (*spatial coherence*). The answer is provided by the classical Young experiment: the necessary condition for the spatial coherence between the two beams is $d\sin\Theta << \lambda/2$.

The high degree of spatial coherence of laser light is shown by the extreme parallelism of the beam of the laser. Because of the laws of diffraction, no laser beam is perfectly parallel: the slightest difference for a given diameter is obtained with a laser beam with a Gaussian profile (mode TEM_{00}) for which the opening angle is in the order of mrad. In a laser beam that has an initial diameter of 0.8 mm and an angle of divergence of 1.1 mrad, the beam diameter is about 110 mm at a distance of 100 m.

4.2.4 Polarization

Lasers can be linearly or randomly polarized. The resonator of a laser creates standing waves of constant linear polarization. If special precautions are not taken, alternate longitudinal modes will have orthogonal polarization (Figure 4.6). Therefore, a laser is never really like a non-polarized thermal light source, it may be randomly polarized, i.e. it may issue a combination of orthogonally polarized radiation which, moreover, can vary over time. Introducing a Brewster angle window as a polarizing element within the laser cavity eliminates a state of polarization and produces a linearly polarized beam.

However, random polarization can be a problem if the beam interacts with polarizing elements or reflective surfaces and is detected by photoelectric sensors. The temporal fluctuation of polarization, *polarization noise*, gives rise to fluctuations in intensity and causes noise in the optical detector. In these applications, the use of a linearly polarized laser is recommended.

Figure 4.6 Polarization of a laser beam

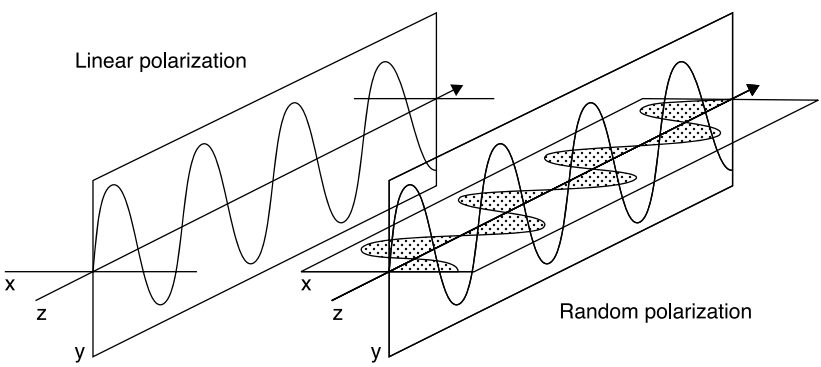

4.2.5 Laser sources for the optical methods of visualization

For the high degree of coherence, the laser appears an attractive light source for optical methods of visualization, especially for the interferometric methods, some of which can only be achieved if a laser is used as the light source.

To use a laser as a light source in flow visualization, it is necessary to provide two optical components. The first is an objective of very small focal length, 1 cm or less, which makes the thin and parallel laser beam divergent. The focus of this lens coincides with that of a subsequent larger diameter lens through which the beam is made parallel before traveling through the test chamber. The set of two lenses is the *beam expander* (Figure 4.7).

The second element is the *pinhole* that is necessary to clean the beam from the background noise of diffraction. Because of its high level of coherence, the laser light generates a significant configuration of diffraction images of rigid bodies and edges so that the cross-section of the beam is not evenly illuminated but disturbed by various fringes and interference patterns that can also generate diffraction of light on particles of dust on optical surfaces. Also, if there are higher-order transverse modes, the distribution of light in the focal plane of the beam expander is not a single bright spot but rather a pattern of diffraction usually in the form of some concentric circles of light and dark alternately. The diameter of the pinhole, which is placed in the focus of the beam expander, must

Figure 4.7 The beam expander

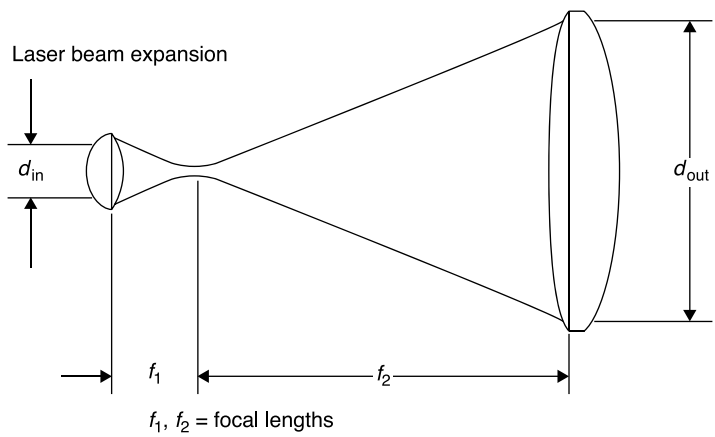

be so small as to let pass only the light of the inner circle, the image of zero-order diffraction; in this case, the cross-section of the beam becomes evenly illuminated. The pinhole and the beam expander form a *spatial filter.*

4.3 Laser-Doppler anemometer (LDA)

4.3.1 The Doppler effect

The laser-Doppler anemometer, invented in 1964 by Yeh and Cummins, is a tool that allows the measurement of the velocity of a particle from the difference in frequency between the light that strikes the moving particle and that is scattered and seen by an observer (*Doppler effect*).

Consider a particle that moves with speed U and is hit by a laser beam of wavelength λ_0 and frequency $f_0 = c/\lambda_0$ (Figure 4.8). Denote with $\overline{e}_i$ the unit vector corresponding to the direction of propagation of the incident beam. The light is scattered by the particle in all directions (Figure 4.1). Consider the light scattered along the unit vector $\vec{e}_s$, the frequency of this radiation is f_s and the wavelength λ_s, the Doppler effect is the difference in frequency $f_S - f_0$.

The speed of the wave fronts of the incident beam with respect to the particle is

$$c - \overline{U} \cdot \vec{e}_i$$

thus, the frequency with which the wave fronts are intercepted by the particle is:

Figure 4.8 Schematic representation of the Doppler effect

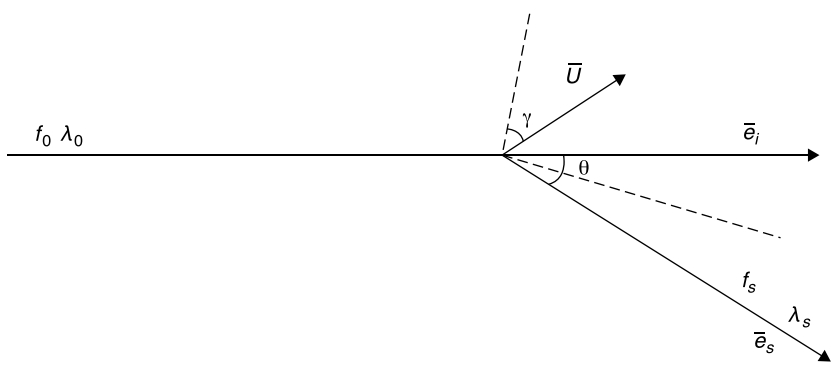

$$f' = \frac{c - \vec{U} \cdot \vec{e}_i}{\lambda_0} = f_0 - \frac{\vec{U} \cdot \vec{e}_i}{\lambda_0} \tag{4.1}$$

The light re-emitted by the particle has the frequency f' and the wavelength $\lambda_s = c/f'$. A fixed observer, who receives the light scattered in the direction $\vec{e}_s$, will intercept the wave fronts with the frequency:

$$f_s = \frac{c + \vec{U} \cdot \vec{e}_s}{\lambda_s} = f' + \frac{\vec{U} \cdot \vec{e}_s}{\lambda_s} \tag{4.2}$$

From Equation (4.2), taking account of Equation (4.1):

$$f_s = f_0 + \vec{U} \cdot \left(\frac{\vec{e}_s}{\lambda_s} - \frac{\vec{e}_i}{\lambda_0} \right)$$

Since $\lambda_S \approx \lambda$, then $\lambda_S \lambda_0 \cong \lambda_0^2$:

$$f_s = f_0 + \frac{\vec{U}}{\lambda_0} \cdot \left(\vec{e}_s - \vec{e}_i \right)$$

The difference in frequency due to the Doppler effect is thus equal to

$$f_D = f_s - f_0 = \frac{\vec{U}}{\lambda_0} \cdot \left(\vec{e}_s - \vec{e}_i \right) \tag{4.3}$$

Recalling the meaning of the difference of two unit vectors, Equation (4.3) can be interpreted by saying that the detected Doppler frequency is proportional to the velocity component in the direction normal to the bisector of the angle θ formed by the laser beam with the direction of observation:

$$f_D = 2 \sin\left(\frac{\theta}{2} \right) \frac{U \cos\gamma}{\lambda_0} \tag{4.4}$$

where γ is the angle, unknown, formed by the velocity vector with the normal to the bisector of the angle θ.

The benefits for an instrument which works on this principle are many:

- It requires no calibration.
- Measurements are made without disturbing the flow.

- A velocity component can be measured in any desired direction (in the case of 2-D and 3-D flow fields, the resultant velocity vector can be obtained by, respectively, two or three measured components).

If the flow is turbulent, it is necessary to measure the speed of a large number, n, of particles and report its statistical distribution (Figure 4.9), it is possible to obtain the average velocity, $\overline{U\cos\gamma}$ and the turbulence intensity, T_u, by calculating:

$$\overline{U\cos\gamma} = \frac{\sum_n u_i \cos\gamma_i}{n} \qquad T_u = \frac{\sqrt{\frac{\sum_n \left(u_i \cos\gamma_i - \overline{U\cos\gamma}\right)^2}{n}}}{\overline{U\cos\gamma}}$$

To measure a velocity component of a particle irradiated with a laser of known frequency, it should be sufficient to measure the frequency of the scattered light: this procedure is unfortunately impossible because it would be necessary to measure the effects on the frequency produced by the velocity of the particle (order $10^1 \div 10^2$ m/s) with respect to the speed of light (order 10^8 m/s) and so the measure would require

Figure 4.9 **Frequency histograms**

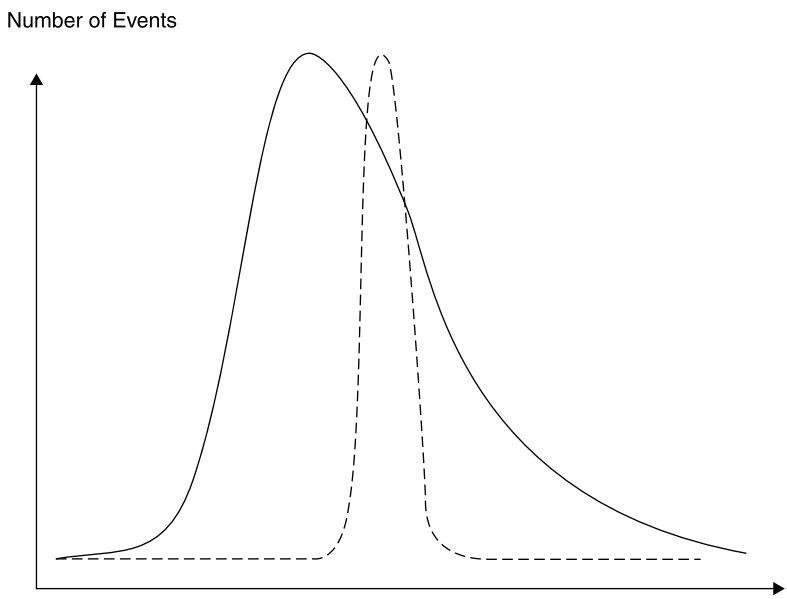

Note: The solid line shows a flow with 27% turbulence intensity; a flow with 2.5% turbulence is characterized by the broken line.

a tool with a sensitivity of $10^{-6} \div 10^{-7}$. The LDA must therefore rely upon a system able to measure the Doppler frequency, f_D directly. This can be done by overlapping two electromagnetic waves with electric vectors

$$\overrightarrow{E_1} = E_1\left(\cos\alpha_1 + i\sin\alpha_1\right) \quad \overrightarrow{E_2} = E_2\left(\cos\alpha_2 + i\sin\alpha_2\right)$$

where $\alpha = 2\pi ft = \dfrac{2\pi ct}{\lambda} = \dfrac{2\pi\ell}{\lambda}$, and ℓ is the optical path; by indicating the intensity of waves with $I_1 = E_1^2$ and $I_2 = E_2^2$ the intensity I_{1+2} of the resulting wave is:

$$I_{1+2} = I_1 + I_2 + 2\sqrt{I_1 I_2}\cos\left(\alpha_2 - \alpha_1\right) \tag{4.5}$$

The resultant light intensity is thus composed of a continuous part and an alternative part that is proportional to the difference of the frequencies of the incident rays, linked in some way to the speed of the particle, in the case of LDA.

4.3.2 The reference beam LDA

In this system, two laser beams converge on the area of measurement (Figure 4.10) and a photodetector is placed on the extension of beam 1. The particle, when crossing the measurement zone, scatters the light from both beams and the photomultiplier receives the beam 2 spread in the direction of beam 1, in addition to the direct beam 1 (the Doppler effect for beam 1 is null since the direction of observation and that of the incident beam coincide). The intensity of beam 1 must be strongly attenuated by a suitable filter to be made comparable with the faintest light scattered by the particle.

Figure 4.10 Schematic of a reference beam LDA

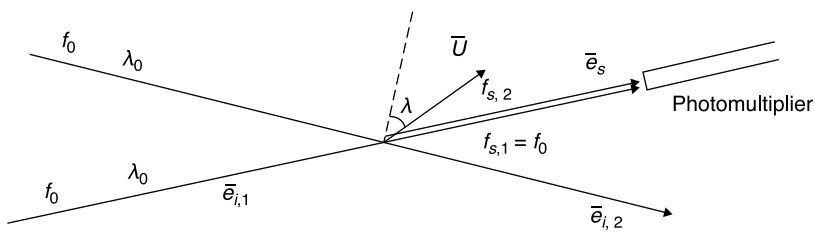

The frequencies of the rays that reach the photomultiplier are:

$$f_{s1} = f_0 \qquad f_{s2} = f_0 + \frac{\vec{U}}{\lambda_0} \cdot \left(\vec{e}_s - \vec{e}_{i2}\right)$$

From Equation (4.5), the output signal from the photomultiplier has the frequency

$$f_{s2} - f_0 = \frac{\vec{U}}{\lambda_0} \cdot \left(\vec{e}_s - \vec{e}_{i2}\right) = f_D$$

In this system, the scattered light must be captured in a very small solid angle, as near as possible to zero, since the relationship between velocity and the Doppler frequency depends on the direction of observation. This feature is a major drawback since it results in a limitation of the intensity of the detected optical signal and therefore requires a high-power laser. The system is also sensitive to vibrations because it requires perfect alignment between the photomultiplier and the laser beam.

4.3.3 Crossed-beams (or interference) LDA

This system represents an improvement on the previous one and is also easier to be interpreted. The moving particle is illuminated by two light beams of equal intensity (Figure 4.11) obtained from splitting one laser beam. The particle scatters the light from each of the two beams: from

Figure 4.11 Schematic of a crossed-beams LDA

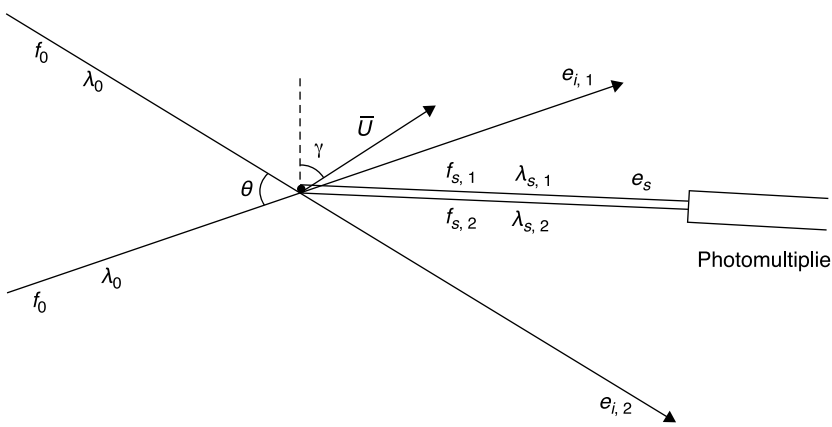

beam 1, with wavelength λ_{s1} and frequency $f_{s1,}$ and from beam 2, with wavelength λ_{s2} and frequency $f_{s2.}$

Using Equation (4.3):

$$f_{s1} = f_0 + \frac{\vec{U}}{\lambda_0} \cdot (\vec{e}_s - \vec{e}_{i1}) \qquad f_{s2} = f_0 + \frac{\vec{U}}{\lambda_0} \cdot (\vec{e}_s - \vec{e}_{i2})$$

Since, as we have seen, the variable part of the photomultiplier signal is only due to the difference of the frequencies, the Doppler frequency, we have:

$$f_D = f_{s2} - f_{s1} = \frac{\vec{U}}{\lambda_0} \cdot (\vec{e}_{i1} - \vec{e}_{i2}) \tag{4.6}$$

From this equation some important conclusions can be inferred:

- The frequency f_D of the output signal of the photomultiplier is directly proportional to the velocity component ($U\cos\gamma$ normal to the bisector of the angle θ formed by the two incident beams).
- The frequency f_D is independent of the direction of observation: this allows great freedom in the choice of configuration (*forward-* and *back-scatter*), and furthermore, allows the scattered light to be captured at a large solid angle and focused on the surface of the photomultiplier that therefore receives a much higher light intensity than in the reference beam system: a less powerful laser can be used.
- The frequency f_D can be made convenient for signal processing by an appropriate choice of the angle θ between the two incident beams.

The crossed-beam system can be analyzed in a different way that leads to the interference principle. Consider the area where the two beams intersect (Figure 4.12): there are two beams of laser light from the same source coherent and with the same wavelength, λ, and the same intensity $I_1 = I_2 = I$. By Equation (4.5):

$$I_{1+2} = 2I\left[1 + \cos(\alpha_1 - \alpha_2)\right] = 2I\left[1 + \cos\frac{2\pi}{\lambda}(\ell_1 - \ell_2)\right] \tag{4.7}$$

Since the pairs of interfering beams have different paths, the light intensity of their sum will vary with the difference in path lengths. The extreme cases are:

Figure 4.12 Formation of interference fringes in the measuring volume of a crossed-beams LDA

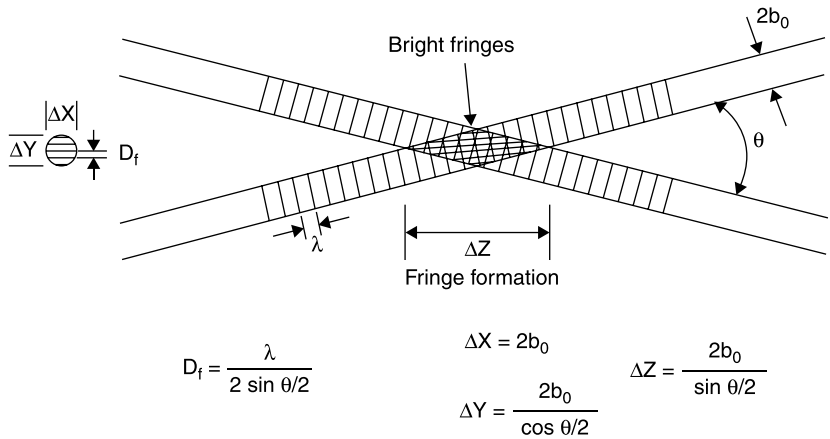

Source: [1]

- the difference in path lengths is equal to a multiple of the wavelength, $\ell_1 - \ell_2 = N\lambda$ (N = 0, ±1, ±2....): the resulting light intensity is $I_{1+2} = 4I$;
- the difference in path lengths is equal to an odd multiple of half wavelengths, $\ell_1 - \ell_2 = (2N + 1)\ \lambda/2$: the resulting light intensity is zero, $I_{1+2} = 0$.

In the area of intersection of the two laser beams, which is the *measurement volume*, a series of parallel interference fringes is generated; the distance between two consecutive fringes is:

$$D_f = \frac{\lambda}{2\sin\left(\frac{\theta}{2}\right)} \tag{4.8}$$

When a particle crosses the measuring volume, it is illuminated by a light variable with the Doppler frequency, recalling Equation (4.4):

$$f = \frac{U\cos\gamma}{D_f} = 2\sin\left(\frac{\theta}{2}\right)\frac{U\cos\gamma}{\lambda_0} \equiv f_D \tag{4.9}$$

so the velocity component normal to the fringes can be calculated by measuring the Doppler frequency and the distance between the fringes.

Figure 4.13 A typical signal of a LDA on an oscilloscope

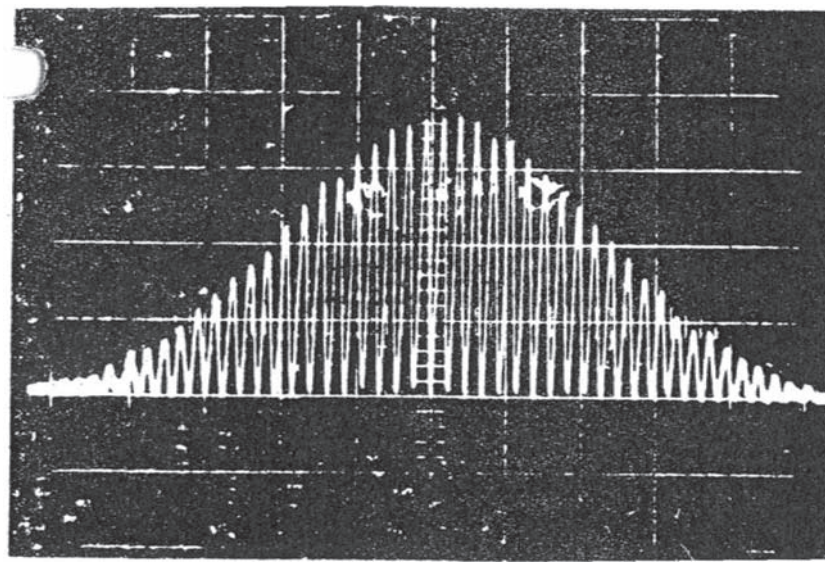

The trace on an oscilloscope of a typical signal is shown in Figure 4.13: since the laser beam has a Gaussian intensity distribution of light, even the signal has the same trend.

The angle of intersection of the two beams should be chosen so that the distance between two adjacent fringes is 10 μm. For Equation (4.9), this leads to signal frequencies of 50 MHz for a velocity component of 500 m/s. The precision with which the velocity of the particle can be measured knowing the Doppler frequency depends on the accuracy with which the distance between the fringes can be measured; the measurement can be done by projecting the magnified image of the fringes together with a microscopic net inserted in the control volume.

If the flow is turbulent (zone of separation, wakes, etc.), speed can be null or of unknown direction. The zero speed is not recognized because there is no output signal from the photodetector, the direction of the velocity component cannot be inferred from Equation (4.9) since the Doppler frequency is independent of the sign of the velocity component.

This ambiguity can be eliminated by passing one of the beams through a Bragg cell, which is an acoustic-optical modulator (Figure 4.14) consisting of a crystal or a liquid, transparent, to which a vibrator (a piezoelectric transducer) sends a pressure wave, and then a wave of an index of refraction with a constant frequency, typically 40 MHz. For the

Figure 4.14 A Bragg cell

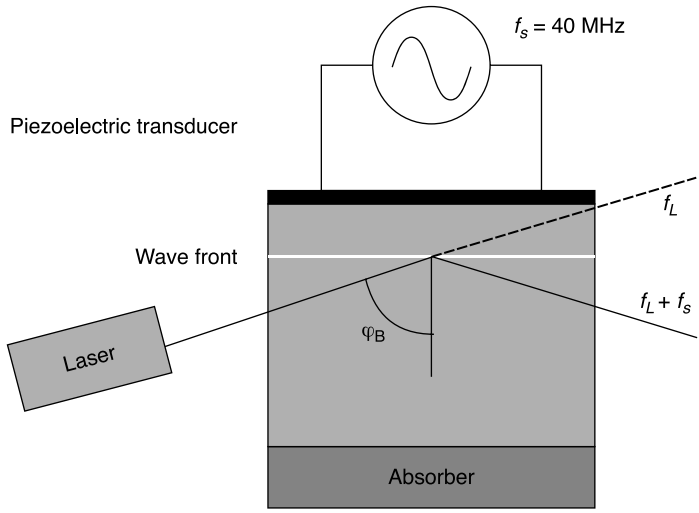

laser beam passing through the cell, this is a change of optical path with the same frequency of the vibrator.

At the intersection of the two beams, the interference fringes are apparently moving in the direction orthogonal to the fringes themselves with a speed that has to be algebraically summed to the particle velocity component normal to the fringes. In particular, a steady particle, due to the moving fringes, emits a signal with the frequency of 40 MHz; if the velocity of the particle is concordant or discordant with the motion of the fringes it will give a signal with a frequency less or greater than 40 MHz.

In another interpretation it can be said that the Bragg cell changes the frequency of the beam (*frequency shift*) that crosses it, giving rise to a constant Doppler signal which acts as a carrier for the signals generated by the moving particles.

4.3.4 System configuration

The LDA comprises three distinct parts:

- an optical emission device, comprising a laser and a system of division of the beam (*beam splitter*);
- a receiving device comprising an optical system as well as a photomultiplier;
- a system for processing signals received by the photomultiplier.

4.3.4.1 Optical emission device

This device consists of a laser beam which is split into two parallel beams by a prism, then the two beams pass through a lens that makes them converge in its focus. The point of intersection of the two beams is the measurement volume. In the case of the reference beam LDA, a neutral density filter is interposed in the path of one of the beams in order to reduce its intensity.

4.3.4.2 Optical receiving device

This device is different depending on the chosen configuration:

- in the reference beam LDA, it consists of a series of very small orifices, e.g. 1 mm in diameter, and a photodetector. The diaphragms are designed to intercept all the light except that coming in the direction of the reference beam:
- the crossed beams LDA includes a lens that allows the capture of scattered light in a large solid angle; a diaphragm in the image plane of the measurement zone stops the light scattered by particles passing through only one of the two laser beams, or worse, possible reflections of laser beams from the model or from the walls and the windows of the test chamber;
- an interferometric filter with the wavelength of the laser stops the light from the environment or from any other source.

4.3.4.3 Forward-scatter and back-scatter

In the reference beam LDA, the direction of observation is that of the reference beam; in the crossed-beams LDA, this direction is free. Taking the forward-scatter signal (Figure 4.15) by placing the sensor on the opposite side of the light source with respect to the measurement zone, is advantageous in terms of signal strength but is not always possible and/or convenient:

- two optical accesses are needed in the test chamber, which is usual in a wind tunnel but can be very difficult in turbomachinery;
- problems in collimation caused by vibration can arise.

By placing the laser and the sensor together (Figure 4.16) the problem of vibrations is eliminated, as they are treated in the same manner by the laser and by the photomultiplier; but operating in back-scatter, the light

Figure 4.15 Configuration of a forward-scatter crossed-beams LDA

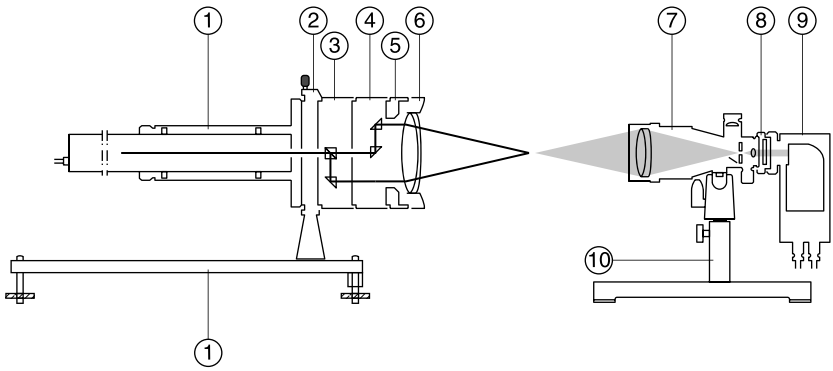

Source: [2]

intensity from the particles is reduced. In the back-scatter configuration the laser power must therefore be increased and/or the two beams can be focused in the measurement volume; with the latter technique, a double benefit is obtained:

- the measurement volume is smaller: it is possible to get measurements closer to the walls of the model or of the test chamber, preventing strong reflections that can distort the signal detection and damage the opto-electronic instrumentation

Figure 4.16 Configuration of a back-scatter crossed-beams LDA

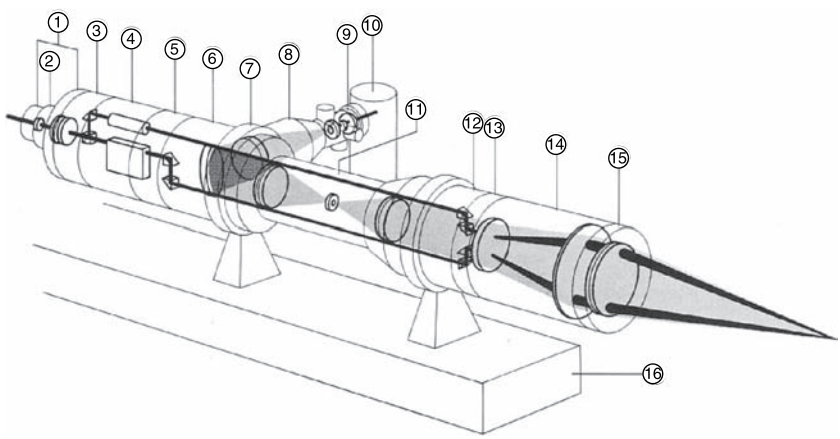

Source: [2]

- the contrast between light in the measuring volume and the surrounding region is greater so the signal from the region under investigation will be sharper, and more easily recognizable by spurious signals: ultimately a gain in SNR (*signal/noise ratio*) is obtained.

The focusing should not be too strong in order to prevent an excessive reduction of the number of interference fringes.

4.3.5 Systems for 2D and 3D measurements

If the direction of speed is not known, it is necessary to measure two components if the motion is 2D, or three components if the motion is 3D. If the flow pattern is constant in time, the various components of velocity can be measured by rotating the optical emission of the LDA, so that the bisector of the angle formed by the interfering beams is normal to the direction of the velocity component to be measured.

If the motion is unsteady, this technique cannot be used because the measurements of different components of velocity would be made at different times: in turbulent flow it is mandatory to measure all components simultaneously. With the same device (Figure 4.17), two components of velocity can be measured in the plane perpendicular to the optical axis, using an argon ion laser: the beam is split into two beams by a beam splitter, the green and blue colors are separated by a prism, pairs

Figure 4.17 **Four beams LDA for the measurement of two components. Backscatter configuration**

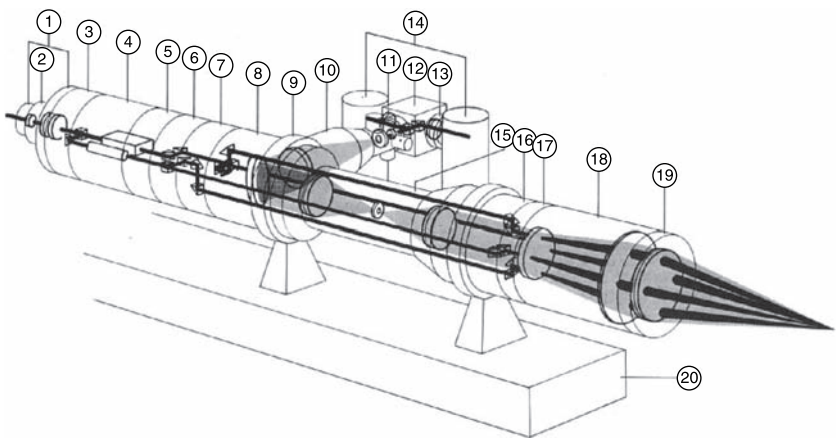

Source: [2]

Figure 4.18 LDA for the measurement of three velocity components

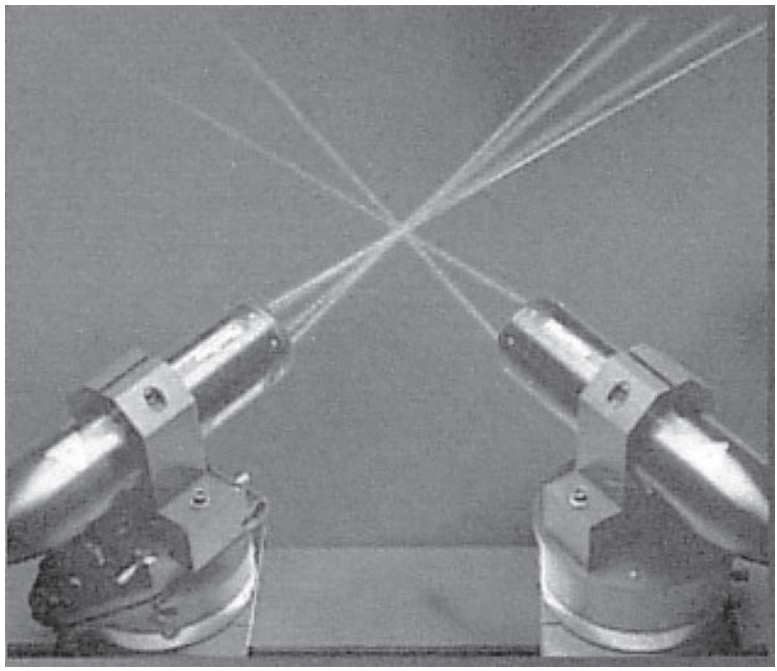

Source: [2]

of each color beams are focused in two perpendicular directions in the same measurement volume.

The light scattered from particles contains both colors; two photomultipliers, each preceded by an appropriate interferometric filter, green or blue, respectively, will measure only one of the two components of velocity.

If a third component of velocity has to be measured, another separate LDA is needed with an optical axis normal to that of the 2D system (Figure 4.18) which uses a third color, such as the purple of an argon ion laser.

4.3.6 Signal characteristics

The LDA can obtain information on the speed of the particles and therefore, if certain conditions are met, on the fluid stream flowing in an extremely small volume and whose position can be controlled with precision.

This information is in the form of a sinusoidal variation in the amount of light that reaches the surface of an optical detector that usually is a photomultiplier, since the intensity of the light scattered by the particles is low. Without going into the details of a photomultiplier, it suffices to say that variations in light intensity are converted into a proportional change in the flow of electrons whose number is amplified by a cascade system of electrodes, called dynodes (Figure 4.19), and finally collected by the anode in the form of an electrical signal variable over time.

An electrical signal whose frequency is proportional to a component of the particle velocity is generated:

$$f_D = KU\cos\gamma$$

where f_D is the frequency of the signal (Doppler frequency) and the constant K is a function of the wavelength of laser light and the geometry of the optical system. This extremely simple relation is the main attraction of LDA. The signals should be well separated in time: this can be achieved with a proper seeding of the stream which means that there should be only one particle at a time in the control volume.

The characteristics of the signal to be analyzed can be summarized as follows:

- There is an intermittent signal that contains a number of periods less than or equal to the number of interference fringes, which means typically between 15 and 100, and the signal can be present for a certain percentage of the total time.
- The frequency of the oscillations can be different for each signal: in the particular case of turbulent motion in which the velocity varies over time, it is necessary to measure these variations in frequency.

Figure 4.19 Schematic of a photomultiplier

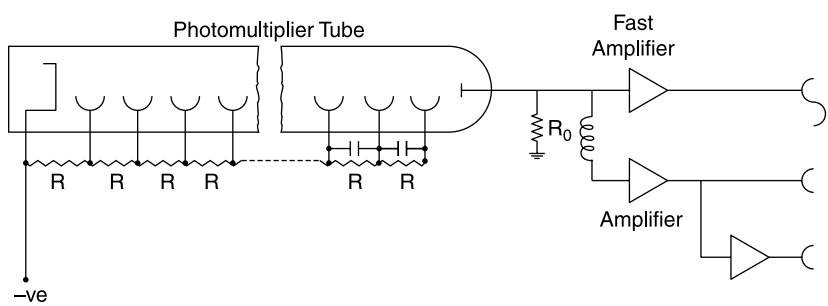

- The frequency range is very wide, typically from a few Hz to 100 MHz.
- The signals are modulated on a continuous level (the pedestal) that can be lowered with a high-pass filter.
- A certain amount of noise is superimposed on these signals due to noise in the photomultiplier and other electronic devices, optical noise produced by the higher order modes of the laser light scattered from outside the measuring volume, dirt, scratches on windows, ambient light, multiple particles, reflections from windows, lenses, mirrors. Furthermore, the signal can be very weak because the particle is too small or the distance of the measuring point from the photomultiplier is large; in some extreme cases, the signal to noise ratio can go down to 1.

A measure of the frequency of each signal is relatively easy (Figure 4.13): it is sufficient to count the number of complete oscillations per unit time, the speed is calculated from the measured frequency, so in theory the measure is obtained. If the motion is turbulent, however, it is unfeasible to memorize the signals from thousands of particles to get the histogram of Figure 4.9 for each component and analyze them manually, of course automated systems are needed.

4.3.7 Systems for signal analysis

The various systems of analysis are based on the following logics:

- direct measurement of the frequency through the use of narrow band filters;
- measurement in the time domain (period counters);
- measurement in the frequency domain (frequency spectrum).

4.3.7.1 Bank of filters

This is a very effective but a very expensive method: it needs a lot of filters connected in parallel, each corresponding to a different frequency. It is obvious that there will be an output signal only from the filter whose frequency is f_D (Figure 4.20). Counting the number of signals passed by each filter, a histogram of the kind of Figure 4.9 can be drawn.

Since each filter requires a certain time (or a number of cycles) to decode the signal, it can immediately be seen that the great advantage of this system is speed: typically it can analyze in a given time a number of

Figure 4.20 Schematic representation of a bank of filters

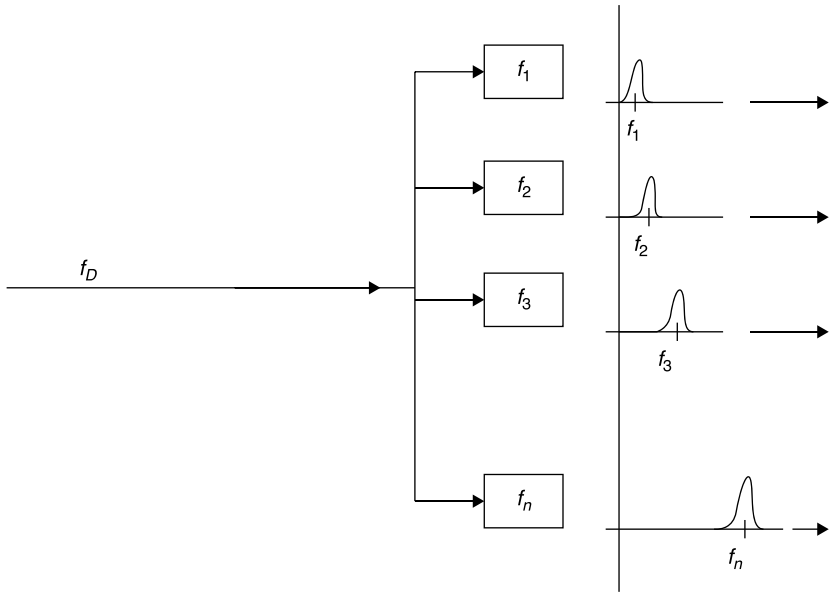

signals 50 times higher than those processed by a tuner that reviews in passing the different frequencies one after the other. Because of the high cost, this system is used only when necessary, as for example in the analysis of supersonic turbulent flows.

4.3.7.2 Variable filter (tuner)

The filter has a window whose center frequency can be changed continuously. The bandwidth of the filter is critical: if the bandwidth is very narrow, there are many signals rejections and to build a good probability curve it is necessary to stay for a long time on each frequency; if the band is broadened, the precision of the measure decreases. This measuring system is very effective, but unfortunately highly inaccurate and relatively slow. It can be considered an excellent tool for tuning and diagnosis of the initial motion, but this is not the system to be chosen for routine measurements.

4.3.7.3 Frequency tracker

This measurement system was the first to be sold in complete systems anemometers. The working principle is illustrated in the block diagram of Figure 4.21: the input signal is mixed with the signal from an oscillator

Figure 4.21 Simplified block diagram of a frequency tracker

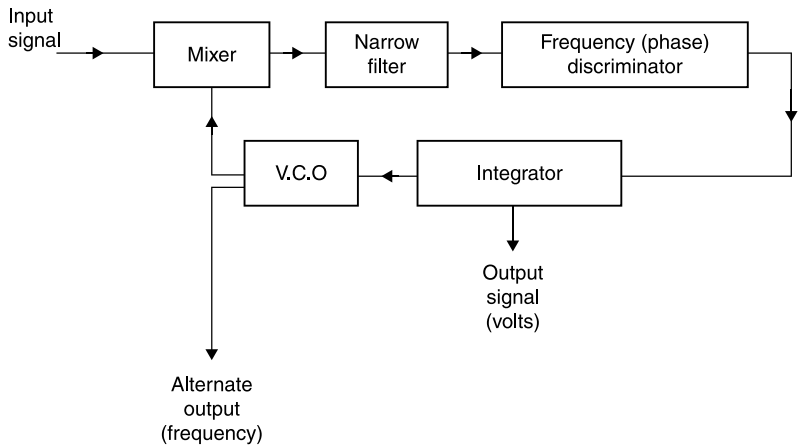

whose frequency is a function of voltage applied to its input (*voltage controlled oscillator*, VCO). The two overlapping signals pass through the narrow filter and are directed to a frequency or phase discriminator, which works by comparing the phases of the two signals and that, through an integrator, generates an output signal in the form of a voltage, proportional to the difference in frequency, that is sent to the VCO. The output frequency of the VCO is then adjusted to remove this difference and is therefore a measure of the Doppler frequency.

This is a slave filter, which adapts automatically to the frequency of the signal. To use the frequency tracker properly, the signal should be continuous (very large concentration of particles). The problem that the signals are discrete is solved by a simple form of memory that allows, when the signal is not present, the oscillation frequency of the VCO to be set on the last reading. The typical problem of this system is that it fails to follow the fluctuations of turbulence beyond a certain limit value, the theoretical maximum permissible intensity of turbulence for a frequency tracker is 0.33.

4.3.7.4 Correlator

The method of correlation is a technique well known from radar technology. Part of the Doppler signal is delayed by a known time τ: this is equivalent to adding a phase equal to the frequency multiplied by τ. The two signals, the original and the delayed one are compared in a cross-correlator which measures the phase difference from which, dividing by the known delay, the frequency is obtained. Correlators are

simple to use and, because of their low cost, are the preferred choice in industrial applications.

4.3.7.5 Period counters

When the number of signals per unit time is low, a high speed analog–digital converter can be used. The output signal of the photomultiplier is amplified, sent to a band-pass filter, digitized by the analog–digital converter and sent to a computer.

If the signal has only one frequency, the time between two zeros, which represent crossings of dark fringes (Figure 4.12), is the period. In order to minimize measurement error, the meter is programmed to count a number of zeros, and the period is obtained by the measured time divided by the number of zeros.

The computer checks the validity of each signal by comparing the time intervals between successive zeros (typically time intervals of 5 and 8 zeros). Only if these times give equal periods within the limits chosen, and only if the global number of zeros is not much smaller than the number of fringes contained in the control volume, is the signal accepted as valid. With these controls it is possible to detect signals disturbed by noise or signals generated by highly oblique particles passing through the control volume or those produced by two particles crossing this volume simultaneously.

Note that periods are measured and not frequencies (number of zeros in a fixed time); Figure 4.22 clearly shows the kind of errors made when measuring the frequency: if the measurement time is too small compared to the duration of the signal, few oscillations and fractions are included in it and therefore the error is large; if the measuring time is larger than the duration of the signal, the error is made of dividing the number of zeros for the gate time, which also includes a part when the signal is absent. As the length of the signal depends on the speed of the particle and the direction in which it crosses the measuring volume, the fixed time counting technique could only be used in quasi-stationary streams.

The period counter was the second system used in commercial anemometers, after the frequency tracker. Both systems are currently used for simple educational applications.

4.3.7.6 Spectrum analyzer

From the mathematical point of view, the easiest way to determine the frequencies contained in a signal is to convert the signal in the frequency domain through Fourier transforms. A simple way to implement the

Figure 4.22 **Errors in fixed time counting techniques**

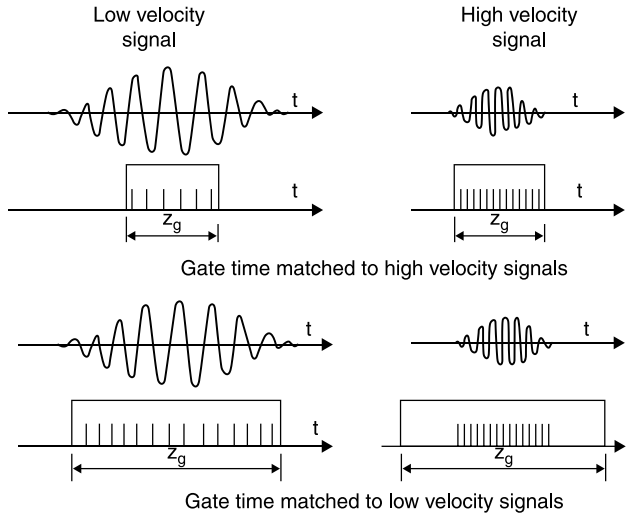

Fourier transform in the hardware of a computer, i.e. in discrete form on a limited number of samples, is called the FFT (*fast Fourier transform*).

The signal from the photomultiplier is digitized in an A–D converter that will take samples whose number must be chosen according to the length of the signal: 8, 16, 32 or 64 with a sampling frequency corresponding to the selected bandwidth. The procedure is applied to all signals coming in; only those due to the passage of particles in the control volume must be selected, therefore the times of arrival and departure of the particle in the volume are recorded and the process of storage signals is started and ended.

A power spectrum is calculated by the equation:

$$S_k = \left| \sum_{n=0}^{N-1} x_n \exp\left(-j \frac{2\pi kn}{2N} \right) \right|^2$$

$$k = -N, -N+1, ..., N-1$$

where N (= number of samples) may have the values 8, 16, 32 or 64.

A post-processor estimates the Doppler frequency using a parabolic interpolation of the measured spectrum. Inspection of the spectrum is also carried out: the measure is discarded if a peak does not appear in the frequency spectrum. Doppler frequencies of the measures that are accepted are sent to the output buffer along with the times of arrival and residence of the particle in the control volume.

The FFT processors are very accurate. With them an experienced user can achieve results not available with other types of processors: signals with low SNR values or even completely immersed in noise can be handled; for this reason the FFT processors are the most suitable for research applications.

4.4 Laser two focus anemometer (L2F)

4.4.1 Principle of operation

In the L2F, also known as a laser transit anemometer (LTA), the fluid stream velocity is obtained, by its definition, by measuring the time taken by a particle driven by the fluid to travel the distance between two light targets generated by two highly focused laser beams. The idea dates back to 1968 when it was introduced by D. H. Thompson. However, a *tracer particle fluid velocity meter* was only suitable for measuring velocities of the order of 20 m/s in the absence of turbulence. In 1973, Tanner, Schödl and Lading introduced new methods of analysis that allowed the extension of the measurements even at moderately turbulent flows (turbulence intensity up to 30%) and at supersonic speeds.

Figure 4.23 shows a particle traveling a trajectory normal to the axes of both beams. A signal of *start* from light scattered by a particle crossing the first focus activates a timer and when the particle crosses the second focus a signal of *stop* is sent to the timer. The *flight time* is the time interval between two pulses of start and stop for the same particle (*correlated pulses*).

Figure 4.23 Correlated pulses

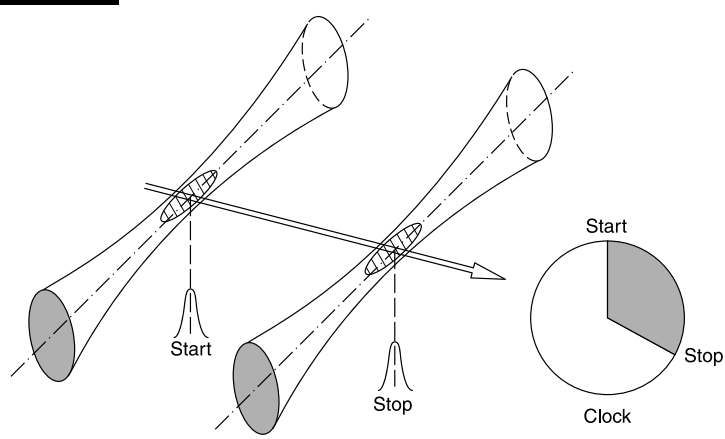

Figure 4.24 Random pulses

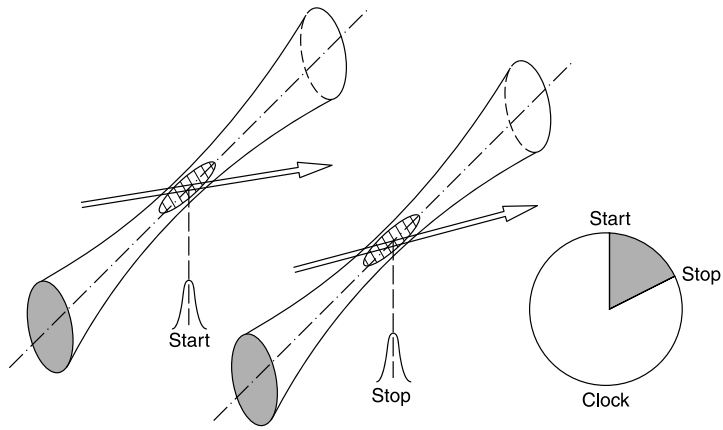

If in the measurement zone there are two separate particles and/or the direction of velocity is not normal to both axes (Figure 4.24), the start and stop pulses are generated by different particles. The time interval measured has no correlation with particle velocity, i.e. *random pulses*.

With a single measurement it is not possible to decide whether the measured time interval is random or if it is the flight time of a particle. Making a significant number of measures of time intervals the data with no correlation are averaged as a background noise while the correlated data will tend to be distributed according to a quasi-Gaussian curve like those in Figure 4.9.

To locate the direction of the velocity in the plane perpendicular to the optical axis, it is necessary to accumulate histograms in all directions of the plane; this is done by rotating one beam around the other (Figure 4.25). Histograms taken at different angular positions produce a 2D histogram, speed–direction. If the velocity vector lies in the chosen plane (2D flow), the histogram shows a peak and both the most likely value of the speed and of the direction of the velocity vector can be read from it (Figure 4.26).

If the flow is not in the plane perpendicular to the optical system, the number of correlated impulses falls. The 3D L2F utilizes this effect to obtain velocity information in three dimensions. Using two colors of a laser, a pair of focal volumes is generated for each beam displaced along the optical axis, as shown in Figure 4.27. The system simultaneously measures the times of flight from *A* to *B* and from *C* to *D*: the distance of the direction of the velocity is obtained by the ratio between the number of data in these two channels.

Figure 4.25 Rotation of the measurement direction

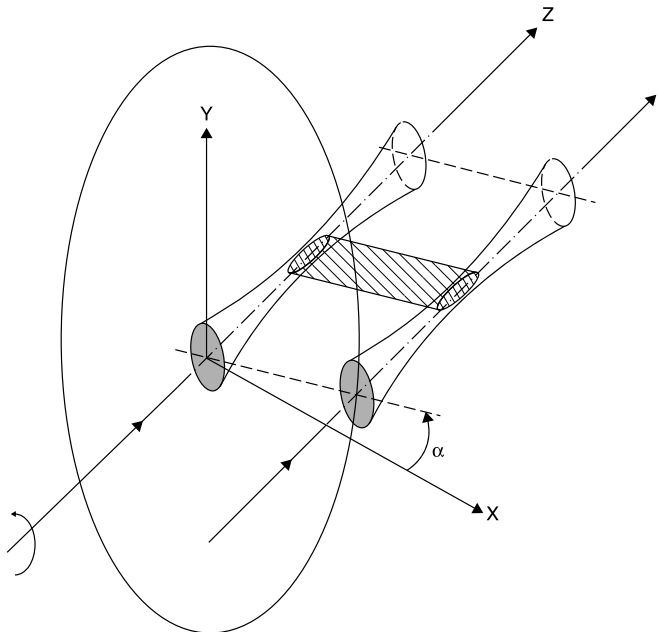

Figure 4.26 2D histogram

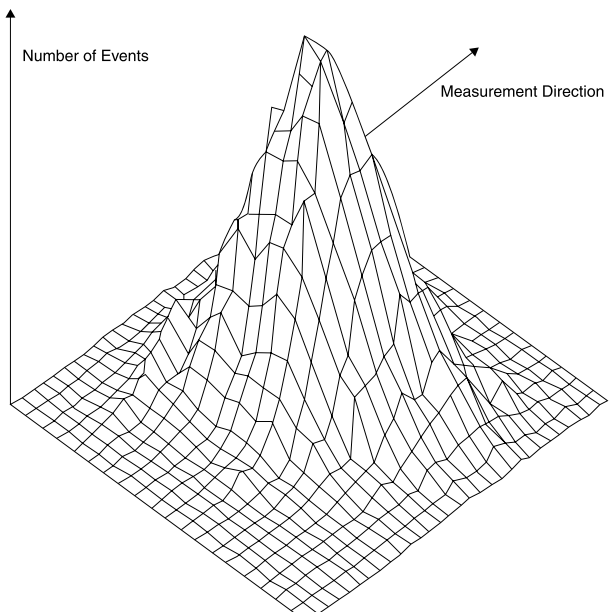

Figure 4.27 Measurement region of a 3D L2F

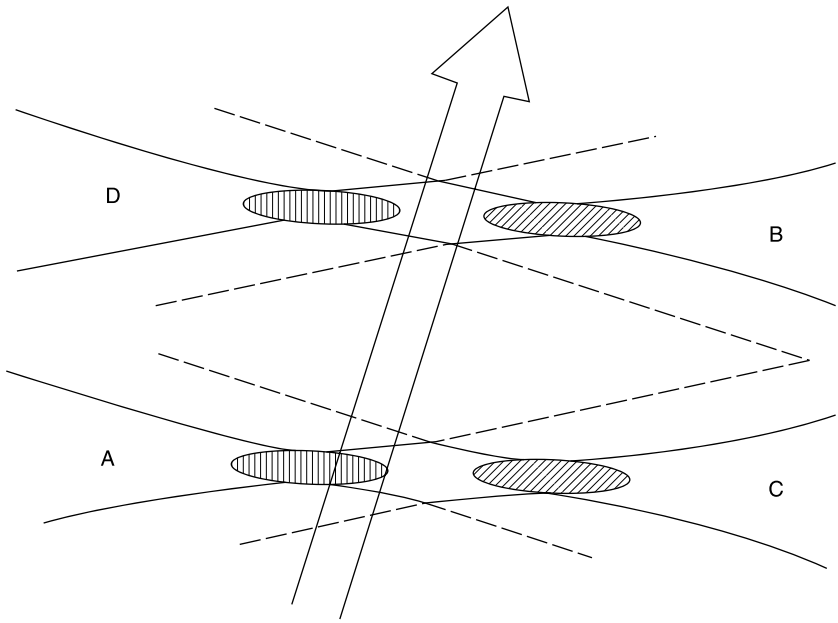

4.4.2 Optical system

As the two focal volumes are thousands of times brighter than the measuring volume of a LDA of equal power, the L2F can be easily used in the back-scatter configuration, which allows placement into a single hardware of both emission and receiving optics, in this way there are no alignment problems since the vibrations are transmitted evenly to both elements.

Figure 4.28 shows a typical L2F optical head: it includes two photomultipliers (detectors 1 and 2), a *beam-splitter* (*Rochon prism*), a

Figure 4.28 Optical head of a L2F

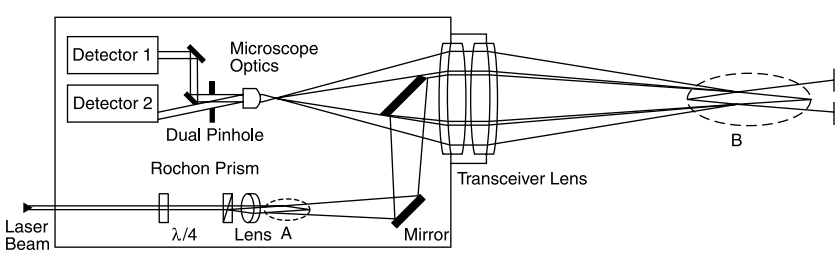

$\lambda/4$, the *transceiver lens,* and mirrors and lenses necessary to focus the laser beams and to create in the measurement of zone *B* the image of the two foci produced in zone A.

The laser light, monochromatic and linearly polarized, passes through a $\lambda/4$, i.e. a filter that slows and overlaps the incident waves; by the superimposition of two electromagnetic waves having the same form but out of phase by 90°, a quarter of wavelength, a circularly polarized wave is created.

The Rochon prism separates the laser beam into two beams of equal intensity: one emerges essentially not deflected, the other with a small angle with respect to the optical axis: a lens therefore focuses the two beams into two distinct focus; their distance can be changed using Rochon prisms with different angles of divergence.

The transceiver consists of two collimator lenses without spherical aberration flanked on all openings; the front collimator is interchangeable to allow for changes in working distance. The particles that pass through the focal volume scatter the laser light in all directions. The transceiver lens captures the back-scattered light and focuses it on a double *pinhole* that acts as a filter for the light background as in it passes only the light from the focal volume. Two broadband photomultiplier tubes convert the light pulses of start and stop into electrical pulses.

The change in the direction of measurement in the plane perpendicular to the optical axis is obtained by rotating around its axis the Rochon prism, the double pinhole optics and other stops, in this way, the off-axis focus is turned around the central focus that remains fixed in space (Figure 4.25). This fact justifies the presence of the $\lambda/4$, because the circularly polarized beam prevents variations of the light intensity of the beam when the prism rotates.

4.4.3 Measurement volume

Each of the two *ideal measurement volumes* can be defined as that zone of the focus contained within the surface on which the light intensity is equal to $1/e^2$ of its maximum value: if the intensity distribution of a laser beam is Gaussian, the surface will be an ellipsoid (Figure 4.29a). The *real measurement volume* is the undefined region from which the scattered light is projected onto each photomultiplier.

To properly define the boundaries of the measurement volume, the scattered light coming back towards the detectors is filtered through calibrated holes that allow only the passage of light from a narrow

Figure 4.29 Measurement volume of L2F: (a) in the plane of the laser beams; (b) in the normal plane

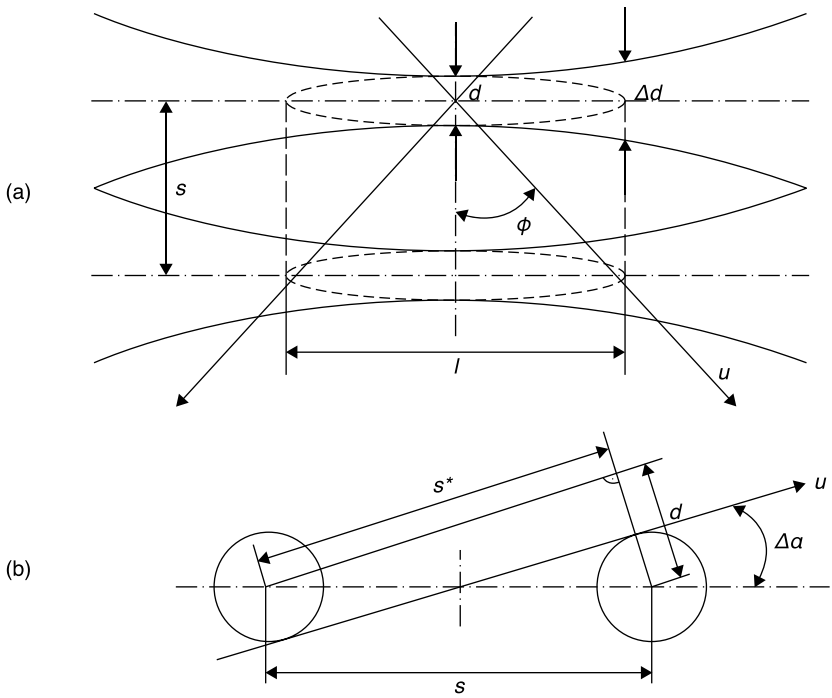

region, which is the real measurement volume. The ability to operate on the signal, setting the threshold level and allowing the passage only to signals of certain characteristics, increases the definition of the measurement zone, making it very close to the theoretical one, for example, very weak signals are typical of light scattered by particles crossing laser beams in areas different from the focus.

The diameter d of the spots in the area of measurement is about 10 μm, the distance s between the two is about 10^2 μm (remember that the size of the spot of an LDA is of the order of 1 mm). If the distance $l \approx 2s$, the angle ϕ shown in Figure 4.29a is 45°. Note in Figure 4.29b that the finite diameter of the spot induces uncertainty about the exact distance traveled by the particle. Figure 4.29b shows that start and stop pulses can be generated by particles traveling either according to the line joining the axes of two laser beams or, at worst, according to the tangent at the bottom left and top right of the beams. The maximum relative error is:

$$\varepsilon = \frac{s - s^*}{s} = 1 - \cos\left(\sin^{-1}\frac{d}{s}\right)$$

The error decreases as the ratio s/d. On the other hand, the probability of two related events decreases when this ratio increases.

4.4.4 Signal processing

The output signals from the photomultipliers are images of the intensity profile of the focal volume with the addition of noise in varying amounts: accurate signal processing techniques are needed in order to achieve a good resolution of flight time.

The signal is sent to an amplifier at fixed gain and then to an adjustable low-pass filter, which allows the elimination of high frequency noise and thus increases the signal to noise ratio, an additional amplifier sends the signal to a constant fraction discriminator (CFD) unit. This emits a pulse output when the signal exceeds a predetermined fraction of its maximum value, the output signal is in this way independent of the size of the input signal. If this amplitude exceeds a trigger level, which may occur when a particle is too large and therefore not indicative of the stream velocity, the CFD discards the measure.

The start impulse enables a precise current to charge a capacitor, whose voltage rises according to a characteristic ramp law, the stop impulse interrupts the charge, so a voltage signal is generated proportional to the time interval between the two pulses (time of flight).

4.4.5 Measurements in periodic motions

If a flow is periodic, it is necessary to correlate the measured velocity with the phase of the periodic phenomenon, e.g. in measurements in turbo engines, the measurement volume sweeps a path in the circumferential row of rotating blades, thus the flow between two blades is present cyclically with a frequency that depends on the speed of rotation and the number of blades. A synchronizer, working like an electronic shaft position encoder detects a pulse generated from the shaft itself. The frequency of the input signal (one lap) is multiplied by the number of blades to generate a pulse per blade (frequency of the blades).

If measurements are made between the blades of a turbo engine in motion, the laser beam must be instantly shut down, in order to prevent strong reflections of the laser beam on the blades. This mode of operation improves the signal to noise ratio as the photocathodes of the photomultiplier are restored during periods of absence of laser light.

Figure 4.30 Diffraction pattern of a Bragg cell

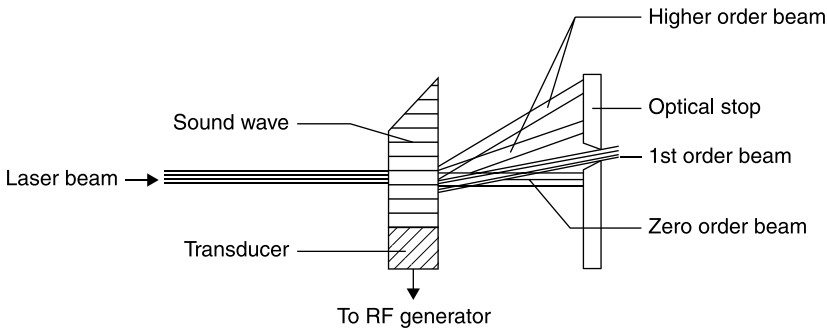

If a turbine disk with 30 blades is running at 10,000 rpm, laser beams encounter a blade 5,000 times a second: no mechanical shutter is capable of such a performance. A Bragg cell is then used which, as already stated, consists of a transparent crystal which is excited by a piezoelectric transducer connected to a high frequency generator; by applying an alternate current to the transducer, a train of acoustic waves is generated inside the crystal, that produces a periodic variation of the refractive index of the crystal which, in turn, generates the periodic diffraction of the laser beam. The outgoing beam oscillates with the frequency of the transducer in turn generating a beam of zero order (non-deviated), beams of the first order, second, and so on (Figure 4.30).

If the piezoelectric transducer is not excited, the incoming beam undergoes no deviation (zero-order beam only exiting the crystal), and is thus interrupted by the optical stop; the Bragg cell and the stop are adjusted so that, with the transducer excited, the beam of the first order is able to exit the hole in the optical stop with a frequency equal to that of the blades.

4.5 Particle image velocimetry (PIV)

Unlike the laser techniques described above, LDA and L2F, which provide velocity measurements at one point, PIV allows the examination of a whole section of the flow field and thus enables simultaneous measurement at different points, that is an essential requirement in unsteady motions. Usually two components of velocity are measured, but using a stereoscopic approach it is possible to obtain three components. The use of modern charged-couple device (CCD) cameras and dedicated computing

hardware permits velocity and vorticity maps in real time to be obtained, of the same type as those obtained in computational fluid dynamics (CFD) with the large eddy simulation technique.

4.5.1 PIV for studies of 2D fields

The test section is illuminated by a sheet of laser light produced by a cylindrical lens (Figure 4.31). This produces an image of the illuminated area on the matrix of pixels (typically $1k \times 1k$) of a CCD camera. To maximize the amount of light that reaches the camera, it should be placed in the direction of forward scatter, but the visual field would be reduced, the location chosen is usually normal to the direction of motion.

In the PIV, velocity vectors are determined by measuring the displacements of particles between two consecutive images of the stream:

$$\overline{V} = \frac{\Delta \overline{S}}{\Delta t}$$

Figure 4.31 Diagram of a PIV apparatus for 2D fields

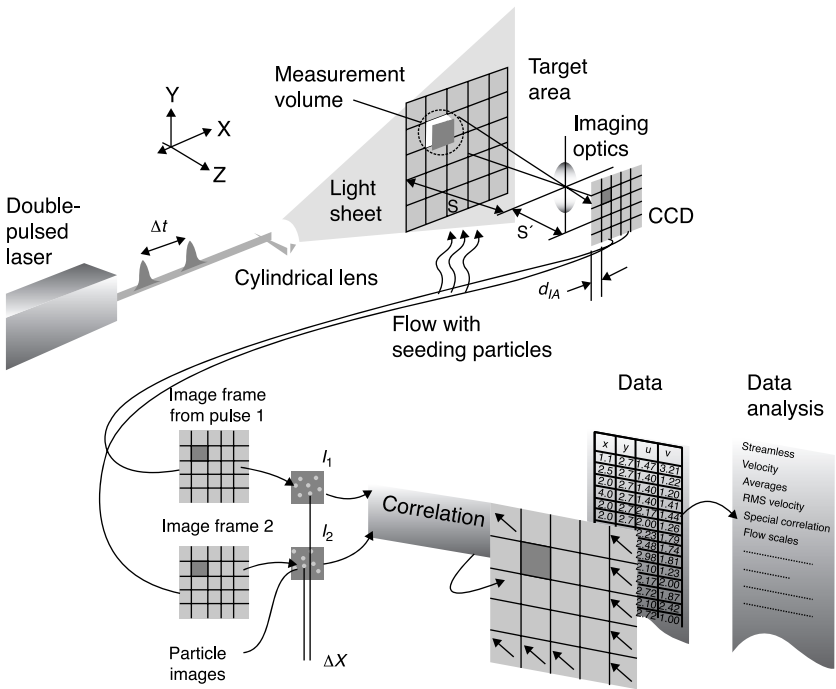

Source: [4]

Figure 4.32 Autocorrelation on double-exposure image

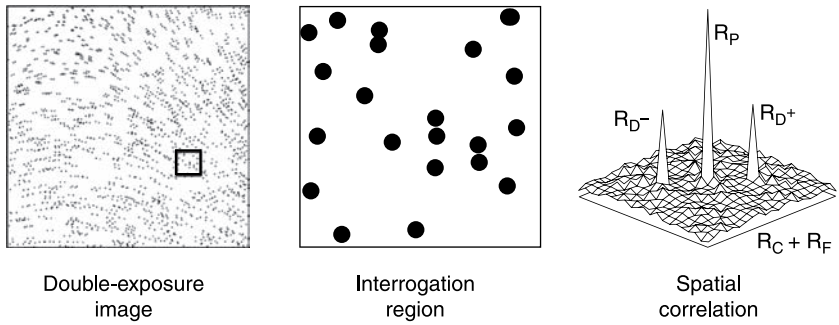

To find the individual velocity vector, the images are divided into *interrogation areas or sections or windows* (Figure 4.32), in which it is assumed that all particles have the same speed. In order to obtain a significant measure, 10 to 25 particles must be contained in each area. The lateral size of the interrogation area, d_{IA}, must be chosen, depending on the size of the structure of the stream that must be investigated. One way to express this is to state that the *velocity gradient* is negligible inside the interrogation area, for example, it must be:

$$\frac{V_{\max} - V_{\min}}{d_{IA}} \Delta t < 5\%$$

The *maximum measurable speed* is limited by the particles that exceed the boundaries of the interrogation area in the time that elapses between the two laser pulses. The condition can be imposed:

$$\frac{V \Delta t}{d_{IA}} < 25\%$$

The *measurement volume* can be defined once the size of the interrogation area and the thickness of the light sheet are known.

There are two possible procedures:

- double-exposure image
- two separate images.

The first procedure allows the movement of particles to be viewed and the structures present in the stream to be highlighted. To each area of interrogation a technique of autocorrelation is applied: denoting by

$I(x, y)$ the intensity of light scattered by the particles, and by ζ and η the shifts in the directions x and y, the convolution integral is applied in the interrogation area and the maximums are found:

$$R(\xi,\eta) = \int_{-\infty}^{\infty}\int I(x,y)^* I(x-\xi, y-\eta)\, dxdy$$

The absolute maximum identifies the null displacement, the overlapping of individual particles. The next maximum identifies the distance in the two directions between two consecutive positions of the particle. This procedure therefore does not determine the direction of the speed so it is not applicable in vortical zones where there are inversions of velocity.

To use the second procedure, it is necessary to use a CCD camera capable of capturing on separate frames the images produced by laser pulses. Once a couple of pulses are recorded, the areas of interrogation of both frames are cross-correlated pixel by pixel. In an interrogation window of $M \times N$ pixels (Figure 4.33), the common particle displacement can be calculated using the algorithm of cross-correlation:

$$C(\Delta x, \Delta y) = \sum_{i=1}^{M}\sum_{j=1}^{N} I_1(i,j)^* I_2(i-\Delta x, j-\Delta y)$$

where Δx and Δy are possible displacements obviously limited by the condition that the particles do not exceed the boundaries of the window. The correlation produces a peak signal that identifies the common particle displacement Δx, Δy). Accurate measurement of displacement, and therefore of the speed, is obtained with a sub-pixel interpolation.

A map of the velocity vector in the whole investigated area is obtained by repeating the cross-correlation for each interrogation area on the two

Figure 4.33 Cross-correlation between two consecutive images

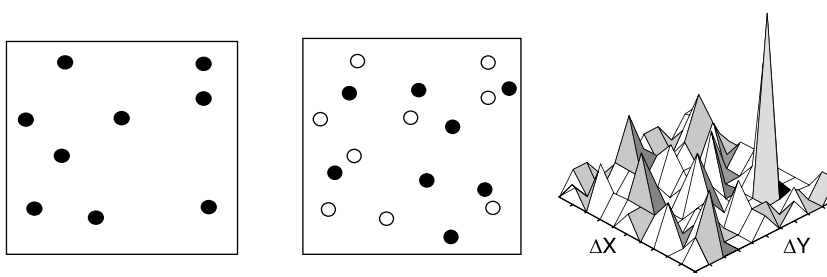

Figure 4.34 Maps of velocity vector and vorticity

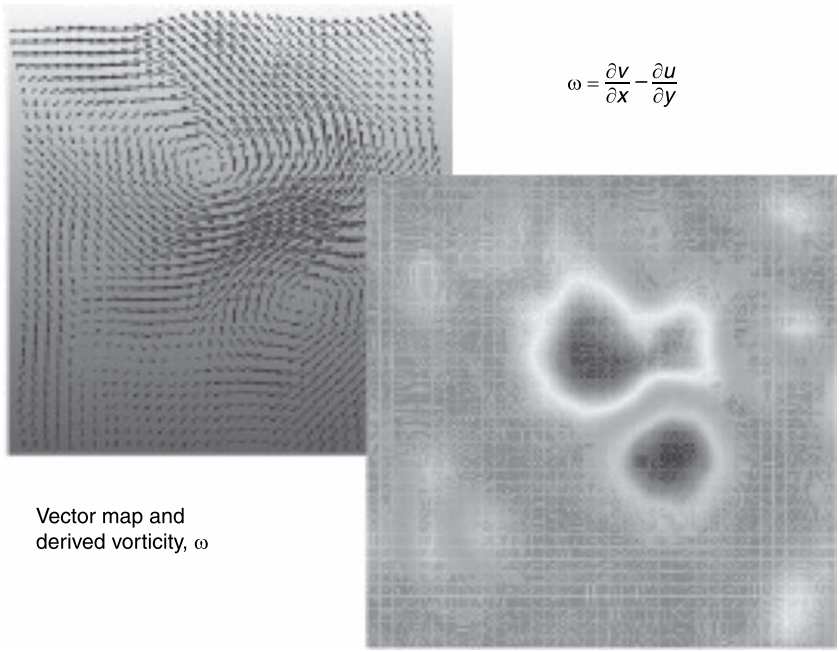

frames (Figure 4.34). In the same figure the corresponding *map of vorticity* is shown calculated from:

$$\omega = \frac{\partial v}{\partial x} - \frac{\partial u}{\partial y}$$

4.5.2 Stereo PIV

The 3D PIV uses the stereoscopic principle to identify the three components of speed in a flat section of the flow field determined by the laser light sheet. The 3D (Δx, Δy, Δz) displacement is estimated by a couple of 2D (Δx, Δy) displacements as seen by the left and right cameras (Figure 4.35). The greater the angle between the two cameras, the more accurate is the determination of the displacement Δz.

The 3D processing requires a numerical model that describes how objects in space are seen by the CCD camera. The parameters of the numerical model are obtained from a preliminary calibration of the

Figure 4.35 Schematic of a stereoscopic PIV system

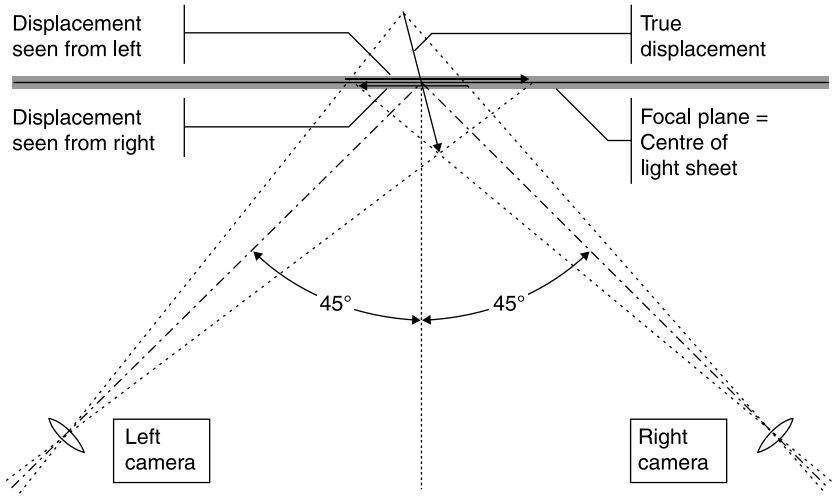

Source: [5]

camera framing markers whose position is known: it serves to identify a common coordinate system for the two cameras.

Obviously, the 3D assessment is only possible within the area covered by both cameras. (Figure 4.36). Because of the perspective distortion, each camera covers a region of the trapezoidal plate light. Careful alignment to maximize the overlap area is required.

The stereoscopic measurement begins by processing the simultaneous images produced by two cameras. Two 2D vector maps are obtained that describe the flow field as seen by each of the two cameras. Using the calibration function with the parameters obtained during calibration of the camera, the points of the interrogation grid are reported from the plane of the light sheet on the left and right image planes (planes of the CCDs). With the 2D displacement seen by both cameras and estimated at the same point of the physical space, the 3D displacement of the particle can be calculated by solving the equations obtained in calibration.

When the light sheet is observed at an angle different from 90°, the image plane of the camera, the plane of the CCD, must be rotated as required to properly focus the entire field of view of the camera. The planes of the image, of the lens and of the object must intersect along a common line in order to obtain a properly focused image. This is called the Scheimpflug condition.

Figure 4.36 Overlapping the visual fields of the two CCD cameras

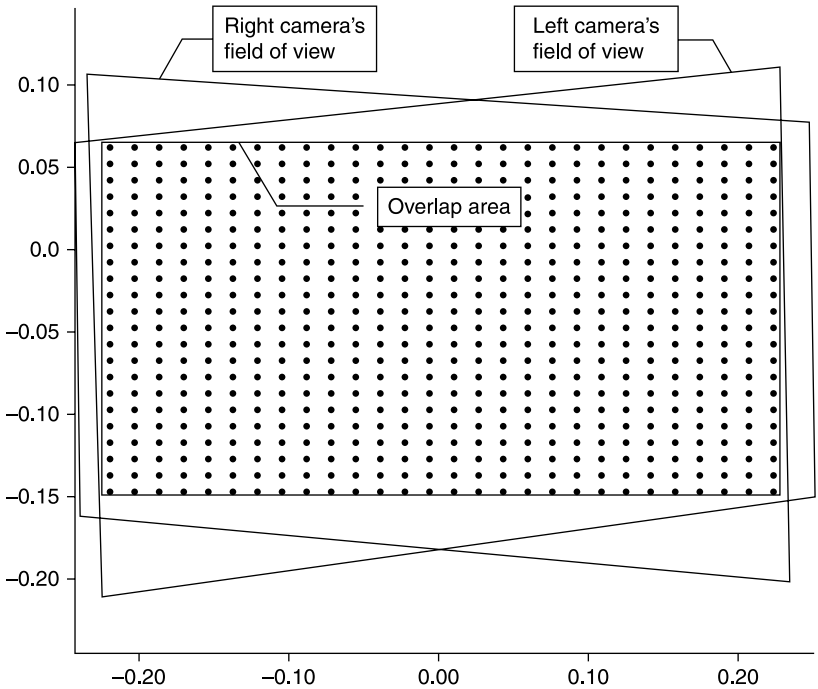

Source: [5]

4.5.3 Time resolved PIV

Time resolved PIV technology is currently available, which obtains 4000 images per second, adding the dimension time to the measures of a fluid-dynamic field. With CTA, LDA and L2F techniques, the behavior in time of speed at a single point could be obtained. The study of the structures present in the stream was delegated to the methods of visualization. The missing element was the combination of spatial information derived from the PIV with the simultaneous history of each point. The next step is time resolved PIV, providing a more thorough examination of the fluid dynamic phenomena and the correlation time–space. The results (Figure 4.37) are similar to those obtained by computational fluid dynamics using large eddy simulation.

Figure 4.37 Succession of images of velocity and vorticity fields obtained in real time

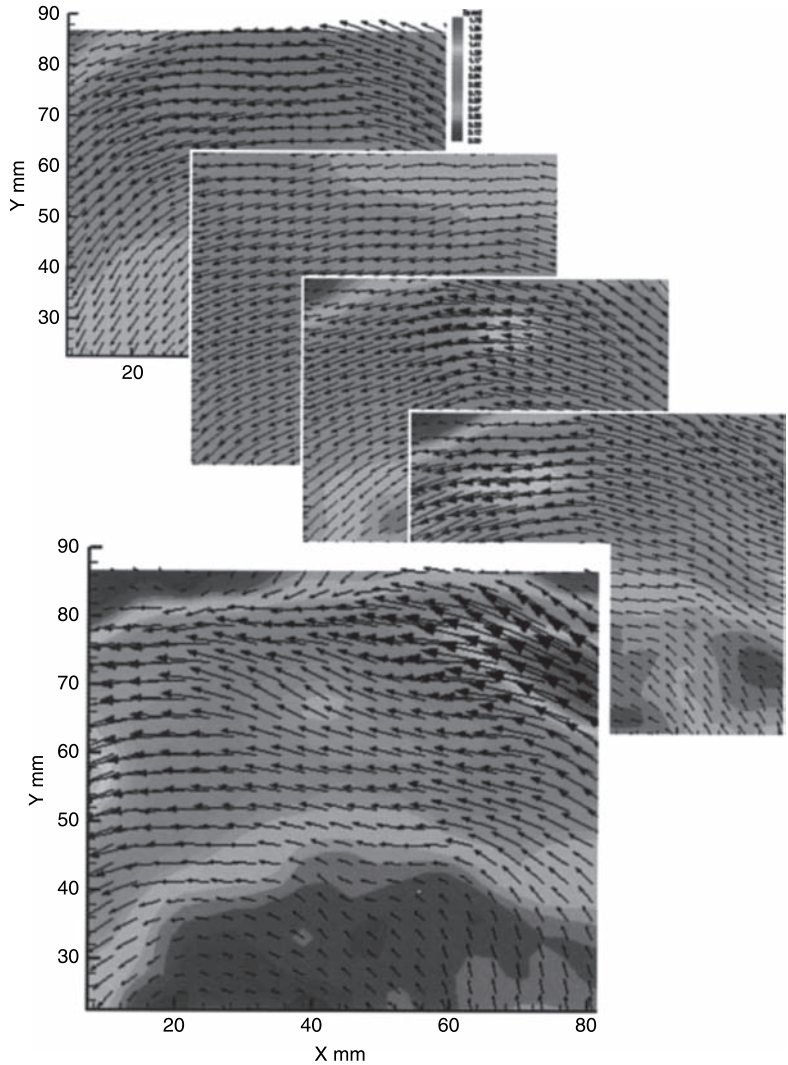

Source: [6]

References

1. M.L. Reithmuller and D. Olivari (1974) *Le velocimètre laser: Principes et application*. Von Karman Institute for Fluid Dynamics, Technical Memorandum 25.
2. DANTEC (1991) *Laser Doppler Anemometer Optics 55X Series*.
3. Polytec (1988) *Laser Dual Focus Velocimeter L2F*. Polytec GmbH.
4. DANTEC (2004) *Principles of Particle Image Velocimetry*. Available at: http://www.dantecmt.com.
5. DANTEC DYNAMICS, *FlowManager 3D PIV*. Available at: http://www.dantecmt.com.
6. TSI (1997) *Particle Image Velocimetry Systems*. Incorporated Fluid Mechanics Instrument Division.

5

Temperature measurements

Abstract: This chapter highlights both contact temperature sensors (thermocouples and temperature sensitive paints) and devices allowing measurements of temperature at a distance: infrared thermo-cameras. Devices and techniques used to measure temperature recovery factor, film coefficient and stagnation temperature of an air stream are described.

Key words: infrared thermo-cameras, temperature sensitive paints, thermocouples.

5.1 Sensors

Temperature measurements are of great importance in problems of heat transfer between a body and a fluid stream. If the flow is incompressible, the only relevant temperatures are the wall temperature, T_w, and the static temperature of the stream, T_∞. In supersonic and hypersonic flows *aerodynamic heating* is present and it is necessary to consider also the stagnation temperature of the stream, $T_{0\infty}$, and the adiabatic wall temperature, T_{aw}.

Temperature sensors can be classified into two main groups: c*ontact sensors* and *remote sensors*. Among the contact sensors *thermocouples* are dominant in point measures, *temperature-sensitive paints* (TPS), are used with success in the mapping of large areas.

In order to obtain reasonably accurate measures of temperature with contact sensors, some basic requirements must be fulfilled:

- as every sensor measures its own temperature, it is necessary that the sensor be in thermal equilibrium with the body;
- the sensor must not conduct heat to or from the point of measurement;

- the probe should not interfere with the way in which heat transfer occurs between the stream and the body: conduction, convection, radiation and mass transfer (evaporation or condensation); for example, if there is radiation, the emissivity of the wall should not be modified by the presence of the sensor.

The remote sensors deduce the temperature by measuring the radiation, infrared or visible, emitted by the body: the measure is not limited to high temperatures (*pyrometry* in the visible), efficient methods have been developed (*thermographic cameras*) which allow the measure in the infrared range, even at temperatures below ambient, with an accuracy comparable to that of a thermocouple.

5.1.1 Seebeck effect and thermocouples

Any two wires of different metals *A* and *B* can be used as a thermocouple if connected as in Figure 5.1. When the temperature of the junction, T_{Jct}, is different from the reference temperature T_{Ref}, a weak potential difference, *E*, is generated at the terminals +/–.

The value of *E* depends on the materials *A* and *B* and on the difference between reference temperature and junction temperature:

$$E = \int_{T_{\mathrm{Ref}}}^{T_{\mathrm{Jct}}} (\varepsilon_A - \varepsilon_B)\, dT$$

where ε_A and ε_B are the thermoelectric power or *Seebeck coefficients of* the two metals.

For small temperature differences, the following linear equation can be used:

$$E = (\varepsilon_A - \varepsilon_B)\left(T_{\mathrm{Jct}} - T_{\mathrm{Ref}}\right) = \varepsilon_{AB}\left(T_{\mathrm{Jct}} - T_{\mathrm{Ref}}\right)$$

where ε_{AB} is the Seebeck coefficient of the couple of metals.

Figure 5.1 Schematic of a thermocouple

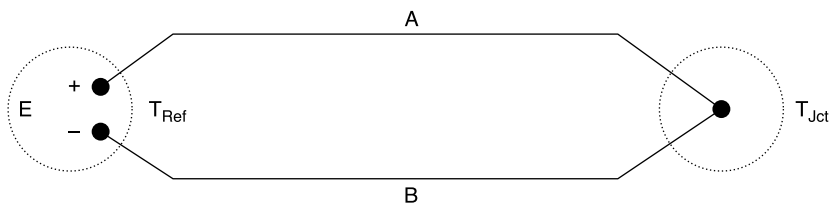

The three most common thermocouples are copper–constantan (type T), iron–constantan (type J) and chromel–alumel (type K): the first element of the couple is positive, the negative wire is coded with the red color. All three types are available in pairs of coated wires with a minimum diameter of 25 μm. For reasons of accuracy and space, the minimum diameter possible should be chosen taking into consideration that wires with a diameter less than 75 μm are very weak.

- Copper–constantan (type T, color codes: blue and red): $\varepsilon_{AB} \approx 40\ \mu V/K$, $T_{max} = 300°C$. Neither wire is magnetic. Junctions can be obtained by welding or brazing with usual welders.
- Iron–constantan (type J, color codes: white and red): $\varepsilon_{AB} \approx 50\ [\mu V/K]$, $T_{max} = 650°C$. Iron is magnetic. The junction can be obtained by welding or brazing with usual welders. The couple iron–constantan can generate a galvanic electromagnetic force: it cannot be used in the presence of water.
- Chromel–alumel (type K, color codes: yellow and red): $\varepsilon_{AB} \approx 40\ \mu V/K$, $T_{max} = 1100°C$. Alumel is magnetic. The junction can be obtained by welding or brazing with silver, at the higher temperatures iron must be used. This couple generates electrical signals when subjected to deformation.

To measure higher temperatures the following thermocouples may be used:

- Platinum–platinum/rhodium: $T_{max} = 1650°C$
- Iridium–ruthenium/iridium: $T_{max} = 2100°C$
- Tungsten–tungsten/molybdenum: $T_{max} = 3200°C$.

Thermocouples can be purchased ready-made or can be made in the laboratory from pairs of wires using a specific thermocouple welder or any suitable welder for fine wires.

The reference temperature can be controlled in several ways:

- melting ice is widely used in laboratory because it is accurate and inexpensive: a thermos can maintain 0°C for several hours if filled with crushed ice and water;
- systems are available that provide reference temperatures controlled electronically; these devices are not as stable as melting ice, and require periodic calibration but are very easy to use;
- other instruments use as a reference the temperature that is generated within the container, assuming that this is not affected by environmental conditions;

- in less accurate measures the room temperature can be used as a reference.

The main difficulty encountered in the use of thermocouples is the need for the junction and the wires not to disturb the temperature distribution in the wall. It is advisable to check the effect of the thermal conductivity of the wires and the heat transfer to or from the junction to determine the measurement error in each individual application:

- In a metal wall, the junction can be welded directly to the metal, taking care not to alter the character of the surface and its emissivity. The simple method of welding the junction to the surface and spreading out the wires parallel to the surface in an isothermal layer, to minimize losses by conduction, can be adopted only in incompressible flows; such a system, causing shock waves in supersonic flows and disrupting the surrounding boundary layer, would completely alter the local temperature conditions: in this case, the sensor should be placed inside the body.
- With models made of insulating material good results can be obtained by using discs of copper or silver, approximately 3 mm in diameter and 0.25 mm thick, inserted into the wall flush with the surface. Figure 5.2 shows this arrangement of the thermocouple used for measurements in a supersonic field: the disk can easily reach the temperature of the surface and quickly follow any change in temperature due to its low heat capacity. The influence of radiation can be reduced by covering the insert with a thin layer of lacquer having an emissivity similar to that of the wall.

Figure 5.2 **Measurement of temperature of a plastic wall with a thermocouple**

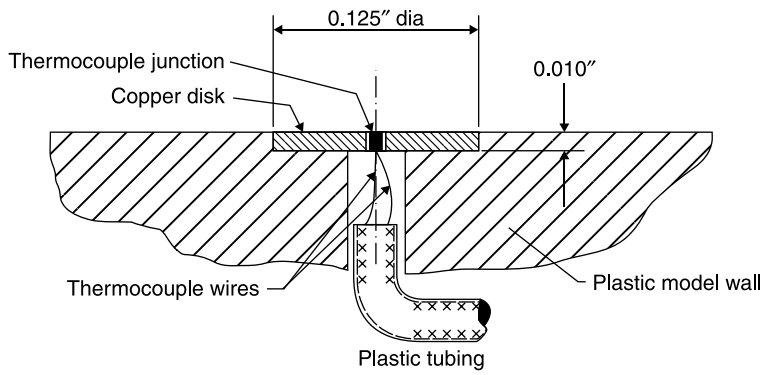

5.1.2 Temperature-sensitive paints (TSP)

The temperature of a body can be measured by using temperature-sensitive paints, and these may be, in order of increasing performance:

- phase-change paints whose basic component is a wax: an isotherm is identified by the line of separation between the solid and liquid phases. With these paints, it is only possible to identify areas of the body that are at temperatures below or above the melting temperature of the wax; the coating can be used only once.
- multi-component paints: each component undergoes a color change at a specific temperature and hence each isotherm is identified by a line of separation between two different colors. In the areas between two isotherms, it can be argued that the temperature is between the two values. The color change is irreversible, so the coating can be used only once.
- a reversible color change can be produced with a coating of liquid crystals. Temperature changes alter the molecular structure of these crystals causing a change in the wavelength, and then in the color, of the scattered light.
- temperature-sensitive paints (TSP) are fluorescent elements (phosphorus), analogous to the pressure-sensitive paints, which, stimulated with an appropriate radiation, emit light whose intensity decreases with temperature (Figure 5.3); the emitted light is of a wavelength

Figure 5.3 Typical dependence of the light intensity emitted by a TSP on temperature

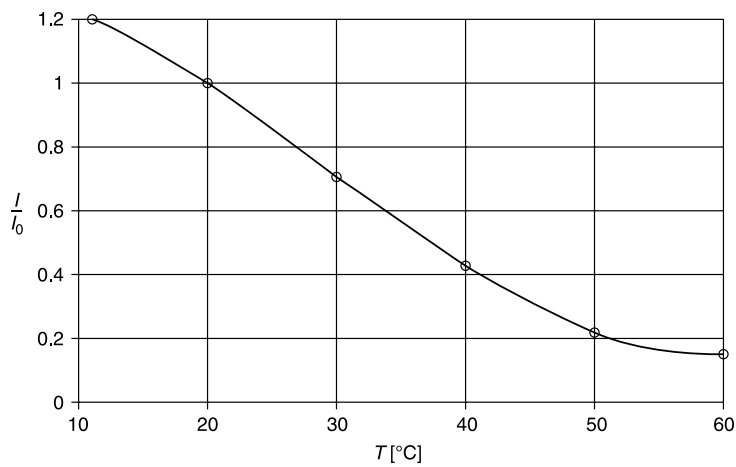

Figure 5.4 Excitation and emission spectra of a TSP

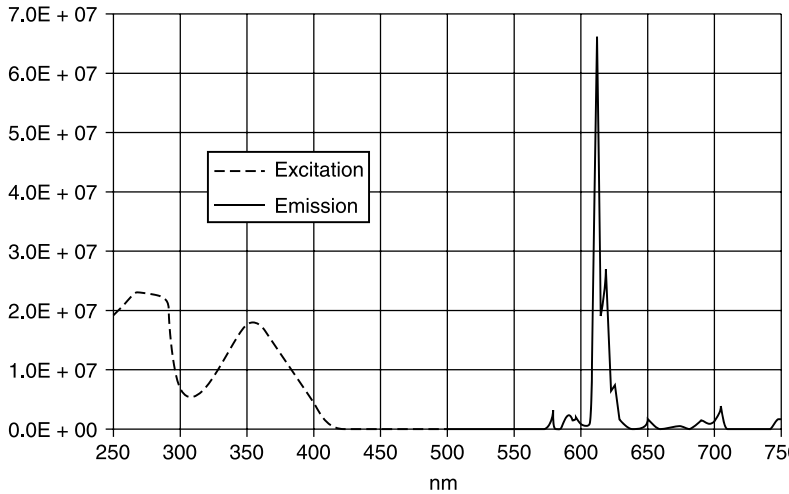

different from that of the exciting light, for example (Figure 5.4), a paint excited with ultraviolet light (280 ÷ 390 nm) emits red light (580 ÷ 630 nm). This feature makes it possible to filter the incident light and measures only the emitted light. Paints have been developed to measure temperatures ranging from ambient up to 1000°C.

The application of the method is subject to some restrictions:

- The thermal properties (emissivity and heat transfer) of the surface can be altered by the coating.
- The need to work in a darkroom or with low light imposes restrictions in applications, but ambient light, as well as exciting light, can be filtered out.
- The response times of phosphorescence to changes in temperature are important in the study of transient phenomena, they differ greatly from one paint to another but are low enough for phosphorus of the type ZnS–CdS. With a moderately strong ultraviolet excitation, such as that produced by a mercury arc lamp, it is suggested that the response time is less than 0.3 s.

5.1.3 Measurement of infrared radiation

The surface temperature of opaque bodies can be calculated by measuring the intensity of the emitted radiation which increases with the fourth

Figure 5.5 Spectrum of electromagnetic radiation

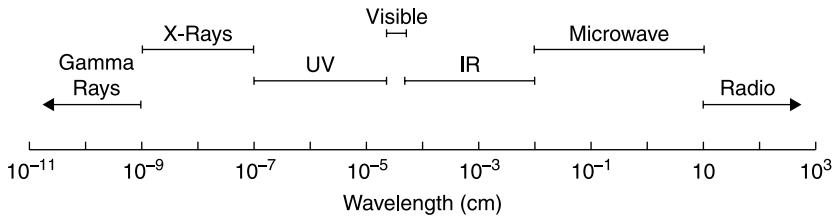

power of the body temperature. The range of wavelengths involved (Figure 5.5), $\lambda = 0.45 \div 100$ μm, goes from the visible, $0.45 \div 0.75$ μm (high temperatures), to the infrared (down to temperatures below ambient temperature).

This type of measurement overcomes some of the difficulties typical of diagnostic methods discussed in the previous paragraphs:

- no alterations of the surface of the model is induced;
- the sensitivity is in the order of tenth of *K*.

The relationship between the temperature of an object and the radiation received by the detector depends on the emissivity of the surface and on the absorption of the optical system: for each model and for each type of test, a prior calibration is therefore needed, for example, using thermocouples embedded in the surface of the model.

In the measurements with infrared camera, both optics and windows of the wind tunnels are critical because glass and quartz cannot be used, being both opaque to infrared radiation. Lenses are usually made of expensive germanium; cheaper materials quite transparent to infrared radiation are lucite, silicone and Domopak film.

The sensors used are indium antimonide (InSb), sprite (HgCdTe), lead selenide (PbSe), covering the field $2 \div 13$ μm: these are therefore suitable for measuring temperatures from 200 *K* to 2000 *K* (with appropriate filters). Since the sensitivity of these sensors increases when their operational temperature decreases, they should be kept at temperatures well below ambient. The different techniques used are:

- cooling with liquid nitrogen at about 80 *K*; liquid nitrogen is difficult to maintain for a long time, not more than 2 hours, so the system is reserved for fixed installations in scientific laboratories;
- cooling to 90 *K* by expansion of compressed argon (Joule–Thomson effect); the argon can be kept easily in cylinders and, unlike liquid nitrogen, its consumption is zero when the thermograph is not used;

- cooling to 70 ÷ 90 *K* with a Stirling pump which, in a closed circuit, compresses and expands helium; the circuit needs to be recharged only after a few thousand hours, the system is therefore suitable for field measurements;
- cooling to 200 *K* with a thermoelectric (Peltier) circuit (thermocouple, in which a potential difference is applied and a temperature difference between junction and reference is obtained), the system is particularly suitable for surveillance cameras on a continuous basis.

If only one sensor is used, it is necessary to send on it in succession signals from each point of the field, i.e. a mechanical scanning of the image is needed. In Figure 5.6, an image of the field is produced by a spherical mirror of 200 mm diameter oscillating 16 times per second around a horizontal axis combined with a prism rotating at 400 revolution/second around a vertical axis; horizontal and vertical scanning, respectively, are performed in this way and the infrared radiation from each pixel is focused in turn on a single indium antimonide (InSb) sensor. The sensor converts thermal radiation into an electrical signal that is used to modulate the intensity of the beam of a cathode ray tube: the vertical position of the beam is synchronized with the position of the oscillating mirror and the horizontal position is synchronized with the rotating prism, each pixel of the field is thus transformed into a corresponding

Figure 5.6 Schematic of AGA thermograph ThermoVision 750

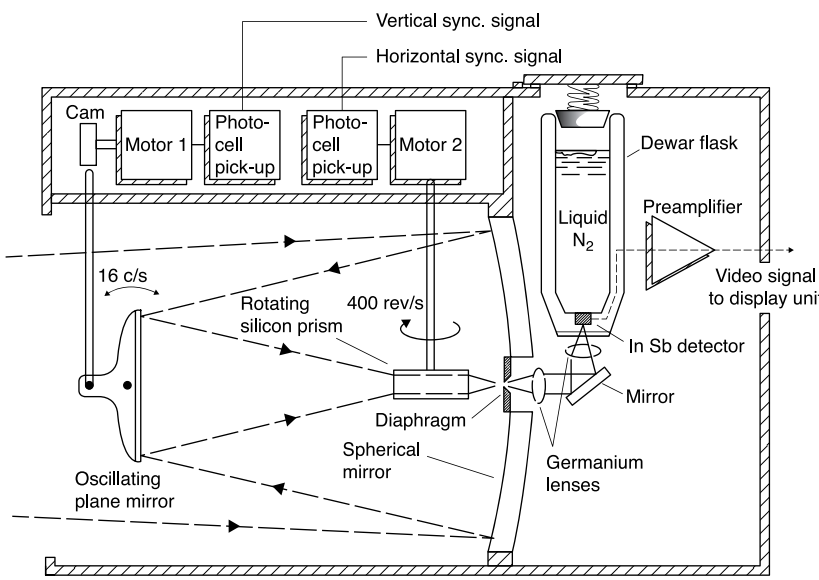

Figure 5.7 Thermographic image of a space shuttle in a hypersonic wind tunnel

pixel of the video screen. With this system, 16 images per second can be obtained.

To increase the frequency of images, multiple sensors can be used arranged in a row to eliminate the vertical scanning: with 10 ÷ 30 sensors and a rotating polygon with 8 ÷ 10 faces 30 images per second can be obtained. The most recent version of the camera provides in the focal plane of the objective a matrix of 320 × 240 uncooled microbolometer (768,00 pixels): 60 images per second are obtained. The resolution of the cameras is about 0.1 *K*, the error is of the order of 2% or 2 *K* (the larger of the two values).

The thermographic image of a model space shuttle in a hypersonic wind tunnel is shown in black and white in Figure 5.7.

5.2 Detection of transition

Transition from a laminar to a turbulent boundary layer can be detected by the increases in adiabatic wall temperature and/or film coefficient. These methods are additional to those listed in Chapter 6 (visualization methods, optical methods), to the measurement of stagnation pressure at

a fixed distance from the wall or to the measures of turbulence in the boundary layer with anemometers (Chapters 3 and 4).

5.2.1 Measurement of the temperature recovery factor

The adiabatic wall temperature is usually expressed in a non-dimensional form, *temperature recovery factor*, r, defined as the ratio between the actual rise in temperature of the adiabatic wall with respect to the static temperature of the stream ($T_{aw} - T_\infty$), and the temperature rise that would occur if the flow were stopped isoentropically ($T_{0\infty} - T_\infty$). The temperature recovery factor can be expressed in terms of the Mach number, the adiabatic wall temperature and the stagnation temperature as follows:

$$r = \frac{T_{aw} - T_\infty}{T_{0\infty} - T_\infty} = \frac{\dfrac{T_{aw}}{T_{0\infty}}\left(1 + \dfrac{\gamma - 1}{2} M_\infty^2\right) - 1}{\dfrac{\gamma - 1}{2} M_\infty^2} \tag{5.1}$$

The recovery factor depends only on the Prandtl number, $\mathrm{Pr} = C_p \mu / \lambda$ where C_p [$JKg^{-1}K^{-1}$] is the specific heat at constant pressure. The Prandtl number is a measure of the relative importance of the dissipation of kinetic energy due to the dynamic viscosity, μ [$Kgm^{-1}s^{-1}$], and the heat conduction due to the coefficient of conductivity, λ [$JK^{-1}m^{-1}s^{-1}$]. In the boundary layer the viscous stresses tend to increase the local temperature to a greater extent when the shear rate is strongest (near the wall), the conductivity creates a heat flow toward the colder areas (furthest from the wall) which makes the temperature near the wall to decrease. For gases, which have $\mathrm{Pr} < 1$, the second effect is more important than the first one, therefore the resulting adiabatic wall temperature is lower than the stagnation temperature.

Equations linking the recovery factor to the Prandtl number are different according to the regime of flow, laminar or turbulent. For a flat plate:

$r = \sqrt{\mathrm{Pr}}$ in the laminar regime,

$r = \sqrt[3]{\mathrm{Pr}}$ in the turbulent regime

Because, for air, Pr < 1, the recovery factor is higher in the turbulent than in the laminar flow regime usually passing through a maximum in the region of transition.

If the transition from laminar to turbulent boundary layer occurs, there are conditions for non-uniform wall temperature on the body and heat flows from the turbulent zone to the laminar zone, leveling out the temperatures (the brass wall in Figure 5.8). In order to measure the true adiabatic wall temperature, care must be taken to minimize the effects of conduction along the wall: the model must therefore be made of an insulating material (the lucite wall in Figure 5.8).

Since the position of the transition, namely the critical Reynolds number, depends also on the intensity of turbulence of the incoming stream, sometimes to determine the quality of a supersonic or hypersonic wind tunnel *transition cones* are used with apex angles of 5° or 10°. The procedure consists of measuring the critical Reynolds number for the whole range of Mach numbers and Reynolds numbers of the wind tunnel and comparing the data obtained with those of similar wind tunnels. Then it can be decided if additional turbulence screens or other modifications of the wind tunnel are needed.

Figure 5.8 **Temperature recovery factor on a 40° cone cylinder**

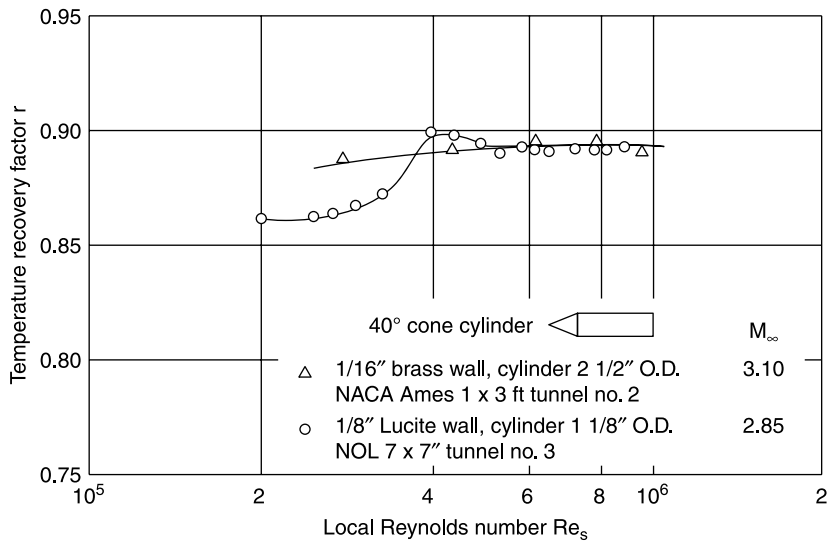

Source: [1]

Figure 5.9 Schematic of the transition cone JPL

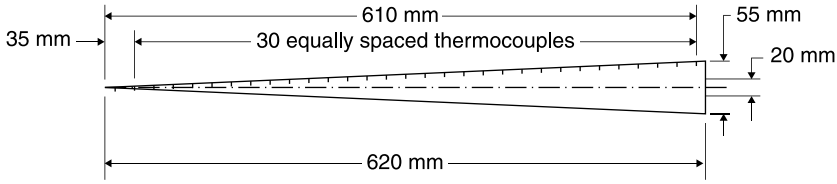

Source: [2]

To apply this technique, the cone should have:

- dimensions such that local Reynolds numbers between 2×10^6 and 7×10^6 can be generated on the surface;
- low heat capacity;
- very accurate surface finish.

The cone of Figure 5.9 is hollow and made of fiberglass, except the tip that is made of steel. Thirty copper–constantan thermocouples are arranged on the surface at intervals of 2 cm. The surface is covered with several layers of plastic coating, straightened and painted.

The cone is calibrated in an oven to check that all the thermocouples are working and that their readings are uniform. Once inserted in the wind tunnel and the test has been carried out, the readings of the thermocouples are converted into temperature recovery factor, r, by Equation (5.1). The typical result of a test is shown in Figure 5.10. In the first part of the cone, where the flow is laminar, the temperature recovery factor has a value of about 0.85, in transition a maximum value of about 0.894 is attained and finally it stabilizes at the turbulent value (0.886).

Figure 5.10 Determination of the critical Reynolds number in a wind tunnel with a transition cone

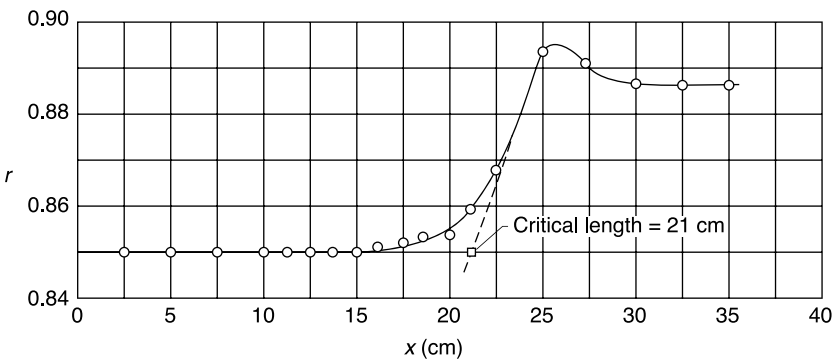

Source: [3]

Note: Unit Reynolds number in the test chamber = 1.4×10^7 m^{-1}; Recr = 3×10^6.

It should be noted that there is not unanimity in the choice of the characteristic length to be used in calculating the critical Reynolds number. The different methods can lead to variations of $l \div 2 \times 10^6$ in the calculation of Re_{cr}.

5.2.2 Measurement of the coefficient of heat transfer by convection

A non-dimensional expression of the film coefficient h [$\mathrm{Jm^{-2}s^{-1}}$] should be used, for example the Nusselt number ($Nu_x = hx/\lambda$) or the Stanton number ($St = Nu_x/\mathrm{Re}_x\mathrm{Pr}$), because numbers can be conveniently expressed in terms of other characteristic numbers. For example, for a flat plate in a gas stream ($\mathrm{Pr} \approx 1$):

$$Nu_x = 0.332\left(\mathrm{Re}_x\right)^{1/2}\left(\mathrm{Pr}\right)^{1/3} \text{ laminar boundary layer}$$

$$Nu_x = 0.0296\left(\mathrm{Re}_x\right)^{0.8}\left(\mathrm{Pr}\right)^{1/3} \text{ turbulent boundary layer}$$

By the change of Nusselt number with the abscissa, the transition from laminar to turbulent regime can be determined. The measurement of h can be made with an *unsteady method*.

In a hypersonic flow, a body, which initially is at room temperature, undergoes aerodynamic heating, the temperature rises very quickly at the beginning then more and more slowly as the difference between the wall temperature and the adiabatic (or recovery) wall temperature decreases. If the model is made with an insulating material, the temperature of each point of the model tends asymptotically to the value of the local adiabatic wall temperature (Figure 5.11).

If the wall temperature is measured with a thermocouple using the technique in Figure 5.2, with the wall made of an insulating material, it can be assumed that all the energy exchanged by convection through the metal disk of area A goes to increase the internal energy of the metal plate to which the thermocouple is welded. The coefficient of heat transfer by convection, h, can be obtained from the unsteady energy balance:

$$\dot{q}A = hA\left(T_{aw} - T_w\right) = mc\frac{dT_w}{dt}$$

$$h = \frac{mc}{A}\frac{dT_w/dt}{T_{aw} - T_w}$$

Figure 5.11 Determination of the coefficient of heat transfer by convection with the unsteady method

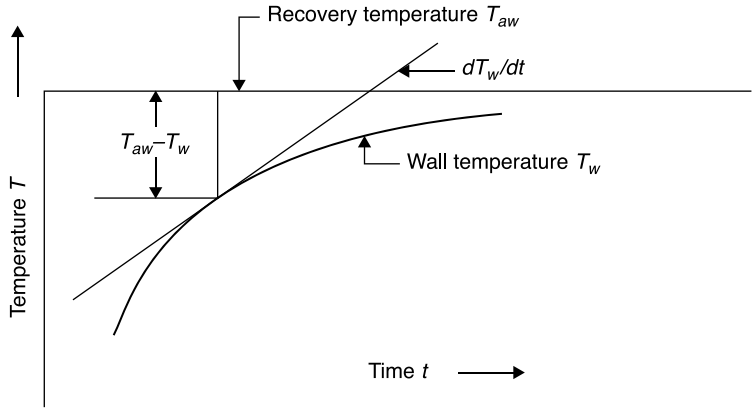

where m is the mass of the disk, c the specific heat of the wall and dT_w/dt the slope of a plot T_w (t) obtained in the measurement (Figure 5.11).

When the flow is not hypersonic, this technique can be still applied, up to Mach numbers close to zero, by a prior heating or cooling of the body with respect to the stream temperature. For $M \to 0$, static temperature coincides both with the stagnation temperature and with the adiabatic wall temperature.

5.3 Measurement of stagnation temperature

The importance of knowing the static temperature of the stream is obvious, considering that internal energy, conductivity, viscosity, specific heat, speed of sound all depend on temperature. Unfortunately, the measurement of static temperature is not possible in a compressible flow since whatever instrument is immersed in the stream, it is surrounded by a boundary layer in which the temperature rises above the stream temperature (remember that, vice versa, it is possible to measure the static pressure of the stream through a hole in the wall, see Chapter 2, since the static pressure remains unchanged in the boundary layer).

Excluding the possibility of making a thermometer run with the same speed of the stream, the static temperature can be determined only indirectly, once one has measured the stagnation temperature, by the equation

Figure 5.12 **Schematic of a probe for measuring the stagnation temperature**

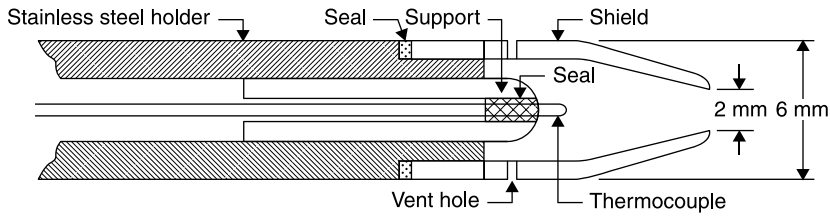

Source: [4]
Note: Screen and support are made of silicon. The exposed surfaces are mirrors. The J-type thermocouple is 0.25 mm in diameter, insulated with fiberglass. Two vents.

$$T_\infty = T_{0\infty}\left(1+\frac{\gamma-1}{2}M_\infty^2\right)^{-1}$$

A probe consisting of a Pitot tube containing a thermocouple (Figure 5.12) and systems to minimize losses by conduction and radiation can be used to measure the stagnation temperature. Despite the best planning procedures, the probes will still read a temperature lower than stagnation temperature and, unfortunately, the correction varies appreciably with temperature, the Reynolds number and the Mach number.

Heat losses are in general: 80% by conduction and radiation from the shield, 15% by conduction from the base, 5% for conduction through the thermocouple wires, but they can change dramatically with changes in the design of the probe. The effectiveness of such a probe is usually defined on the basis of a recovery factor, r, given by:

$$r = \frac{T_m - T_\infty}{T_{0\infty} - T_\infty}$$

where T_m is the measured temperature. The following conditions will apply:

- *Shape of the probe*: The chamber has an opening in the front for the thermocouple and ventilation holes immediately downstream of the thermocouple. The walls of the chamber are mirrors to reduce heat losses by radiation from the junction of the thermocouple.
- *Temperature sensor*: Any thermocouple capable of withstanding the temperatures to be measured can be used. The junction should be far away from the support so as to leave a long section of the wires exposed to hot air to reduce losses by conduction. The heat capacity of

the junction should be as small as possible to reduce the response time of the probe.

- *Anti-radiation shield*: An anti-radiation shield must surround the temperature sensor. The temperature of the shield is different from that of the sensor and therefore the temperature measured is influenced by heat transfer by radiation. To minimize this effect, the shield must have low conductivity, like the silicon shield in Figure 5.12, and the surface must be a mirror. The effectiveness of the shield can be enhanced by heating it or by using multiple shields (up to five).
- *Ventilation holes*: As the air temperature in the stagnation chamber of the probe tends to decrease, due to conduction and radiation, it is necessary to provide vent holes to continuously replace the air in the chamber. When it is necessary to measure temperature fluctuations, the exchange of air helps in not damping fluctuations. The best ratio between area of the holes and entrance area of the probe, A_V/A is a function of heat loss and should still be small so that air does not assume appreciable speed. Usually this ratio varies between 0.2 and 0.4.
- *Effects of Reynolds and Mach numbers*: The presence of a normal shock wave at the entrance of the probe does not alter the value of the stagnation temperature. Obviously the performance of the probe deteriorates with increasing temperature (increasing losses due to all types of heat transfer): Figure 5.13 illustrates the typical decrease of

Figure 5.13 **Effects of Reynolds and Mach numbers on the recovery factor of a stagnation temperature probe**

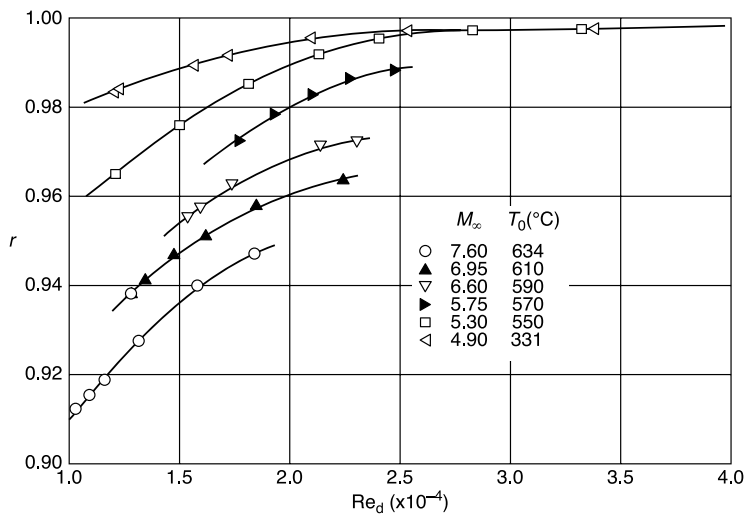

the recovery factor with decreasing Reynolds number and with increasing Mach number. Figure 5.14, derived from the data of Figure 5.13, shows the rapid decrease of the recovery factor that occurs when the Mach number exceeds the value 5. It can be concluded that in a supersonic wind tunnel ($M < 5$), a probe with a single shield has a recovery factor very close to 1 if the Reynolds number of the probe is greater than 20,000. For hypersonic wind tunnels ($M > 5$), probes can be made more accurate using small heating elements and thermocouples in the base of the probe, with additional heaters and thermocouples on the inner side of the shield. This will provide heating to balance the losses: in practice, the base is heated until it reaches the

Figure 5.14 **Probe for measuring the stagnation temperature: decrease of the recovery factor with temperature and Mach number**

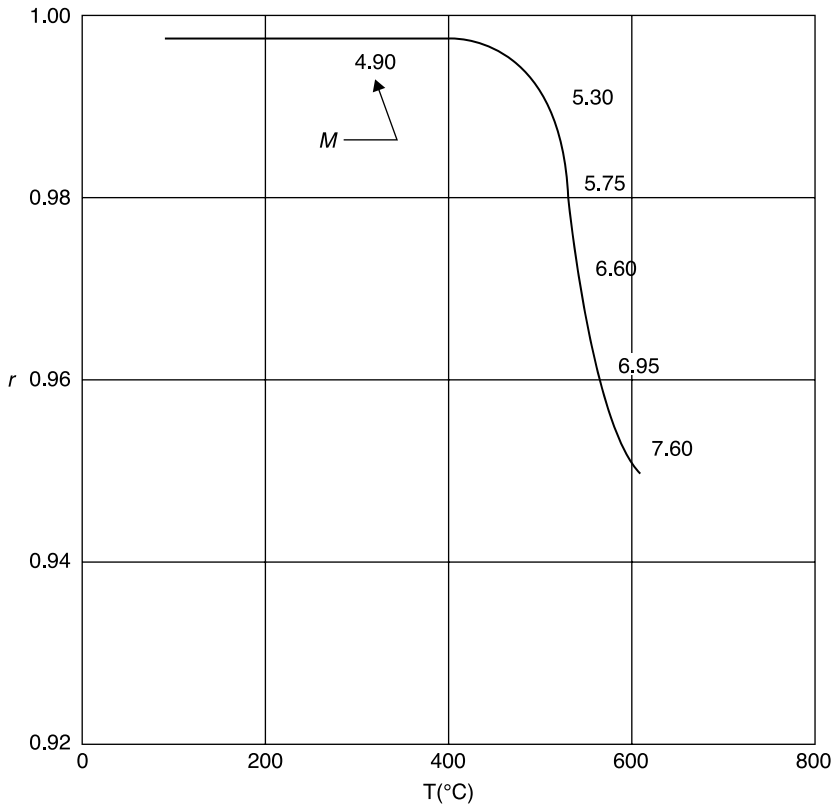

Source: [4]
Note: Re_d = 20,000. Probe with a single screen

same temperature as the main thermocouple and subsequently the shield is heated until its internal temperature is equal to that of the thermocouple. After another balancing all the temperatures are equal and the losses by conduction and radiation are zero (recovery factor equal to one).

References

1. G.R. Eber (1954) "Wall temperature determination on conducting and insulating material, D" in Part 1 of *Physical Measurements in Gas Dynamics and Combustion*, R. Landenburg ed., vol. IX of *High Speed Aerodynamics and Jet Propulsion*, Princeton, NJ: Princeton University Press.
2. F. Hugh (1959), "*Transition Reynolds number Measurements in the CWT Supersonic Cart Using a 5-Degree Cone*," Cooperative Wind Tunnel Report K-329, July.
3. A.O. Ross (1953) "Determination of Boundary-Layer Transition Reynolds Numbers by Surface-Temperature Measurement of a 10° Cone in Various NACA Supersonic Wind Tunnels," NACA Tech. Note 3020.
4. E.M. Winkler (1954) *Stagnation Temperature Probes for Use at High Supersonic Speeds and Elevated Temperatures*, NAVORD Report 3834.

6

Flow visualization

Abstract: This chapter highlights flow visualization methods; special emphasis is devoted to optical methods that can be used when density changes are present due to changes in temperature and/or composition of the fluid or to high Mach numbers of the stream (compressible flow).

Key words: hydrogen bubble, interferometer, Schlieren, shadowgraph.

6.1 Objectives of the visualization

Flow visualization provides information on the whole flow field immediately understandable without the need for data processing. Since air and water are transparent, the flow field can be made visible only indirectly and therefore one of the following techniques is needed:

- light scattering by gaseous, solid or liquid particles seeded in the stream;
- behavior of materials deposited on the surface of the body immersed in the flow;
- changes of the refractive index produced by changes in density (*optical methods*).

Pressure- or temperature-sensitive paints, liquid crystals, infrared thermography and particle image velocimetry cannot be considered as visualization methods since they are true measurement techniques.

6.1.1 Streamlines of the external field

Visualization of the external field is particularly interesting when there is separation of the boundary layer or in general when the flow is three-dimensional. If the flow is unsteady, it can be defined as:

- *Streamlines*: lines tangent to the direction of the instantaneous speed; these cannot be visualized.
- *Pathlines*: all points crossed in time by each particle; these can be visualized with long exposure photography.
- *Streaklines*: instantaneous positions of all the particles that have passed through given points; these can be visualized with low exposure photography.

Only if the flow is steady do streamlines, pathlines and streaklines overlap, and the streamlines can be visualized.

The techniques for displaying streamlines in a plane containing the velocity vector make use of particles carried by the stream:

- *in air*: smoke from wood, charcoal, incense or tobacco, vapor of mineral oil or steam produced by dry ice + hot water;
- *in water*: hydrogen bubbles, inks, particles of aluminum, lycopodium or coffee.

To visualize the streamlines in a plane orthogonal to the direction of the asymptotic velocity, flakes of wool or silk linked to screens are placed across the stream or smoke or vapor illuminated by a light sheet normal to the direction of motion is used.

6.1.2 Streamlines on the surface of a body

In three-dimensional flows, streamlines near a solid surface can be very different from those of the external stream. Surface streamlines can also be very complicated in the zone of the boundary layer, separation and near obstacles on the surface and below a vortex.

Particles or wool tufts can be used as for the external stream but it is much more appropriate to spread a non-volatile liquid (oil), possibly with the addition of dyes, on the surface: oil moves under the action of tangential stresses and then in the direction of streamlines that appear as streaks in the oil film.

6.1.3 Transition and separation of the boundary layer

Apart from the study of laminar profiles, the main reason for the interest in knowledge of the *transition* is in monitoring the effectiveness of transition strips. Diffusive flows of mass, momentum and energy in the boundary layer increase more or less abruptly in the transition from the laminar to the turbulent regime.

In the zones of *separation* tangential stresses (diffusive flows of momentum) decrease to zero and become negative.

- The variations in tangential stresses can be highlighted by covering the body with a film of non-volatile liquid.
- The different diffusion of mass in laminar and turbulent zones may be shown by making use of the sublimation of a solid, such as naphthalene, or the evaporation of a liquid, as in the china clay method.
- The different diffusion of energy can be highlighted with heat-sensitive coatings.

6.1.4 Changes in density

The density variations in a fluid can be visualized using the optical methods (shadowgraph, Schlieren and interferometry), which highlight the changes in the refractive index of the fluid. These methods furthermore allow measurements of density (especially interferometry). These optical methods, besides being non-intrusive and giving a global view of the flow field, as do all methods of visualization, have peculiar advantages and disadvantages:

- The inertia of the system is practically zero, the study of unsteady motions is possible with the temporal discrimination allowed by the speed of the shut-off system (camera, video camera). This feature is particularly useful in supersonic wind tunnels and even more in hypersonic ones in which the duration of the tests is very short.
- Optical methods are able not only to visualize streams at Mach numbers lower than those considered typical of compressible aerodynamics, but can also visualize changes in fluid density due to heat transfer or mass diffusion.
- All optical methods give the value of the density variations integrated along the optical path; increasing difficulties are encountered in

interpreting the images going from two-dimensional plane fields to axially symmetric fields and to three-dimensional fields.

- Limits on these methods are low density hypersonic motions and low density gradients.

6.2 Visualization techniques

6.2.1 Wool or silk tufts

Wool, silk or nylon tufts 5 ÷ 15 mm long are glued at one end on the surface of the model and the other end is left free. If the position of the tufts has to be often changed, scotch tape can be used to fix the tufts to the model. The presence of the tufts can be a trigger for a premature transition so the tufts should be placed gradually from the trailing edge, checking whether the inclusion of new rows of tufts affects the downstream conditions.

If the tufts are short enough not to interfere with the external field, it is easy to interpret their behavior: the presence of a turbulent boundary layer is highlighted by a lively movement of the tufts, the separation of the boundary layer is highlighted by the tendency of the tufts to move violently and to rise from the wall pointing upstream (Figure 6.1 b).

Figure 6.1 **Flow on a delta wing visualized with silk tufts**

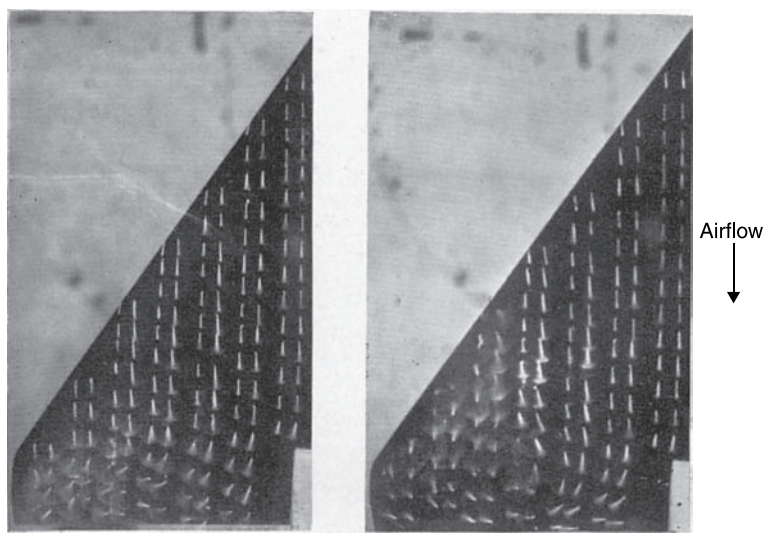

(a) $C_L = 0$ (b) $C_L = 0.34$

Figure 6.2 Vortices downstream of a delta wing visualized with tufts mounted on a grid across the test chamber

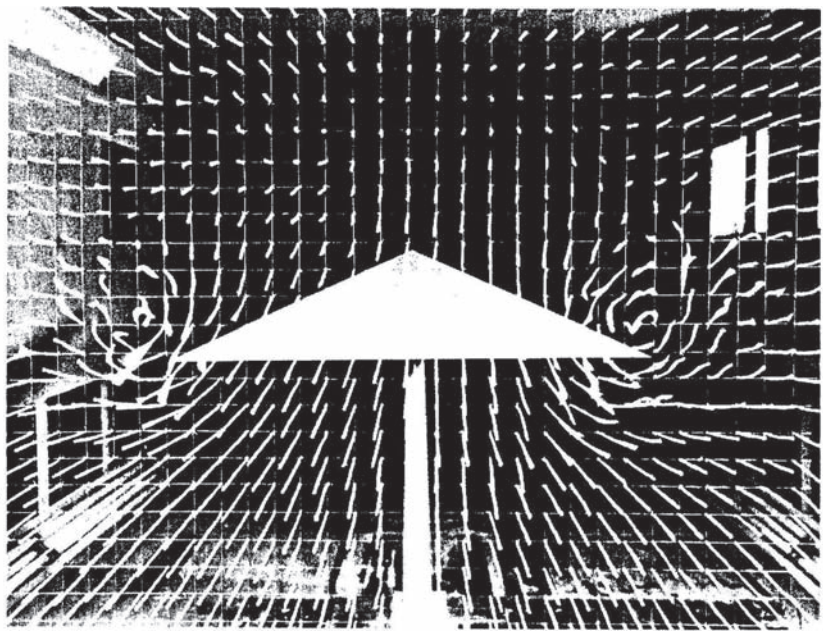

Source: NASA

In order to visualize the external flow, the tufts must be supported by a grid perpendicular to the stream: in Figure 6.2, the free vortices downstream of a delta wing at incidence are shown.

6.2.2 Solid particles floating on a liquid

Many basic aerodynamic experiments were conducted by Prandtl and co-workers by moving the models in tanks containing water. Very fine particles of aluminum or coffee or lycopodium may be used to visualize streamlines, separation of boundary layer and eddies that are generated on the model partly submerged in the liquid. The vortices that are generated downstream of a cylinder moving in a liquid, photographed with a long exposure, are shown in Figure 6.3.

Figure 6.3 Vortices downstream of a cylinder visualized with aluminum powder

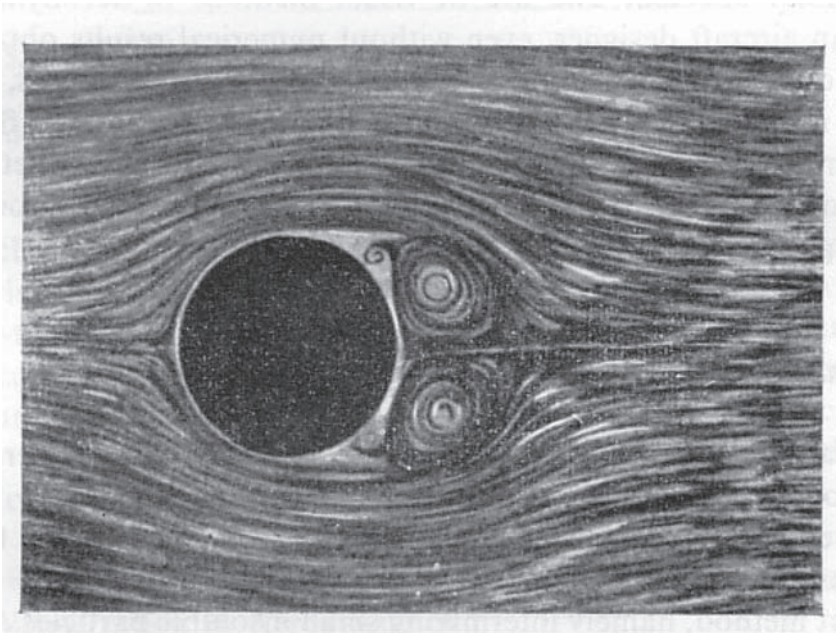

6.2.3 Smoke

The smoke consists of a suspension of solid and/or liquid particles in a gas. The required characteristics of smoke in wind tunnel applications are:

- must not form deposits on the model or in the pipes that lead to the injectors;
- must have a density similar to that of air: in this way, the effect of buoyancy is null;
- must be clearly visible, non-poisonous, and non-corrosive;
- must be inexpensive, easily produced and controllable.

The most common methods used to produce smoke are based on the combustion of organic materials or the evaporation of a liquid. Combustion involves long preparation time and the production of solid particles forming deposits. The preferred option is the evaporation of mineral oil (e.g. kerosene) that is heated by the Joule effect in an apparatus designed by Preston and Sweeting (Figure 6.4), which is operational in

Figure 6.4 A mineral oil vapor generator

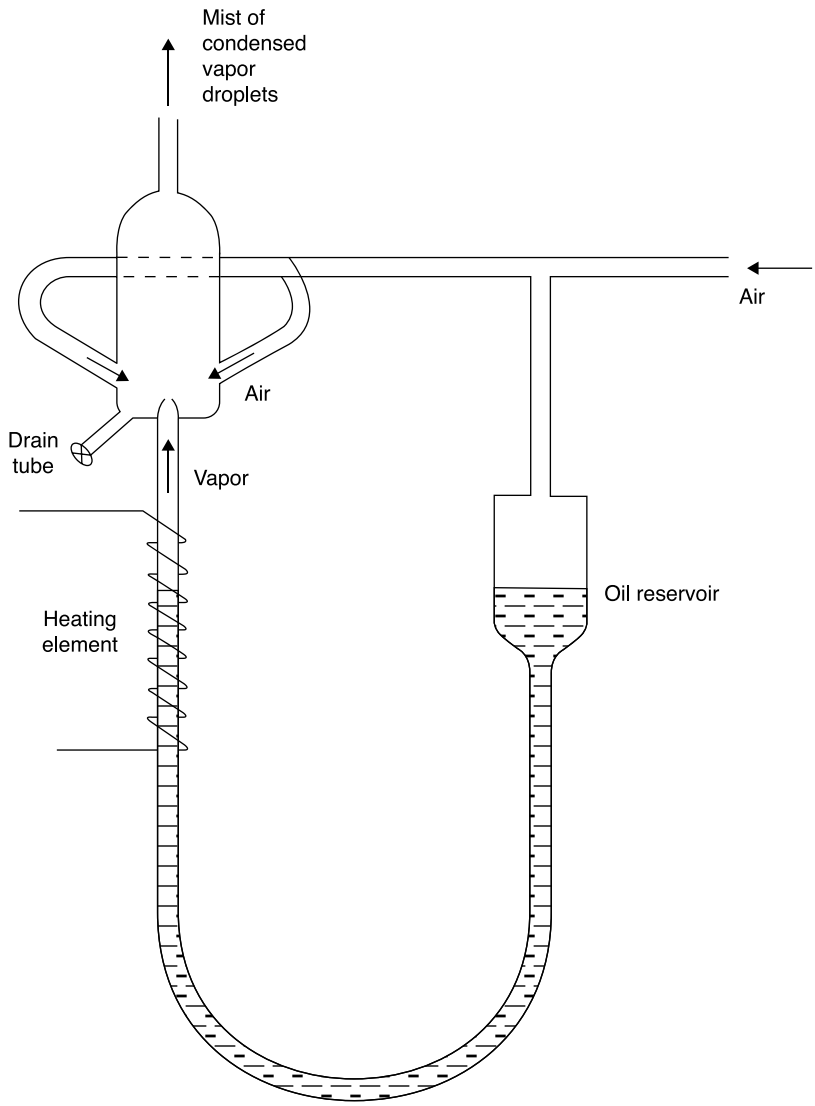

about 5 minutes. The adjustment of the flow of smoke to be sent to the injector is achieved by regulating the flow of air that feeds the apparatus. Sometimes the air supply is drawn from the stream in order to obtain the automatic adjustment of the injection rate of smoke to the varying speed of the stream.

The main problem presented by the technique of injecting a thread of smoke or vapor into a stream of air, or ink in a stream of water, is the

Figure 6.5 A smoke wind tunnel

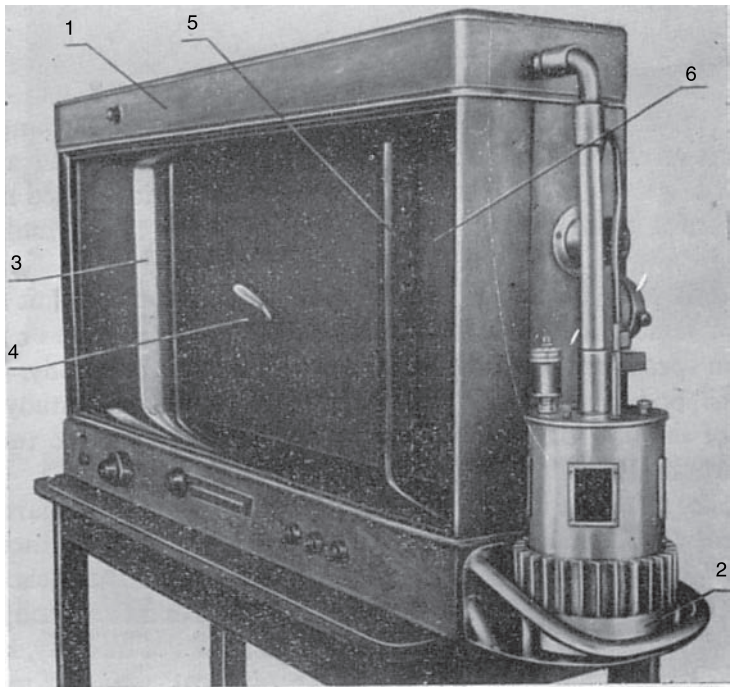

need not to disturb the flow. On the other hand, if well-defined filaments are needed, it is necessary that the injection speed be equal to that of the stream and at the same time that the wake produced by the injector not be turbulent. The latter requirement limits the applicability of the method at very low speeds in order to keep the Reynolds number of the injector below the critical value.

In air, the technique is used in special smoke tunnels, used for pedagogical purposes (Figure 6.5): to obtain a good contrast with the smoke filaments, one of the side walls of the test chamber is black and a system of lamps illuminates the model from above and from below. The streamlines on a stalled airfoil visualized with this technique are reported in Figure 6.6. In this case, the smoke is injected through a comb of injectors upstream of the test chamber.

6.2.4 Hydrogen bubbles

If a difference of potential is applied between a metallic wire immersed in a stream of water and a metal plate on the bottom of the channel, by

Figure 6.6 Stall of an airfoil visualized with smoke filaments

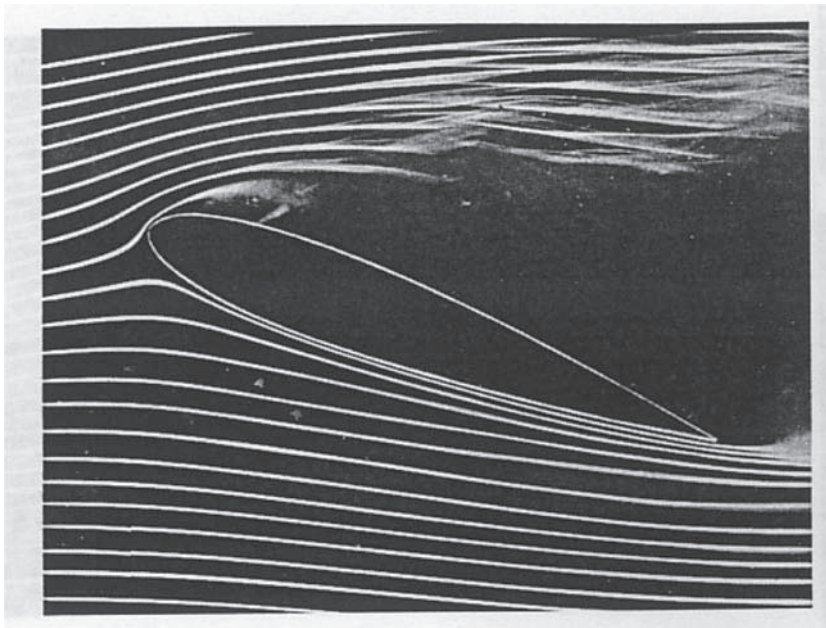

electrolysis of water from the wire, a continuous stream of bubbles of hydrogen or oxygen is generated, depending on the sign of the difference of potential applied. It is preferred that the wire is the cathode since the amount of bubbles of hydrogen produced is twice that of oxygen. Wires with a diameter of the order of hundredths of millimeters are used so that the bubbles, which have a size comparable to the diameter of the wire, do not rise too quickly to the surface. Adding an electrolyte to water is not strictly needed because the usual presence of salts dissolved in tap water is sufficient; anyway sodium chloride or sodium sulfate can be added to water. The applied voltages are 100–200 V.

If the cathode is a thin wire normal to the direction of the stream and a short electrical pulse is applied, a line of hydrogen bubbles is generated along the wire (Figure 6.7).

With a power supply pulsed with a constant frequency, successive lines of bubbles are obtained separated by a constant time interval (*time lines*). These lines are carried by the stream and deform according to the profiles of local speed.

Also, if the wire is partially covered with an insulating varnish, emission of bubble packs can be achieved which provide an indication of the speed profiles in the stream (Figure 6.8). The time period during which the

Figure 6.7 Time lines generated with hydrogen bubbles

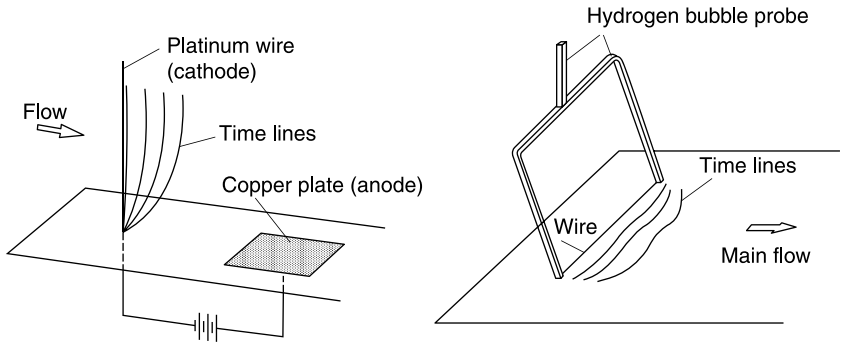

Source: [1]

bubbles survive in the stream is limited. The spread of bubbles increases with the Reynolds number and is very rapid in turbulent flow. The application of the method is therefore limited to very slow streams, with speeds of the order of 20–30 cms^{-1}.

6.2.5 Oil film

The use of a film of a non-volatile liquid is based on the principle that the film moves in the direction of the tangential stresses acting on the model.

Figure 6.8 Velocity profiles in a contraction obtained with packs of bubbles

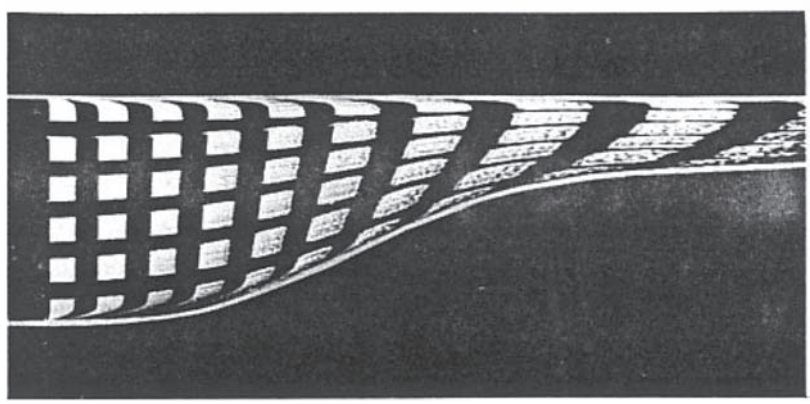

Source: [2]

The technique is particularly suitable in visualizing surface streamlines (Figure 6.9) and flow separation (Figure 6.10). The transition can be detected as the surface stresses may be able to remove the fluid in the turbulent zone, while the laminar zone remains wet (Figure 6.11). Alternatively, before the liquid is swept away by the turbulent region, a difference can be observed in the shape of the waves on the surface of the liquid with respect to those formed in the laminar region: the wavelength is greater in the turbulent region. The latter method can be used in tests of short duration in intermittent tunnels.

The viscosity of the liquid should be chosen as a function of the speed of the tunnel and the duration of the test: the maximum viscosity is

Figure 6.9 Streamlines on a delta wing visualized with an oil film (lampblack + kerosene)

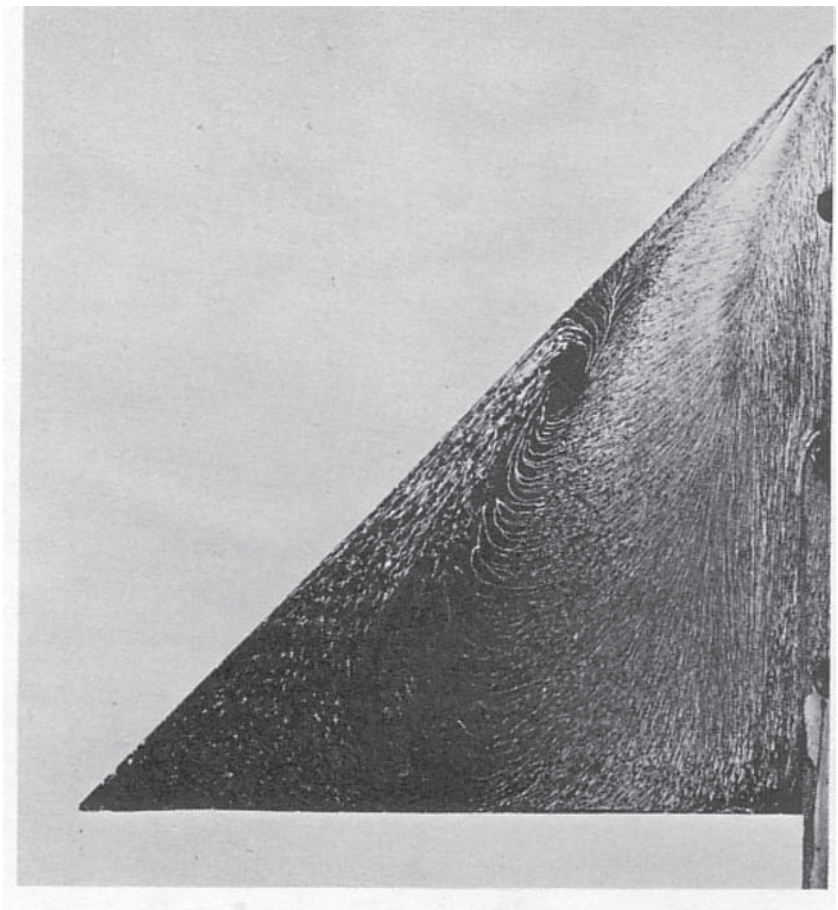

Figure 6.10 Flow separation on a sweptback wing of an orbiter model visualized with an oil film

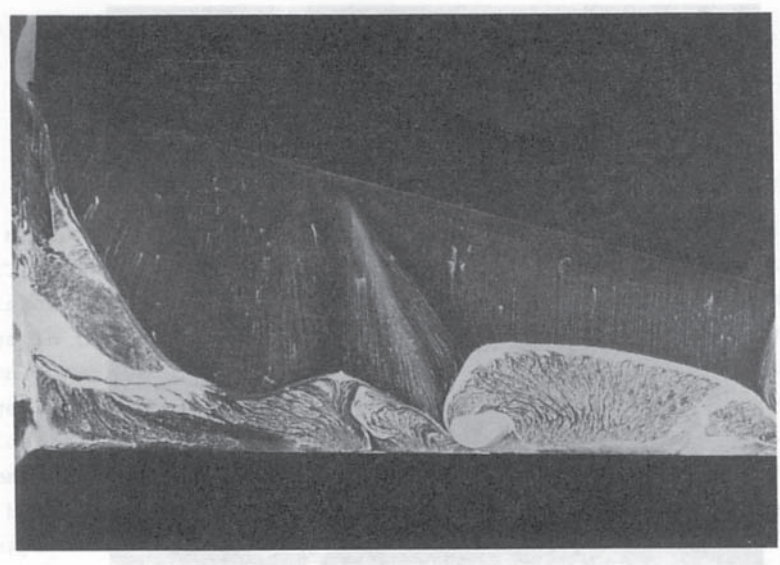

Source: NASA, Ames Research Center

Figure 6.11 Boundary layer transition on a double delta wing visualized with oil and titanium dioxide

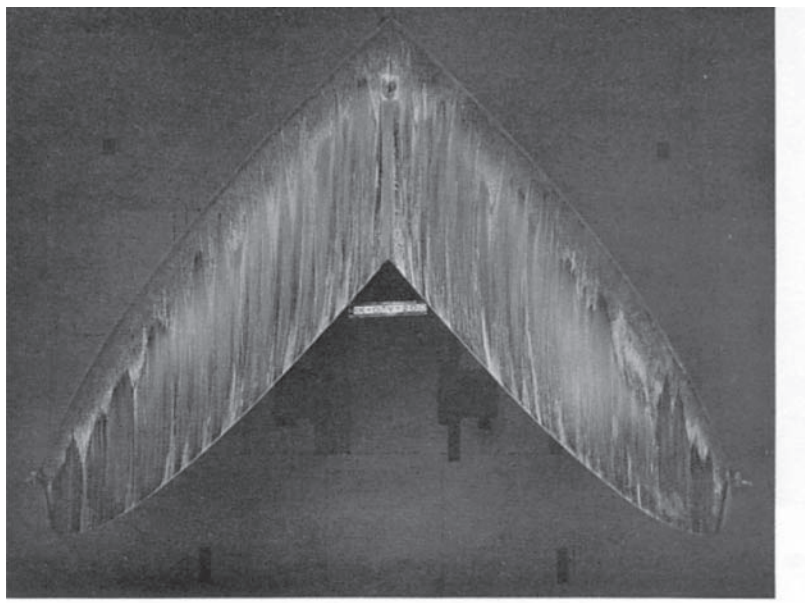

required in tests in continuous supersonic wind tunnels. At low speeds wind tunnels are most suitable, in order of increasing viscosity: kerosene, light diesel oil, light oil for transformers. In high speed wind tunnels, often the static pressure in the test chamber is so low that liquids with high vapor pressure tend to evaporate; in these cases, oil for vacuum pumps must be used. In cryogenic wind tunnels, liquids with a low freezing point such as propane must be used.

The heavy mineral oils suitable for high speed wind tunnels are naturally fluorescent and can therefore be observed with a good contrast illuminating them with ultraviolet lamps; lighter oils can be made more observable using fluorescent additives.

An alternative is the addition of pigments: lampblack on clear models, white pigments such as titanium dioxide (Figure 6.11) or kaolin on dark models. An additive, e.g. oleic acid to titanium dioxide, is usually used to control the flocculation of the paint. One advantage in using the oil–lampblack mixture is the fact that it can be stored in bottles for an indefinite time. The mixture of titanium dioxide or kaolin and oil is instead a real paint: it tends to dry in the air and therefore it must be prepared just in time for each test.

To avoid the parallax error that would be made if photographing curved surfaces, the model can be covered with a self-adhesive plastic-coated white paper on which the oil–lampblack mixture is applied; after the test, the paper is removed and made plane before photographing. Alternatively, on completion of the test, the produced pattern is removed with a transparent adhesive sheet that is then photographed and possibly stored for later analysis.

6.2.6 The china clay method

This is the most effective evaporative method, developed at the National Physics Laboratory in the UK during the Second World War: the model is sprayed with a transparent cellulose adhesive containing suspended powdered kaolin (china clay); when the glue is dry, the model surface is accurately smoothed and becomes permanently white. If a liquid with a similar refractive index is sprayed onto the kaolin (with refractive index $n = 1.56$), the refraction of light in crystals that make up the layer is inhibited and the layer is therefore transparent. Turbulent zones, where the evaporation of the liquid is increased, turn white faster than the laminar zones (Figure 6.12). The choice of liquid is made according to its evaporation rate and the speed of the tunnel: at low speeds, methyl ethyl

Figure 6.12 **Boundary layer transition visualized with the china clay method**

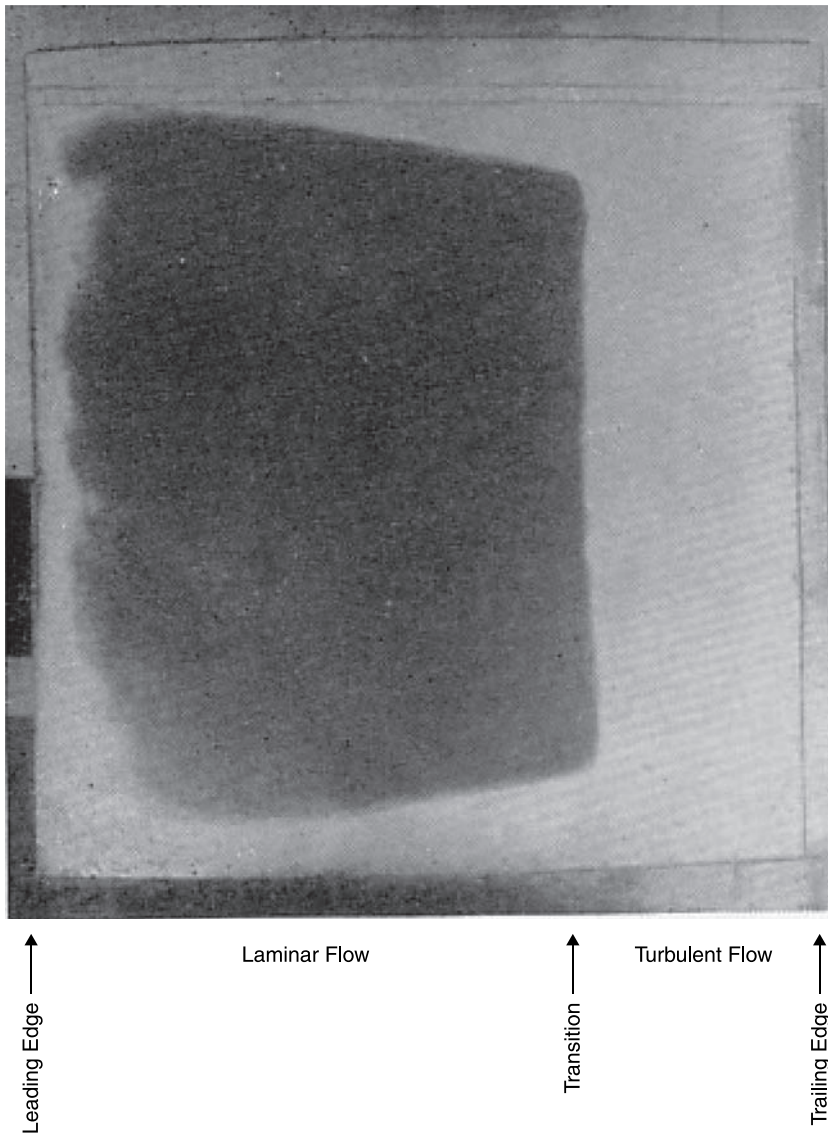

salicylate (n = 1.56) was successfully used; for speeds of few m/s, acetone was also used. As mentioned, the coverage of the model with the kaolin is permanent and can be used repeatedly for different tests.

6.2.7 Sublimating solids

In high speed wind tunnels, the china clay method has been replaced by methods based on the sublimation of a solid. The sublimating solid is diluted in a spraying solution in a highly volatile liquid that evaporates before the test. In continuous supersonic tunnels, a solid is used with a slow sublimation rate such as azobenzene; in intermittent supersonic wind tunnels, a solid with a fast sublimating rate like exachloroethane is used. In subsonic and transonic wind tunnels, solids with an average rate of sublimation like acenaphthene are widely used. Suitable solvents are benzene and xylene. The method has the disadvantage of providing images with a poor contrast (Figure 6.13).

Figure 6.13 **Boundary layer transition visualized with a sublimating material**

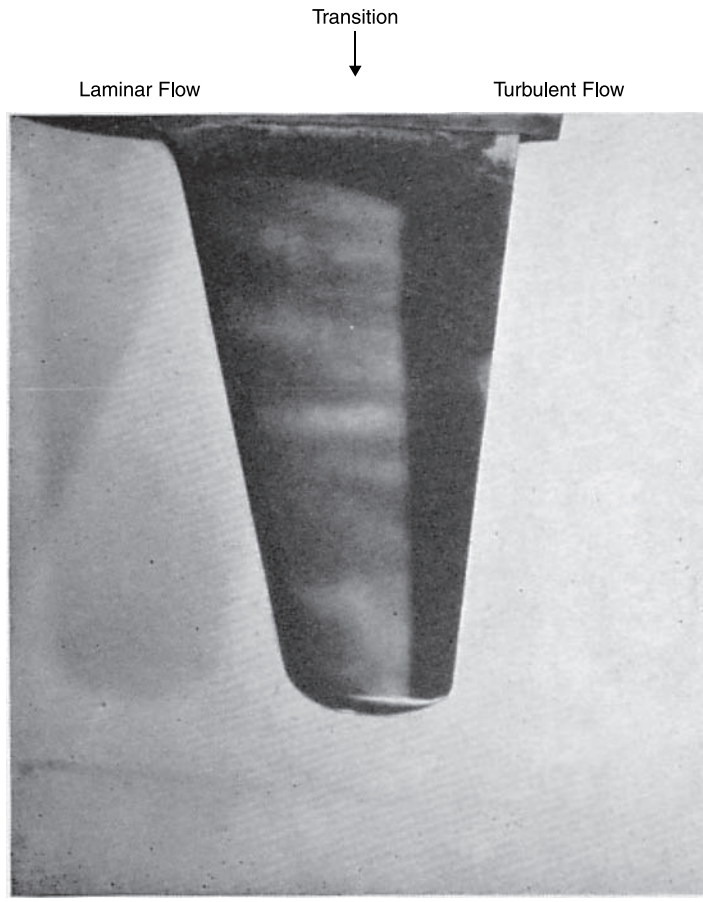

6.3 Principles of operation of optical methods

Optical methods allow the detection of density variations that occur in a fluid due to changes in temperature and/or speed and/or composition. The principle on which these methods are based is that the variation of density, ρ, produces a variation of the refractive index, n, of the fluid which in turn influences the trajectory (*refraction*) and the phase of the light rays that pass through the fluid. Appropriate optical devices convert the resulting effect in changes of light intensity on a screen or on a photograph.

The index of refraction, n, of a transparent medium, which is the ratio between the speed of light in vacuum and the speed of light in the substance, is related to the density by the *Lorenz–Lorentz equation:*

$$\frac{n^2 - 1}{n^2 + 2} = \rho R(\lambda) \tag{6.1}$$

where $R(\lambda)$ is, for each substance, a function of the wavelength, λ of the light.

When the index of refraction $n \cong 1$, as in the case of gases (see Table 6.1), Equation (6.1) can be expanded in series and, stopping the

Table 6.1 Refractive index of some substances

Substance	Index of Refraction, n [–] (Sodium D line)
Quartz	1.45843
Gelatin	1.516–1.534
Canada balsam	1.53
Crown Glass	1.517
Flint Glass	1.575–1.89
Water (15°C)	1.33377
Air (0°C, 760 mm Hg)	1.0002926
Carbon dioxide	1.000448–1.000454
Helium	1.00036–1.00036
Nitrogen	1.000296–1.000298
Water vapor	1.00249

series at the first two terms, the simpler *Gladstone–Dale equation* is obtained:

$$n = 1 + K(\lambda)\rho = 1 + \frac{\beta(\lambda)}{\rho_s}\rho \tag{6.2}$$

where $K(\lambda) \cong 1.5\ R(\lambda)$ and ρ_s is the density at standard conditions (T = 0°C, p = 760 mmHg).

The values of β for some gases are reported in Table 6.2.

Changes in the Gladstone–Dale constant with the wavelength are limited to a few percentages (see Table 6.3).

Table 6.2 Values of constant β for λ = 589.3 nm

Gas	$\beta_* 10^4$
Air	2.92
Carbon dioxide	4.51
Nitrogen	2.97
Helium	0.36
Oxygen	2.71
Water vapor	2:54

Table 6.3 Gladstone–Dale constant for air

Wavelength λ nm	Gladstone–Dale constant $K_* 10^3\ m^3 kg^{-1}$
262.0	0.2426
296.0	0.2380
334.0	0.2348
436.0	0.2297
470.0	0.2287
479.8	0.2284
489.0	0.2281
505.0	0.2276
510.0	0.2276
521.0	0.2272
546.0	0.2269
578.0	0.2265
579.0	0.2263
614.7	0.2261
644.0	0.2258

Figure 6.14 Effects of a change of refractive index on a light ray

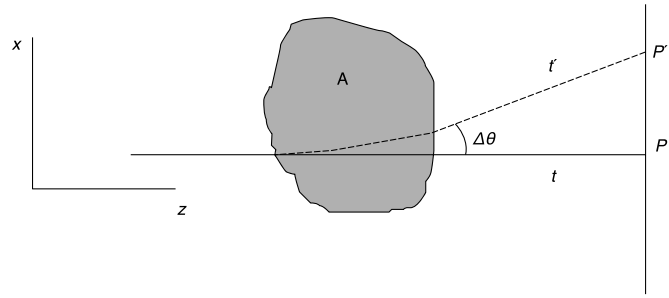

Assume that the fluid is confined in a region of space and that the region is crossed by a beam of parallel rays of monochromatic light that propagate along the axis z. A generic ray (Figure 6.14), in the absence of disturbance, i.e. the properties of the fluid are uniform in the region, reaches the screen at the point P at time t; if the fluid properties are not uniform, the trajectory of the ray deviates of an angle $\Delta\Theta$ from the straight line due to the phenomenon of refraction and the ray reaches the screen at the point P' at the time t' Since a change in density is related to a change in refractive index, and thus to the speed of light in the medium, the various rays reach the screen at different times. Appropriate optical systems highlight separately, by variations in the brightness of the image, the displacement PP' (shadowgraph) or the deflection $\Delta\Theta$ (Schlieren method) or the phase delay Δt (interferometric methods).

We will show below that the *shadowgraph method* is sensitive to the gradients of the gradients of density, the *Schlieren method* and the *differential interferometer* visualize the values of density gradients, and the *separated beam interferometer* measures the difference $\Delta\rho$ between the local density and a reference density. It is then obvious that an interferogram obtained with a separated beam interferometer lends itself to a quantitative analysis of the density field much better than a shadowgraph that requires a double integration resulting in heavy approximation errors.

6.4 Deflection of a light beam in the presence of a constant gradient of refractive index

Assume that the beam, which initially propagates in the z direction, encounters a zone where there is a gradient of refractive index

Figure 6.15 Deviation of a light beam in the presence of a constant gradient of refractive index

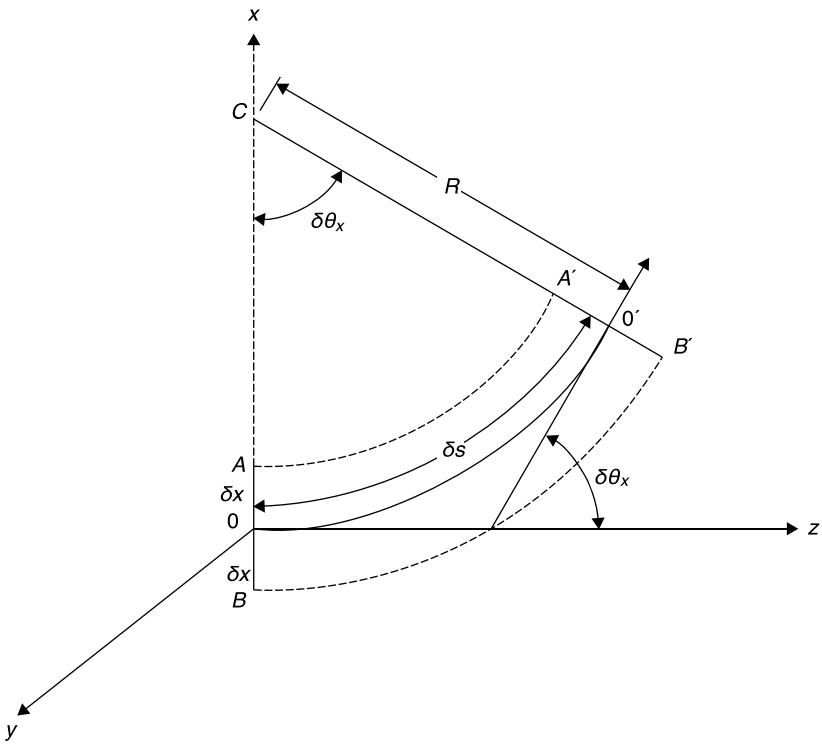

(Figure 6.15). Denoting with n the refractive index at the point 0, at points A and B of the beam, at a distance of $\pm\delta x$ from the z axis, the refractive index takes the values respectively:

$$n_A = n + \frac{\partial n}{\partial x}\delta x \qquad n_B = n - \frac{\partial n}{\partial x}\delta x \tag{6.3}$$

Since there is an inverse relationship between the refractive index and the speed of light, c, the speed of light at points A and B is such that:

$$\frac{c_A}{c_B} = \frac{n_B}{n_A} = \frac{n - \dfrac{\partial n}{\partial x}\delta x}{n + \dfrac{\partial n}{\partial x}\delta x} < 1 \tag{6.4}$$

therefore, the beam deflects toward the positive x axis. After a time, δt the wave front AB is in the position $A'B'$ deflected by the angle $\delta\theta_x$ with

respect to AB. The rays passing through A and B in time δt travel distances δs_A and δs_B proportional to the speeds c_A and c_B, respectively. Indicating with R the radius of curvature of the ray passing through the origin of the axes, we can write:

$$\frac{\delta s_A}{\delta s_B} = \frac{c_A}{c_B} = \frac{n - \frac{\partial n}{\partial x}\delta x}{n + \frac{\partial n}{\partial x}\delta x} = \frac{R - \delta x}{R + \delta x} \tag{6.5}$$

which yields:

$$\frac{1}{R} = \frac{1}{n}\frac{\partial n}{\partial x} \quad \text{and then} \quad \delta\theta_x = \frac{\delta s}{R} = \frac{1}{n}\frac{\partial n}{\partial x}\delta s = \frac{\partial \ln n}{\partial x}\delta s \tag{6.6}$$

which is the required relationship between the deflection of the light rays and the gradient of the index of refraction.

Similarly, if there is a gradient of n in the y direction, constant and greater than zero, the beam undergoes a deflection towards the positive y axis given by:

$$\delta\theta_y = \frac{1}{n}\frac{\partial n}{\partial y}\delta s$$

The total deflections that the beam suffers through a test chamber of width L are therefore, respectively:

$$\theta_x = \int_0^L \frac{1}{n}\frac{\partial n}{\partial x}dz \qquad e \qquad \theta_y = \int_0^L \frac{1}{n}\frac{\partial n}{\partial y}dz \tag{6.7}$$

where s can be replaced with z as the deviations are usually infinitesimal.

6.5 Shadowgraph

If the flow field is traversed by a light beam (Figure 6.16a), the image that is formed spontaneously on a screen perpendicular to the axis of propagation is called a shadowgraph. If the beam is made parallel by a lens (Figure 6.16b), the shadow will have the same aspect ratio as the model. The images produced are carriers of information so implicit that it is very difficult, if not impossible, to infer density variations from an examination of the image.

Figure 6.16 The shadowgraph method: (a) divergent light rays; (b) parallel rays

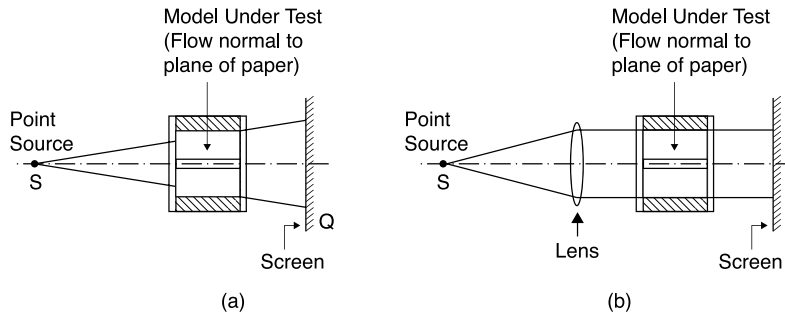

To understand the operating principle of the shadowgraph in detail, the behavior of the index of refraction within the field must be considered. Let *AB* and *CD* (Figure 6.17) be the undisturbed paths of two adjacent rays. If there is a variation in the index of refraction, the rays are deflected: if the gradient of the index of refraction, $\partial n/\partial x$, is constant, i.e. $\partial^2 n/\partial x^2 = 0$, the two rays are deflected by the same angle and remain parallel (Figure 6.17a): the illumination on a screen placed downstream of the test chamber is uniform. If $\partial^2 n/\partial x^2 > 0$, the deflected rays diverge (Figure 6.17b), because the ray passing in *A* meets zones with a stronger gradient of index of refraction with respect to the gradient met by the ray passing in *C*; a darker zone is generated on the screen. Finally, if $\partial^2 n/\partial x^2 < 0$, the rays converge (Figure 6.17c) and a brighter zone is obtained on the screen.

The shadowgraph is successfully used for the visualization of surfaces of discontinuity in the index of refraction (density) like the shock wave, or of layers with strong and variable density gradients (dynamic and thermal boundary layers).

Figure 6.17 Effects of the gradient of refractive index on the deflection of light rays

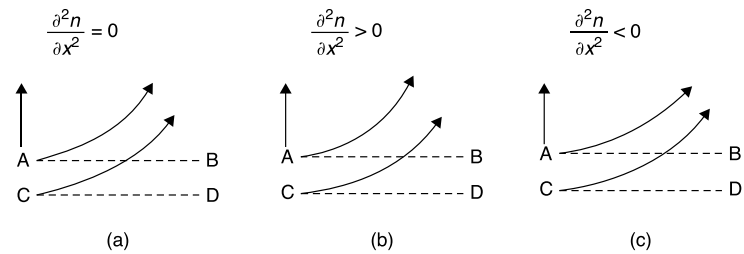

Figure 6.18 Evolution of density, its gradient and the gradient of gradient within a shock wave

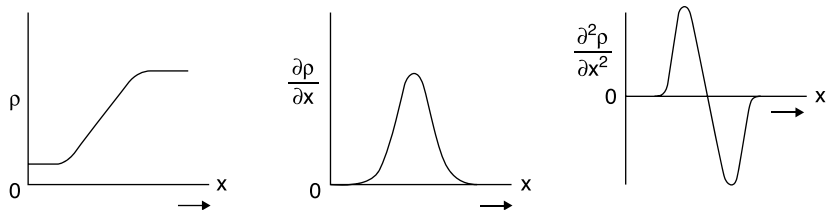

Consider, for example, the case of a jump in density across a shock wave (Figure 6.18). In the same figure are shown the evolution of density and of the gradient of the gradient of density inside the wave, considered of finite thickness. In the front of the wave $\partial^2 n/\partial x^2 > 0$ and the screen displays a dark line, in the back $\partial^2 n/\partial x^2 < 0$ and the screen displays a bright line. Therefore a shock wave appears on the screen as a succession of two light bands: the first dark and the second bright (Figure 6.19).

Figure 6.19 Shadowgraph of shock waves and wake on a sphere in a stream at $M = 1.6$

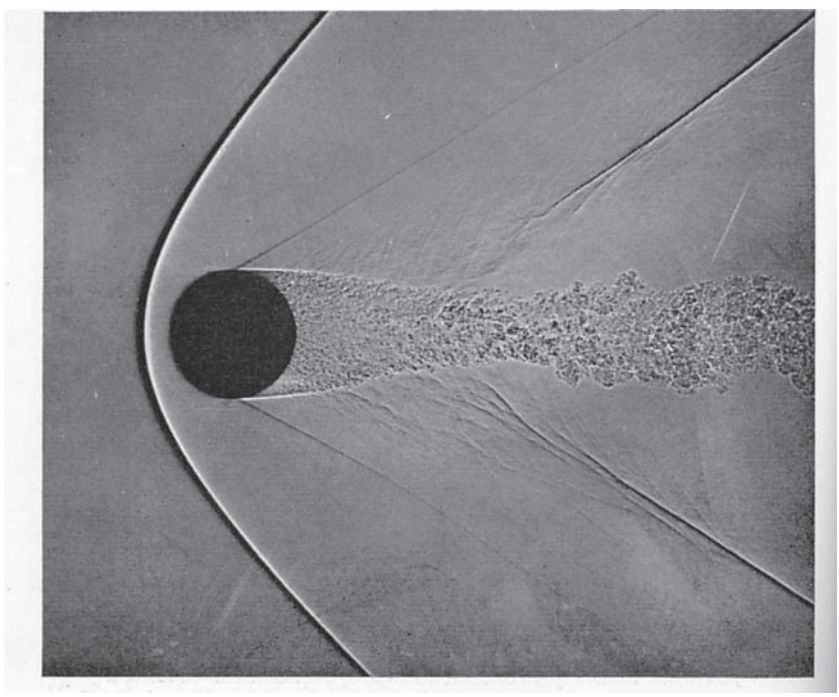

It can be shown that the contrast of light, C, produced at each point of the screen is given approximately by:

$$C(x,y) = \frac{\Delta I(x,y)}{\bar{I}} = \ell \int_0^L \left(\frac{\partial^2}{\partial x^2} + \frac{\partial^2}{\partial y^2} \right) \ln n(x,y)\, dz \qquad (6.8)$$

where I is the light intensity and ℓ is the distance of the disturbance from the screen.

Calculation of density from Equation (6.8) requires a double integration of the local contrast (appropriate devices are needed to measure the light intensity). Moreover, Equation (6.8) becomes less reliable in the description of phenomena that are best viewed with the shadowgraph (i.e. discontinuities in the value of the index of refraction). In fact, large variations in the density gradient will produce, starting from a certain distance from the phenomenon, an intersection of the various rays that destroy the correspondence between points of the test field and the image obtained on the screen that is the basis of Equation (6.8).

The shadowgraph is very simple from the viewpoint of the optical components required, and is useful for the visualization of fluids in which there are discontinuities in density, but it is essentially a qualitative method as the calculation of the distribution of the index of refraction from Equation (6.8) seems rather difficult, if not impossible. One can say briefly that with this method small changes in n are not detected and large variations in n cannot be calculated.

6.6 The Schlieren method

Any apparatus that produces images in which the brightness depends on the local deviations that light rays undergo when crossing the test zone is generally classified as Schlieren. Strictly speaking, the shadowgraph is also a Schlieren, but currently this name is attributed solely to the method proposed by Toepler in 1866.

In this system (Figure 6.20), a first lens produces a beam of parallel light rays passing through the test chamber, a second lens produces an image of the test chamber on a screen and an image of the light source in its focal plane. A *knife edge* or *cut-off* is introduced into the focus, to cut a fraction of the image of the source.

To understand how the system works, it should be noted that the light source is of finite size, usually rectangular 10 mm × 1 mm (Figure 6.21,

Figure 6.20 Schematic of the Toepler–Schlieren method

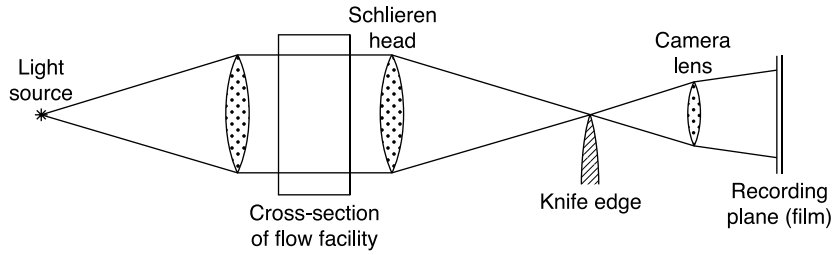

Source: [4]

bottom left). Each point of the source (Figure 6.21) produces a pencil of parallel rays passing through the entire test chamber and is focused in a point; the focus consists of the focal points of all the pencils that have crossed the test chamber, bearing with them all the information. In the absence of disturbances in the test chamber, cutting part of the focus with a knife edge only makes the light on the screen reduced, without any loss of part of the image of the test chamber on the screen. The loss in brightness is proportional to the fraction of the image of the light source cut by the knife edge, $(b - a)/b$, where b is the height of the light source and a is the height of the part of it not intercepted by the knife edge (Figure 6.22b). Usually the knife cuts half of the focus ($a = b/2$).

On the other hand, every ray that passes through the test chamber is the sum of rays coming from all the points of the source and focuses on all the points of the image of the source, and for this reason the image of

Figure 6.21 Pencil of rays generated from various points of a light source of finite size. In detail at the bottom left the system used to generate a rectangular source

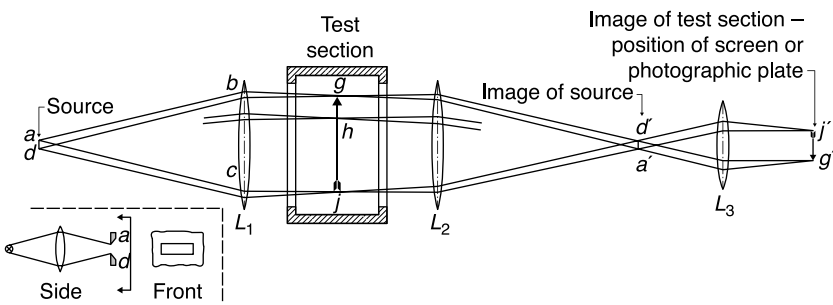

Source: [5]

Figure 6.22 (a) Displacement of an image of the source due to the deflection of a ray. (b) Relative positions of the images of source and knife edge

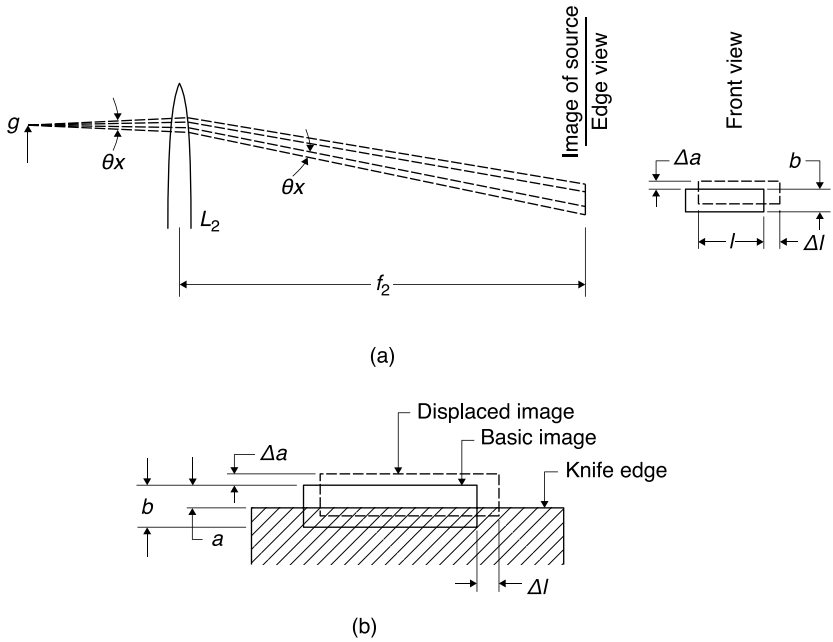

Source: [5]

the source can be thought of as the overlapping of all the images produced by all the rays passing through the test chamber.

If there is a density gradient in the test chamber, the ray passing through that point is deflected either upwards or downwards depending on the sign of the density gradient, and the corresponding image of the source moves by $\pm\Delta a$ with respect to the knife edge and then is cut more or less than other images of the source formed by the undisturbed rays (Figure 6.22b). This shift and the resulting change of lighting of the corresponding point on the screen are proportional to the deflection angle.

Assuming that θ_x is small, from Figure 6.22a is obtained that:

$$\Delta a(x, y) = f_2 \tan\theta_x(x, y) \cong f_2\theta_x(x, y) \tag{6.9}$$

When $\Delta a(x, y)/a = \pm 1$, the maximum deviation angles, $\theta_{x\max}$, is reached, beyond which no further changes occur in brightness (*saturation of Schlieren*) because the source images are either completely cut by the knife or not cut at all.

The contrast at the point (x, y) of the image is given, for Equation (6.6) and Equation (6.9), by

$$C(x,y) = \frac{\Delta I(x,y)}{\bar{I}} = \frac{\Delta a(x,y)}{a} \cong \frac{f_2}{a}\int_0^L \frac{\partial \ln n(x,y)}{\partial x} dz = \frac{\theta_x(x,y)}{\theta_{x\max}} \tag{6.10}$$

The sensitivity, s, defined as the relative deflection, $\Delta a(x,y)/a$, obtained at the knife for the unit deflection of the ray in the test chamber

$$s = \frac{\Delta a(x,y)/a}{\theta_x} = \frac{f_2}{a} = \frac{C(x,y)}{\theta_x(x,y)} = \frac{1}{\theta_{x\max}}$$

increases with the focal distance of the second lens. To increase the sensitivity, the value of $b = 2a$ can also be reduced, but this means a decrease in global brightness. An excessive sensitivity may otherwise not be desirable because even the small gradients of density present in the laboratory are magnified, thereby introducing a *noise* in the image.

Note that the Schlieren system is only sensible to the component $\Delta a(x, y)$ of the displacement normal to the knife edge (Figure 6.22b); since this shift is a function of the gradient of the refractive index in this direction, the knife must be oriented appropriately depending on the phenomenon to be visualized (normal shock wave, oblique shock wave, boundary layer, etc.). Although a rectangular source and a straight-edged knife are commonly used, rarely for particular applications can other shapes be used, for example, a circular source and a ring knife can be used if a uniform sensitivity in all directions is required. Usually on the photos obtained with the Schlieren system are reported the type and orientation of the used knife edge to make easier the interpretation of the image (Figure 6.23).

In Figure 6.24, the Schlieren images for different operating conditions of a de Laval nozzle are shown.

Since the eye is more sensitive to changes in color than in brightness, it is preferable to use Schlieren configurations that obtain color images in which every nuance of color corresponds to a particular density gradient in the flow. One approach is easily achievable replacing the knife with some transparent and colored parallel stripes, made of sheets of cellulose acetate or gelatin filters. No more than three colors are generally used and the three-color filter is positioned parallel to the light slit. The combination red–yellow–blue gives the better contrast: the undisturbed

Figure 6.23 **Schlieren photograph of a double wedge in a flow at $M = 1.6$ and its interpretation**

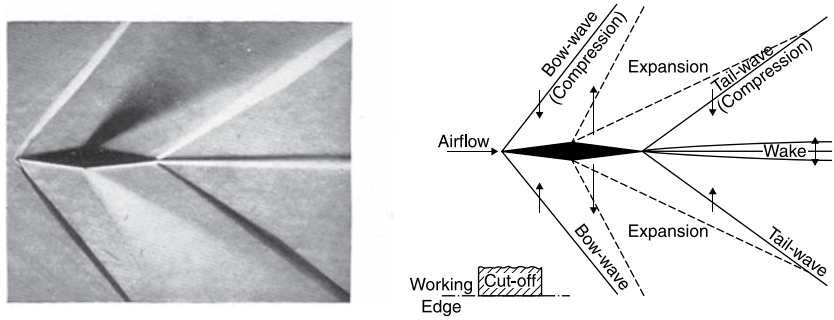

field is yellow, the gradients deflecting the rays in a direction give red zones and those deviating them in the opposite direction give blue zones.

Using Equation (6.10) quantitative results from a Schlieren could be obtained using a photodensitometer on the photographic negative. Quantitative results could also be obtained by doing a direct scan of the focal plane of the Schlieren system with a photomultiplier. In practice, significant difficulties arise in the accurate photometric analysis of the image, and also for the aforementioned problem of saturation: this can be avoided only if the knife is replaced by a gradual filter with various shades of gray. Once again, the filter should be placed so that the direction of change of gray is in the same direction of the density gradient to be measured.

The Schlieren system is usually not used to get the value of density, but is extremely useful in the qualitative description of the test field.

For the large diameters ($D > 100$ mm) required to illuminate the windows of a supersonic wind tunnel, lenses are usually replaced with concave mirrors; in fact, a mirror is easier to build and less expensive than a lens because:

- the internal quality of the glass is not important;
- it is necessary to work on only one surface;
- a mirror absorbs less light than a lens;
- chromatic aberration is eliminated.

Mirrors with a protecting glass, like those for home use, cannot be used since a double reflection is produced, the first on the covering glass and the second on the mirror surface. The reflecting surface must therefore be exposed to the air: aluminum is usually used, because its oxide (Al_2O_3) is transparent.

Figure 6.24 **Schlieren images of flow in a supersonic nozzle at different ambient pressures**

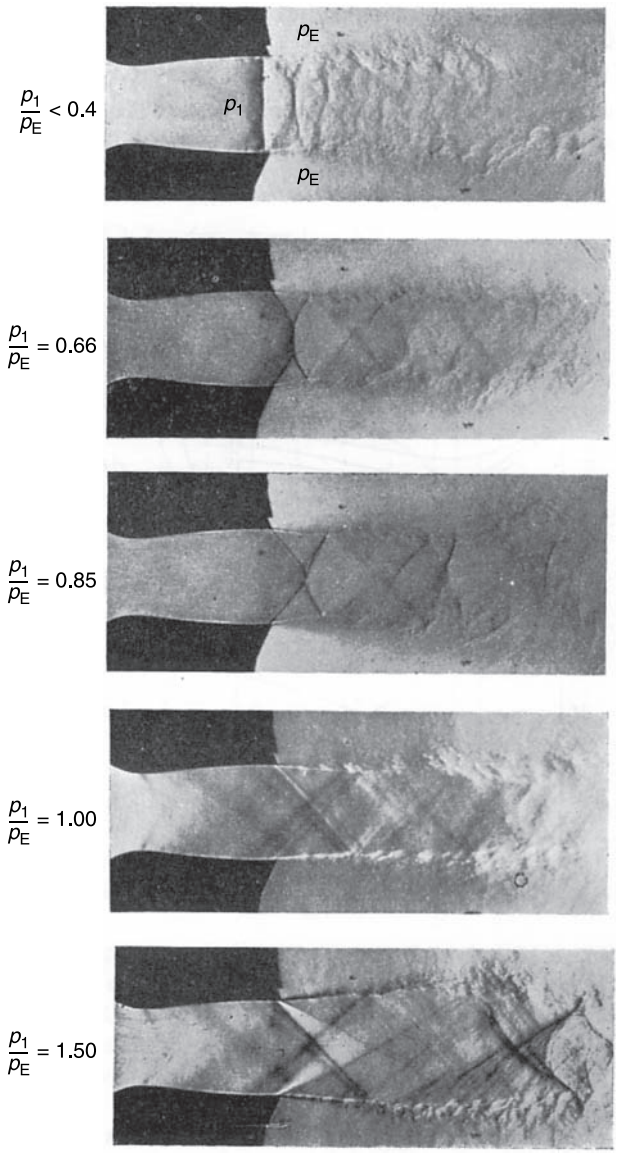

Source: [6]

When using mirrors, the source and the knife should be placed outside the optical axis (Figure 6.25) the mirrors should be in the form of an offset paraboloid. The production of mirrors of this type, however, is

Figure 6.25 *Z*-configuration of a Schlieren system with mirrors

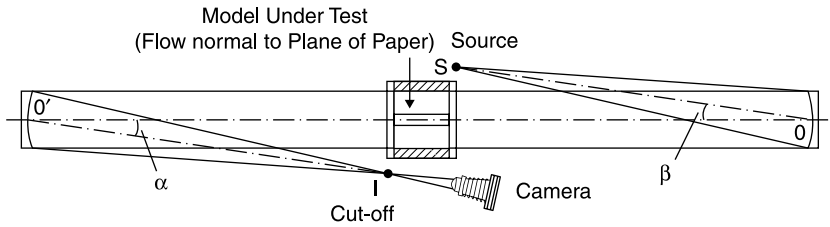

expensive and spherical mirrors are preferred; this approximation is allowed if the ratio between focal length and diameter of the mirror is more than 10.

To minimize the aberrations due to a spherical mirror, the offset angles α and β of Figure 6.25 must be small and also of opposite sign so that the source and the knife are on opposite sides of the axis of the two mirrors. The first precaution minimizes the effects of astigmatism, the second, the effects of coma. It is also necessary that the astigmatism distorts the image only in the direction parallel to the edge of the knife; this may be done by placing the source, the knife and the optical axis of the system in the same plane.

6.7 Interferometry

Two beams interferometry is based on the comparison between the optical paths of pairs of light rays that pass through a test field in which the index of refraction, n, is not homogenous. The *optical path* traversed by a light ray is defined as the curvilinear integral

$$\ell = \int n(x,y,z)\,ds \tag{6.11}$$

where ds is an element along the path and $n(x, y, z)$ is the distribution of the index of refraction in the test field. (In a vacuum, where $n = 1$, the optical path coincides with the geometrical path.) Pairs of coherent light rays that travel different optical paths can create interference, in particular, negative interference, a black point, if the difference between the optical path of the two rays is equal to an odd number of half wavelengths, see Equation (4.7):

$$\Delta\ell = \pm(2N+1)\frac{\lambda}{2} \qquad [n = 0, 1, 2 \ldots\ldots] \tag{6.12}$$

and positive interference in a point, where the brightness is equal to four times the brightness of the single rays, see Equation (4.7), if the optical path difference is equal to an even number of half wavelengths (a multiple of wavelengths):

$$\Delta\ell = \pm 2N\frac{\lambda}{2} = \pm N\lambda \tag{6.13}$$

In the image of the test chamber, a pattern of stripes, *interference fringes,* is generated. This phenomenon occurs only if the two interfering beams are generated by coherent sources (i.e. sources that emit light waves with the same wavelength and constant phase difference). Because it is impossible to obtain two distinct and perfectly coherent sources, it is necessary to use a single source and split the beam into two beams which are then recombined.

In order to introduce a classification of different systems it can be assumed that all light rays are straight and parallel to the axis z. Assume that the pairs of conjugate rays lie in the plane x, z (Figure 6.26) and that in the test field are separated by the distance d. If the coordinates of the two input rays in the test field are indicated by ζ_1 and ζ_2, and the coordinates of output with $\overline{\zeta}_1$ and $\overline{\zeta}_2$, the difference in optical pathlengths of the two rays is given by:

$$\Delta\ell = \int_{\zeta_1}^{\overline{\zeta}_1}\left[n\left(x+\frac{d}{2},y,z\right)\right]dz - \int_{\zeta_2}^{\overline{\zeta}_2}\left[n\left(x-\frac{d}{2},y,z\right)\right]dz \tag{6.14}$$

Unfortunately from this equation it is not possible to determine $n(x, y, z)$ since in it are two unknowns: the distribution of the refractive index

Figure 6.26 Schematic of a two beam interferometer

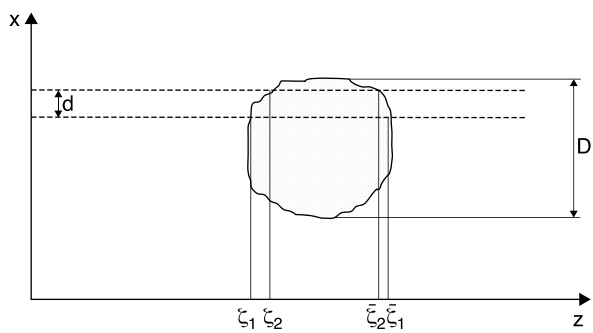

along two trajectories. All systems used for optical interferometry reduce the number of these unknowns to one. One can identify two types of different devices depending on the distance between the two rays and therefore interferometers will be classified as *separate beams interferometers* and *differentials interferometers*.

If D is the diameter of the test field, when $d/D > 1$, one of the two conjugate rays will pass outside the test field, usually through a medium with a constant and known refractive index $n = n_0$. These rays form a reference beam that is made to interfere with the test beam. The difference in optical path in this case is:

$$\Delta\ell = \int_0^L \left[n(x,y,z) - n_0 \right] dz \tag{6.15}$$

where L is the size of the test chamber in the z direction. The separate beams interferometers are therefore sensitive to the absolute change in refractive index or density. The typical instrument of this class is the *Mach–Zehnder interferometer*.

Differential interferometers are characterized by a very small ratio between the separation of the rays and the diameter of the test field, $d/D << 1$: in practice, both the two conjugate rays pass through the test field, separated by an infinitesimal distance d. These interferometers are also called *Schlieren interferometers* because the optical apparatus is very similar to the Schlieren system.

Developing Equation (6.14) in a Taylor series truncated at the linear terms, since d is infinitesimal, we have:

$$\Delta\ell = d \int_0^L \frac{\partial n}{\partial x} dz \tag{6.16}$$

similar to Equation (6.10) for $n \cong 1$.

Many differential interferometers have been made, some of them can only operate using a laser as a light source, the most commonly used is the *Wollaston prism interferometer*.

There are many advantages using differential interferometers with respect to separated beam interferometers:

- separated beams interferometers cannot be used whenever the difference in optical paths between the two beams is higher than the coherence length (the presence of thick glass windows in one of two paths);

- in a differential interferometer, since both the interfering rays pass in the test chamber separated by an infinitesimal distance, they are equally affected by any vibration;
- differential interferometers do not require the elaborate and sophisticated alignment procedures needed in separated beams interferometers;
- differential interferometers can be made in large dimensions because the mirrors used, which are the same of the Schlieren system, easily reach a diameter of 50 cm, with costs much lower than those of the high quality optical components of a Mach–Zehnder interferometer;
- the cost of a differential interferometer is extremely low because the optical components of the Schlieren equipment are usually already available in any fluid dynamics laboratory.

6.7.1 Ideal Mach–Zehnder interferometer

The main advantage of this type of interferometer is the fact that the two path lengths can be separated at will so that tests can be made also on very large objects, such as test chambers of wind tunnels.

The beam of parallel rays coming from the light source *LS* (Figure 6.27) is split into two beams by a *beam splitter*, BS_1, covered with TiO_2, which reflects approximately 35% of incident light, placed at 45° with respect to the optical axis. After reflection on the two mirrors, M_1 and M_2, covered with aluminum that reflects at least 90% of incident light, the two beams are recombined downstream of the beam splitter BS_2. The working section, *WS*, is located between M_1 and BS_2 in Figure 6.27, but it could be located in any one of the sides of the rectangle at will.

Since the interference fringes are generated downstream of the beam splitter BS_2, there is a problem of focusing contemporarily two objects (the fringes and the test section) at different distances from the screen *G′*: in order to do that, the lens L_2 is inserted downstream of BS_2 in order to produce a virtual image of the fringes at the center of the test chamber. To enable fine-tuning of the focus, the beam splitter, BS_2, has a translational degree of freedom.

If the four plates are exactly parallel to each other, undisturbed waves arrive in BS_2 perfectly in phase with each other so that the light intensity on the screen is uniform. The method is called *infinite width fringe* or *zero fringes*.

Figure 6.27 The Mach–Zehnder interferometer

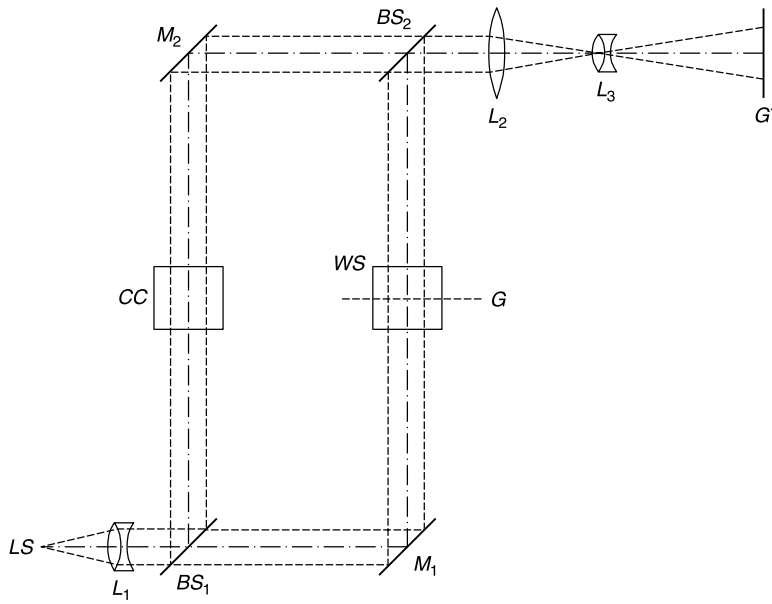

Source: [7]

If a change in density is introduced in the test chamber, the phase change that develops produces interference fringes which are lines of constant density (Figure 6.28). The difference in optical path between two consecutive fringes is equal in absolute value to a wavelength.

The number of fringes that are generated, and therefore the resolution that can be achieved in identifying the density distribution in the field, depend on the variations of density and therefore cannot be controlled by the operator.

If a better resolution is needed, straight and parallel fringes can be generated: this may be achieved by rotating of a small angle, ε, the beam splitter BS_2 around an axis normal to the plane of Figure 6.29. A purely geometrical optical path difference between the pair of conjugate rays that meet at P is thus generated given by:

$$\Delta\ell = \overline{OP} - \overline{OC} = 2b\left(\frac{1}{\text{sen}2\varepsilon} - \frac{1}{\tan 2\varepsilon}\right) = 2b\tan\varepsilon \cong 2b\varepsilon \qquad (6.17)$$

which is the same for all points on the normal to the plane at P, so straight fringes are produced parallel to the axis of rotation of the beam splitter, as shown in Chapter 4 for the crossed-beams laser-Doppler anemometer.

Figure 6.28 Contour interference fringes obtained with the zero fringes method

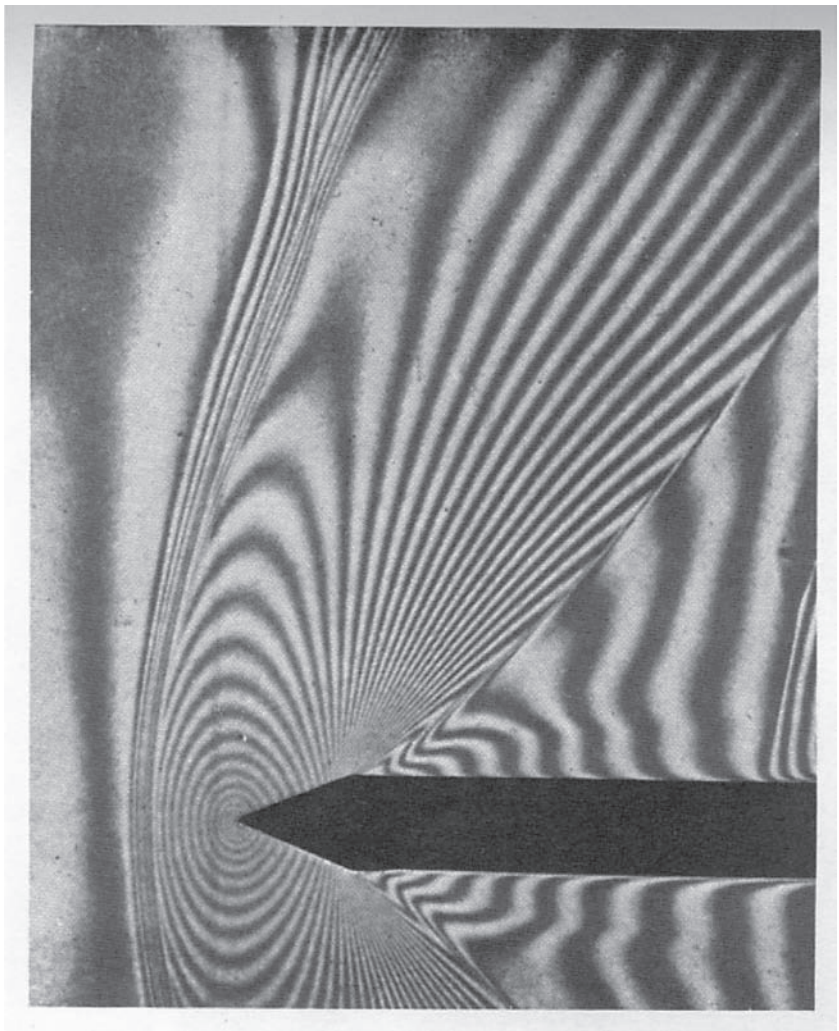

Source: [7]

At point O and, provided that the angle 2ε is small enough, all along its bisector rays with the same optical path interference and then at the point O', there is the fringe of order 0. Assuming that N bright fringes exist between O' and P, the difference of optical path length for the rays meeting in P is:

$$\Delta\ell = N\lambda = 2b\varepsilon \tag{6.18}$$

Figure 6.29 Generating finite width fringes

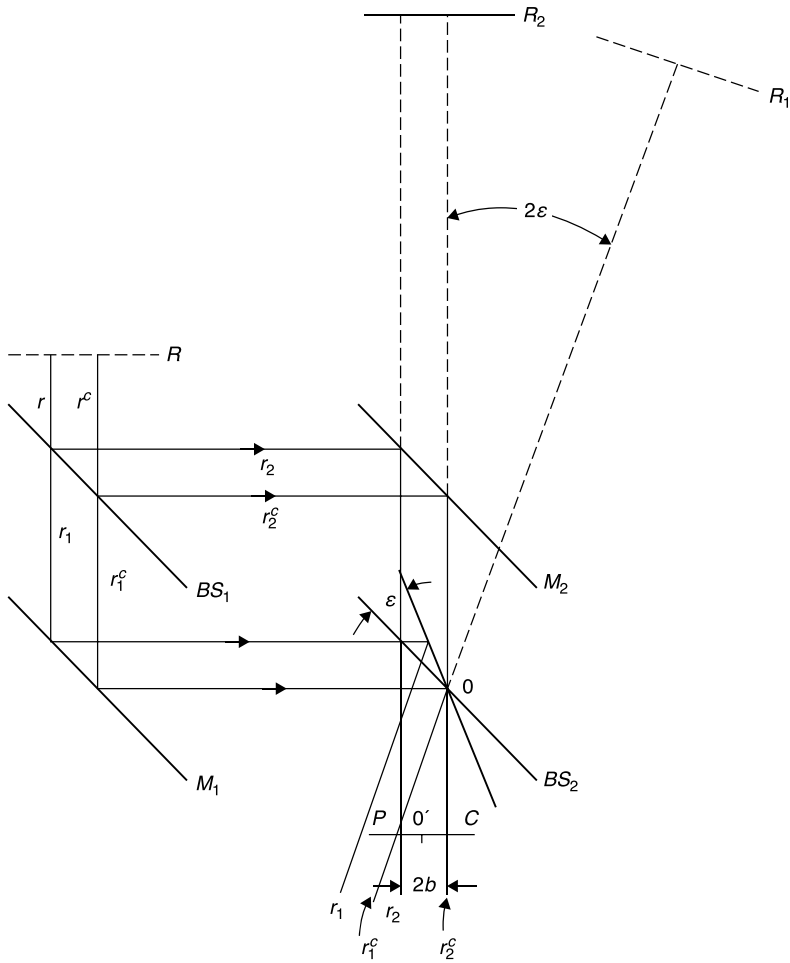

Source: [7]

Therefore, the distance between two consecutive fringes is given, in agreement with Equation (4.8) for small angles, by:

$$w = \frac{b}{N} = \frac{\lambda}{2\varepsilon} \tag{6.19}$$

The introduction of a disturbance in one of the two optical paths produces a fringe shift (Figure 6.30). If a fringe moves one fringe thickness compared to the corresponding position in the undisturbed stream, this

Figure 6.30 Interferogram of flow on a bullet

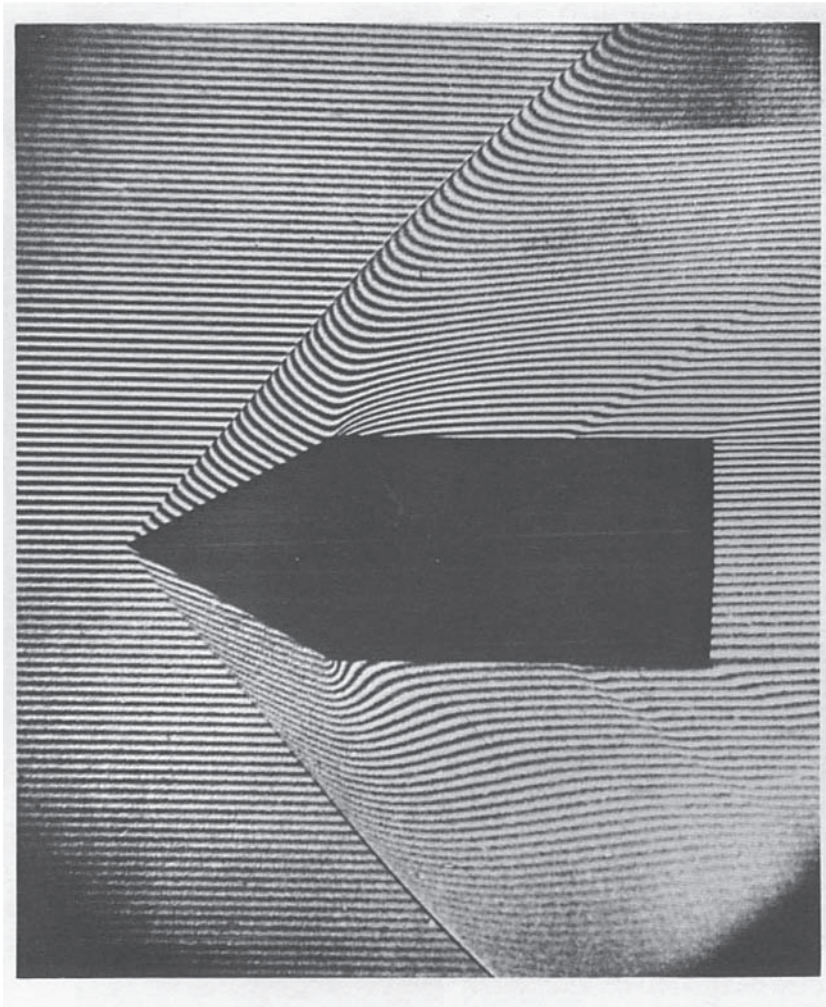

means that the difference in optical path is changed by one wavelength, in absolute value. With a simple measurement of displacements as multiples or submultiples of fringes width, the density variations can then be calculated with the desired resolution.

Contour fringes can be obtained also with the system of finite width fringes by superimposing a no-flow image on an image obtained in the presence of flow. The regions where the fringes are displaced of $N\lambda$ become visible as bright stripes that represent points of equal density, or isopicnals (Figure 6.31).

Figure 6.31 **Density contours obtained by superposition of flow and no-flow images**

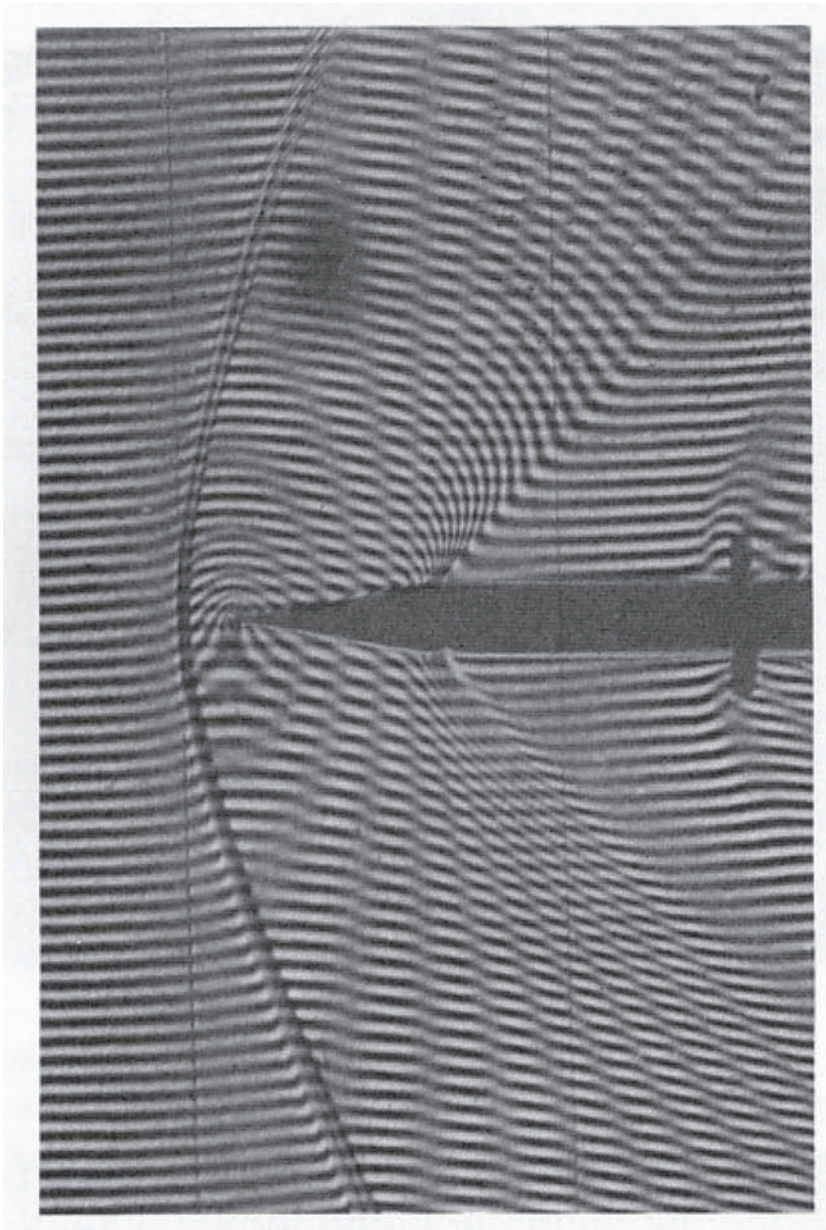

Source: [8]

6.7.2 Real Mach–Zehnder interferometer

In the preceding paragraph the assumptions of monochromatic and point light source were made. The basic requirement, in order to ensure that the two intersecting beams give interference, is that the phase difference of rays remains constant in all the observation time. This is linked to conditions on the spectral amplitude of the light emitted (temporal coherence) and the finite extension of the source (spatial coherence).

Consider the extreme case of only two sources whose wavelengths differ by $\Delta\lambda$: the system of fringes disappears when the Nth bright fringe produced by the light with wavelength λ falls on a dark fringe produced by the wavelength $\lambda + \Delta\lambda$. The difference in amplitude of the fringes is, for Equation (6.19) $\Delta w = \Delta\lambda/2\varepsilon$ and the condition of cancellation of the fringes is:

$$N\Delta w = \frac{w}{2} \rightarrow N = \frac{\lambda}{2\Delta\lambda} \tag{6.20}$$

then with a given λ and a given amplitude of the spectrum of the source, the equation allows calculation of the maximum number of fringes that can be obtained: for red light (λ = 632.8 nm) and an interferometric filter with bandwidth, $\Delta\lambda$ = 1 nm, about 300 fringes can be generated.

With a white light fringe, this phenomenon clears all except the white fringe of zero order and a few colored fringes on each side of it (Figure 6.32, top). This particular feature is used to follow the fringe shift through a shock wave: with the white light it is very easy to follow the brightest zero-order fringe (Figure 6.32, bottom).

A finite source may be regarded as consisting of many source points, so in every point on the screen the light intensity is the result of some interfering pairs rather than a single pair. The interference is obtained only if the difference in optical path between a pair of ray changes by no more than $\lambda/2$ on the whole source.

From Figure 6.33, we can see that there are a number of beams of parallel rays from each point of the source entering the interferometer; between the two extremes there is an angle of $2\omega_{o.}$ If the central beam enters the interferometer at 45° from the surface of the first beam-splitter and if the produced fringes are perpendicular to the plane of the centers, from simple geometric considerations it can be found that the maximum number of fringes in the field is:

$$2N \leq \frac{1}{\omega_0^2} \tag{6.21}$$

Figure 6.32 White light interferometry and its use to detect the fringe shift across a shock wave

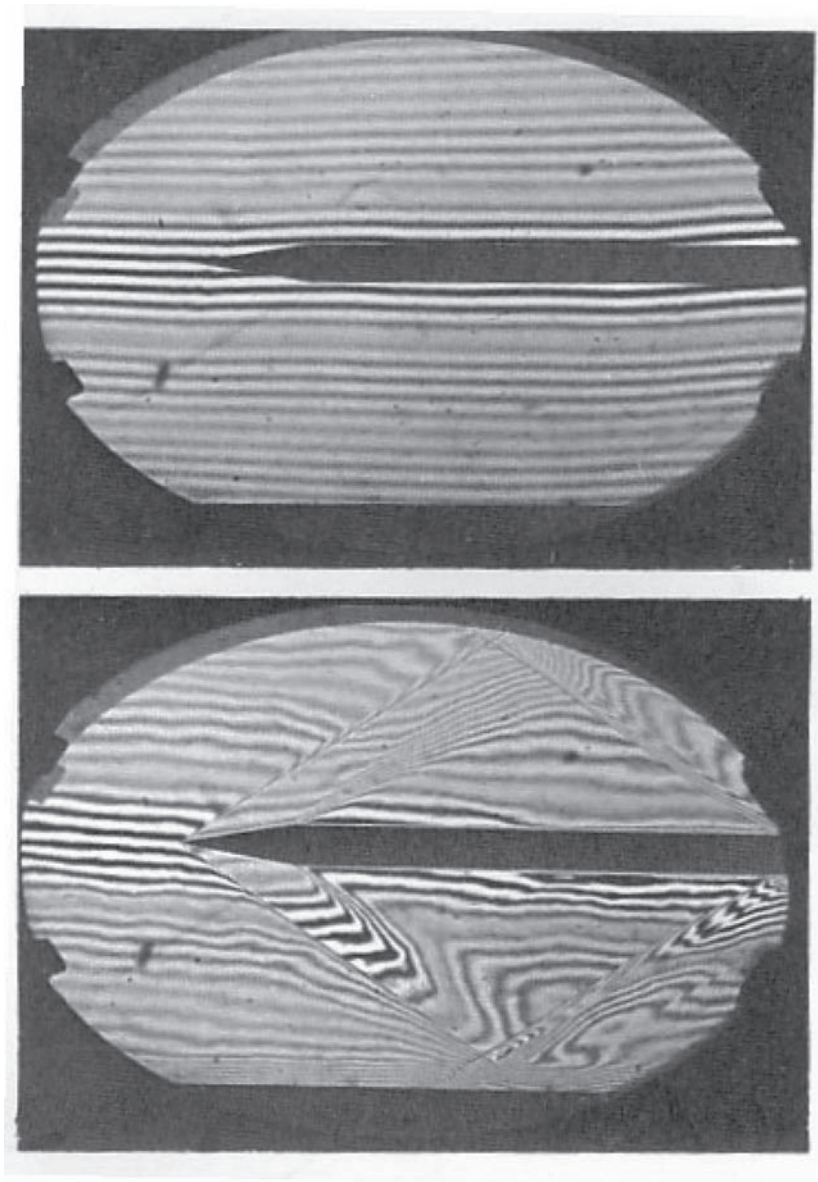

Source: [7]

Figure 6.33 Opening angle of a finite light source

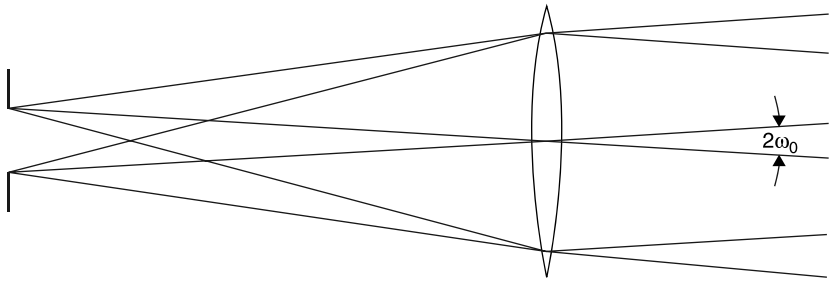

It is also difficult to obtain good contrast of the fringes in the presence of dispersion in the various optical components. The limited spatial and temporal coherence of the normal light source, usually mercury arc lamps filtered with a narrow band interferometric filter ($\Delta\lambda$ = 1 nm), implies the need for strictly equal path lengths which limits the tolerance in the initial assessment of the instrument to a few wavelengths. If the test chamber has windows, these introduce an optical path difference between the test and reference beams of the order of a few centimeters and it is therefore necessary to make the two path lengths equal, introducing into the reference path a pair of glasses identical to the windows of the test chamber (the *compensation chamber,* CC, of Figure 6.27) or by passing also the reference beam through the test chamber in an area where the density is constant and is known.

In practice, the Mach–Zehnder interferometer requires five adjustments and high quality precision optics: all optical surfaces, including the windows in the test chamber, must be machined with great precision, so that the thickness of the mirrors must be constant within a tolerance of less than $\lambda/12$. This type of interferometer requires adequate structural rigidity and must operate in the absence of vibrations that could alter the optical path difference between the two beams.

Using a gas laser, which acts as an ideal point source for monochromatic and coherent light, the coherence length is of a few decimeters (see Chapter 4) and most of these difficulties disappear. The use of a laser has the following effects:

- tolerance in the initial set-up of the interferometer is of some decimeters;
- there is no need to make equal the thickness of the optical components in the two paths;
- a large number of well-contrasted fringes is easily obtained;
- three of the five fine adjustments of the interferometer become

redundant, there remain only the controls on spacing and inclination of the fringes.

Unfortunately, the coherence of laser light introduces new difficulties:

- the rear surface of the beam splitters and each surface of the windows of the test section reflect light in the direction of the main beams: since this light is coherent with that of the main beams, spurious fringes are generated that may also have a high contrast; this phenomenon can be eliminated by treating the concerned areas with an anti-reflective coating (e.g. $MgFl_2$ reflecting only 4% of incident light);
- laser light is diffracted on each object placed in the beam out of focus, including dust particles and fingerprints on lenses and mirrors: diffracted light is coherent and produces other spurious fringes; this requires an extreme and continuous cleaning of the optics surfaces. The problem is greatly alleviated if the laser beam is passed through a spatial filter (see Section 4.2.5).

6.7.3 Wollaston prism interferometer

A scheme of this type of differential interferometer is shown in Figure 6.34. The configuration is similar to that of a Schlieren system in which the knife is replaced by a Wollaston prism between two crossed polarizers. In its no-fringe basic configuration, the center of the prism coincides with the focus of the second Schlieren lens [9].

The Wollaston prism (Figure 6.35) consists of two prisms of bi-refracting material such as quartz or calcite, glued together so that the optical axes of the two prisms are mutually perpendicular. The effect of the prism is to separate a ray of incident light into two diverging rays that are linearly polarized in directions perpendicular to each other.

Figure 6.34 **A differential interferometer with a Wollaston prism**

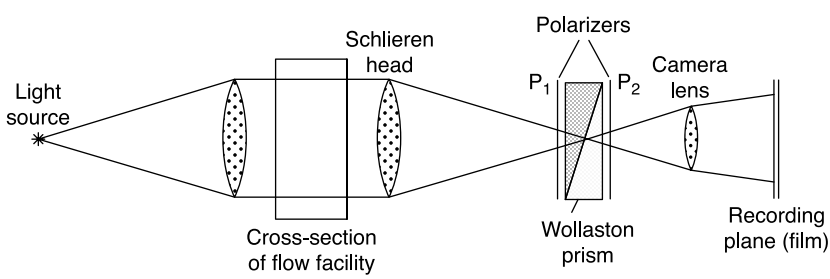

Source: [4]

Figure 6.35 Separation of the rays in a Wollaston prism

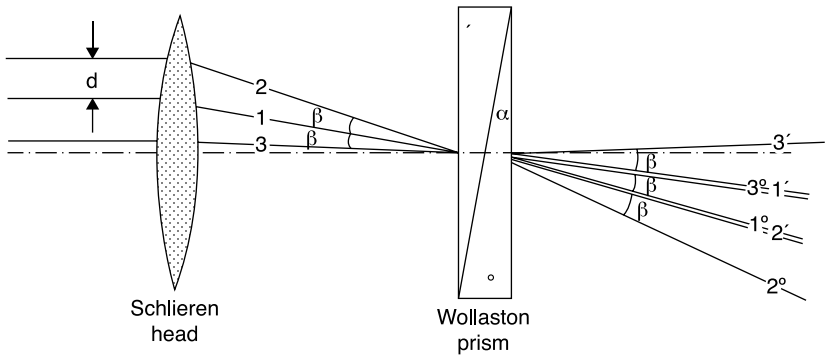

Source: [4]

An incident ray is in fact separated in the first part of the prism in an ordinary and an extraordinary ray that propagate at different speeds and are therefore subject to different indices of refraction, n_o and n_e. Due to the orientation of optical axis, the ordinary ray of the first part of the prism becomes extraordinary for the second prism and vice versa, so these two components are separated by an angle $\beta = 2\alpha(n_e - n_o)$, considering that the angle α of the prism is small.

The incident ray 1 is thus separated into two rays 1′ and 1° polarized and forming an angle β (the symbols ′ and ° indicate the direction of polarization in the plane of the figure and perpendicular to it respectively). In the convergent beam, hitting the prism is ray 2 forming an angle β with ray 1, which is separated into 2′ and 2°; ray 2′ therefore overlaps 1° and they may interfere only if they have an equal polarization direction; this condition is achieved through the polarizer, P_2, which is rotated 45° with respect to the two directions ° and ′. The optical axis of the polarizer P_1 is parallel or normal to that of the polarizer P_2 in order to make the two interfering beams of the same intensity. The same procedure applies to rays 1 and 3 (1′ and 3° can interfere), and so on. The interfering rays come from different points of the test chamber, which they crossed separated by a distance $d = \beta \star f_2$. If these rays pass through regions of different refractive index, they have a phase difference that produces interference.

The edges of rigid bodies normal to the separation distance d will appear with a double image or gray zone of thickness d (or $d_* \cos\gamma$ where γ is the angle between the normal to the edge and the separation distance d). The formation of this double image is due to the fact that the wall stops one of the two beams that should interfere.

A shift s of the prism along the optical axis of the lens with respect to the focus of the Schlieren involves the formation of parallel and equidistant fringes on the screen. The thickness of the fringes in this mode of operation, fringes of finite width, is inversely proportional to s:

$$w = \frac{\lambda f_2}{\beta s} = \frac{\lambda f_2^2}{ds} \tag{6.22}$$

A rotation of the prism around the optical axis causes the rotation of the system of fringes. The configuration shown in Figure 6.34 requires a point light source or a laser. If such a source is not available, a configuration with two Wollaston prisms has to be used: the rays of light separated in the first prism are recombined in the second prism (Figure 6.36). The purpose of the first prism is to improve optical coherence and it is clear that the two prisms must be identical.

Figures 6.37, 6.38 and 6.39 show the interferograms of a candle flame obtained with oblique, horizontal and vertical fringes and with zero fringes.

Of particular interest is the visualization of a shock wave. Due to the high density gradient across the wave, the configuration of the fringes cannot be treated with the linearized Equation (6.16) and the full Equation (6.14) must be taken into account. Only the pairs of conjugate rays that pass one upstream and one downstream of the shock wave can contribute to the formation of the configuration. The wave, with infinitesimal thickness, appears thick d or $d\cos\gamma$ in analogy with the formation of double image of the edges of rigid bodies already described above.

In the method of pre-existing fringes, the shock wave cannot be

Figure 6.36 **Interferometer with two Wollaston prisms; shown here is the light source side, the right side is equal to that of Figure 6.34 without the polarizer P_1**

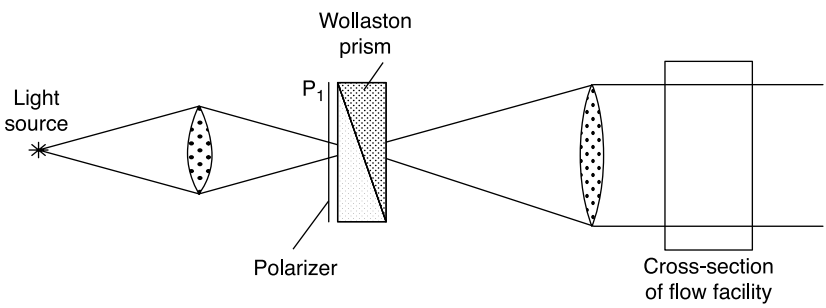

Source: [4]

Figure 6.37 Schlieren interferogram of a candle flame. Oblique fringes; on right, zero fringes

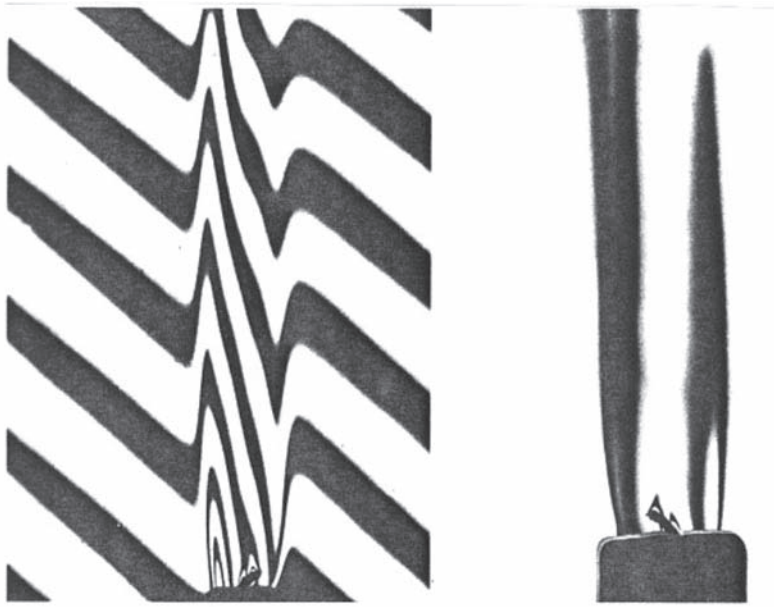

Source: [4]

Figure 6.38 Schlieren interferogram of a candle flame. Horizontal fringes; on right, zero fringes

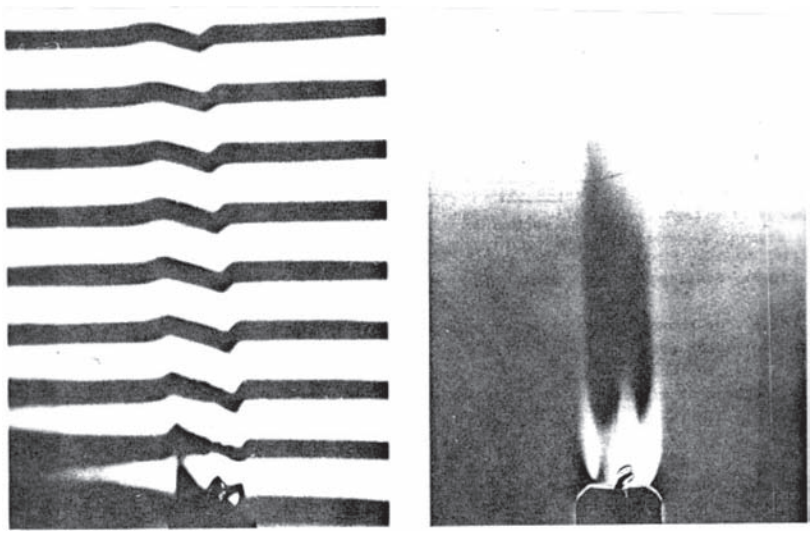

Source: [4]

Figure 6.39 Schlieren interferogram of a candle flame. Vertical fringes; on right, zero fringes

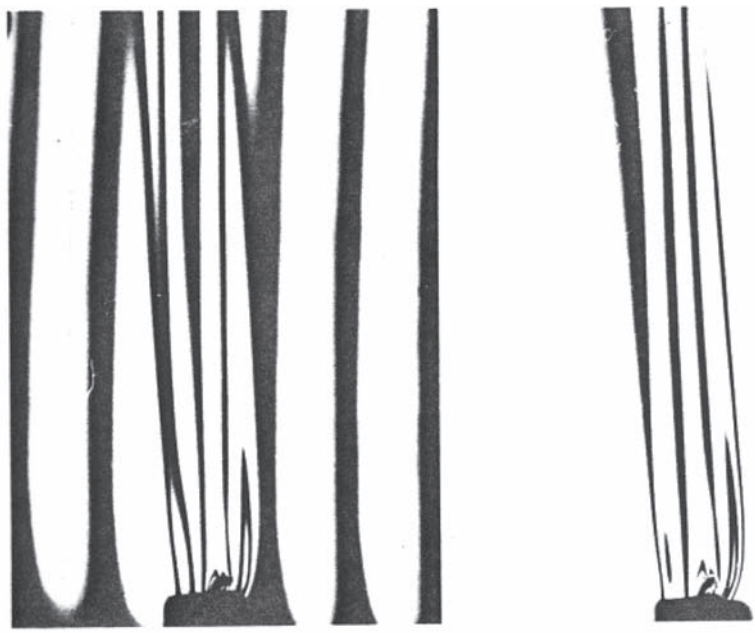

Source: [4]

displayed with fringes normal to the wave (γ= 90°). It is not convenient to have fringes parallel to the wave, it is preferable to use oblique fringes (Figure 6.40); from the relative displacement of the fringes it is possible to calculate the density jump across the wave.

6.7.4 The reflection plate interferometer

The simplest differential interferometer [10] consists of a glass plate on which the rays reflected from the first and the second surface of the plate are made to interfere. The plate can be put immediately after the test chamber before the second mirror of the Schlieren system. In this case, a beam of parallel rays hits the plate (Figure 6.41): ray 1 is reflected in part on the upper surface of the plate (ray 1′) and partly propagates within it undergoing a refraction in passing from air to glass. The ray refracted, in turn, partly passes into the air and is in part reflected by the lower surface and refracted through the upper surface (ray 1″). Among all the rays that reach the plate, there is a ray 2 that produces a reflected

Figure 6.40 Schlieren interferogram of a shock wave with vertical or oblique fringes

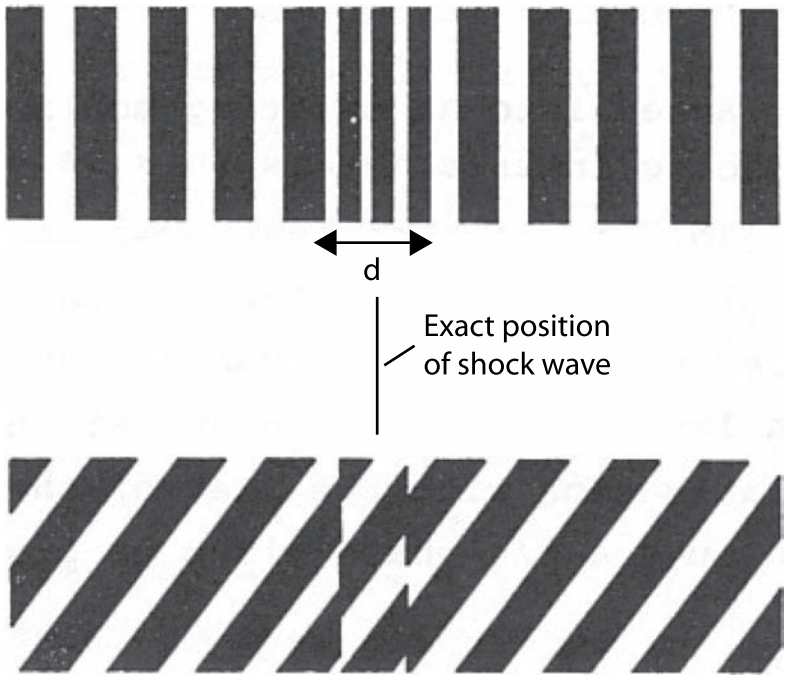

Source: [4]

ray 2′, overlapping 1″ and giving rise to interference. Similarly, there is a radius 3 that generates a ray 3′ interfering with the ray 2″, and so on. The difference in optical path between interfering rays is equal for all rays and is given by the geometric path of the refracted ray in the slab, multiplied

Figure 6.41 Reflection plate interferometer. Parallel rays

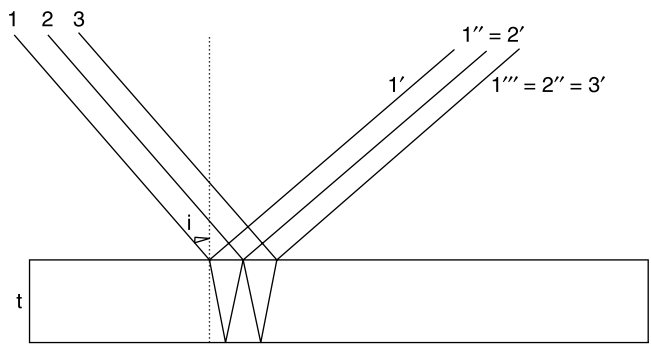

by the refractive index of glass, n_v, minus the path in air of the ray reflected from the upper surface, multiplied by the refractive index of air, n_a.

With simple geometrical considerations it is easy to write

$$\Delta\ell = 2t\sqrt{n_v^2 - n_a^2 \sin^2 i} \tag{6.23}$$

where t is the thickness of the slab and i is the angle of incidence of the beam on the plate.

If the beam has passed through an object with a constant density, interference fringes are not formed and the uniform brightness of the beam downstream of the plate (no fringes) depends on the optical path difference given by Equation (6.23). If the density of the test field is variable, interference fringes are formed that are loci of equal density gradient.

Separation distance between the interfering rays is given by

$$d = \frac{tn_a \sin 2i}{\sqrt{n_v^2 - n_a^2 \sin^2 i}} \tag{6.24}$$

In fact, in this type of interferometer, rays that interfere are more than two because there are multiple reflections inside the slab, for example, there will be a radius 1‴ which also interferes with the radius 3′, but successive reflections decrease in intensity and thus contribute more and more negligibly to the phenomenon of interference. Apart from the inability to generate finite width fringes, this type of interferometer is limited due to the fact that a plate of interferometric quality, which is therefore expensive, is needed.

These constraints can be removed if the plate is in the focus of the Schlieren system replacing the knife edge. The cone of light reflected from the first face of the plate interferes with the one refracted and then reflected from the second surface of the plate (Figure 6.42). The area of the plate affected by the cone of light is the order of mm^2 and therefore the quality of the slab is virtually irrelevant.

Since the single rays have different incidence on the plate, the optical paths are different from ray to ray, so even in the case of a uniform field, fringes will be present (finite width fringes), the width of which is at a first approximation inversely proportional to the thickness of the slab. The distance of separation of the rays that interfere at a distance D from the focus is given by:

$$d = \frac{tn_a \text{sen} 2i}{\sqrt{n_v^2 - n_a^2 \text{sen}^2 i}} \frac{f}{D} \tag{6.25}$$

Figure 6.42 Reflection plate interferometer in the focus of a Schlieren system

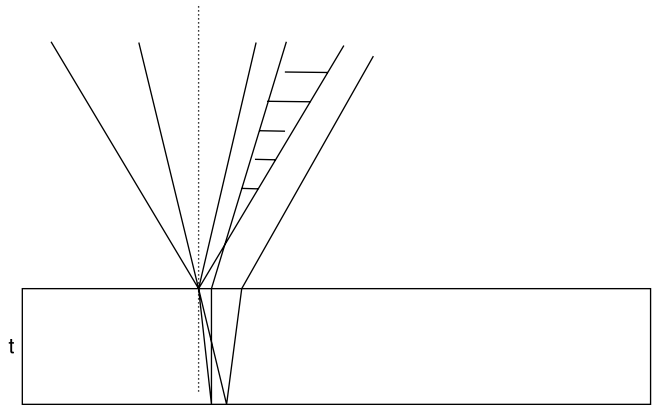

Source: [4]

Separation varies with the angle of incidence and therefore the sensitivity varies from point to point in the test section. The thickness of the fringes is given approximately by:

$$w \cong \frac{\lambda D}{\sqrt{\Delta \ell^2 + d^2}} \tag{6.26}$$

The choice of the angle of incidence is dictated by the need to have fringes as far as possible straight, parallel and of uniform thickness. Since the reflected rays from the first and second face of the slab can be considered as coming from two point sources, the surfaces of interference, constructive or destructive, are hyperboloids of revolution (Young's experience) that are the loci of points which have a constant geometric path difference between the two coherent sources in phase with each other (Figure 6.43).

It is obvious that the shape of the fringes depends on the position of the observer with respect to the line joining the two light sources (axis of revolution of the hyperboloid): circular, elliptic or hyperbolic fringes can be observed with increasing angles between the direction of observation and the axis of revolution.

In Figure 6.44 are shown fringes obtained at different angles of incidence with three plates of different thickness. With all the plates fairly straight and parallel, fringes are obtained with angles around 45°. At small angles of incidence, fringes are curved; at too large angles of incidence, the phenomenon of multiple reflections will take place with a

Figure 6.43 Standing waves produced by two sources in phase; on right, equal phase surfaces (hyperboloids)

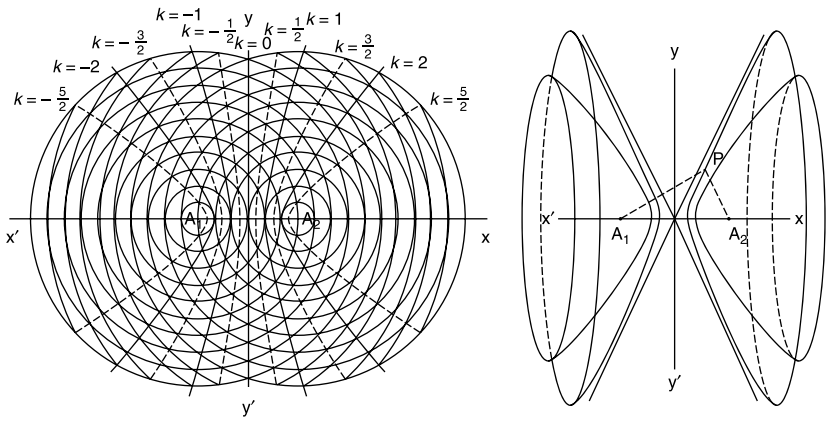

Figure 6.44 Fringes produced by plates of various thicknesses at different angles of incidence

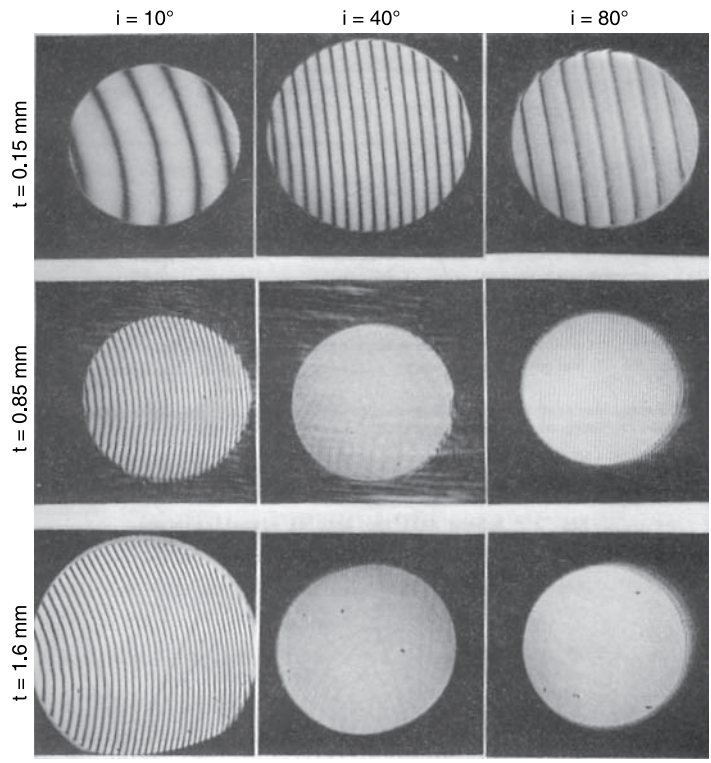

Source: [11]

loss of sharpness of the fringes. Few fringes are generated by the thinner slide (t = 0.15 mm) and fringes too numerous and almost indistinguishable with the thickest one (t = 1.60 mm).

6.8 Quantitative analysis of Schlieren images and interferograms

6.8.1 Problem set-up

The objective of the analysis is the determination of the function $n(x, y,z)$ by Equations (6.10), (6.15) and (6.16) depending on the type of optical system: Schlieren, separated beams interferometer or differential interferometer, respectively. In general, this problem has no solution, unless the test field shows some kind of geometric symmetry allowing a reduction of the independent variables of the function $n(x,y,z)$ from three to two.

The analysis of an arbitrary field would require many images of the field taken from various angles. If the field has some symmetry, the number of images required is reduced: a single image is sufficient in the case of a two-dimensional plane field or of an axially symmetric field with an axis of symmetry normal to the direction of observation.

6.8.2 2D plane fields

Equations (6.10), (6.15) and (6.16) can be immediately solved if the index of refraction n is independent of z, i.e. if $n = n(x,y)$. Quasi two-dimensional fields can be achieved in a test chamber of a wind tunnel if the model has a constant section and extends from one window to the other, and the direction of the rays, z, is normal to the entry windows. The presence of the windows is equivalent to a jump in the index of refraction along the z axis.

In the case of a Schlieren system, light rays pass undisturbed through the first window of the test chamber, which is normal to the direction of the rays, all parallel to the axis z (Figure 6.45). On the output window, a ray deflected of the angle θ_x, given by Equation (6.7), will pass in the outside environment, of refractive index n_a, with the angle given by the equation:

$$n_a \operatorname{sen}\theta_a = n \operatorname{sen}\theta_x \quad \Rightarrow \quad \theta_a \cong \frac{n}{n_a}\theta_x \tag{6.27}$$

Figure 6.45 **Deflections of light rays passing through a test chamber bounded by two glass windows**

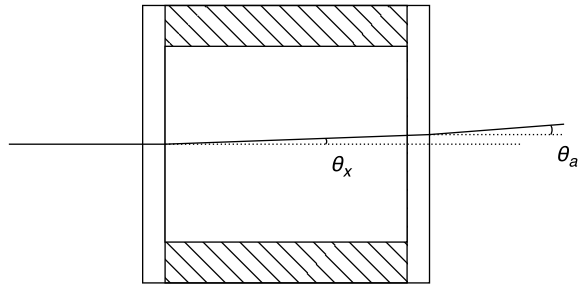

Then the local contrast, for Equations (6.10) and (6.27), is given by:

$$C(x,y) = \frac{\Delta I(x,y)}{\bar{I}} = \frac{f_2 L}{a}\frac{1}{n_a}\frac{\partial n(x,y)}{\partial x} \tag{6.28}$$

The index of refraction can be calculated in a point (x, y) by integrating the measured contrast on a Schlieren image from a point (x_0, y), where the index is known, through the equation:

$$n(x,y) - n(x_0,y) = \frac{a n_a}{f_2 L}\int_{x_0}^{x} C(x,y)\,dx \tag{6.29}$$

In the case of a separated-beams interferometer, the effect of the windows is eliminated by including in the reference path two compensation plates having the same thickness and the same quality of the windows, or by passing the reference beam in a zone of the test chamber where density is a constant. Equation (6.15) gives then:

$$n(x,y) - n_0 = \frac{\Delta\ell(x,y)}{L} \quad \text{i.e.} \quad \rho(x,y) - \rho_0 = \frac{\Delta\ell(x,y)}{K(\lambda)L} \tag{6.30}$$

In the case of *differential interferometry*, the effect of the windows of the test chamber is irrelevant because both interfering rays pass through the test chamber and then through the same windows. The index of refraction can be calculated by Equation (6.16):

$$n(x,y) - n(x_0,y) = \frac{1}{Ld}\int_{x_0}^{x} \Delta\ell\,dx \tag{6.31}$$

In both classes of interferometers the difference of optical paths can be related to the displacement of the fringes, Δw, and to the wavelength, λ, of light. The displacement of the fringes produced by the disturbance is given by:

$$\xi(x,y) = \frac{\Delta w(x,y)}{w} = \frac{\Delta \ell(x,y)}{\lambda} \tag{6.32}$$

The sensitivity, s, of the interferometer is defined as the fringe shift divided by the jump of index of refraction

$$s = \frac{\Delta w(x,y)/w}{\Delta n(x,y)} = \frac{\Delta \ell(x,y)}{\lambda \Delta n(x,y)} = \frac{L}{\lambda} \tag{6.33}$$

Equations (6.30) and (6.31) allow, taking into account Equation (6.32), the calculation of the index of refraction in terms of fringe shift:

$$n(x,y) = n_0 + \frac{\xi(x,y)\lambda}{L} \text{ separated-beams interferometer} \tag{6.30′}$$

$$n(x,y) = n(x_0,y) + \frac{\lambda}{Ld}\int_{x_0}^{x} \xi(x,y)\,dx \text{ differential interferometer} \tag{6.31′}$$

In the case of infinite width fringes, the resulting fringes are curves of constant refractive index (separated-beams interferometer) or curves of constant gradient of refractive index (differential interferometer). Recalling Equation (6.13), the difference in refractive index between two consecutive fringes in separated-beams interferometer is simply:

$$n_{N+1} - n_N = \frac{\lambda}{L} \tag{6.34}$$

and the difference in gradient of refractive index between two consecutive fringes in the differential interferometer is:

$$\left(\frac{\partial n}{\partial x}\right)_{N+1} - \left(\frac{\partial n}{\partial x}\right)_N = \frac{\lambda}{Ld} \tag{6.35}$$

6.8.3 Axially symmetric fields

Assume that the field is symmetrical about the x axis and that the direction of observation is z (Figure 6.46). The local value of the refractive index becomes a function of x and $r = \sqrt{y^2 + z^2}$ where r is the distance from the axis of symmetry.

Assuming that the rays of light go through the test section along the z direction, as in the case of Figure 6.46, if there is no refraction on the edge of test section, i.e. if $n(r_\infty) = n_0$, the problem can be solved transforming Equations (6.10) (6.15) and (6.16) in the axially symmetric coordinate system:

In the Schlieren system:

$$\frac{C(y)}{y} = \frac{2f_2}{a}\int_{r=y}^{r=r_\infty} \frac{d\ln n(r)}{d\left(r^2\right)} \frac{d\left(r^2\right)}{\sqrt{r^2 - y^2}} \tag{6.36}$$

Figure 6.46 Cross-section of an axially symmetric field

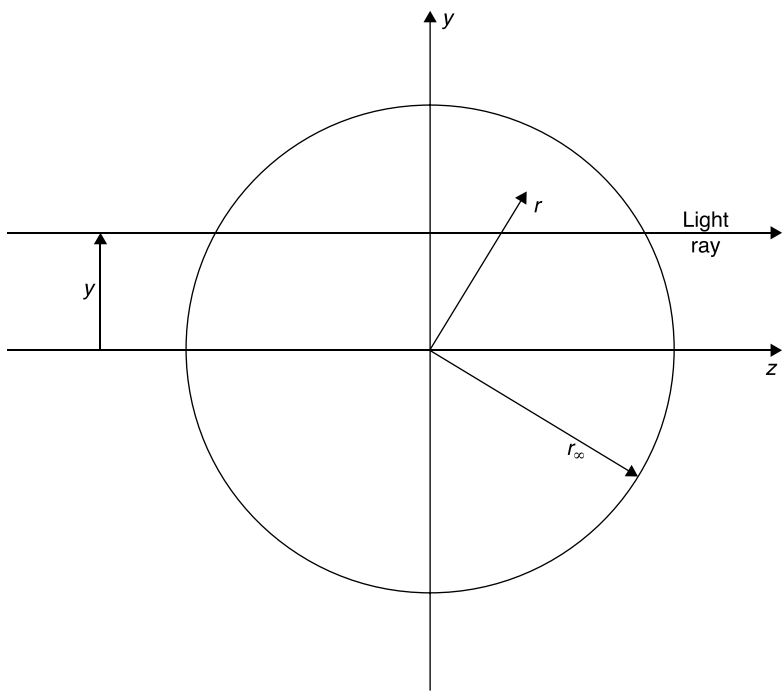

Source: [4]

In the separated-beams interferometer:

$$\Delta\ell = \int_{r=y}^{r=r_\infty} \left[n(r) - n_0 \right] \frac{d\left(r^2\right)}{\sqrt{r^2 - y^2}} \tag{6.37}$$

In the differential interferometer:

$$\frac{\Delta\ell}{y} = d\int_{r=y}^{r=r_\infty} \frac{dn(r)}{dr^2} \frac{dr^2}{\sqrt{r^2 - y^2}} \tag{6.38}$$

The integration is performed starting from the y coordinate of the ray in question until the outer radius, r_∞ enclosing the axisymmetric field is reached. It is assumed that the index of refraction is $n_\infty = n_0 = \text{const}$ for $r > r_\infty$, i.e. outside the test field.

Equations (6.36), (6.37) and (6.38) are integral equations of the Abel type. The quantity to be determined, n or dn/dr, must be calculated from inside the integral. In principle, there are two ways to solve this problem. The first way is analytic (Abel inversion). The solution can be obtained by applying to both sides once again the operator

$$\int_r^{r_\infty} [\cdots\cdots] \frac{d\left(y^2\right)}{\sqrt{r^2 - y^2}}$$

and reversing the order of integration in the double integral created at the second member. For example, in the case of separated-beams interferometer, Equation (6.37), the Abel inversion provides:

$$n(r) - n_0 = -\frac{1}{\pi} \frac{d}{d\left(r^2\right)} \int_r^{r_\infty} \Delta\ell(y) \frac{d\left(y^2\right)}{\sqrt{r^2 - y^2}} \tag{6.39}$$

The integration should be done on the measured function $\Delta\ell(y)$, difference of the optical paths. Since this is available as a set of discrete values, these values should be fitted with an appropriate analytic function. A disadvantage of this approach is the further differentiation of the function needed in Equation (6.39).

Applying the Abel inversion to Equations (6.36) and (6.38), is obtained directly:

$$n(r) - n_0 = -\frac{n_0 a}{\pi f_2} \int_r^{r_\infty} \frac{C(y)}{2y} \frac{d(y^2)}{\sqrt{r^2 - y^2}} \tag{6.40}$$

$$n(r) - n_0 = -\frac{1}{\pi d} \int_r^{r_\infty} \frac{\Delta \ell(y)}{y} \frac{d(y^2)}{\sqrt{r^2 - y^2}} \tag{6.41}$$

In the first member of Equation (6.38), the approximation was made:

$$\ln \frac{n(r)}{n_0} = \ln \left[1 + \frac{n(r) - n_0}{n_0} \right] \cong \frac{n(r) - n_0}{n_0}$$

Surprisingly the results for the differential interferometer, Equation (6.41), and the Schlieren system, Equation (6.40), are less complicated than that for the separated-beams interferometer, Equation (6.39), because the index of refraction can be achieved without the need for additional differentiation of the function approximating the experimental data.

Figure 6.47 **Subdivision of the axially symmetric field in annular zones with thickness *h***

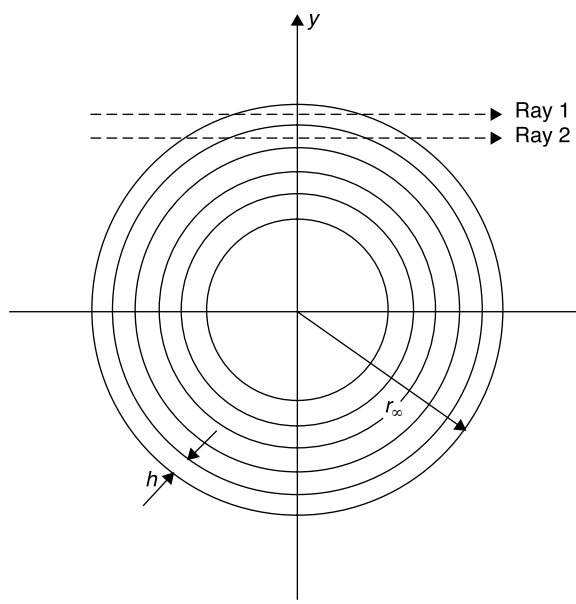

Source: [4]

The second method for solving the axially-symmetric problem prevents the use of the Abel inversion through a numerical procedure. To this end, the cross-section of the axially-symmetric field is divided in rings of radius r (Figure 6.47). The amount to be determined is a supposed constant in each zone. The procedure is a step-by-step solution that starts from the outer edge r_∞ of the field and can be easily computed.

References

1. C.R. Smith and R.D Paxson (1983) "A technique for evaluation of three-dimensional behavior in turbulent boundary layers using computer augmented hydrogen bubble wire flow visualization," *Exp. Fluids* 1: 43–9.
2. F.A. Schraub, S.J. Kline, J. Henry, P.W. Runstadler, and A. Little (1965) "Use of hydrogen bubbles for quantitative determination of time-dependent velocity fields in low-speed water flows," *J.Basic Eng.* 87: 429–44.
3. R.L. Maltby and R.F.A. Keating (1962) "The surface oil flow technique for use in low speed wind tunnels," Part I.3 in *Flow Visualization in Wind Tunnels Using Indicators*, compiled by R.L. Maltby, AGARDograph 70.
4. W. Merzkirch (1987) *Techniques of Flow Visualization*. AGARD-AG-302.
5. H.W. Liepmann and A. Roshk (1960) *Elements of Gas Dynamics*. New York: John Wiley & Sons, Inc.
6. L. Howarth (ed.) (1953) *Modern Developments in Fluid Dynamics: High Speed Flow*. Oxford.
7. B. Landenburg and D. Bershader (1954) *Interferometry*, A,3 in Part 1 of *Physical Measurements in Gas Dynamics and Combustion*, R. Landenburg ed., vol. IX of *High Speed Aerodynamics and Jet Propulsion*. Princeton, NJ: Princeton University Press.
8. H.I. Ashkenas and A.E. Bryson (1951) "Design and performance of a simple interferometer for wind tunnel measurements," *J. Aeronaut. Sci. 18*: 32.
9. R.D. Small, V.A. Sernas and R.H. Page (1972) "Single beam Schlieren interferometer using a Wollaston prism," *Applied Optics* 11(4), April.
10. L.H. Tanner (1965) "Some laser interferometers for use in fluid mechanics," *J. Sci. Instrum.* 42: 834–7.
11. G.P. Russo and V. Marzuillo (1982) "*Un Sistema di Visualizzazione Multiruolo per Applicazioni Termofluidodinamiche*", Atti del VI Congresso Nazionale dell'AIMETA, Genova, 7/9 October, pp. 245–56.
12. R.C. Pankhurst and D.W. Holder (1952) *Wind tunnel technique*, London: Pitman.

7

Measurements of aerodynamic forces

Abstract: This chapter highlights methods used to measure the forces acting on a model in a wind tunnel: from pressure measurements on the surface or in the wake of the body to counterweight, strain-gage and magnetic suspension balances.

Key words: counterweight balances, magnetic balances, strain gages balances.

7.1 Types of supports for models in wind tunnels

Measuring the aerodynamic forces acting on a stationary model in a test chamber of a wind tunnel is easier than measuring the same forces on a model in free flight or put into rotation by a windmill. Nevertheless, this measure is very sensitive to the almost inevitable interference of the support system on the aerodynamics of the model that comes in addition to the interference of the walls, real or virtual, of the test chamber. Only magnetic levitation of the model is free from support interference, but so far it has been tested only on simple models in small research wind tunnels.

The support system of the model in the test chamber must allow both the necessary rigidity (it requires that the maximum error in the angle of attack be in the order of one-hundredth of a degree) and the ability to change the set-up at will (in stationary tests to evaluate the polar and in unsteady tests, with oscillating or rotating models, to measure the derivatives of stability).

Models of complete airplanes are usually supported in the center of the test chamber:

- in the classic layout (Figure 7.1), with three parallel rigid rods (two hinged under the wings and one under the tail), the variation of the angle of attack is obtained by moving the tail support vertically; the three rods are partially shielded with fairings fixed to the floor in order to reduce their aerodynamic drag;
- rarely used are pyramidal supports, which, as we shall see, would allow a better resolution of forces;

Figure 7.1 **Airplane model on three parallel supports in the 5-metre pressured low speed wind tunnel at DRA in Farnborough**

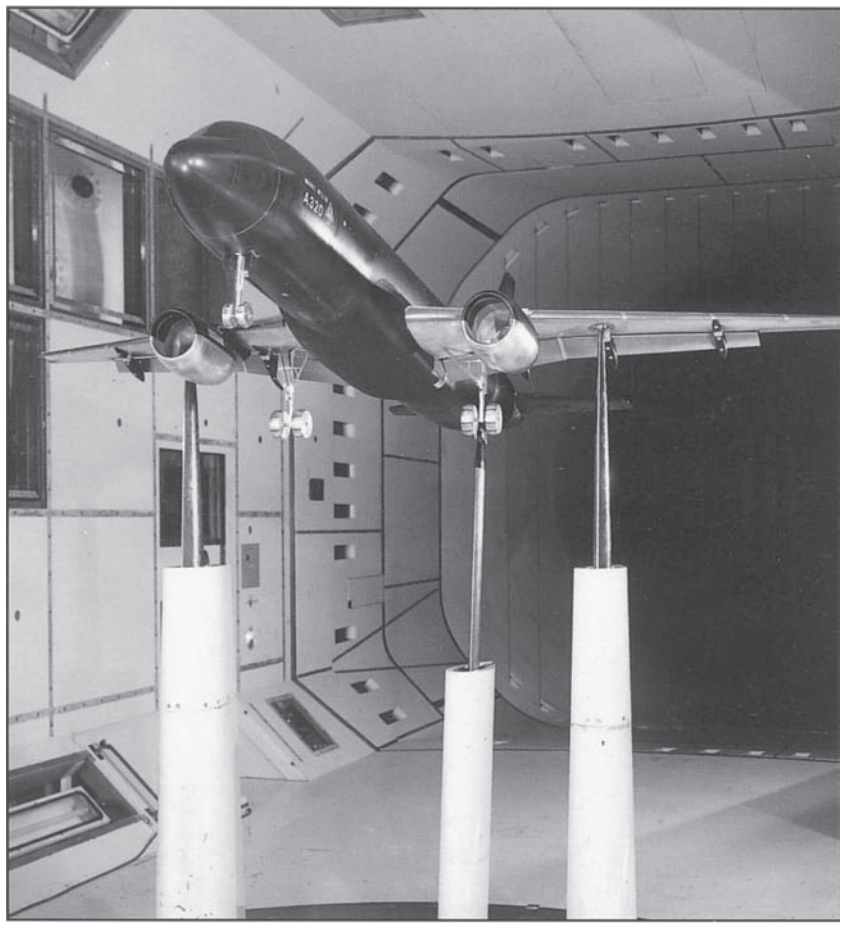

- in the first wind tunnels, suspension wires were used which had the advantage of not transmitting moments; with time it was found that the wakes of the threads produced more interference than shielded rigid rods and furthermore induced a drag that was ten times that of the tested model;
- in the transonic field, and even more in the supersonic field, the presence of any support generates shock waves that interfere with those generated by the model. The solution consists in adopting a less interfering back support (*sting*) that, however, since it eliminates the wake, alters the base drag. This support allows large variations of the angle of attack (Figure 7.2) and therefore is particularly suitable for testing (also in a subsonic stream) models of combat aircraft that fly with high angles of attack, even beyond stall.

The stings may take a variety of shapes depending on the model tested, the type of interference preferred, stiffness required: straight

Figure 7.2 Swiveling sting support

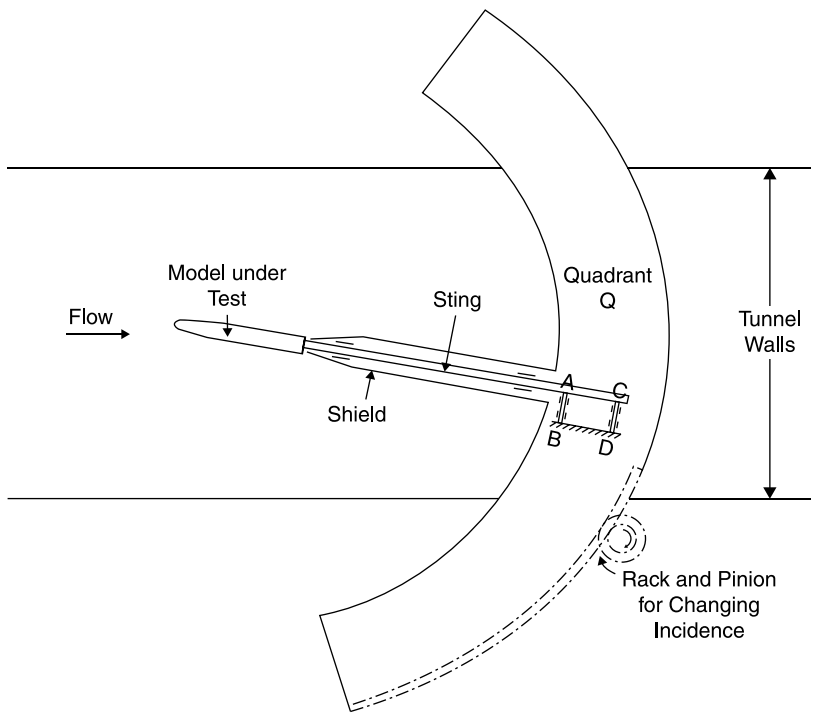

support, double sting and Z support are shown in Figures 7.3, 7.4 and 7.5.

Figure 7.3 Straight sting support

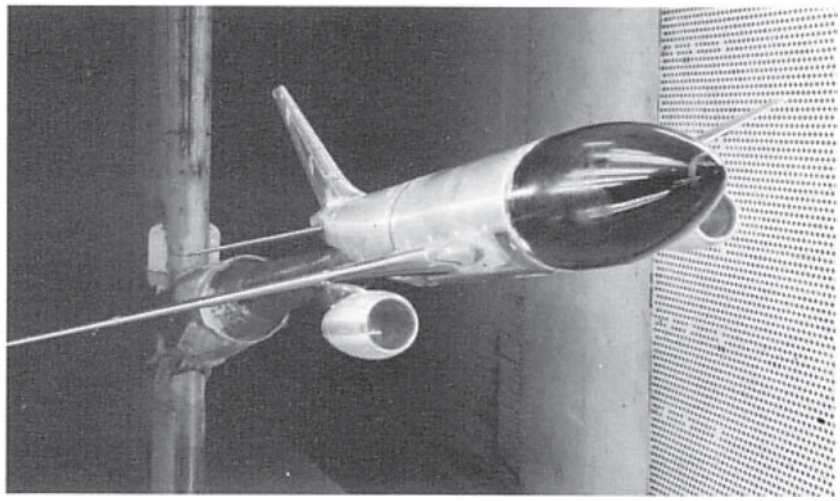

Source: ARA Transonic wind tunnel TWT, Bedford, UK

Figure 7.4 Double sting

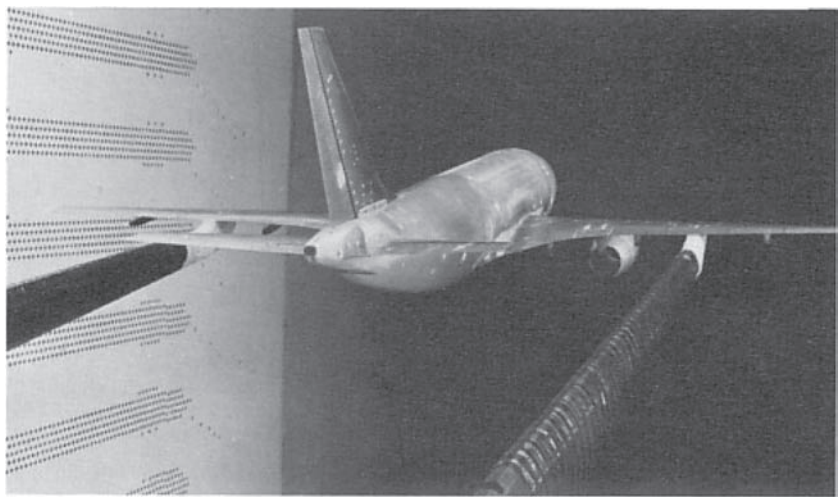

Source: ARA, Bedford, UK

Figure 7.5 **Airbus model on variable elbow sting in a transonic wind tunnel**

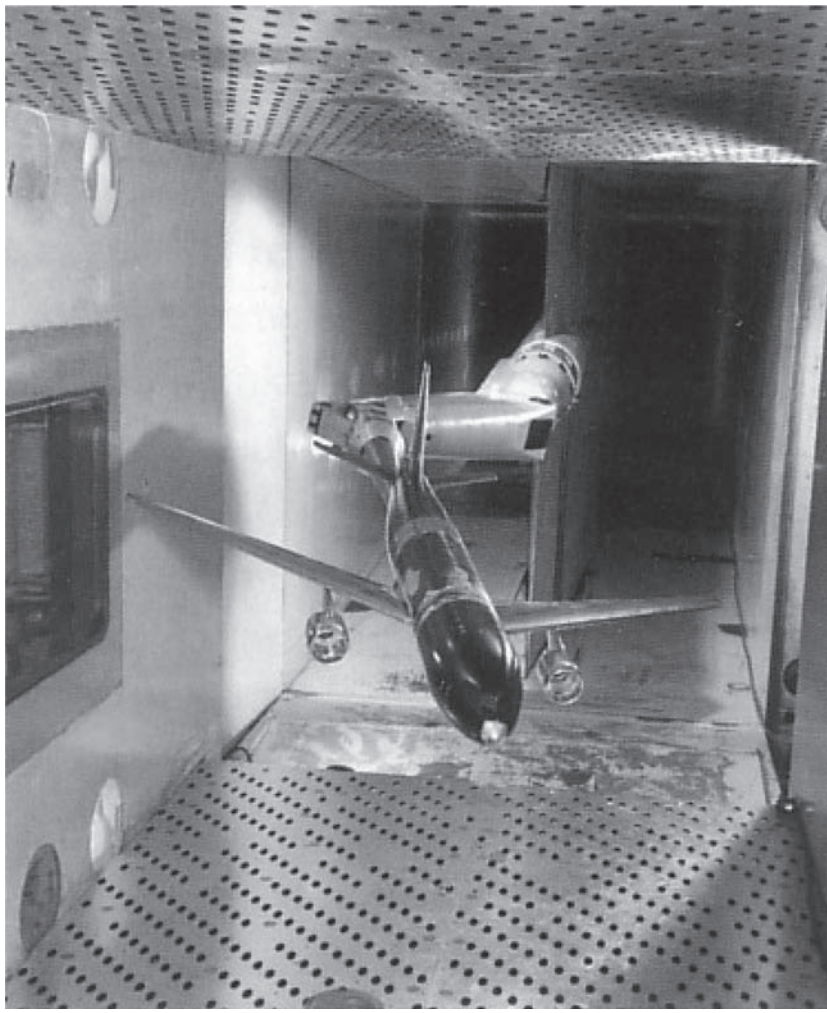

Source: ONERA S2MA

If tests are performed in the presence of ground (automobiles, trains, airplanes taking off and landing, air cushion vehicles), and models are particularly heavy, the models rest on the floor of the test chamber that is also the platform of the balance (Figure 7.6), in this case the floor does not properly simulate the runway or the street since a boundary layer grows on the floor of the test chamber that is not present on the road. It is necessary in these cases that the boundary layer be removed immediately

Figure 7.6 A Ferrari F–1 car in the FIAT Research Center wind tunnel at Orbassano, Turin, Italy, 1976

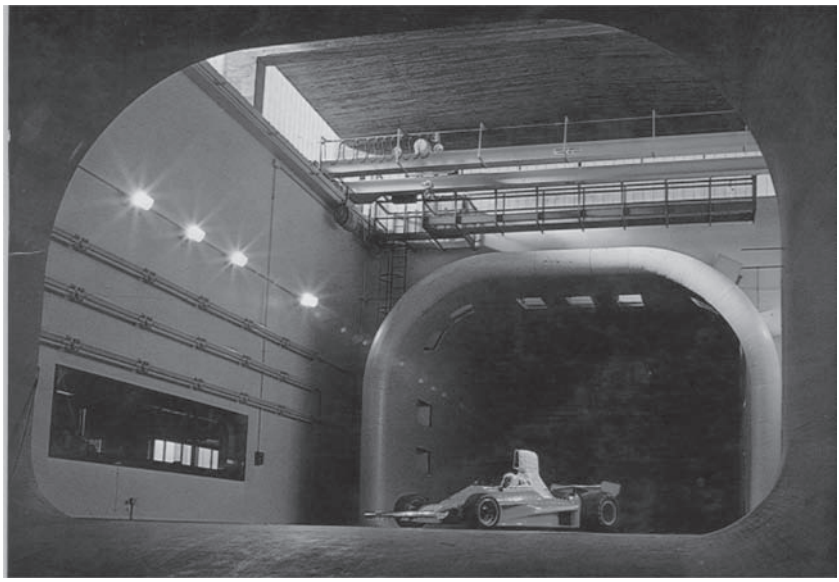

upstream of the model or a moving belt traveling at the same speed of the flow be provided on the floor.

A 2D model, an airfoil, must go from wall to wall in the test chamber (even in open test chambers, two parallel walls are needed to support the model), and is typically mounted on a tube going through the two walls allowing the change in the angle of attack of the model (Figure 7.7). Great attention must be paid in ensuring the seal between model and walls to prevent communication between the lower and the upper sides of the model which would lead to the formation of tip vortices, typical of finite wings, and the destruction of two-dimensionality of the motion, already compromised by the presence of the boundary layer on the two walls. In this way the model is not free to move and the aerodynamic force cannot be measured with balances and must be calculated from pressure measurements made in a row of holes on the centerline of the model.

In some cases, in order to double the Reynolds number referred to the chord of the wing, half-models are used mounted on a wall of the test chamber, simulating the plane of symmetry of the airplane (ignoring in this case the presence of the boundary layer). The model is fixed on a

Figure 7.7 An airfoil NACA-0012 in the adaptive-walls wind tunnel at DIAS at University Federico II in Naples, Italy

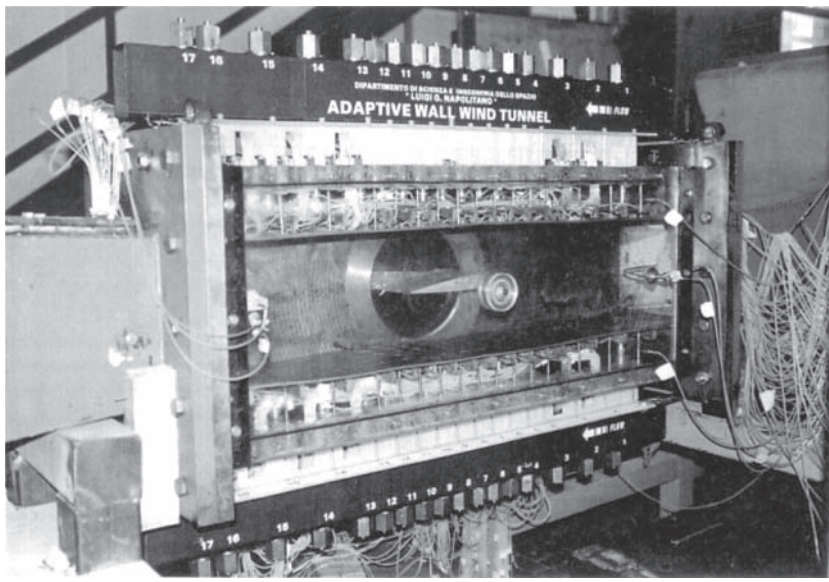

circular support flush with the wall (Figure 7.8) with a variable incidence with respect to the direction of the asymptotic velocity.

With fixed models the behavior of the aircraft during maneuvers cannot be studied; supports oscillating in a vertical plane (Figure 7.9) or rotating (Figures 7.10 and 7.11) must be used.

Another important problem is to evaluate the aerodynamic interference between two bodies that fly close to each other: this is the case of a bomb, a missile, an ejection seat or a tank dropped from an airplane or the presence of a tanker refueling the airplane. The classic technique used to test in a wind tunnel the trajectory of loads dropped from planes is to follow with a video camera the free-fall of models of the store with a properly scaled density (models made with balsa wood), position of center of gravity and moments of inertia. At the end of the 1970s another technique was established, known as *captive trajectory store testing*: models of aircraft and store are supported separately (Figures 7.12 and 7.13) and the store is moved according to a trajectory calculated by a computer in real time, taking into account the inertial characteristics of the model and the measured aerodynamic forces.

Figure 7.8 A wall-mounted Airbus half-model in a transonic wind tunnel

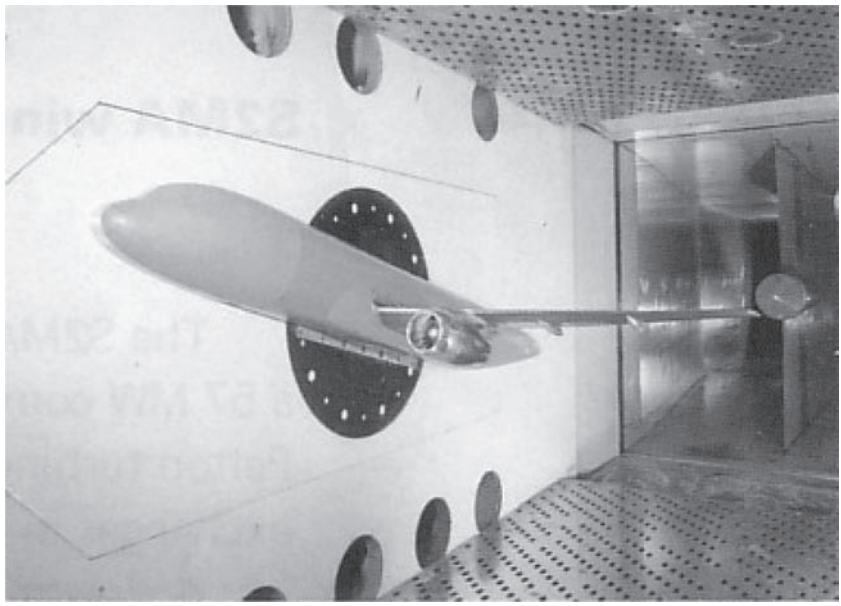

Source: ONERA S2MA

Figure 7.9 A model of fighter airplane on an oscillating support

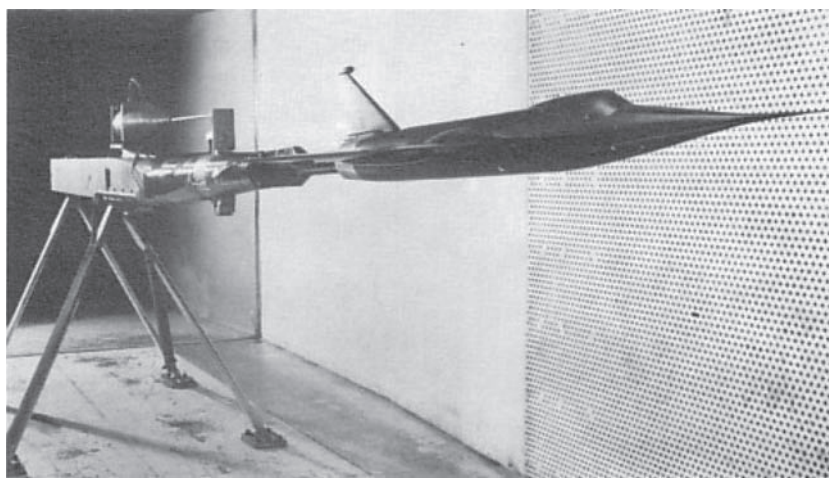

Source: RAE oscillating rig, UK

Figure 7.10 Model of the Euro-fighter aircraft on a rotating balance

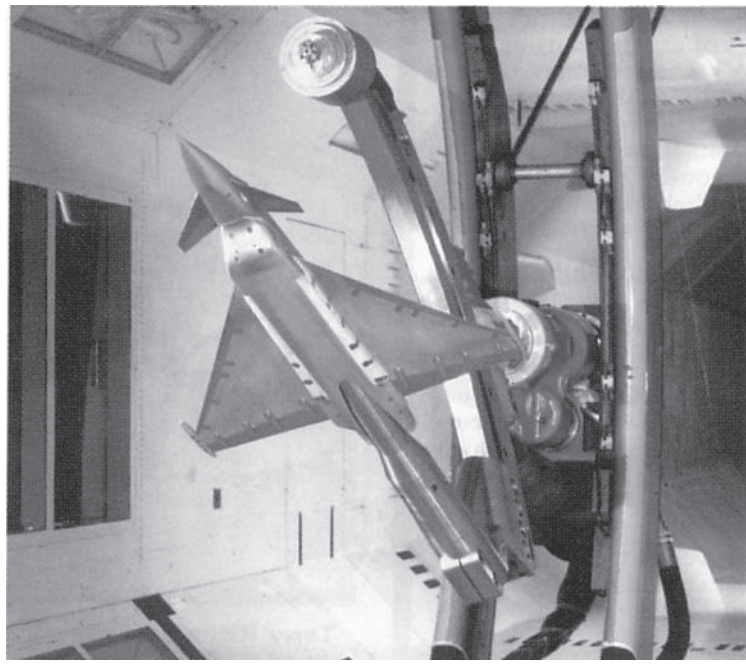

Figure 7.11 Schematic of the rotating balance at ARA Bedford, UK

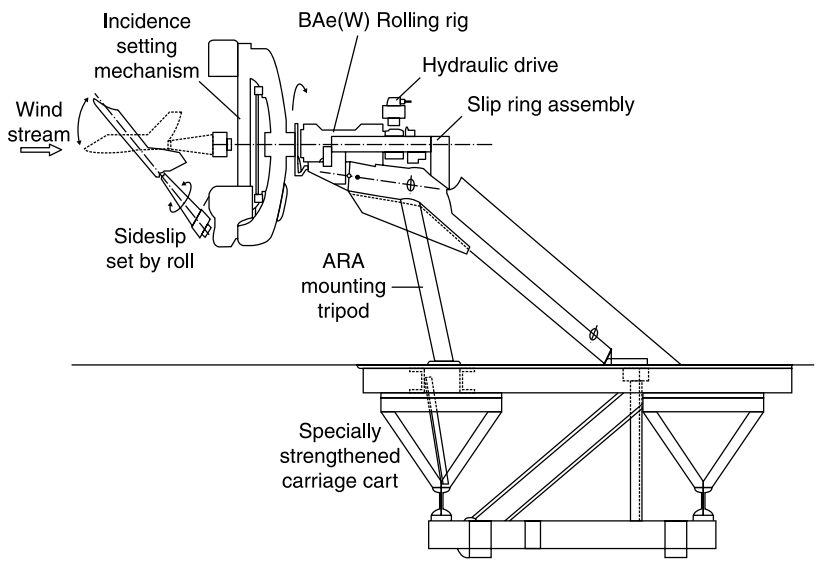

Figure 7.12 TSR (Two Sting Rig) captive store trajectory simulator at ARA, Bedford, UK

Figure 7.13 Schematic of the captive store trajectory system at ARA, Bedford, UK

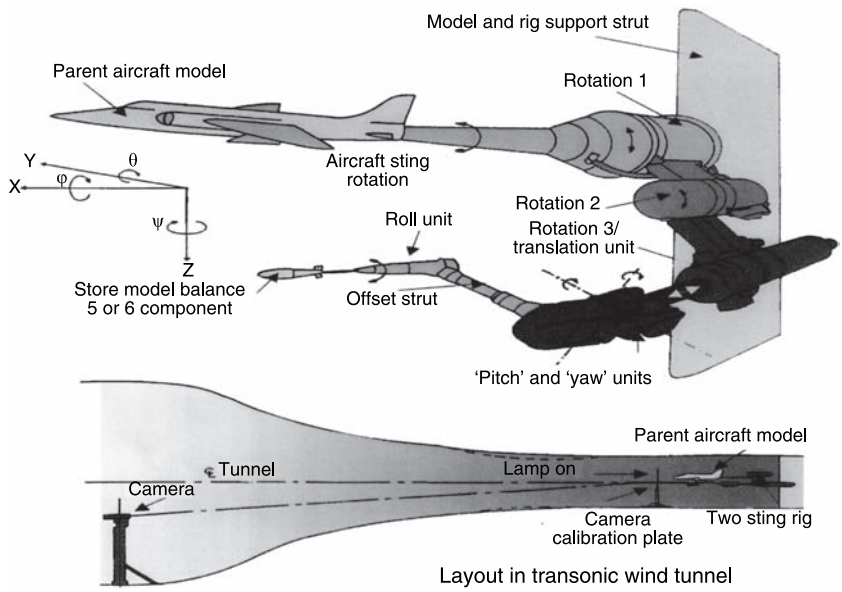

Layout in transonic wind tunnel

7.2 Calculating the aerodynamic forces from pressure measurements

Lift, pitching moment and *form drag* acting on a model can be determined by integrating the measured pressure distribution on the surface.

If the model is 2D (an airfoil) the so-called *indirect method* could also be used to calculate:

- *profile drag* by measuring the losses of stagnation pressure in the wake (conservation of momentum in the direction of the asymptotic velocity);
- *lift,* in a wind tunnel with a closed test chamber, by the distribution of pressures on the two walls perpendicular to those supporting the model (conservation of momentum in the direction normal to the direction of the asymptotic velocity).

The *friction drag* could be calculated by measuring the stagnation pressure near the surface or it could be calculated for 2D models by the difference between profile drag and form drag.

Although the determination of the forces and moments with these methods is often considered only as an alternative to a balance, it should be noted that:

- pressure measurements provide, besides the resulting forces, a large amount of local information and, while it is possible to integrate the distribution of pressure to obtain the forces, it is not possible, conversely, to derive the distribution of pressures from the forces measured with balances;
- the determination of the forces from pressure measurements are well suited only for airfoils and 2D bodies of revolution, as in 3D models the measure of pressure becomes cumbersome even in the simplest cases and the data processing is more laborious than for measurements made with balances: an accurate 3D test requires a large number of holes and tubes, in the order of hundreds (Figure 7.14);
- as has been said, the only possible method for the determination of aerodynamic forces on 2D models is based on pressure measurements;
- in some cases, the model may be too small to allow a sufficient number of pressure taps to be made on the surface;
- at supersonic speeds, the method of exploration of the wake may be inaccurate.

Figure 7.14 A wing model of a Fokker plane with 250 holes and pressure pipes

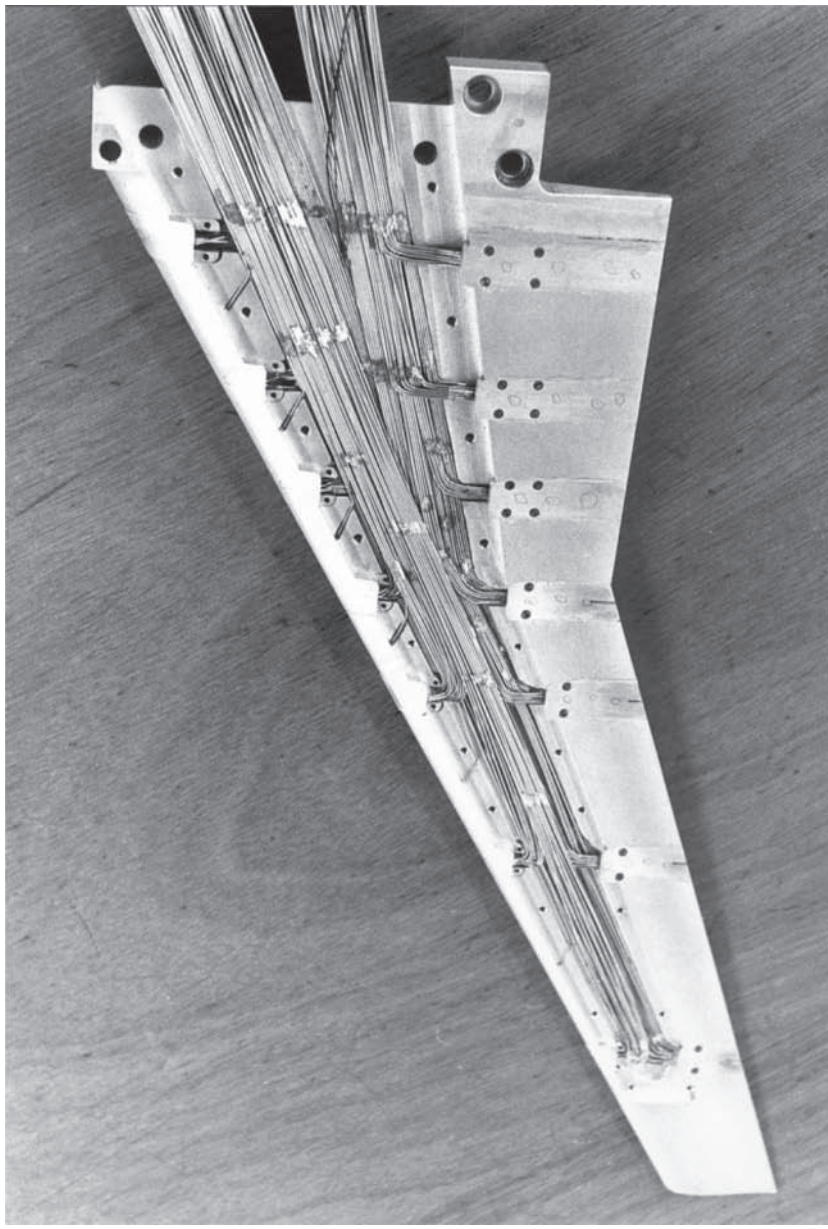

In each case, what the most appropriate method to be adopted must be evaluated. In the development of a new airplane, pressure measurements, usually combined with flow visualization, are made even when the resultant forces are measured with a balance.

7.2.1 Calculation of lift, pitching moment and form drag by the distribution of pressures on the model

The distribution of the pressures acting on the model is measured in a number of holes drilled normal to the surface. Measuring instruments are:

- multitube manometer;
- transducers each connected in succession to the holes of one or more pneumatic scanning valves (Scanivalve, see Chapter 1);
- an electronic device scanning as many transducers as pressure taps.

Since the aerodynamic force is due to the difference between the pressure acting on the surface and the static pressure in the asymptotic stream, the tank of the multitube manometer or one of the chambers of each differential transducer is often put in communication with that pressure. The pressure coefficient

$$C_p = \frac{p - p_\infty}{\frac{1}{2}\rho U_\infty^2} = \frac{p - p_\infty}{q} \tag{7.1}$$

can be obtained then, in incompressible flow, dividing the readings of the differential multitube manometer by the reading of a differential pressure gage connected to a Pitot-static tube placed in the undisturbed stream.

Since the maximum pressure is the stagnation pressure, the maximum value of the pressure coefficient is $C_p = 1$ in an incompressible flow and slightly greater than 1 in a compressible flow. The negative pressure coefficient can reach the value $C_p = -10$

The distribution of pressure coefficients is given by a diagram in which is reported the coefficient normal to the surface (Figure 7.15) or to the main axis of the body, which, in the case of an airfoil, is the chord (Figure 7.16).

The force normal to the surface acting on an element of size $1_* ds$, is given by (Figure 7.15):

$$dF = C_p q ds \tag{7.2}$$

Figure 7.15 Distribution of the pressure forces on a lifting airfoil

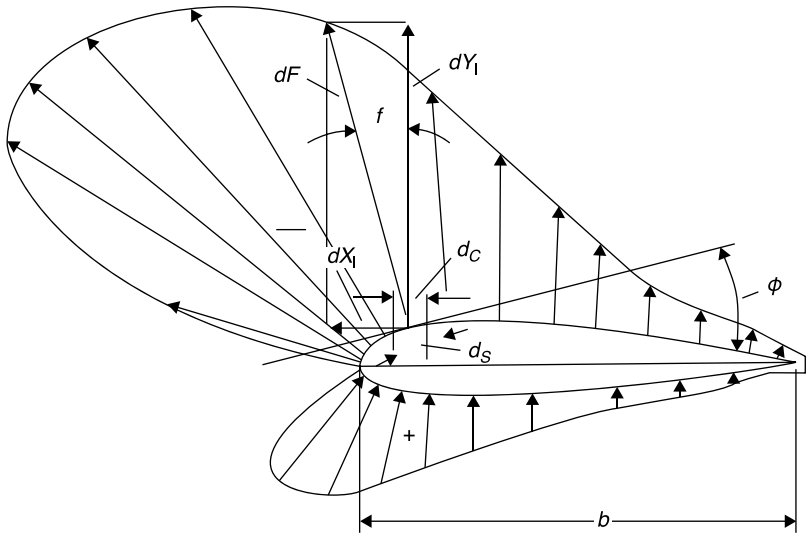

From Equation (7.2) the elemental forces acting normally and along the chord can be derived

$$dY_l = C_p q ds \cos\phi = C_p q dc$$
$$dX_l = C_p q ds \operatorname{sen}\phi = C_p q dy \tag{7.3}$$

In integrating to the whole airfoil, it must be remembered that the force acting on the lower surface must be subtracted from the force dY in each element of the chord "dc"; similarly in the calculation of the force dX on the front in each section "dy" the corresponding force acting on the back of the airfoil must be subtracted. Thus the force Y in the section is calculated by Equation (7.4) where $C_p = C_{pl} - C_{pu}$

$$Y = q\int_0^c C_p dc \tag{7.4}$$

It follows that when the distribution of pressure coefficients is that normal to the chord (Figure 7.16), the distance between the upper curve and lower curve represents the distribution of loading perpendicular to the chord. The integral (7.5) represents the enclosed area:

$$\int_0^c C_p dc = A(z) \tag{7.5}$$

Figure 7.16 Distribution of the pressure coefficients on the chord of a lifting airfoil

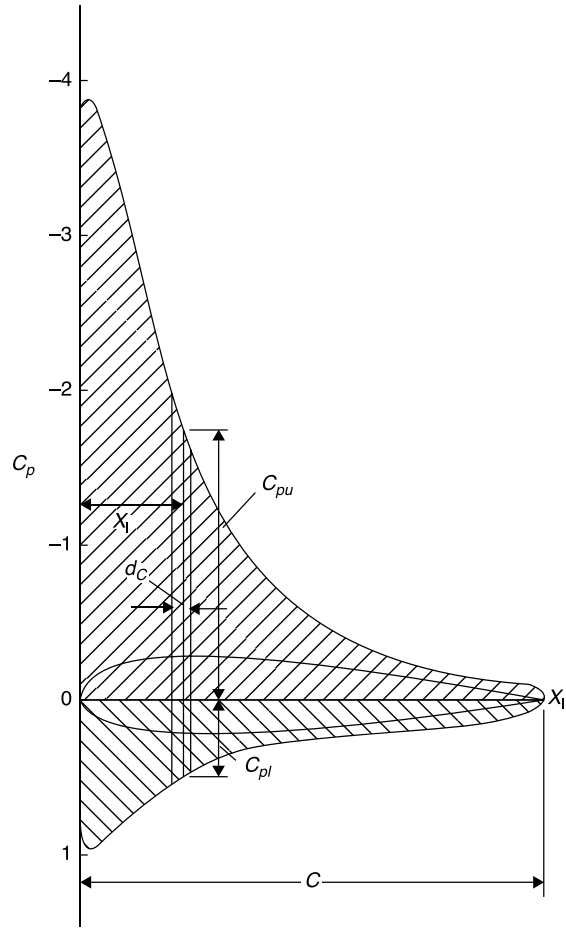

If the wing is not twisted, the value of Equation (7.5) can be calculated in each section and a diagram like that of Figure 7.17 can be built and the total normal force, Y_t, calculated as:

$$Y_t = q\int_{-b/2}^{b/2} A(z)\,dz \tag{7.6}$$

where the integral is the area of the diagram of Figure 7.17.

The total force, X_t, in the direction of the chord is calculated in a similar way by the equation:

Figure 7.17 Distribution of normal force along the wing span

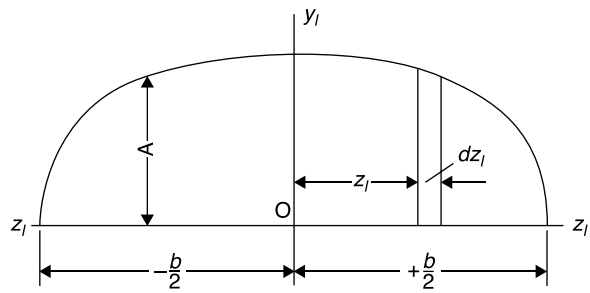

$$X_t = \iint_S C_p q dy dz = q\int_{-b/2}^{b/2} dz \int_{y_l}^{y_u} C_p dy \tag{7.7}$$

where y_u and y_l are respectively the maximum distance of the upper and lower profile from the chord and $C_p = (C_p)_{\text{ant}} - (C_p)_{\text{post.}}$

The integral

$$\int_{y_l}^{y_u} C_p dy = B(z) \tag{7.8}$$

is the area of the diagram $C_p(y)$ of Figure 7.18. Bringing back to the diagram the values along the wingspan (Figure 7.19), the resultant force, X_t, can be derived from Equation (7.9) where the integral represents the area of the diagram of Figure 7.19:

$$X_t = q\int_{-b/2}^{b/2} B(z)\, dz \tag{7.9}$$

Figure 7.18 Distribution of pressure coefficients parallel to the chord of a lifting airfoil

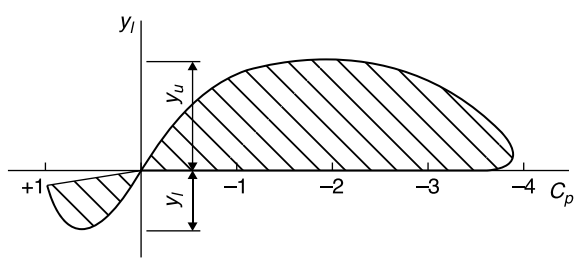

Figure 7.19 Distribution of the force parallel to the chord along the wing span

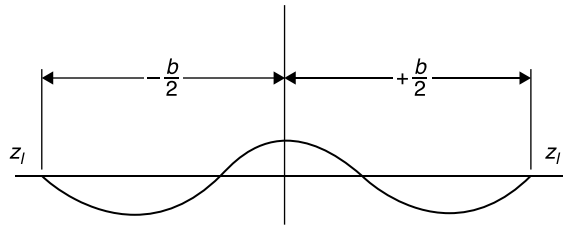

Also the aerodynamic moments acting on the wing can be obtained from the distribution of pressures, for example, the pitching moment with respect to the leading edge is given by:

$$M_z = q\int_0^c C_p x dc \tag{7.10}$$

Finally, the lift, L, and the form drag, D_f, of the wing can be obtained from:

$$\begin{aligned} L &= Y_t \cos\alpha - X_t \operatorname{sen}\alpha \\ D_f &= Y_t \operatorname{sen}\alpha + X_t \cos\alpha \end{aligned} \tag{7.11}$$

It must be stressed that, lacking a measure of tangential stresses, only the part of the drag due to the integral of pressures, that is the form drag, can be obtained from pressure measurements.

7.2.2 Calculation of lift by the distribution of pressures on two walls of the test chamber

In wind tunnels with a closed test chamber with a rectangular shape, it would be possible to calculate the lift acting on a model with a constant section supported between two walls of the test chamber (two-dimensional plane flow), through integration of the pressure on the other two walls. This method stems from the principle of conservation of momentum: the lift generated by the airfoil induces an uneven distribution of pressure on the walls, which are streamlines.

Since the disturbance induced by the airfoil will propagate at infinity upstream and downstream, it should be necessary to integrate these pressures on a domain much larger than the test chamber. Therefore, a

correction factor has to be introduced to take into account the finiteness of the domain of integration.

In the case of supersonic motion, the field is necessarily limited by the intersection with the walls of the shock waves generated on the leading edge and on the trailing edge.

7.2.3 Calculation of the profile drag by measuring the pressure in the wake of the model

The profile drag of a body can be found by measuring the deficit of momentum that occurs in the wake. Consider (Figure 7.20) an airfoil immersed in a stream and apply the equation of balance of momentum in the direction of the stream between a section (1) infinitely upstream of the body, where the velocity and pressure are those of the undisturbed flow, and a downstream section (2) where velocity and pressure are variable in the wake. Denoting by $\underline{\underline{u}}$ the unit tensor and by $\underline{i}$ the versor of the x axis:

$$\int_{-\infty}^{+\infty}\left(p_\infty + \rho_\infty U_\infty^2\right)_1 dy - \int_{-\infty}^{+\infty}\left(p + \rho U^2\right)_2 dy - \int_S \left(p\underline{\underline{u}} + \underline{\underline{\tau}}_\mu\right)\cdot \underline{n}\cdot \underline{i}\, dS = 0 \tag{7.12}$$

Figure 7.20 Determination of profile drag with the Jones method

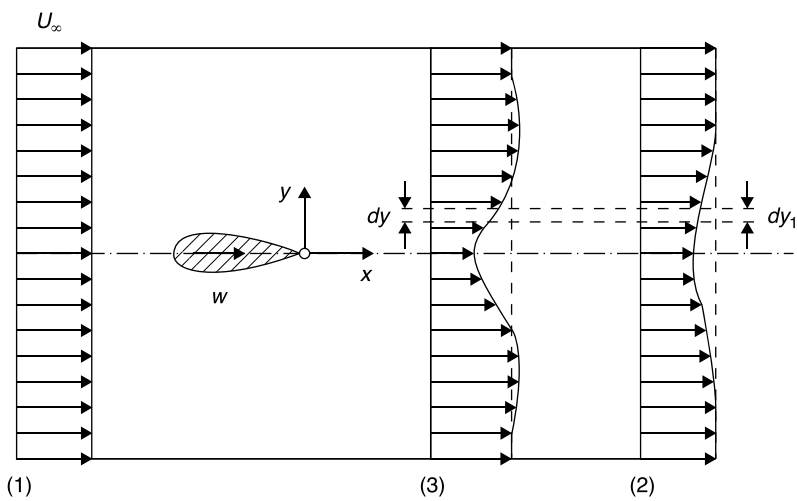

The third integral represents the profile drag, D_p, sum of the form (or wake) drag generated by normal stresses and of the friction drag generated by the viscous stress tensor, $\underline{\underline{\tau_\mu}}$. Therefore, the profile drag, D_p, can be calculated from the equation:

$$«\overset{«}{_p}«⇚\int_{-\infty}^{+\infty}\left({}_{\infty}+\rho_{\infty}\ {}_{\infty}^{2}\right)_1 \quad -\int_{-\infty}^{+\infty}\left(\ +\rho\ {}^{2}\right)_2 \tag{7.13}$$

Integrals of Equation (7.13) must be extended from $-\infty$ to $+\infty$ as for the conservation of mass is:

$$\int_{-\infty}^{+\infty}\left(\rho_\infty U_\infty\right)_1 dy=\int_{-\infty}^{+\infty}\left(\rho U\right)_2 dy \tag{7.14}$$

which shows that the velocity outside the wake at the station (2) must be greater than U_∞ in order to compensate for the flow deficit that occurs in the wake.

Taking account of Equation (7.14), Equation (7.13) can be written:

$$D_p=\int_{-\infty}^{+\infty}\left(p_\infty-p_2\right)dy+\int_{-\infty}^{+\infty}\rho_2 U_2\left(U_\infty-U_2\right)dy \tag{7.15}$$

Since the test chamber has a finite size it is necessary to use some approximations to measure the drag profile. Of all the methods devised to calculate the drag from the balance of momentum, the most commonly used is that of Jones. This method allows the calculation of drag from measurements made only in the wake with an error < 2%.

In an incompressible flow, assuming that the pressure in the station (2) is equal to the pressure of the undisturbed stream, p_∞, i.e. that station (2) is chosen at a very large distance downstream of the airfoil and that outside the wake of the velocity $U \approx U_\infty$, the integral can be extended only to the wake (from $-y_w$ to y_w):

$$D_p=\int_{-y_w}^{y_w}\rho U_2\left(U_\infty-U_2\right)dy \tag{7.16}$$

Since the test chamber has a limited length, a control station (3) not far from the airfoil (e.g. after 2 ÷ 3 chords) must be used. Assuming that between the stations (2) and (3) the Bernoulli theorem is valid (no turbulence in the wake):

$$p_{03} = p_3 + \rho\frac{U_3^2}{2} = p_\infty + \rho\frac{U_2^2}{2} \tag{7.17}$$

The equation of continuity, for incompressible flow, is:

$$\int_{-y_w}^{+y_w} U_3 dy = \int_{-y_w}^{+y_w} U_2 dy \tag{7.18}$$

It is assumed that the wake has the same size in sections (2) and (3) and that the wake is not turbulent: in these two assumptions lies the inaccuracy of the method of Jones. Equation (7.16) becomes:

$$D_p = \int_{-y_w}^{+y_w} \rho U_3 \left(U_\infty - U_2\right) dy = \rho U_\infty^2 \int_{-y_w}^{+y_w} \frac{U_3}{U_\infty}\left(1 - \frac{U_2}{U_\infty}\right) dy \tag{7.19}$$

Taking into account Equation (7.17), the drag coefficient is calculated from:

$$C_{D_p} = \frac{2}{c}\int_{-y_w}^{+y_w} \sqrt{\frac{p_{03} - p_3}{p_{0\infty} - p_\infty}}\left(1 - \sqrt{\frac{p_{03} - p_\infty}{p_{0\infty} - p_\infty}}\right) dy \tag{7.20}$$

To determine the drag coefficient using Equation (7.20) it is therefore sufficient to use Pitot tubes and static pressure tubes: the undisturbed stream conditions, $p_{0\infty}$ and p_∞, are measured upstream of the airfoil, the distributions of stagnation and static pressure in the wake section may be obtained with a wake-rake consisting of a series of static and Pitot tubes connected to a multitube manometer.

In the case of compressible flow Equations (7.17), (7.18), (7.19) and (7.20) become:

$$p_{03} = p_3\left(1 + \frac{\gamma - 1}{2}M_3^2\right)^{\frac{\gamma}{\gamma-1}} = p_\infty\left(1 + \frac{\gamma - 1}{2}M_2^2\right)^{\frac{\gamma}{\gamma-1}} \tag{7.21}$$

$$\int_{-y_w}^{+y_w} \rho_3 U_3 dy = \int_{-y_w}^{+y_w} \rho_2 U_2 dy \tag{7.22}$$

$$D_p = \int_{-y_w}^{+y_w} \rho_3 U_3 \left(U_\infty - U_2\right) dy = U_\infty^2 \int_{-y_w}^{+y_w} \rho_3 \frac{U_3}{U_\infty}\left(1 - \frac{U_2}{U_\infty}\right) dy \tag{7.23}$$

$$C_{D_p} = \frac{2}{c}\int_{-y_w}^{+y_w} \left(\frac{p_{03}}{p_{0\infty}}\right)^{\frac{\gamma-1}{\gamma}} \left(\frac{p_3}{p_\infty}\right)^{\frac{1}{\gamma}} \sqrt{\frac{1-\left(\frac{p_3}{p_{03}}\right)^{\frac{\gamma-1}{\gamma}}}{1-\left(\frac{p_\infty}{p_{0\infty}}\right)^{\frac{\gamma-1}{\gamma}}}} \times \left[1-\frac{1-\left(\frac{p_\infty}{p_{03}}\right)^{\frac{\gamma-1}{\gamma}}}{1-\left(\frac{p_\infty}{p_{0\infty}}\right)^{\frac{\gamma-1}{\gamma}}}\right] dy \tag{7.24}$$

7.3 Measuring the aerodynamic forces with balances

7.3.1 Classification of balances

The balance is an important tool in a wind tunnel as it allows the direct measurement of the aerodynamic forces acting on the model. Aerodynamic balances are very complex because, unlike balances used to measure weight, they need to measure a force of which are unknown, and variable during the experiment, the direction, the sign and the point of application. In the most general 3D field, it is therefore necessary to measure three forces acting along three axes to find the direction of the aerodynamic force and three torques acting around the same axes to determine the point of application of the force. In the case of 2D motion, it is enough to measure two forces and one moment.

The balances may be classified as:

- *permanent balances:* they are part of the wind tunnel and are placed outside the test chamber (Figures 7.1, 7.6 and 7.8); typically one axis is directed in the direction of the axis of the wind tunnel, and hence of the asymptotic velocity, and another is vertical (so the weight of the model affects only one component of the force and one moment);
- *sting balances*, dedicated to each model and incorporated into the sting support (Figures 7.2, 7.3, 7.4 and 7.5); an axis generally coincides with the central axis of the model.

Figure 7.21 Components of the aerodynamic force

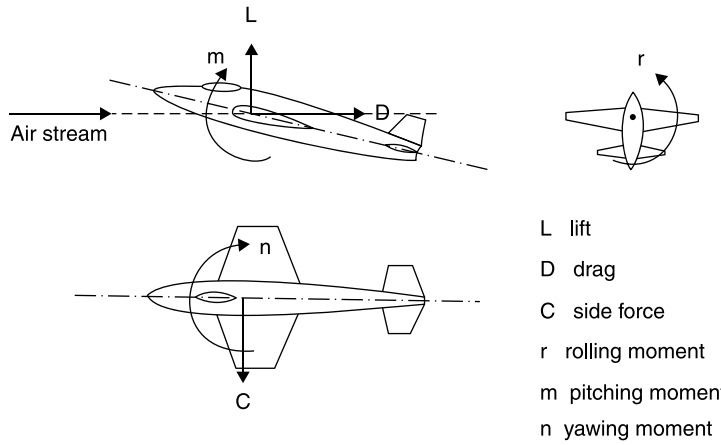

These two systems of axes are respectively the *wind axes* and the *body axes*. Usually forces and moments are referred to the wind axis and have the usual names: *lift, drag* and *side force* and *moments of yaw, roll* and *pitch* (Figure 7.21).

Balances are also classified according to the number of the measured components:

- one-component balances, able to measure the drag of non-lifting bodies (sphere, cylinder normal to the direction of the velocity and symmetrical airfoils at zero incidence);
- two-component balances measure lift and drag;
- three-component balances measure lift, drag and pitching moment;
- four-component balances measure also the rolling moment;
- six-component balances give a complete measure of the interaction between body and fluid stream.

Usually, three-component balances are used, sufficient to study symmetrical flight (side force and roll and yaw moments are zero); only rarely are six-component balances required.

In mechanical balances, the force acting on the model is transmitted through a system of levers through a steel yard along which the weights needed for balancing are slid. In electrical balances, the movements produced by forces cause changes in capacitance, inductance or resistance of an electrical circuit; also quartz transducers are used and, mainly, strain gages.

Depending on the method used for the measurement of the force, balances can be classified as: *null reading* or *deformation balances*. In both systems it is necessary for the body to move, even if infinitesimally, in the direction of the applied force:

- the null reading balances measure the force required to bring the model to the position it had before the application of the aerodynamic force;
- strain gages balances measure the deformation due to the displacement of the model due to the aerodynamic force.

Both methods can be used with any type of support of the model and in any type of wind tunnel. It is just a historical accident that the null reading method has been associated with the permanent balance, which is typical of the low speeds wind tunnels, while the deformation balances were associated with a sting support, mandatory in supersonic wind tunnels.

- The advantages of permanent balances are the fact that when the measure is made, the model is again in the initial state, the high resolution, the ability to maintain calibration over long periods of time. The disadvantages are the high cost and the time required for the initial alignment and calibration.
- The advantages of a sting balance are that the initial cost is lower, though this can be offset by the necessity of having to build many balances with different measuring ranges to suit different needs, and that tests are allowed at very high angles of attack. The disadvantage is the fact that the relationship between displacement and applied force must be determined by calibration and can also be nonlinear, and that at the moment of the measurement the model has shifted from its original position.

No balance can be used for all tests on all possible models, but a permanent balance is more versatile, thanks to the width of the measurement range and the adaptability to unforeseen uses.

7.3.2 Permanent balances

The fundamental difficulty in the design of permanent balances is that they are called upon to measure forces and moments with a high accuracy in the whole range up to the maximum load without appreciable distortions in the structure and down to a small fraction of it. For

example, an experiment on a wing with laminar profile can be followed by tests on a bluff body (such as a radar antenna), and the balance itself should be able to measure the drag of both bodies with sufficient precision. For this reason, permanent balances are designed to have a sensitivity equal to 10^{-4} of the full scale: in this way also in measured quantities hundred times smaller than the maximum range the accuracy does not fall below 1%. (The same problem occurs with the majority of measuring instruments, but while it is quite normal to provide a laboratory with many pressure gages for different pressure ranges, a wind tunnel is equipped with a single null reading balance, which is therefore "permanent.")

Usually the balance is mounted outside the test chamber and the connections are made with the model suspended with wires or mounted on rigid struts. In practice, there are not two balances which adopt the same system and a full discussion of all the sophisticated configurations would occupy too much space. Most connections can be classified into two types: *parallel links and virtual center.*

7.3.2.1 Supports with parallel links

In the schematic of Figure 7.22, the model is supported by wires and forces are measured by 6 dynamometers. The usual components of forces and moments along and around wind axes are calculated, once the weight of the model has been set equal to zero in dynamometers *C*, *D* and *E*, from the equations:

$$\text{Lift} = -(C + D + E)$$

$$\text{Drag} = A + B$$

$$\text{Side force} = -F$$

$$\text{Rolling moment} = (D - C)b/2$$

$$\text{Yawing moment} = (A - B)b/2$$

$$\text{Pitching moment} = -Ec$$

The balances on parallel links are widely used but the wires have given way to rigid rods such as those in Figure 7.1. They can be built and aligned with minimal difficulty, but have the following disadvantages:

- the moments are proportional to small differences between large forces, this would adversely affect the precision of the measurement;

Figure 7.22 Measurement of the aerodynamic force with six dynamometers

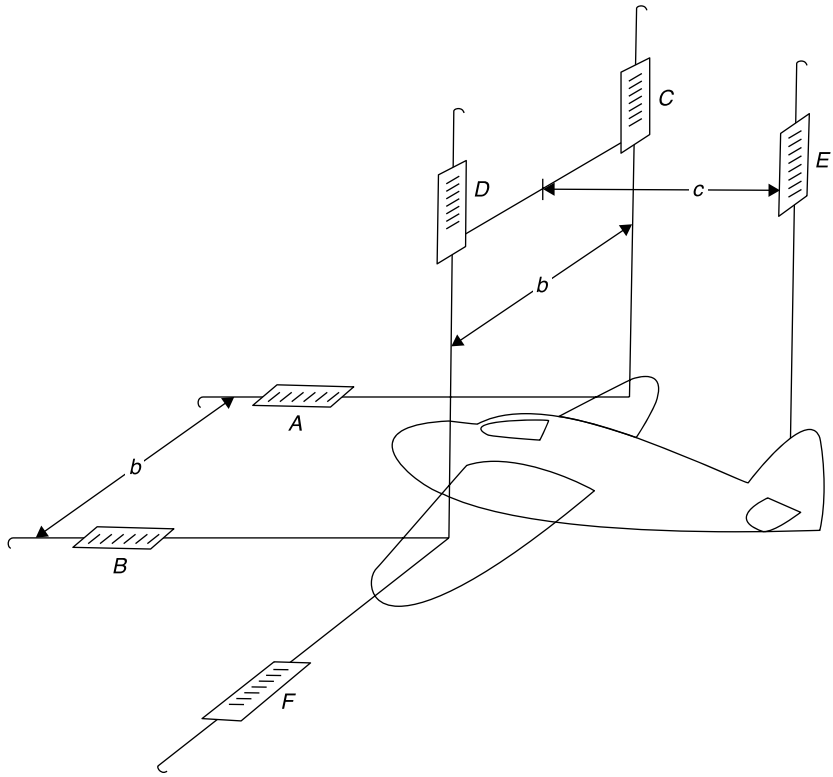

Source: [1]

- the center of resolution of forces is not on the model and then the moments are to be transported;
- drag and lateral force introduce moments of pitch and roll respectively, and these interactions should be removed from the final data;
- the drag of the supports that protrude from the fairing must be taken into account.

All this makes the following mandatory:

- a prior calibration of the balance with known weights needed in order to identify the interaction between the various components;
- measurements taken in a test without a model to determine the drag of the supports (the interference that occurs when model and support are connected remains unknown).

7.3.2.2 Supports with a virtual center

Some of the problems of systems with parallel links are eliminated in the *pyramidal support* (Figure 7.23) where the moments are referred to the center of resolution and the six components are inherently separate and read directly from six units that do not need to add or subtract components. Sensitive issues to be considered in the design and calibration of this type of balance are the perfect alignment of the inclined rods and their deflections. Truncated rods must be carefully aligned so that their extensions pass through a common point. The forces and moments are:

Figure 7.23 Virtual center balance

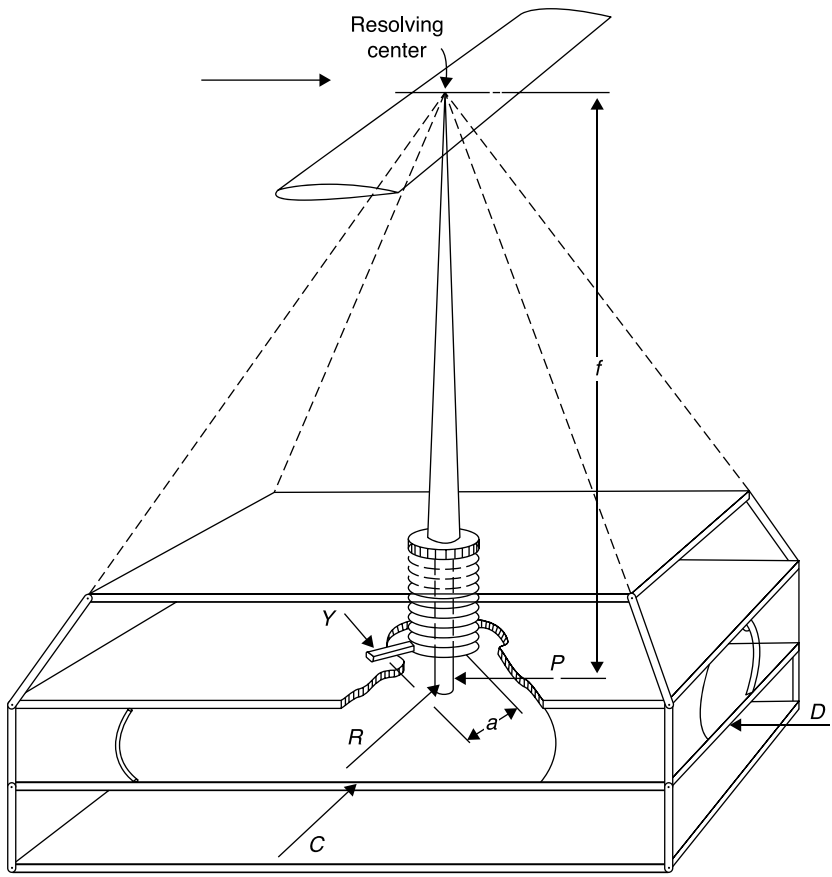

Source: [1]

Figure 7.24 **Automatic counterweights balance**

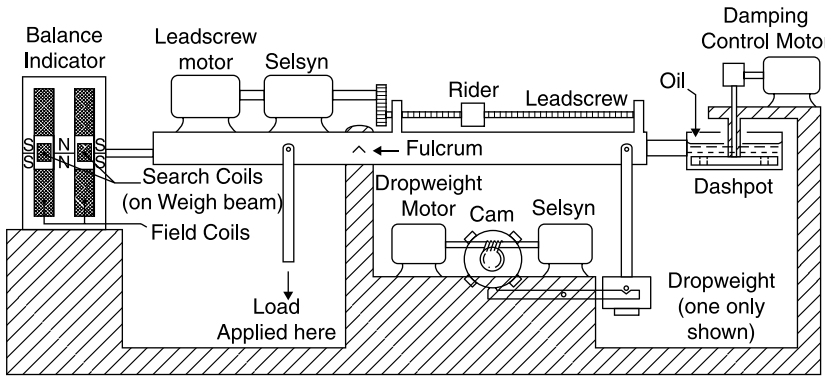

Lift = vertical force

Drag = $-D$

Side force = $-C$

Rolling moment = Rf

Yawing moment = $-Ya$

Pitching moment = Pf

7.3.2.3 Dynamometric elements

For each component to be measured manually or automatically (Figure 7.24), balances are used which employ a sliding weight on a worm and cam mechanism to add or remove additional weights. Other types of dynamometers have a load cell, in which the force is balanced by a pressure exerted by a fluid, or strain gages, used more frequently in deformation balances.

7.3.3 Deformation balances

7.3.3.1 Resolution of forces

The bending moment produced in a sting by the aerodynamic force is proportional to the difference of the readings of two strain gages, assumed to be identical, compressed on one side and elongated on the other side of the sting. The sting is made with a series of hollow sections properly oriented to offer different flexibility depending on the direction of the

Figure 7.25 Sting with three-component strain gage balance

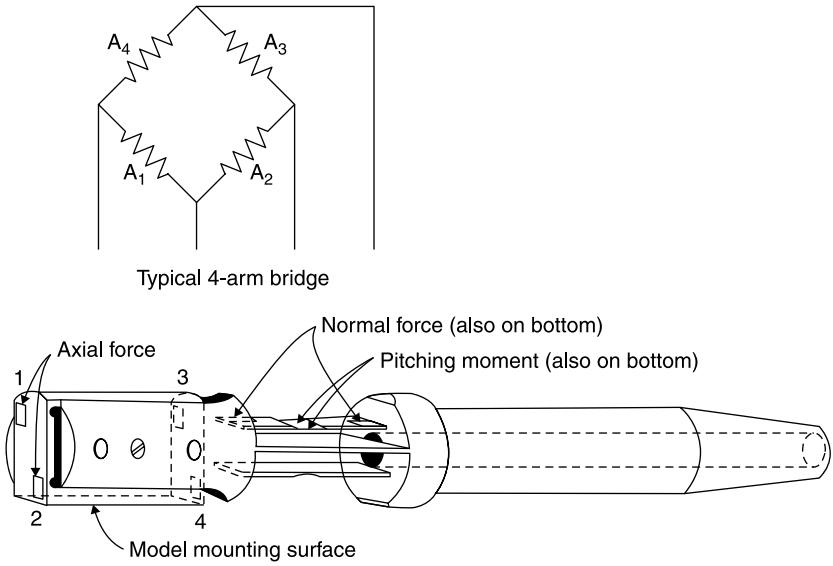

Source: NASA design

components to be measured. In the scheme of Figure 7.25, strain gages are arranged in pairs on the horizontal plates of the frame at the measuring lift and pitching moment. The force and the moment can be calculated from the bending moments, M_1 and M_2, as computed by the deformation detected by two pairs of strain gages placed at two points at a distance x_1 and x_2 from the origin of the axes. The force normal to the line joining the two points is given by:

$$F = \frac{M_1 - M_2}{x_1 - x_2}$$

and the moment is determined by the equation:

$$M = \frac{M_2 x_1 - M_1 x_2}{x_1 - x_2}$$

In Figure 7.26, strain gages are arranged on the vertical sides in order to measure drag (axial force) but also normal force contributes to deformations.

The rolling moment can be measured by one or more pairs of strain gages placed at ±45° with respect to the axis of the sting: the torque is

Figure 7.26 Interaction of normal force on axial force

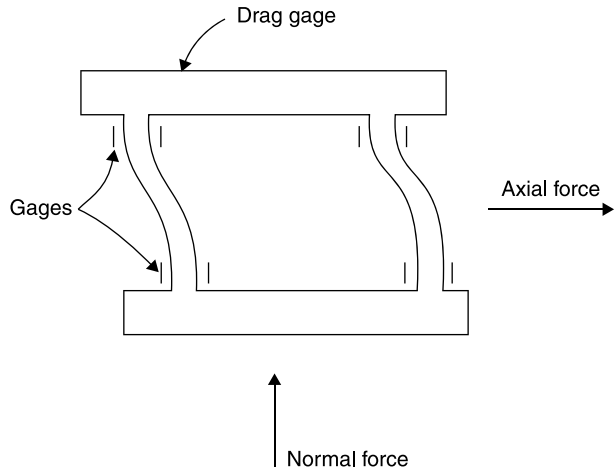

proportional to the differences between strains in these two main directions. Alternatively, the rolling moment can be measured in terms of tension and compression on either side of the central axis of the sting. In the usual procedure the rear of the sting is connected to the tunnel through a buffer that allows the freedom to roll through a braking element to which are attached strain gages.

The strain balances rarely have six components as they are usually designed ad hoc for a particular model. The arrangement of strain gages can be quite complicated even considering the need to compensate for the temperature sensitivity. Since strain gages cannot be considered perfectly equal to each other, an accurate calibration is needed, which can be very challenging with six components.

7.3.3.2 Resistance strain gages

In resistance strain gages, the elongation caused by the deformation of the element on which they are mounted produces a change in electrical resistance. The relative change in resistance is a multiple (*gage factor*) of deformation, ranging from two to five in the wire strain gages (see Section 1.4.2). The deformation measured can be related to the force or the bending moment acting on the element. The wire is usually bent zig-zag or spiral to increase the effective length and is embedded in a thin Bakelite support that is glued onto the rod. The typical lengths of strain gages are 0.5 to 1 cm, much larger than those used in structural analysis. Semiconductors have a gage factor of order 100 but are

much more common in pressure transducers than in aerodynamic balances.

7.3.3.3 Temperature sensitivity

A change in temperature of 1°C produces the same change in resistance produced by a strain numerically equal to α/G, where α is the temperature coefficient of resistance and G is the gage factor. If $\alpha = 1/300°C^{-1}$, approximate value for many pure metals, the apparent deformation is in the order of 1/600, which would correspond in steel to a stress of approximately 700 Nmm^{-2}, the order of maximum allowable stress; the magnitude of the error can be reduced considerably by using an appropriate material for wire (for the constantan $\alpha \approx 0°C^{-1}$). A low temperature coefficient must take precedence over other desirable qualities for the material and is the main reason for the low popularity of semiconductor strain gages in wind tunnel balances.

In addition to the choice of a suitable material, however, other precautions are necessary to minimize errors due to temperature changes. The simplest method of temperature compensation is to provide a second not stretched strain gage near each strain gage and put them in two adjacent sides of a Wheatstone bridge: in this way the temperature changes do not alter the balance of the bridge. The changes in resistance due to temperature are also negated when the responses of two adjacent active strain gages must be subtracted to obtain a force or a moment.

The balances for intermittent wind tunnels and shock tubes can also be thermally insulated. Balances were also used with air conditioning in wind tunnels for continuous operation, particularly those in which large variations in stagnation temperature occur. These precautions should be regarded as additional to the use of a balanced bridge, using a material with a low temperature coefficient of resistance.

The strain gages are also sensitive to moisture in a fairly random way. One reason for not attempting to waterproof each strain gage is the fact that in this case it is more difficult to dry once they are wet, and if problems are expected, the entire balance can be sealed after placing a desiccant inside the enclosure.

7.3.3.4 Frequency response

The deformation balances have the advantage of a much faster response: in a null reading balance, even if automatic, the inertia of the system

will not allow the measurement of rapidly varying forces. The only limit to the frequency response of a deformation balance is fixed by the natural frequencies of the sting and the model. In addition to the measurement of forces on oscillating models, strain gages can be used to measure the hinge moments of control surfaces: before the introduction of the strain gages hinge moments were measured by connecting the control surface to a balance outside the wind tunnel; the unsteady hinge moments could not be measured by any convenient method.

7.3.4 Calibration of balances

Whichever balance is used, it is essential to carry out a prior calibration applying known forces in the various directions. The easiest way to apply the forces is to use weights and apply them in different directions using appropriate pulleys.

Imperfections in the alignments of the axes of the balance with the stream and interactions of different measured components may occur so that, for example, the application of a force of pure drag may slightly affect the reading of the lift and, generally, of all other components. The procedure to investigate and eliminate the interactions of a complex balance is impressive: the initial set-up of a six-component balance in a large wind tunnel can require months of work.

It is possible to measure the effect on each component of the application of forces along the other axes in turn, find empirical relationships and store them in a computer to use during testing to measure the actual components free from the interactions.

The procedure can be simplified if the interactions are so small that they can be considered linear and hence can be summed. A matrix of coefficients of influence, $[C_{ij}]$, for each applied force, $\{F_A\}$, on the measured forces, $\{F_M\}$, can be determined

$$\{F_M\} = [C_{ij}]\ \{F_A\}$$

This matrix can then be inverted to determine, from the readings of the balances, the components of the applied force free from interactions:

$$\{F_A\} = [C_{ij}]^{-1}\{F_M\}$$

7.3.5 Magnetic support and balance system

In these systems, the model is supported by magnetic forces without any solid support and its aerodynamic interference; the aerodynamic forces are measured through the electrical currents required by the magnetic fields to keep the model in equilibrium with the desired attitude. The first system was built at ONERA in 1957. Since then, many plants have been built in Europe, the United States and Japan.

7.3.5.1 Principle of operation

A magnetic support and balance system is composed of five elements:

1. a magnetic core within the model;
2. a set of electromagnets placed outside the test chamber to keep the model in the desired position;
3. an optical system for detecting the position of the model;
4. a system for monitoring the intensity of the electrical current flowing in the electromagnets;
5. an overall management system.

In the plant built at the NASA Langley Research Center (LARC) in 1964, we see in Figure 7.27 a simple example showing the principle of operation of the system. The balance has a single component because the test model is a sphere, the stream is directed downward and hence the direction of the aerodynamic force (drag) coincides with that of gravity.

The system for detecting the position of the model consists of a light beam incident on a photocell. The magnetic field, provided by a magnet coaxial to the wind tunnel, supports the weight of the sphere which intercepts the light beam; the downward displacement of the model due to the aerodynamic force makes the illumination of the photocell vary which results in sending, through its control system, more current in the electromagnet to restore the original position of the model. From the increase in electrical current the intensity of aerodynamic drag can be inferred.

7.3.5.2 The core

The core of the model is usually a permanent magnet made with samarium–cobalt or Alnico. The Alnico provides a greater intensity of

Figure 7.27 An early one-component magnetic balance made at NASA LARC

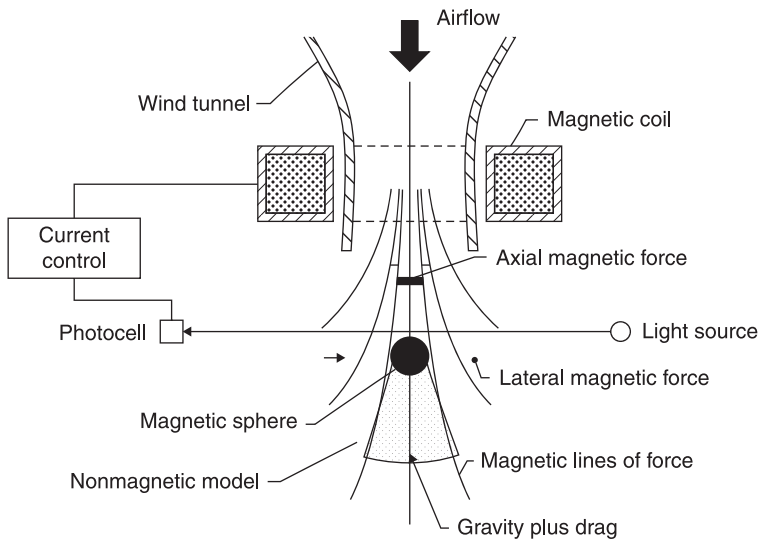

magnetization than samarium–cobalt, but is characterized by a more rapid decrease in the intensity of magnetization and a greater sensitivity to shocks.

An alternative is a core consisting of a solenoid made with a superconducting material (NbTi) wrapped around a core of superconducting material (NIOMAX CN 61/25). Superconducting materials provide virtually zero electrical resistance at extremely low temperatures, in the order of a few degrees *K*. For this reason, the coil is placed in a cylindrical Dewar vessel containing liquid helium.

Permanent magnets have the advantage of being relatively inexpensive and provide an intensity of magnetization that is practically constant. That means significant simplifications in the calibration procedure of the forces acting on the model as a function of electrical current flowing in the electromagnets. The disadvantage of this type of core is the limited strength of the magnetization vector: this requires, for the same forces and magnetic moments, larger electromagnets and a greater electric power.

The drawbacks of the core made with a superconducting solenoid are:

- the complexity of building the core and the model;
- the complexity of the procedure used;

- operational life of about 70 minutes before the complete evaporation of liquid helium;
- decline of the current in the solenoid during operation (difficulty in calibration).

7.3.5.3 Electromagnets

Electromagnets consist of coils, usually copper, wrapped tightly around a laminated core of ferromagnetic material (soft iron, steel, cobalt). Electromagnets require a refrigeration system, generally water, to dispose of heat produced by the dissipated electricity.

Each plant is characterized by its pattern of electromagnets around the test chamber and by their constructive solutions. The schema of a quite complex plant built at the Southampton University is shown in Figure 7.28: ten magnets, disposed in antagonistic pairs, ensure the

Figure 7.28 **Positions of magnets in a six-component balance at Southampton University, UK**

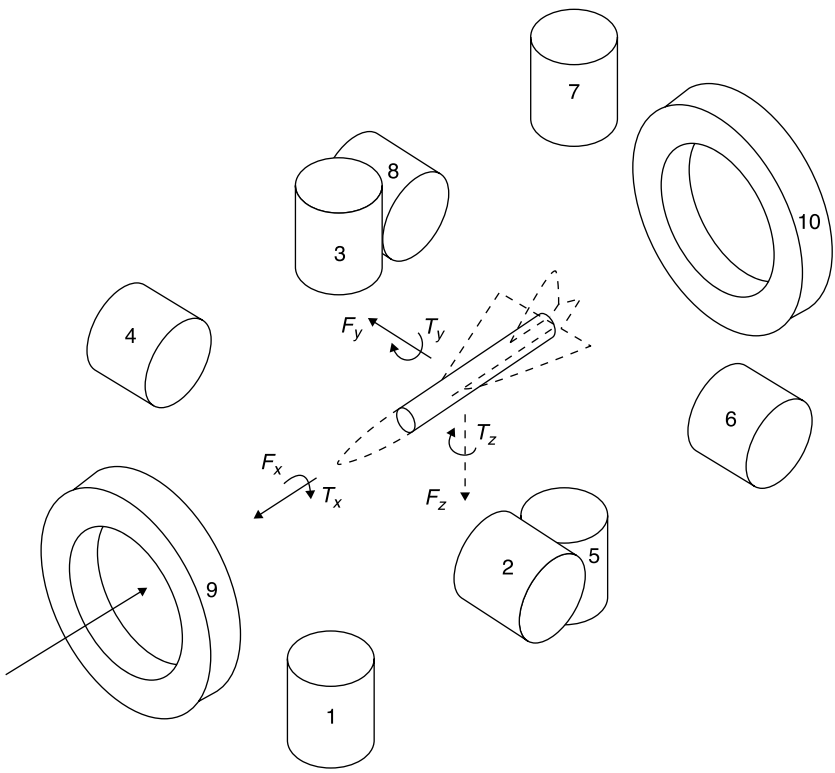

symmetry along the three axes of the wind tunnel, then the system is able to control all degrees of freedom of the model. Magnets 1, 3, 5, 7 control vertical position and pitch angle, magnets 2, 4, 6, 8 control transverse position and yaw angle, while magnets 9 and 10 control the longitudinal position. The roll angle is controlled by the electromagnets from 1 to 8.

7.3.5.4 Position and attitude sensors

Model position detection system can be formed by optical sensors and helium–neon lasers outside the test chamber. The sensors are a combination of linear photodiodes. A typical sensor consists of 1024 photodiodes and has a linear dimension of 1 in., the precision of position detection is therefore about 25 μm. Laser beams, to illuminate the sets of linear photodiodes, are made plane through cylindrical lenses. The position and attitude of the model are obtained by the shadow of the model on the sensors and are measured by the number of illuminated photodiodes. Models are usually painted in matt black in order to avoid possible light reflections.

The number and location of optical sensors and lasers are functions of the number of degrees of freedom to be controlled. Figure 7.29 illustrates the schema of a system of position and attitude sensors in a balance with five degrees of freedom; lacking the sensitivity to roll, only tests on axially symmetric bodies are allowed. The longitudinal position is detected by sensor 2 through the partial shielding of the drag laser beam; the vertical position and the pitch angle from sensors 1 and 5 through the partial shielding of the horizontal laser beams, and finally the transverse position and the yaw angle by sensors 7 and 4 through the partial shielding of the vertical laser beams. Other detection systems may be an X-ray system or a television system.

7.3.5.5 Determination of forces and moments

The number of degrees of freedom of the system depends on both the number and location of the electromagnets and the number of households accommodated within the model. The system in Figure 7.29 can control, for example, only five degrees of freedom (the three shifts and two rotation axes of pitch and yaw) because there is only one core whose magnetization vector is characterized by a single component along the longitudinal axis of the model.

In the case of a model aircraft, the rolling moment is obtained with magnetic cores put in the wings, or building the wings with magnetic material.

Figure 7.29 **Arrangement of position sensors in a five-component balance**

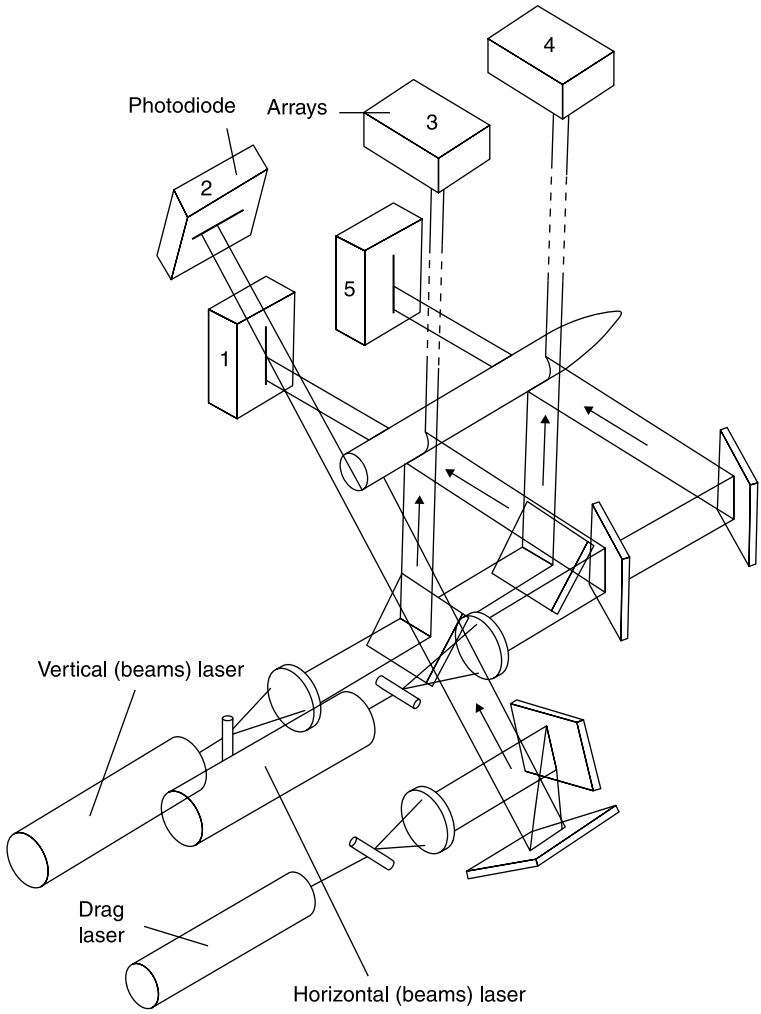

7.3.5.6 Limitations of magnetic balances

The disadvantages of magnetic balances have so far limited the spread of their use to industrial wind tunnels: the first is the high investment and management costs due to maintenance and to the high consumption of electricity and of cryogenic liquids.

In addition to this economic aspect, the use of magnetic balances can also lead to some technical and operational problems such as:

- interference from high intensity magnetic fields on control and measurement systems as pressure transducers housed in the model;
- the risk of damage to both the model and wind tunnel due to the possible loss of control of the model;
- the difficulty of performing certain experiments as, for example, simulation of propulsion. This type of testing requires the use of gas to be expelled from the model to simulate the presence of a jet. In a conventional wind tunnel, gas is supplied to the model through the support, in a magnetic suspension system, the gas must be contained in tanks housed within the model with space problems;
- the difficulty of flow visualization (Schlieren, interferometry, etc.) both for the poor optical access to the model and for the possible interference with the optical control systems.

For all these reasons, to date, magnetic balances have been used only in small wind tunnels, primarily for research purposes.

References

1. W.H. Rae and A. Pope (1984) *Low-Speed Wind Tunnel Testing*. New York: John Wiley & Sons, Ltd.
2. A.K. Martynov (1965) *Practical aerodynamics*, International Series of Monographs in Aeronautics and Astronautics.
3. H. Schlichting and K. Gersten (2000) *Boundary layer theory*, Springer.

Index

Related titles:

Leveraging Information Technology for Optimal Aircraft Maintenance, Repair and Overhaul
(ISBN 978-1-84569-982-6)
Aimed at professionals in the aviation industry and students of Aircraft Maintenance, this book covers the use and management of technology in the Aviation Maintenance, Repair, and Overhaul (MRO) context. This book will provide a backdrop of current trends in the industry where Airlines are tending to retain their aircraft longer on the one hand, and rapidly introducing a new genre of aircraft such as the A380 and B787 into service. This book aims to provide industry professionals and students of Aviation MRO (at all levels) with the necessary principles, approaches and tools to respond effectively and efficiently to the constant development of new technologies - both in general and within the Aviation MRO profession. It highlights the unique information requirements for Aviation MRO and delves into the detailed aspects of information needs from within the industry such as Engineering and Maintenance Planning, Aircraft/Engine/Component Configurations, Materials Management, Logistics, and Technical Documentation. It will highlight the difference between on-wing and off-wing maintenance with their unique information processing needs. This book is designed as a primer on IT services for Aircraft Engineering professionals and a handbook for IT professionals servicing this niche industry.

Modelling and Simulation of Integrated Systems in Engineering: Issues of methodology, quality, testing and applications
(ISBN 978-1-85709-078-2)
This book places particular emphasis on issues of model quality and ideas of model testing and validation. Mathematical and computer-based models provide a foundation for explaining complex behaviour, for decision-making, for engineering design and for real-time simulators for research and training. Many engineering design techniques depend on suitable models. Assessment of the adequacy of a given model for an intended application is therefore critically important. Generic model structures and dependable libraries of sub-models that can be applied repeatedly are increasingly important. Applications are drawn from the fields of mechanical, aeronautical and control engineering, and mainly involve non-linear lumped-parameter models

described by ordinary differential equations. Topics considered repeatedly in the context of these applications include: system identification and parameter estimation; parameter sensitivity analysis; model optimisation; and inverse simulation.

Spacecraft Thermal Control
(ISBN 978-1-84569-996-3)
This book covers the necessary material to allow an engineer to perform the design and qualification of a Space Thermal Control System in a comprehensive way. Beginning with the fundamentals of Space Missions and following with the indispensable background on Heat Transfer, a full description of current thermal control technologies is then presented. The overall view presented in *Spacecraft Thermal Control* details the complete process in the design and validation (analysis and tests) of these systems. Finally relevant data on material properties are given.

Orbital Mechanics and Formation Flying: A digital control perspective
(ISBN 978-0-85709-054-6)
Aimed at students, faculty and professionals in the aerospace field, this book provides practical information in the development, analysis, and control of a single and/or multiple spacecraft in Space. This book is divided into two major sections: single and multiple satellite motion. The first section will analyze the orbital mechanics, orbital perturbations, and attitude dynamics of a single satellite about the Earth. Using the knowledge of a single satellite motion, the translation of a group of satellites called formation flying or constellation is explained. Formation flying is one of the main research topics in the last few years and this book explains different control approaches to control the satellite attitude motion and/or to maintain the constellation together. The control schemes are explained in the discrete domain such that it can be easily implemented on the computer onboard the satellite. The key objective of the book is to show the reader the practical and the implementation process in the discrete domain.

Details of these and other Woodhead Publishing books can be obtained by:

- visiting our web site at www.woodheadpublishing.com
- contacting Customer Services (e-mail: sales@woodheadpublishing.com; fax: +44 (0) 1223 832819; tel.: +44 (0) 1223 499140; address: Woodhead Publishing Limited, 80 High Street, Sawston, Cambridge CB22 3HJ, UK)

If you would like to receive information on forthcoming titles, please send your address details to Customer Services, at the address above. Please confirm which subject areas you are interested in.

Aerodynamic measurements

From physical principles to turnkey instrumentation

GIUSEPPE P. RUSSO

Oxford Cambridge Philadelphia New Delhi

Woodhead Publishing Limited, 80 High Street, Sawston,
Cambridge CB22 3HJ, UK
www.woodheadpublishing.com

Woodhead Publishing, 1518 Walnut Street, Suite 1100,
Philadelphia, PA 19102-3406, USA

Woodhead Publishing India Private Limited, G-2, Vardaan House, 7/28 Ansari Road,
Daryaganj, New Delhi – 110002, India
www.woodheadpublishingindia.com

First published 2011, Woodhead Publishing Limited

British Library Cataloguing in Publication Data
A catalogue record for this book is available from the British Library.

Library of Congress Control Number: 2011919190

Woodhead Publishing ISBN: 978–1–84569–992–5 (print)
ISBN: 978–0–85709–386–8 (online)

Typeset by RefineCatch Limited, Bungay, Suffolk
Printed in the UK and USA

Contents

List of figures

List of tables

Preface

Nowadays instrumentation is supplied as a turnkey apparatus displaying the results of measurements on the screen of a personal computer. Compared to the tedious data handling (in the sense of made by hands) of few decades ago this is a wonderful improvement and allows making many detailed measurements compared to the few data achievable in the hand made experiments: the resulting graphs often compare well with those obtained with CFD.

Nevertheless despite this shifts to automated systems, the basic methods and theory have not changed, In fact it is now more necessary than before to clearly and thoroughly understand the basic test techniques and objectives so that test can be planned and carried out knowing the limits and the approximations of the instrument used.

The present book presents a comprehensive review of the theoretical bases which experimental techniques used in aerodynamics are based on. Limitations of each method in terms of accuracy, response time, and complexity are addressed. The book will therefore serve as a guide in choosing the most pertinent technique for each type of flow field: 1D, 2D, 3D, steady or unsteady, subsonic, supersonic of hypersonic.

The bulk of the book originated in a course on "Experimental Aerodynamics" that the author taught for 34 years at the Università di Napoli "Federico II".

The book is intended primarily for aeronautical and mechanical engineering students entering the field of experimental aerodynamics since it is felt that, although having a good knowledge of the theory, they may in many cases have had little opportunity of becoming familiar with experimental practice. It is hoped that the work may also be of value as a reference book for the research worker and for the model-testing personnel of wind tunnels.

Acknowledgements

After years of teaching I scarcely remember the sources of those I now consider as my ideas. I can say that I am indebted with the Princeton series, the NACA, NASA and AGARD Reports, the classical books on wind tunnels by Pope-Goin and Pankhurst-Holder, the websites of the manufacturers of instruments.

I thank my students in Naples that with their endless discussions highlighted the less understandable items of the subject of aerodynamics measurements.

I wish to express my thanks to Glyn Jones and Jonathan Davis at Chandos Publishing who constantly followed my effort giving me always pertinent suggestions.

I thank Donna White at RefineCatch Ltd for her careful and competent proofreading and for the work done in bettering many figures of the book having a low resolution.

About the author

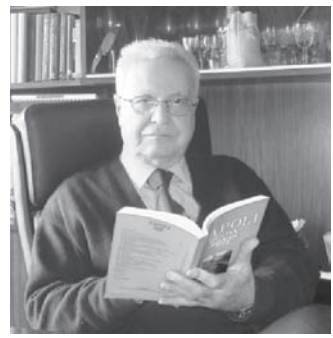

Giuseppe P. Russo, Aeronautical Engineer, is a recently retired Associate Professor of Experimental Aerodynamics at the Università degli Studi di Napoli "Federico II", Dipartimento di Ingegneria Aerospaziale (DIAS). Prior to that, he was Assistant Professor of Gas dynamics from 1967 to 1982 at the same university. He has been the author of about 70 scientific papers, a consultant of Centro Italiano di Ricerca Aerospaziale (CIRA), of Agenzia Spaziale Italiana (ASI) and of Alfa Romeo Avio. He was a Member of the Fluid Dynamic Panel of AGARD/NATO from 1992 to 1997. He was Chairman of the Naples branch of the AIDAA (Associazione Italiana di Aeronautica ed Astronautica) from 1996 to 2010. He is one of the founders of the Science Centre "Città della Scienza" in Naples.